The Importance of Photoevaporation in the Evolution of Protoplanetary Discs

Andrew David Sellek

Supervisor: Prof. Cathie J. Clarke

Institute of Astronomy
University of Cambridge

This dissertation is submitted for the degree of
Doctor of Philosophy

Trinity College October 2023

Dedicated to my ever-supportive parents...

Declaration

This thesis is submitted for the degree of Doctor of Philosophy. I hereby declare that it is the result of my own work and includes nothing which is the outcome of work done in collaboration except as declared below. Except where specific reference is made to the work of others, the contents of this dissertation are original and are not substantially the same as any work that has already been submitted in whole or in part for any degree or other qualification at this or any other university. It does not exceed the prescribed word limit of 60,000 words for the Degree Committee for the Faculty of Physics & Chemistry.

The following Chapters contain material which has been published, or are in preparation for publication, in peer-reviewed journals:

1. **Introduction**

   Section 1.2.2 is partly based off of Section 2 of
   The general applicability of self-similar solutions for thermal disc winds
   Sellek A. D., Clarke, C. J., Booth R. A., 2021, MNRAS, 506, 1

   Section 1.2.3 is partly based off of Section 5.2 of
   The importance of X-ray frequency in driving photoevaporative winds
   Sellek A. D., Clarke, C. J., Ercolano B., 2022, MNRAS, 514, 1

2. **Chapter 2**

   is adapted from the majority of
   The general applicability of self-similar solutions for thermal disc winds
   Sellek A. D., Clarke, C. J., Booth R. A., 2021, MNRAS, 506, 1

3. **Chapter 3**

   Section 3.3 is adapted from
   The importance of X-ray frequency in driving photoevaporative winds
   Sellek A. D., Clarke, C. J., Ercolano B., 2022, MNRAS, 514, 1

Section 3.4 is based on ongoing work - which is yet to be published - in collaboration with
Barbara Ercolano, Tommaso Grassi, Giovanni Picogna, Christian Rab & Cathie Clarke

4. **Chapter 4**

    Section 4.2 is adapted from Section 8.3 of
    The general applicability of self-similar solutions for thermal disc winds
    Sellek A. D., Clarke, C. J., Booth R. A., 2021, MNRAS, 506, 1

    Section 4.3 is based on modelling - which is yet to be published - that I have carried out as part of the JWST GO 2260 collaboration with
    Ilaria Pascucci, Cathie Clarke, Naman Bajaj, Chengyan Xie, Andras Gaspar, Jane Morrison, Uma Gorti, Richard Alexander & Giulia Ballabio

5. **Chapter 5**

    is adapted from
    A dusty origin for the correlation between protoplanetary disc accretion rates and dust masses
    Sellek A. D., Booth R. A., Clarke, C. J., 2020, MNRAS, 498, 2

Andrew David Sellek
October 2023

The Importance of Photoevaporation in the Evolution of Protoplanetary Discs

Andrew David Sellek

Protoplanetary discs consist of gas and dust - the remnants of the star formation process - found around stars in the first few million years of their life. Photoevaporation, whereby high-energy radiation from the central star heats disc material causing it to flow away in a wind, is one process thought to contribute to their ultimate dispersal. Previous studies have failed to reach a consensus on the main radiation which is responsible for this process, variably finding the X-ray, Extreme Ultraviolet, or Far Ultraviolet. These paradigms make very different predictions for the amount of mass lost to the winds, and consequently how important they are for disc evolution.

The primary aim of the thesis is to tackle this uncertainty from the following directions: a) by understanding the microphysical processes that underpin the differences in existing models in order to establish a comprehensive methodology for future state-of-the-art photoevaporation simulations that resolve the present disagreements; b) by considering how different wind models appear in observations of atomic forbidden emission lines and so how both line profiles and spatially resolved emission may be used to constrain the wind's nature; c) by including photoevaporation in models of disc evolution on secular timescales that predict its interplay with other processes - and how this manifests in disc demographic surveys - and thus determine how it contributes to the disc's ultimate dispersal.

I conclude that while EUV-driven models have underestimated the role of X-ray due to a lack of detail in the spectrum, the X-ray driven models have underestimated the cooling from molecular emission lines. Thus; the true picture may be expected to be somewhat intermediate between the two extremes. Constraints from disc demographics require low enough rates that discs survive to the age of older star forming regions even around low-mass stars, and there is time for dust to deplete considerably before the wind disperses the gas. Conversely, ratios of emission lines require a high enough mass-loss rate to ensure the wind is only weakly ionised.

Acknowledgements

First and foremost none of this work would have been been possible without Cathie's guidance over the last four or so years. I have always come away from our discussions re-energised, re-focused and with a deeper understanding of the subject and how my work fits into the wider picture. While keeping me on track, Cathie has also given me the space to explore ideas, collaborate widely and grow as a researcher and I will always be extremely grateful for her invaluable support.

Thank you to all the other members of the DISCSIM group - especially my fellow students for many years Chiara, Maggie, Hannah and Francesco - for the interesting conversations and their companionship on various trips. Particular thanks must also go to Richard Booth, for it was through working with him that I became captivated by the field of protoplanetary discs. Richard has been an invaluable font of computational insights, theoretical knowledge, feedback on drafts and writing tips (particularly reminders of how to structure a paragraph well!).

My next thanks go to Barbara Ercolano, for her ever-speedy support with MOCASSIN and job applications, and for inviting me to get involved with her group's work coupling hydrodynamics and thermochemistry. Moreover I would like to apologise to Tommaso Grassi, for the number of PRIZMO bug fixes I have requested (and for making him code the solution to a 5x5 matrix equation by hand) and thank him and Giovanni Picogna for all their support in getting PLUTO and PRIZMO working sensibly. Last but not least, thank you to Christian Rab for his insights into thermochemical modelling.

I was lucky enough to spend last April in the warmer climes of Tucson, thanks to the support of Dustbusters. Thanks go to everyone at the University of Arizona who hosted my visit, in particular Ilaria Pascucci for all her time, hospitality and guidance on the observations. The project that became most of Chapter 4 was initiated by this visit and I thank everyone involved in GO 2260 for having me onboard and for all the useful discussions over the last twelve months which have shaped the direction of the project. Particular thanks also go to Martin Schlecker for kindly letting me his spare room for the duration of the visit, and helping me to make the most of my visit exploring the city.

And thank you to everyone else who has provided stimulating discussions over the years, particularly Tom Haworth for helping me maintain a side interest in external photoevaporation, and my examiners for a stimulating and enjoyable viva which helped reinforce both my own understanding and the strength of the arguments set forth herewithin.

Turning to practicalities, thank you to Paul Hewett and Debbie Peterson for all their assistance from fielding queries about funding and submissions, to their support for students leaving for and returning after lockdown. Thanks must also go to all of the IoA Professional Services Staff who curcially keep the institute functioning as both a workspace and a community. Likewise thank you to all the organisers of all the IoA's seminars, colloquia, journal clubs and workshops for giving their time to enable these enriching activities. I also acknowledge the support of the Science and Technology Facilities Council through my studentship.

Moreover, no PhD would be possible without a good cohort to enjoy (and endure) it with - to Alex, Andy, Annabelle, Aoife, Chiara, Clay, Erik, Johnny, Maggie, Marc, Payton, Sam, Savvas, Stefan, and Steve, thank you for the camaraderie, for putting the entertainment into every tea and coffee and for organising a myriad of social events. Particular thanks must go to those of you - plus Jess and Zofia - who have recently formed the core of the regular Wednesday/Thursday evening boardgamers or the "Trachea Lads" who took on Frank's fiendish quizzes but sadly were never quite in line for a heritage pub tour. Thank you too to all the coffee-time cruciverbalists - especially Tom, Aneesh, and Lewis for inviting me to join in the first place, and all those who kept it going virtually throughout lockdown - and sorry to all those who don't know one end of an anagram from the other for subjecting you to our mystifying hobby.

Another major feature of the last few years has been my time helping to run Cambridge Hands-On Science (CHaOS). It has been an honour to help such an exciting and impactful project along the way alongside many dedicated committee members, a true pleasure to see it blossom anew after the pandemic made our activities so difficult and incredibly fun to think up so many new ways to use strawberry laces. Even the virtual 'tour" socials were a highlight of my week throughout the summer of 2020.

I have couldn't have been luckier to end up sharing a house with Rakesh, Maraia, Lillian, Tim and Jake in the last three years. Not only has having such a good group of friends close at hand made life all the more enjoyable and kept me all the more sane, but the supportive and thoughtful atmosphere has certainly helped me get through these challenging last stages of a PhD. Thank you to my other friends from Trinity, particularly Harry who can always be relied on to keep me abreast of the stargazing side that helped get me into astronomy (especially by pointing the Northumberland telescope at things too faint for me to see) and to be keen for college brunch on a Sunday.

No part of my academic career would have felt complete without my school friends Sam - who in particular it seems has been dogging my footsteps throughout exams, supervisions, crosswords, pub quizzes and more (though thankfully we didn't have to share an office too) - and Jon by my side (look how well I did, Sam, by refraining from calling you a *thorn in* my side.). But seriously, our friendship has no doubt been a linchpin of our respective successes and I wouldn't have had it any other way.

And finally, an unexpectedly large part of this work was conducted from my family home as the world repeatedly locked down in 2020 and 2021. I was lucky to spend this time with my brother James, my mum, and my dad who all made an uncertain world feel safe and supported me through those isolating times. Mum and Dad played a crucial role in setting me on the right path from a young age - indeed, credit must go to Mum for predicting my career right from the age of six after discovering that I had been explaining the big bang theory to my class teacher - and supported my ambitions: from sitting on the stairs watching an eclipse to ferrying me to and from endless astronomy talks. So thank you, for everything.

Table of contents

List of figures

List of tables

Nomenclature

Acronyms / Abbreviations

BC/BLVC Broad (Low Velocity) Component

CEL Collisionally Excited Line

CTTS Classical T Tauri Star

EUV Extreme Ultraviolet

FITS Flexible Image Transport System

FRIED FUV Radiation Induced Evaporation of Discs

FUV Far Ultraviolet

FWHM Full Width at Half Maximum

HVC High Velocity Component

HWHM Half Width at Half Maximum

IFIP Inverse First Ionisation Potential

IR Infrared

ISM Interstellar Medium

LTE Local Thermodynamic Equilibrium

LVC Low Velocity Component

MHD Magnetohydrodynamic

NC/NLVC Narrow (Low Velocity) Component

NIR Near Infrared

PDR Photodissociation Region

SC Single Component

SED Spectral Energy Distribution

UV Ultraviolet

WTTS Weak line T Tauri Star

Numerical Codes used in This Work

CHIANTI Dere et al. (1997)

FARGO3D Benítez-Llambay & Masset (2016)

MIRISIM Klaassen et al. (2021)

MOCASSIN Ercolano et al. (2003)

PINTOFALE Kashyap & Drake (2000)

PLUTO Mignone et al. (2007)

PRIZMO Grassi et al. (2020)

Disc Evolution Booth et al. (2017)

JWST Pipeline Bushouse et al. (2022)

Instrumentation and Organisations

ALMA Atacama Large Millimetre/submillimetre Array

DR3 (Gaia) Data Release 3

ESO European Southern Observatory

GO General Observers program

IFU/IFS Integral Field Unit/Integral Field Spectrograph

MIRI Mid Infrared Instrument

MRS Medium Resolution Spectrometer

MUSE	Multi Unit Spectroscopic Explorer	
NIST	National Institute of Standards and Technology	
VISIR	VLT Imager and Spectrometer for mid Infrared	
VLT	Very Large Telescope	

Physical Constants

σ_{SB}	Stefan-Boltzmann Constant	$5.670 \times 10^{-5}\,\mathrm{g\,s^{-3}\,K^{-4}}$
c	Speed of light	$2.998 \times 10^{10}\,\mathrm{cm\,s^{-1}}$
G	Gravitational Constant	$6.674 \times 10^{-7}\,\mathrm{m^2\,g^{-1}\,s^{-2}}$
h	Planck Constant	$6.626 \times 10^{-27}\,\mathrm{erg\,s}$
k	Boltzmann Constant	$1.381 \times 10^{-16}\,\mathrm{J\,K^{-1}}$
m_H	Hydrogen Mass	$1.674 \times 10^{-24}\,\mathrm{g}$

Mathematical Symbols

α	Spectral Index / Effective Viscosity Parameter
α_B	Case B Recombination Rate Coefficient
β	Escape Fraction
χ	Angle between Streamline Tangent and Radial Direction
$\dot{M}$	Mass loss rate (accretion or wind)
ε	X-ray Heating Efficiency / Dust-to-gas Ratio / Energy Density
Γ	Heating Rate
γ	Ratio of Specific Heat Capacities / Power Law Index of Viscosity
κ	Opacity
Λ	Cooling Rate
λ	Wavelength / Magnetic Lever Arm
$\mathscr{M}$	Mach Number

μ	Mean Molecular Weight
ν	Frequency
ν	Kinematic Viscosity
Ω	Orbital Frequency
Φ	EUV Photon Flux / Gravitational Potential
ϕ	Azmithual Angle / Elevation from Midplane in Self-Similar Solutions
ρ	Density
Σ	Surface Density
σ	Cross-section
τ	Logarithmic Temperature Gradient / Optical Depth
θ	Co-latitudinal Angle / Angle of Streamline Tangent to Midplane in Self-Similar Solutions
$\mathbf{g}_{\mathrm{eff}}$	Effective Gravity
ξ	Ionisation Parameter
A	Area of a Streamline Bundle
a	Dust Grain Size
A_{ij}	Einstein Coefficient for Spontaneous Emission
A_i	Abundance of Element i
B	Bernoulli Constant
b	Logarithmic Density Gradient
B_ν	Planck Function
c_{S}	Flux
C_{ij}	Einstein Coefficient for Collisional (De-)Excitation
E	Energy

EM	Emission Measure
F	Flux
g	Degeneracy
H	Disc Scale Height
h	Disc Aspect Ratio / Enthalpy
i	Inclination
l	Specific Angular Momentum
L_*	Stellar Luminosity
L_{acc}	Accretion Luminosity
L_{X}	X-ray Luminosity
M_*	Stellar mass
N	Column Density
n	Number Density
n_{13-31}	Infrared Spectral Index in range $13-31$ μm
n_{crit}	Critical Density
R	Cylindrical Radius
r	Spherical Radius
R_*	Stellar Radius
r_G	Gravitational Radius
R_{A}	Alfvén Radius
r_{b}	Radius at the Base of a Streamline
R_{C}	Disc Scale Radius
R_{eff}	Radius of Curvature
s	Arc Length Along a Streamline

St	Stokes Number (Dimensionless Stopping Time)	
T	Temperature	
t	Time / Age	
t_ν	Viscous Timescale	
t_{stop}	Stopping Time	
u	Gas Velocity	
u_{f}	Fragmentation Velocity	
v	Velocity / Dust Velocity	
z	Vertical coordinate	

Units

au	Astronomical Units	1.496×10^{13} cm
eV	Electronvolt	1.60×10^{-12} erg
Myr	Megayear (Million years)	3.154×10^{13} s
pc	Parsec	3.086×10^{18} cm
G_0	Habing Unit	$1.6 \times 10^{-3}\,\mathrm{erg\,cm^{-2}}$
$L_\odot$	Solar Luminosity	$3.846 \times 10^{33}\,\mathrm{erg\,s^{-1}}$
$M_\odot$	Solar Masses	1.989×10^{33} g
$M_\oplus$	Earth Masses	5.972×10^{27} g
M_{J}	Jupiter Masses	1.899×10^{30} g

Chapter 1

Introduction: The Motivation for Photoevaporative Winds

1.1 Introduction to Protoplanetary Discs

Protoplanetary discs are regarded as the site of the start of the planet formation process, a hypothesis with its roots in the 18$^{\text{th}}$-century Nebular Hypothesis of Swedenborg (1734), Kant (1755) and Laplace (1796) for the Solar System's formation. Though still practically prehistory on the timescales of the development of the field of exoplanets, it wasn't until the 1980s that these discs - specifically their warm dust component - began to be systematically observed as an excess over the stellar blackbody in the infrared spectral energy distributions of young stellar objects (Lada & Wilking, 1984). For many years, such SED studies dominated the way we thought about disc evolution; only in the past decade have high resolution observations in both the infrared and submillimetre taught us about the structure and composition of protoplanetary discs and - perhaps most excitingly - provided abundant evidence for ongoing planet formation in these discs.

In several systems, a planet or circumplanetary material is now thought to have been detected directly. In the PDS 70 system, a planet has been directly imaged at near-infrared wavelengths (Keppler et al., 2018; Müller et al., 2018) and - along with a second planet (later also directly imaged, Mesa et al., 2019) - confirmed to be accreting Haffert et al. (2019). A circumplanetary disc surrounding the second planet has since been resolved in the dust submillimetre continuum emission (Benisty et al., 2021). Other candidate direct detections include AB Aurigae b (Currie et al., 2022) and a suggestion of circumplanetary CO gas in AS 209 (Bae et al., 2022b). More indirect evidence for planets in discs also includes perturbations to the gas kinematics (see Pinte et al., 2022, for a review) and substructures (see Bae et al., 2022a, for a review).

However, estimated disc masses are frequently much greater than the mass contained within typical planetary systems. Some earlier dust-mass estimates seemed too small to form the solid mass contained in exoplanets (Greaves & Rice, 2010; Najita & Kenyon, 2014; Manara et al., 2018), potentially pointing to planet formation at a young stage, though even then very high efficiencies would be needed (Tychoniec et al., 2020). However, if observational biases are taken into account then things are more plausible, though still require a high efficiency (Mulders et al., 2021). Moreover, the gas masses of discs may be one to two orders of magnitude higher than the dust masses, whereas the solar system gas giants planets have a combined total mass of $\sim 450\ M_\oplus$ compared to around $130\ M_\oplus$ in heavy elements (Guillot et al., 2014). To understand the context in which planets form - including the timescales of the process and their composition - we must therefore account for the fate of the rest of the mass and the processes that drive disc evolution.

The evolution of circumstellar discs was already apparent in the earliest surveys, with Lada (1987) defining a system of classification depending on the whether the SED was rising or falling, as quantified through the spectral index $\alpha = \frac{\mathrm{d}\ln(\lambda F_\lambda)}{\mathrm{d}\ln\lambda}$. Within this system, positive indices are designated as Class 0 (Andre et al., 1993) and Class I discs, while decreasing indices correspond to Class II, and Class III systems are those with indices consistent with stellar blackbodies. Class 0 and Class I systems are understood as representing those discs that are still significantly embedded in an infalling envelope (Adams et al., 1987) - and so may be termed the protostellar phase - with the Class 0 phase roughly defined as the stage when the envelope mass exceeds the stellar mass (Andre & Montmerle, 1994). By the Class II phase, this infall has terminated and most of the mass is in the star; this is the classic protoplanetary disc phase and the longest evolutionary stage. Finally, as discs disperse, they briefly pass through the Class III phase on their way to becoming remnant debris discs.

Naturally much of the material may end up on the star - especially during the Class 0 and I phases - and the accretion process is detected in most protoplanetary discs down to accretion rates of $\sim 10^{-11}\ M_\odot\ \mathrm{yr}^{-1}$ by measuring either the UV continuum luminosity excess (Alcalá et al., 2014, 2017), or line luminosities from Hα (Fedele et al., 2010) or C IV (Alcalá et al., 2019). As the angular momentum of material in a Keplerian disc increases as $l \propto R^{1/2}$, this requires the redistrubution or loss of angular momentum from disc material. In Section 1.3.1 I summarise hypothesised mechanisms for this. The spectroscopic signature of accretion was historically key to the identification of low-mass pre-main-sequence stars, known as T Tauri stars (Joy, 1945). However, it was later realised that as well as the accreting Classical T Tauri stars (CTTS), there was another population of low-mass stars with X-ray fluxes that imply youth, but lacking the signature of accretion (Walter, 1986; Walter et al., 1988), which have become known as Weak Line T Tauri stars (WTTS). Above $\sim 2\,M_{\odot}$, pre-main sequence stars are usually termed Herbig Ae/Be stars (Herbig, 1960).

In the absence of further forces, the dust would follow the gas perfectly. However, discs contain substantial gas pressure gradients. These provide pressure support to the gas, reducing the centripetal force and leading to sub-Keplerian rotation. The dust, with its higher internal density, is more negligibly supported and adopts Keplerian orbits. This velocity difference means dust experiences a headwind, creating aerodynamic drag. The drag applies a torque to the dust, reducing its angular momentum and causing it to spiral inwards (Whipple, 1973; Weidenschilling, 1977). This process, termed *radial drift*, greatly enhances the rate at which dust reaches the star compared to viscous accretion alone. The dust-gas drag forces depend on grain size and so in Section 1.3.2 I summarise dust growth and derive equations for the drift velocity.

However the majority of this thesis is devoted to an alternate fate: material may be removed from the star-disc system entirely in the manner of a wind. There are a multitude of contrasting models for such winds, which in turn make varied predictions for the significance of winds on a disc's evolution. On the one hand, *photoevaporation* could occur whereby high-energy radiation heats the disc's upper layers, thus establishing thermal pressure gradients that accelerate the wind material such that it becomes unbound. When the radiation is from the central star this is termed *internal photoevaporation* while other nearby stars may drive *external photoevaporation* (when they provide sufficient ultraviolet fluxes, see Section 1.3.4). Alternatively, *magnetically-driven winds* involve acceleration either due to gradients in the magnetic pressure, or centrifugal forces as material is forced to co-rotate with the field. In reality, winds may exist on a continuum between these two extremes, leading to the definition of *magnetothermal* winds (Bai, 2017) as those where both magnetic and thermal effects play a role. While in Section 1.3.3 I summarise magnetically-driven winds as an important alternative, this thesis is concerned with resolving several questions about the nature of internal photoevaporation, namely:

1. What sort of high-energy radiation is most important for wind driving?
2. How important are photoevaporative winds for protoplanetary disc evolution and dispersal?
3. Can observations of winds be understood using photoevaporation, or must magnetic fields be invoked?

I devote the remainder of the introduction to setting each of these questions into context.

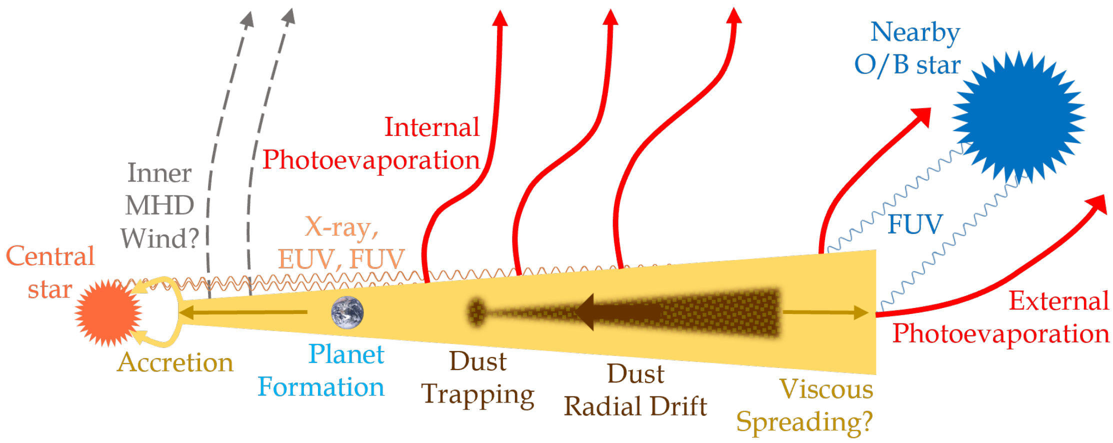

Fig. 1.1 A sketch of the key evolutionary processes that disperse protoplanetary discs.

1.2 Launching Physics of Winds

1.2.1 Basic Energetics

We must consider the energetics of photoevaporation in order to constrain where and when it can act. Starting from the momentum equation of fluid dynamics

$$\frac{\partial \mathbf{u}}{\partial t} + \mathbf{u} \cdot \nabla \mathbf{u} = -\frac{1}{\rho}\nabla P - \nabla \Phi, \tag{1.1}$$

we recast the second term using the identity $\mathbf{u} \cdot \nabla \mathbf{u} = \frac{1}{2}\nabla u^2 - \mathbf{u} \times (\nabla \times \mathbf{u})$ such that

$$\frac{\partial \mathbf{u}}{\partial t} + \frac{1}{2}\nabla u^2 - \mathbf{u} \times (\nabla \times \mathbf{u}) + \frac{1}{\rho}\nabla P + \nabla \Phi = 0. \tag{1.2}$$

Assuming a steady state and integrating along a streamline, we find that the Bernoulli function

$$B = \frac{u^2}{2} + \int \frac{dP}{\rho} + \Phi \tag{1.3}$$

is a conserved quantity. The second term is the specific enthalpy $h = \int \frac{dP}{\rho}$; if for now we neglect heating and cooling in the wind then this takes on its adiabatic form $h = \frac{1}{\gamma-1}c_{\mathrm{S,ad}}^2 = \frac{\gamma}{\gamma-1}c_{\mathrm{S,isoT}}^2$. Decomposing the velocity into its poloidal and toroidal components (the latter of which we write using the conserved specific angular momentum l), we find that

$$B = \frac{u_p^2}{2} + \frac{\gamma}{\gamma-1}c_{\mathrm{S,isoT}}^2 - \frac{GM_*}{r} + \frac{l^2}{2R^2}. \tag{1.4}$$

As $r \to \infty$, $B \to \frac{u_p^2}{2} \geq 0$; thus to succesfully launch a wind that escapes the system requires $B > 0$. Since the wind material starts off with u_p highly subsonic, the energy to do so comes from the enthalpy: this is converted into kinetic energy by pressure gradients until such time as the wind achieves escape velocity. Thus, assuming $r \approx R$ at the base and that the angular momentum is Keplerian,

$$c_{\mathrm{S,isoT}}^2 \geq \frac{\gamma - 1}{2\gamma} \frac{GM_*}{R}. \tag{1.5}$$

Equivalently, such considerations give an escape temperature that the gas must reach at any given radius (Alexander et al., 2004b; Owen et al., 2012)

$$T_{\mathrm{esc}} \approx \frac{GM_* \mu m_H}{2k_B R}. \tag{1.6}$$

In reality, due to the microphysics of the heating and cooling, winds tend to be heated to certain temperatures (or temperature ranges) - corresponding to certain sound speeds - so this becomes a condition on the allowable launch radii (Liffman, 2003):

$$R \geq \frac{\gamma - 1}{2\gamma} \frac{GM_*}{c_{\mathrm{S,isoT}}^2}. \tag{1.7}$$

Assuming $\gamma = 5/3$ for an atomic wind, the critical radius beyond which launch is possible is

$$R_{\mathrm{crit}} = 0.2 r_G, \tag{1.8}$$

where the gravitational radius

$$r_G = \frac{GM_*}{c_{\mathrm{S,isoT}}^2} \approx 8.9 \text{ au} \frac{M_*}{M_\odot} \left(\frac{c_{\mathrm{S,isoT}}}{10 \text{ km s}^{-1}} \right)^{-2}. \tag{1.9}$$

This is in good agreement with the results of hydrodynamic calculations (Font et al., 2004; Clarke & Alexander, 2016) and hence is the typically adopted limit for photoevaporative winds (Alexander et al., 2014).

I assumed above that the wind was adiabatic while in reality both heating and cooling occur throughout the disc and wind. While the quantity given by Equation 1.3 will still be conserved, we can no longer find a simple closed form for the enthalpy integral but must integrate along the thermodynamic trajectory described by the streamline. Therefore, Equation 1.4 will no longer be exactly conserved. In particular, the temperature increases strongly as material passes from denser disc regions - where radiation may not penetrate well - to the more readily-heated wind. This will correspond to a large enthalpy increase and so ought to mark the transition from bound disc material with $B < 0$ to unbound wind material with $B > 0$ (Wang & Goodman, 2017).

1.2.2 Hydrodynamics

The mass-loss rate in the wind can be defined as the integral of the mass flux over a surface

$$\dot{M} = \oiint \rho(\mathbf{r})\mathbf{u}(\mathbf{r}) \cdot \mathrm{d}\mathbf{S}. \tag{1.10}$$

Convenient choices for the surface include the wind base (e.g. Hollenbach et al., 1994; Font et al., 2004), the sonic surface - which is especially convenient as the wind speed is by default known there (e.g. Owen et al., 2012), or the outer radius of a simulation domain (e.g. Owen et al., 2010; Wang & Goodman, 2017; Picogna et al., 2019).

For spherical surfaces, the area element (using standard coordinate notation) is

$$\mathrm{d}\mathbf{S} = r^2 \sin(\theta) \mathrm{d}\phi \mathrm{d}\theta \hat{\mathbf{r}}, \tag{1.11}$$

which resolved in the direction of the velocity becomes

$$dS = \hat{\mathbf{u}} \cdot \mathrm{d}\mathbf{S} = r^2 \sin(\theta) \sin(\chi) \mathrm{d}\phi \mathrm{d}\theta, \tag{1.12}$$

where χ is the angle between the streamline and the radial direction. Thus denoting $A = r^2 \sin(\theta) \sin(\chi)$, then for any given streamline bundle, the flux along it

$$\rho u A \tag{1.13}$$

is also conserved. Thus, differentiating along with a streamline coordinate s, we find that

$$\frac{\partial \ln(A)}{\partial s} = -\frac{\partial \ln(\rho)}{\partial s} - \frac{\partial \ln(u)}{\partial s} \tag{1.14}$$

Starting from the equations of momentum conservation in the steady state, assuming $P = \rho c_{\mathrm{S,iso}}^2$ and eliminating the density we derive the equation for the velocity $\mathbf{u} = u\hat{\mathbf{s}}$ of a flow, in terms of the sound speed c_S and the effective gravity $\mathbf{g}_\mathrm{eff}$:

$$(u^2 - c_{\mathrm{S,iso}}^2)\hat{\mathbf{s}} \cdot \nabla \ln u = \hat{\mathbf{s}} \cdot \mathbf{g}_\mathrm{eff} + c_{\mathrm{S,iso}}^2 \frac{\partial \ln A}{\partial s} - \frac{\partial c_{\mathrm{S,iso}}^2}{\partial s}. \tag{1.15}$$

Clarke & Alexander (2016) argued that in the underlying disc - which is cold and thin - gravitational and centrifugal forces balance (the pressure gradient is subdominant by a factor

$(H/R)^2$, where H is the disc scale height and is typically $\lesssim 0.1$). The material that supplies the wind flows vertically through the cold, thin, disc and eventually passes through the wind base, where it is heated and strongly accelerated. The gravitational and centrifugal forces are barely changed compared to their midplane values, but once in the wind region, which is much hotter than the underlying disc, the pressure gradient has greatly increased. Since all quantities in the wind solution vary over a length scale of order r or less, the magnitude of the acceleration associated with the pressure gradient, $\frac{1}{\rho}\left|\frac{\partial P}{\partial r}\right| \approx \frac{c_\mathrm{S}^2}{r}$, exceeds gravity and centrifugal force at the wind base, so long as $\frac{c_\mathrm{S}^2}{r_\mathrm{b}} > \frac{GM_*}{r_\mathrm{b}^2}$. Thus where the launch radius $r_b > r_G$ (as defined in Equation 1.9)[1] we can neglect the gravitational and centrifugal forces (i.e. the effective gravity). As one moves to larger radii, the gravitational and centrifugal terms decline much faster (as $1/r^2$ and $1/r^3$ respectively) than the pressure gradient ($1/r$ in an isothermal wind) and thus the approximation is strengthened.

Thus, neglecting effective gravity, and assuming an isothermal wind - we see that photoevaporative winds can be understood as a nozzle flow where converging streamlines lead to the acceleration of the wind while it is subsonic and diverging streamlines correspond to acceleration in the supersonic regime. Any temperature gradients merely act to offset the sonic surface from the minimum area of the streamline bundle slightly. Hence, we see that such winds are transsonic and the typical velocities to which winds are accelerated must be on the order of the sound speed c_S.

Clarke & Alexander (2016) further show how such winds may be treated in a coordinate system local to the streamlines. In this case, the momentum equation may be resolved parallel to the streamlines, which is equivalent to the Bernoulli function treated earlier, and perpendicular to the streamlines (which defines the direction with unit vector $\hat{\mathbf{l}}$). The latter may be expressed as

$$\frac{u^2}{R_\mathrm{eff}} = \frac{1}{\rho}\hat{\mathbf{l}} \cdot \nabla P, \tag{1.16}$$

where R_eff is the radius of curvature, showing that the pressure gradients normal to the streamlines balance an effective inertial/centrifugal force due to the streamline curvature. Streamlines of the wind initially curve outwards due to the radial pressure gradient, but eventually curve back upwards as the decrease in pressure with altitude becomes more important. This approximation - which neglects the gravitational and centrifugal forces - is valid so long as the curvature term also dominates over these forces. Since the velocities

[1]For externally photoevaporating discs where winds are driven by an external source of FUV radiation, the large gravitational radius means that the disc radius is typically smaller than r_G. In this "subcritical" regime, the least bound material at the disc edge dominates the mass loss (Adams et al., 2004; Haworth & Clarke, 2019); the strong dependence on a particular radius means self-similar solutions have limited applicability to this problem.

are on the order of c_S, this occurs for $r > \frac{R_{\rm eff}}{r} r_G$ (Clarke & Alexander, 2016); in practice the streamlines are typically sufficiently curved near the base that $R_{\rm eff} < r \approx r_{\rm b}$, making the approximation reasonable even for winds launched from $r_{\rm b}$ somewhat inside r_G.

In Chapter 2, I discuss how self-similar solutions may be derived within this framework and explore their properties and applicability under broad conditions.

1.2.3 Energetics Revisited

The transsonic requirement derived above means that information cannot propagate back along the streamlines from arbitrary distance, but only from as far as the sonic surface. Consequently the subsonic wind base does not know about what happens in the supersonic region. The mass loss is thus set by the conditions at the first sonic surface[2] the material encounters (Owen et al., 2012). Thus whichever radiation can penetrate furthest into the flow and yet cause material to reach temperatures such that a transsonic wind becomes energetically favorable will be the one to drive the wind. Determining which radiation this is relies on understanding the heating provided by each band - and the cooling processes that offset it - given the physical conditions in such a region. While I discuss these processes in more depth in Chapter 3, for now I present a simple summary of the possible contributors, in particular the different energy bands and their luminosities.

The Energy Equation

The evolution of the total energy density $E = \rho\varepsilon_{\rm tot} = \frac{1}{2}\rho v^2 + \rho\varepsilon_{\rm th} + \rho\Phi$ in a static potential Φ is described by the energy equation

$$\frac{\partial E}{\partial t} + \nabla\cdot((E+P)\mathbf{v}) = \rho(\Gamma - \Lambda), \tag{1.17}$$

for radiative heating and cooling rates per unit mass Γ and Λ respectively.

The corresponding equation (in conservative form) for the thermal energy density $\rho\varepsilon_{\rm th}$ is

$$\frac{\partial}{\partial t}(\rho\varepsilon_{\rm th}) + \nabla\cdot(\rho\varepsilon_{\rm th}\mathbf{v}) = \rho\frac{D\varepsilon_{\rm th}}{Dt} = \rho(\Gamma-\Lambda) - P\nabla\cdot\mathbf{v}. \tag{1.18}$$

The additional term on the right-hand side compared to equation (1.17) represents the "PdV" work done on a fluid element by expansion in the presence of a diverging velocity field (which adiabatically cools the gas). The energy lost from the thermal contribution is used to accelerate the wind by pressure gradients along the streamlines and is not entirely lost from the system.

However, in establishing a steady state thermal balance, we are more interested in the thermal evolution at a particular location:

$$\frac{\partial\varepsilon_{\rm th}}{\partial t} = (\Gamma-\Lambda) - (\gamma-1)\varepsilon_{\rm th}\nabla\cdot\mathbf{v} - \mathbf{v}\cdot\nabla\varepsilon_{\rm th}. \tag{1.19}$$

[2]There will usually only be one, else shocks are needed to join the flows (Johnstone et al., 1998).

Thus, while adiabatic cooling is relevant for the cooling of a fluid element, the advection of thermal energy also plays an important role when setting the thermal balance in an Eulerian sense. This thermal flux could potentially offset the adiabatic cooling if material flows from hot to cold and should also be considered.

In steady state, integrating equation (1.17) over a volume following a streamline bundle and using mass conservation gives

$$\dot{M}\Delta\varepsilon_{\mathrm{tot}} = L_{\mathrm{heat}} - L_{\mathrm{cool}}, \tag{1.20}$$

where $\Delta\varepsilon_{\mathrm{tot}}$ is the difference between the mass-flux-weighted average energy density at either end of the bundle. Owen et al. (2010) argue that since in their X-ray–driven models $\dot{M}\Delta\varepsilon_{\mathrm{tot}} \lesssim 8\% L_{\mathrm{X}}$, then assuming that all the X-ray goes into heating, the advected energy is negligible compared to L_{heat} and we can assume $L_{\mathrm{heat}} \approx L_{\mathrm{cool}}$.

Moreover, integrating for the thermal energy density $\varepsilon_{\mathrm{th}}$,

$$\dot{M}\Delta\varepsilon_{\mathrm{th}} = L_{\mathrm{heat}} - L_{\mathrm{cool}} - L_{\mathrm{adiabatic}}. \tag{1.21}$$

Hence, by comparison we conclude that $\dot{M}\Delta\varepsilon_{\mathrm{tot}} = \dot{M}\Delta\varepsilon_{\mathrm{th}} + L_{\mathrm{adiabatic}}$ and the advected energy is the net result of any advected thermal energy plus any which adiabatic cooling has converted to kinetic energy. Since the wind consists of unbound material, and is being accelerated, it is reasonable to assume the dominant contribution to the advected energy is an increase in kinetic energy - since the wind ends up supersonic, this is likely of greater magnitude than any change in thermal energy i.e. $\dot{M}\Delta\varepsilon_{\mathrm{tot}} >> \dot{M}\Delta\varepsilon_{\mathrm{th}}$ and hence $L_{\mathrm{adiabatic}} \approx \dot{M}\Delta\varepsilon_{\mathrm{tot}}$ and probably shouldn't be significantly offset by thermal advection.

1.2.4 Microphysics: Heating

Disc Thermal Structure

Before focusing on the processes which dominate heating in the wind, I consider those which are active in the underlying disc as this sets the disc's vertical structure and in turn its vertical extent and ability to intercept high-energy radiation.

While accretion heating and cosmic-ray heating may play roles in the innermost and outermost regions respectively, most disc material is heated through thermal accommodation with dust grains i.e. the dust is heated by (mostly IR/optical/UV) radiation and then collisions between gas particles and dust grains cause them to equilibrate. At the simplest level, the dust may be assumed to be at its blackbody equilibrium temperature resulting from a balance of optically thin heating and cooling i.e.

$$\frac{L_*}{4\pi r^2}\pi a^2 = 4\pi a^2 \sigma_{\rm SB} T^4, \tag{1.22}$$

which implies that $T \propto r^{-1/2}$. Although this is the most common model assumption for a temperature profile, such a profile ignores opacity effects and the disc geometry.

In reality, the disc is exceedingly optically thick in the radial direction; the bulk of the material, including the disc midplane, is therefore instead heated by reprocessed radiation emitted by the directly heated disc surface (while the midplane often remains optically thick to this radiation, it is much less so). The heating thus depends on the total amount of radiation intercepted by the vertical column of gas at any radius, which scales with the angle subtended by the disc surface. Assuming the surface lies at some fixed number of scale heights, the angle is $\alpha \propto H/R$. Self-consistently solving for the temperature in such a flared disc results in a slightly shallower profile $T_{\rm mid} \propto R^{-3/7}$ (Kenyon & Hartmann, 1987; Chiang & Goldreich, 1997).

These crude estimates of the radial run of temperature bracket well the range of observed slopes (Andrews & Williams, 2005; Law et al., 2022).

While these dust radiative transfer effects are well-understood, they are diffusive - and therefore multi-dimensional - in nature. Common solutions include flux-limited diffusion (Levermore & Pomraning, 1981; Kuiper et al., 2010) or Monte Carlo radiative transfer (Pinte et al., 2006; Dullemond et al., 2012), but these are too expensive for on-the-fly use in hydrodynamical simulations and typical approaches (Owen et al., 2010; Wang & Goodman, 2017) pin the temperature structure to a pre-calculated dust temperature structure (e.g. Chiang & Goldreich, 1997; D'Alessio et al., 2001) beyond a certain column density.

Photoionisation and photoelectric effect

Winds are heated by absorbing high-energy radiation. X-rays ($E > 100$ eV) and Extreme Ultraviolet (EUV, $E > 13.6$ eV i.e. enough to ionise H) deposit energy by photoionisation of atoms. The Far Ultraviolet (FUV, $6 - 13.6$ eV), while by definition unable to ionise atomic hydrogen, contributes to photoionisation heating via elements with smaller ionisation potentials (e.g. C and S). The FUV is also strongly absorbed by dust; where the absorbed energy is enough to liberate an electron, this is called the photoelectric effect.

In either case, the liberated "photoelectron" carries excess energy over the ionisation energy. Through collisions, it may thermalise with the gas, resulting in heating. However, this electron may also collisionally excite or even ionise atoms (Maloney et al., 1996). Thus, depending on the degree of ionisation, only a fraction of the energy goes into heating; this can be as low as 10% for the typical ionisation level of an X-ray heated wind (Shull & van Steenberg, 1985) but $\rightarrow$ 100% at high levels of ionisation when there are fewer neutral species to ionise.

The photoionisation cross-section of H may be written as (Osterbrock & Ferland, 2006)

$$\sigma_\nu = \sigma_0 \left(\frac{\nu}{\nu_1}\right)^{-4} \frac{\exp[4 - 4/\varepsilon \tan^{-1} \varepsilon]}{1 - \exp(-2\pi/\varepsilon)}, \tag{1.23}$$

where $\varepsilon = \sqrt{\nu/\nu_0 - 1}$ with $\nu_0 = 13.6\,\mathrm{eV}/h$ and $\sigma_0 = 6.3 \times 10^{-18}$ cm^2. As an approximation, the cross-section scales approximately as ν^{-3} in the EUV, steepening towards $\nu^{-3.5}$ at high energies. Hence, while a typical EUV penetration depth may be a column of $N_\mathrm{H} \sim 1/\sigma_0 \approx 10^{17}$ cm^{-2}, soft X-rays on the order of 100 eV should penetrate a $N_\mathrm{H} \sim 10^{20}$ cm^{-2} and hard X-rays with $E > 1000$ eV an even higher $N_\mathrm{H} \sim 10^{23}$ cm^{-2}.

However, other elements also contribute to the cross-section. Elements such as carbon, nitrogen and oxygen, where the valence shell is the $n = 2$ shell (also called the L shell), can be ionised by removing electrons from either the valence shell or the inner ($n = 1$ or ‘K”) shell. These inner-shell ionisations require energies of 100s eV, so inner-shell ionisation of metals becomes relevant for X-rays and can come to dominate the total photoionisation cross-section, which at 1000 eV is around 10 times higher than that of hydrogen alone. When, inner shell ionisation occurs, it leaves a vacancy which is then filled by an electron from the valence shell. The energy lost in this transition may be radiated, but could also be used to liberate further valence electrons; the latter is called the Auger effect. The total photoionisation cross-section as a function of energy is shown in Figure 1.2 with the atom which dominates the cross-section (assuming the gas phase composition of Savage & Sembach, 1996) indicated by the shading under the curve.

EUV heating

The EUV is so effectively absorbed by photoionisation that it tends to form an essentially fully-ionised region bounded by a thin ionisation front, analogous to the Strömgren sphere (Strömgren, 1939). This region is in ionisation-recombination equilibrium. However, photons that are emitted by recombinations to the ground state are necessarily themselves ionising and so are quickly reabsorbed. These recombinations to the ground state create a diffuse EUV field, allowing EUV photons to propagate non-radially once these photons stop being absorbed on the spot.

The net rate of recombination is therefore to excited electronic states of hydrogen, denoted “case B” recombination with rate $\alpha_B(T)$. This is balanced by the net rate of ionisation given simply by the stellar ionising photon flux Φ.

$$\Phi = \int \alpha_B(T) n_e n_{\mathrm{H\,II}} dV \sim \int \alpha_B(T) n^2 dV. \quad (1.24)$$

To drive a wind, the EUV must reach at least $r_G \approx 10$ au for a solar-mass star. Following Hollenbach et al. (1994), we can approximate the density as the average for a Strömgren sphere of radius r_G

$$n_G = \left(\frac{3\Phi}{4\pi\alpha_B r_G^3}\right)^{1/2} \approx 10^5 \mathrm{cm}^{-3} \left(\frac{\Phi}{10^{41}\ \mathrm{s}^{-1}}\right)^{1/2}. \quad (1.25)$$

Thus, in order for it to be extended, an EUV wind must have densities $< 10^5$ cm^{-3} such that the EUV can penetrate throughout.

Without a strong contribution from the photosphere, the origin and magnitude of this ionising flux (which is observationally challenging to determine due to foreground hydrogen absorption) for low-mass stars is debated. Alexander et al. (2004a) ruled out accretion hotpots as unable to produce a significant level of ionising photons (due to a combination of absorption in the stellar atmosphere and the accretion streams themselves), while possible chromospheric activity is poorly understood. Nevertheless, the value of Φ can exceed solar levels (e.g. Gahm et al., 1979; Alexander et al., 2005) with $10^{41} - 10^{42}$ s^{-1} often assumed. Limits can also be placed using free-free emission at cm wavelengths, resulting in similar values (Pascucci et al., 2014). More recently, EUV luminosity estimates have been obtained by extrapolating from observed X-ray spectra using coronal models, finding a scaling $L_{\mathrm{EUV}}/L_{\mathrm{X}} \propto L_{\mathrm{X}}^{-0.4--0.5}$ (Chadney et al., 2015; King et al., 2018).

X-ray heating

Due to their lower cross-section, X-rays can penetrate a somewhat denser wind $n \lesssim \frac{1}{r_G \sigma} \lesssim 10^7$ cm^{-3}. The lower photoionisation cross-sections, combined with higher densities which make recombination more effective, lead to lower levels of ionisation. X-ray production by recombination is totally negligible, requiring an electron with energy ~ 100 times greater than the average ($\sim kT \approx 0.86$ eV) for a 10^4 K gas (very rare under a Maxwell-Boltzmann distribution). Diffuse photons are thus predominantly created by fluorescence following inner-shell ionisation of heavy elements; X-ray fluorescence results $< 10\%$ of the time (Glassgold et al., 1997) so is also safely neglected.

While metals such as O are the principal sources of ionisation, collisions between metal ions and neutral species - especially hydrogen - may transfer charge. In particular, the ionisation energies of oxygen and hydrogen are so closely matched that the degree to which each is ionised becomes almost identical (Osterbrock & Ferland, 2006).

Compared to the EUV, X-ray is much easier to constrain in surveys (e.g. Preibisch et al., 2005; Telleschi et al., 2007a; Güdel et al., 2007a). Consequently, the relationship between X-ray luminosity L_{X}, and stellar properties is better understood. Although accretion and jet shocks may also contribute, the X-ray is generally thought to be predominantly coronal in origin (Ercolano et al., 2008b). This means that X-ray emission is driven by stellar magnetic activity, which in turn requires a convective dynamo to be acting. The X-ray luminosity of stars thus drops off above $2-3\ M_{\odot}$ (i.e. for Herbig Ae/Be stars) (Flaccomio et al., 2003; Preibisch et al., 2005) once energy transport in the star becomes radiative rather than convective. The X-ray luminosity is constant for the first few Myr (the typical lifetime of discs) before beginning to drop after $3-7$ Myr (Getman et al., 2022), seemingly scaling with the volume of the young, contracting star.

The high-energy spectrum can be modelled with several components that give the relative contributions (emission measures) of plasmas of different temperature (Mewe, 1991) - to create X-ray emission these plasmas are typically at $10^{7}-10^{8}\ \mathrm{K} \approx 1-10\ \mathrm{keV}$. For simplicity, the spectra are usually fit with single-temperature or two-temperature models (Mewe, 1991; Getman et al., 2005), though these may be somewhat degenerate in the allowed solutions due to foreground absorption. Nevertheless these fits can typically retrieve the peak of the underlying temperature distribution well. The cooler component in these two-temperature is a relatively constant $\approx 10^{7}$ K, while the hotter component gets hotter (and increasingly dominates the flux), for more X-ray–luminous stars (Preibisch et al., 2005), In turn these quantified relationships allow a variety of synthetic two-temperature X-ray spectra for use in simulations to be produced (Ercolano et al., 2021). Conversely, Ercolano et al. (2009) used RS CVn binaries, which contain a giant with comparable deep convective zones to T Tauri stars, as a template for a continuous emission measure distribution in order to include the cooler plasma components (present in the chromosphere) which emit at longer wavelengths (crucially, including the EUV) in their synthetic spectra. To avoid the biases in two temperature fits that can result from absorption, Güdel et al. (2007a) instead assumed a parametric form for the emission measure distribution for their fits.

While this discussion focused on coronal activity, there does seem to be some connection to accretion. The non-accreting WTTS actually seem to have a higher X-ray luminosity than the CTTS (Stelzer & Neuhäuser, 2001; Telleschi et al., 2007b). Allowing for three-temperature fits, Telleschi et al. (2007a) found that for some CTTS an additional, softer component at $2-3\times10^{6}$ K was found. This "soft excess" is also evident in anomalously high O VII/O VIII line ratios (Güdel et al., 2007b; Güdel & Telleschi, 2007) which require plasma at similar temperatures to create. While these temperatures are similar to those expected in accretion shocks, the densities are much lower Güdel et al. (2007b). Therefore it seems that the accretion streams present for CTTS alter the corona in a way that produces an additional soft excess at low temperature (which, being coronal in origin, still depends on coronal activity) but lowers the X-ray luminosity overall (Preibisch et al., 2005; Güdel et al., 2007b). The first star to produce evidence of a softer component was TW Hya (Kastner et al., 2002), in which, seemingly uniquely, the hard spectrum is entirely absent (a two temperature fit finds components at 2.6×10^6 K and 10^7 K, Nomura et al., 2007).

FUV heating

Aside from the self-shielding of particular frequencies centred on molecular transitions, the depth of penetration of FUV depends mainly on the dust cross-section as $N \sim 1/\sigma$. Usually this is parametrized as $N = 10^{21}/\sigma_H$ cm^{-2}, where σ_H is the dust cross-section per hydrogen atom. This may be affected by either the depletion of dust or the growth of dust grains (such that their area-to-volume ratio decreases). Consequently, the FUV typically penetrates at least as far as the higher energy ($\sim$ 1000 eV) X-ray. The dust cross-section (assuming small grains as these are most likely to make it into a wind, see Section 1.2.7) is also shown in Figure 1.2. Polyaromatic hydrocarbons - larger molecules consisting of several aromatic carbon rings - are also important for FUV absorption.

FUV can also dissociate molecules including H_2 or CO. When FUV photons are abundant, the H_2 photodissocation front is set by the dust attenuation, while for weak FUV fields, the reformation of H_2 becomes relatively more effective and instead self-shielding becomes more important for molecular survival. The transition happens when $G_0/n \lesssim 0.04$ cm^3 (Draine & Bertoldi, 1996)[3]. Much like photoelectrons, the dissociation products carry excess energy ($0.25 - 0.45$ eV, Stephens & Dalgarno, 1973) which can thermalise with the surroundings and therefore photodissociation also contributes to heating. Moreover, FUV excitation of molecules can also lead to heating via pumping (Field et al., 1966). The absorption of FUV typically excites a molecule both electronically and vibrationally (following the Franck-Condon principle). The excited molecule will first decay to the ground vibrational state of the excited electronic state through collisions (Kasha's rule). From here, it may decay radiatively to the ground electronic state, either to the vibrational continuum (in which case it is dissociated) roughly 10% of the time (Stecher & Williams, 1967), or otherwise to a vibrationally excited but bound state. This decays to the ground vibrational state either by

[3] G_0 is the FUV field (over the energy range $6 - 13.6$ eV) in multiples of the Habing unit, which is 1.6×10^{-3} erg cm^{-2} (Habing, 1968).

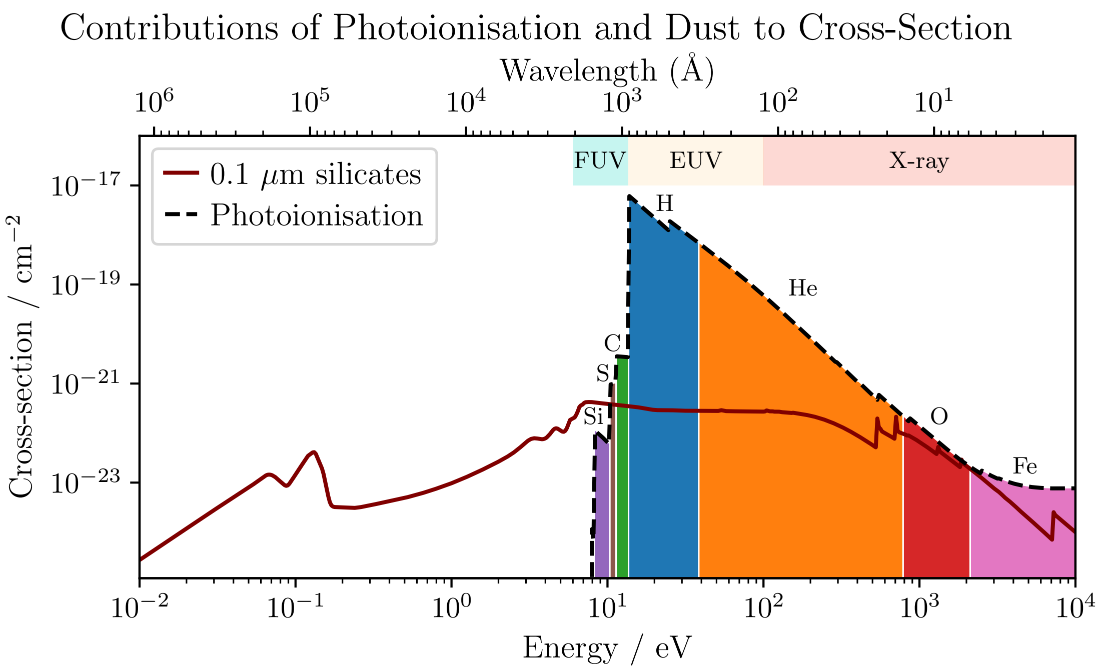

Fig. 1.2 Comparison of continuum cross-sections in the FUV, EUV and X-ray regimes. The total photoionisation cross-section for neutral gas is shown by the dashed line, with the coloured areas indicating where each element dominates (Verner & Yakovlev, 1995; Verner et al., 1996). X-ray and EUV are dominated by photoionisation. In the FUV, the photoionisation of S and C dominates the cross-section above 10.36 eV, while at longer FUV wavelengths (and near-UV, optical and IR wavelengths) the dust (calculated for 0.1 μm silicate grains following Draine, 2003a,b) dominates.

infrared fluorescence or collisional de-excitation; the latter transfers energy (up to 2.6 eV, London, 1978) from the molecule's vibrational energy into thermal energy.

The UV spectrum may contain several components (Nomura & Millar, 2005). There is a photospheric blackbody contribution, which is weak for cooler, low-mass, stars but grows strongly with stellar effective temperature. Secondly, for accreting systems (where accretion rate is positively correlated with stellar mass), the accreting material shocks, creating hotspots on the stellar surface; the emission from these hotspots is sometimes modelled as Brehmsstrahlung (Nomura & Millar, 2005), or otherwise as a hotter blackbody of 9000 – 15000 K (Matsuyama et al., 2003; Gorti & Hollenbach, 2004; Ercolano & Owen, 2016). Finally, a significant luminosity may be emitted in the Lyman α line (Ardila et al., 2002; Herczeg et al., 2004), which can be significant for the pumping of H_2. In the case of TW Hya, the photospheric contribution dominates the continuum below ~ 4 eV (the near UV), while in the FUV, which is responsible for the photoelectric effect and photochemistry of molecules, the accretion luminosity dominates.

1.2.5 Microphysics: Cooling

The wind cools principally through collisionally excited lines of atoms and/or molecules (i.e. in much the reverse of the main heating processes in which excited (photo)electrons transfer energy to the fluid through collisions). In this case, colliders - predominantly electrons and protons in highly ionised gas, atomic H in neutral gas, and H_2 in molecular gas - transfer some of their kinetic energy to an atom/molecule during a collision, exciting it into some higher energy state. Though the reverse process of collisional de-excitation also happens, atoms/molecules in the upper energy level may de-excite through a spontaneous radiative transition at the rate given by the Einstein coefficient A_{21}. Then, the energy transferred to the atom/molecule during collisional excitation is lost through radiation - rather than being returned to the gas - and hence this is a source of cooling. By solving the equation of detailed balance,

$$C_{12} n_{\rm coll} n_1 = C_{21} n_{\rm coll} n_2 + \beta A_{21} n_2, \tag{1.26}$$

where $1-\beta$ is the fraction of emitted radiation that is reabsorbed (and thus doesn't contribute to cooling), one may establish that the relative population of the upper state n_2/n_1, and the resultant cooling rate Λ are, respectively,

$$\frac{n_2}{n_1} = \frac{g_2}{g_1} \frac{\exp(-\Delta E_{12}/k_B T)}{1+\beta \frac{n_{\rm crit}}{n_{\rm coll}}}, \tag{1.27}$$

$$\Lambda = \beta A_{21} \Delta E_{12} n_X \left(1 + \frac{g_1}{g_2} \exp(\Delta E_{12}/k_B T) \left(1 + \beta \frac{n_{\rm crit}}{n_{\rm coll}}\right)\right)^{-1}. \tag{1.28}$$

The cooling from this line will become significant when $T \gtrsim T_{\rm ex} = \frac{\Delta E_{12}}{k_B}$, so long as there is a sufficient density n_X of the species X. These equations are written in terms of a *critical density* of colliders below which radiation will dominate over collisional de-excitation:

$$n_{\rm crit} := \frac{A_{21}}{C_{21}}, \tag{1.29}$$

While the exact transitions that may be available to cool disc and wind material depend on its density, composition, ionisation state and temperature, there are always some species that can provide this cooling. In Chapter 3, I consider in more detail the possible transitions - in particular atomic fine structure lines and molecular rovibrational transitions - that permit these sort of cooling processes, and explore which are relevant to winds from protoplanetary discs. Beyond acting as coolants, atomic fine structure lines also provide excellent direct probes of emission from winds that are observed in spectroscopic surveys. For example, the Ne II transition which emits at 12.81 μm is a leading candidate for tracing photoevaporative winds (see Section 1.4.2 and Chapter 4).

1.2.6 History of Photoevaporation Models

Photoevaporation was first proposed to explain the long lifetime of H II regions around massive stars by resupplying them with material (e.g. Hollenbach et al., 1994). It was consequently natural to assume the heating was due to the EUV. Since EUV is very easily absorbed, a large amount of energy can be deposited locally leading to efficient heating. However, once the gas reaches $\sim 10^4$ K, the Lyman alpha and optical fine structure line cooling can be excited. The cooling rates are such strong functions of temperature that a well-controlled thermostatic effect is produced such that the EUV-heated gas is to good approximation isothermal at 10^4 K.

Under this assumption of isothermal EUV-heated gas, Hollenbach et al. (1994) produced the first photoevaporation models, consisting of a hydrostatic atmosphere inside r_G and a wind external to this. They self-consistently calculated the ionisation equilibrium (including the diffuse field created by recombinations) and the vertical hydrostatic equilibrium, thus finding the density profiles of the atmosphere and winds (not to be confused with that of the underlying disc). A key result was that the radial density profile had two regimes:

$$n(r) = \begin{cases} n(r_G)\left(\frac{r}{r_G}\right)^{-1.5} & r \leq r_G \\ n(r_G)\left(\frac{r}{r_G}\right)^{-2.5} & r \geq r_G \end{cases}. \tag{1.30}$$

At small radii $R < r_G$, the dominant flux was the diffuse flux from the atmosphere directly above R, whereas for $R > r_G$, the lower densities and approximately constant density with height meant the dominant flux is from the atmosphere at r_G (Shu et al., 1993). Note, however, that simulations which directly solve the hydrodynamics do not find such a sharp decline in the density profile around r_G (Yorke & Kaisig, 1995; Richling & Yorke, 1997).

The basis for many applications of the Hollenbach et al. (1994) model was to simply assume the material leaves the disc from $R > r_G$ at the sound speed with the density given by Equation 1.30. This gives a simple mass-loss profile that can then be used to look at the dispersal of discs (Shu et al., 1993; Clarke et al., 2001). Conversely, Font et al. (2004) used this density as a boundary condition for hydrodynamic wind simulations, finding that the mass loss was actually dominated by the region $1/5 \lesssim r/r_G < 1$: though the flow there was initially bound, it accelerates to become unbound. Moreover, the wind was launched subsonically at $u_b/c_S \sim 0.3 - 0.4$, lowering the overall mass-loss rate by a factor ~ 3.

Alexander et al. (2004b) first assessed the impact of X-rays on the heating of winds, concluding the mass-loss profiles were at best comparable to the EUV, the higher densities being somewhat offset by their cooler temperatures (in that case around 6000 K) and lower velocities. However, Ercolano et al. (2009) showed that X-rays drive winds from a larger area, potentially resulting in higher integrated mass-loss rates; these winds were definitively X-ray–driven as reducing the EUV luminosity (via pre-screening by material inside the computational domain) did not reduce their mass-loss rate estimates. This is because the higher density, largely neutral, material is very optically thick to EUV photons, which can only penetrate and heat the inner regions (Ercolano & Owen, 2010; Owen et al., 2012). They concluded softer X-rays < 1000 eV were particularly important as once they pre-screened their spectrum enough to absorb these, a significant wind could no longer be launched.

The important role for X-ray suggested by static models was corroborated by the hydrodynamical calculations of Owen et al. (2010, 2011b, 2012), in which most wind material never even passes into the EUV-heated region. To make this calculation tractable, these works assumed thermal equilibrium with the temperatures prescribed as a pre-calculated function of the local density and X-ray flux via the ionisation parameter (Tarter et al., 1969, see Section 3.2.4). This equilibrium relationship was established using the MOCASSIN Monte Carlo radiative transfer code (Ercolano et al., 2003, 2005, 2008a). The same methods, but with updated prescriptions that are also functions of the column density (to account for attenuation) and use luminosity-dependent spectra, have been applied by Picogna et al. (2019); Ercolano et al. (2021); Picogna et al. (2021) with qualitatively similar results, though smaller errors compared to post-processing with MOCASSIN.

Thus, several works suggest that X-rays can drive dense, EUV-opaque, high mass-loss rate winds. In addition, metal and/or carbon depletion seems able to boost the mass-loss rates in the winds (Ercolano & Clarke, 2010; Wölfer et al., 2019).

Conversely, the work of Wang & Goodman (2017), which aimed to better understand the line spectra of the winds by including thermochemistry in the model, suggests EUV - not X-ray - has the dominant role. The chemistry was handled using a simple chemical network of 24 species, with abundances updated according to reaction rates with each hydrodynamical timestep. Likewise to avoid assumption of thermal equilibrium they directly calculated heating rates from ray tracing - for simplicity using just 4 bins spanning the FUV, EUV and X-ray - and cooling rates from a variety of molecular and atomic processes. These processes lead to a hotter, more tenuous, highly ionised, wind in which EUV photoionisation and adiabatic cooling were the key elements of the thermal balance, suggesting that thermal equilibrium cannot be assumed. Moreover, the X-rays were seemingly important only for helping puff up the underlying disc, with molecular cooling processes active in the X-ray–heated region and seemingly responsible for offsetting their heating. The FUV was likewise important to the heating in these underlying layers. As expected for an EUV wind, the overall mass-loss rates were below those of X-ray models.

However, Nakatani et al. (2018b) performed a similar exercise but found instead that at solar metallicity thermal winds were mostly FUV-driven. In this case X-rays assisted mainly by increasing ionisation levels in the gas; this provides more electrons for recombination, thus shifting the ionisation equilibrium for the grains towards neutral grains for which the FUV photoelectric effect is more effective. In the absence of FUV, X-rays did not drive a wind in these models, regardless of the X-ray spectral hardness. This agreed with previous studies on FUV-driven winds (Gorti & Hollenbach, 2009) showing that given the lower temperatures of FUV-heated gas (a few 100 K), the wind was restricted to the outer disc at $r \gtrsim 50$ au. However, Owen et al. (2012) argued that since FUV winds should only become supersonic at $r > 100$ au whereas X-ray winds can at much smaller radii, then the winds should be X-ray–driven over most of the disc, so long as $L_{\rm FUV}/L_{\rm X} < 100$. Nakatani et al. (2018b) indeed use a ratio of $L_{\rm FUV}/L_{\rm X} = 300$, which may therefore be responsible for their lack of effective X-rays. Komaki et al. (2021) extended these studies across a range of stellar masses (and corresponding FUV and X-ray luminosities).

FUV winds are very sensitive to the dust properties and a reduction in the cross-section due to coagulation and drift has been found to mildly aid the winds (Gorti et al., 2015). Similarly Nakatani et al. (2018a,b) found that mass loss peaked at depleted metallicities $Z/Z_{\odot} \sim 0.1$: higher metallicities result in decreased FUV penetration while lower metallicities make the heating inefficient.

Between all these works, we can summarise five key differences in their methodology

1. the treatment of radiative transfer (whether it is limited to radial ray tracing or whether scattering (particularly of EUV) is allowed)

2. the shape of the irradiating spectrum (whether X-rays, EUV and FUV are all included, in what ratios, and with how many energy bins)

3. the atomic cooling processes included (which species are included, how many levels they have, and the treatment of escape fractions)

4. the inclusion of molecular heating and cooling processes

5. the assumption of radiative thermochemical equilibrium (as opposed to including hydrodynamic contributions from adiabatic cooling ie. PdV work)

A key aim of this thesis - specifically Chapter 3 - is therefore to understand how these differences in the spectra and the thermochemistry produce the discrepant results of recent photoevaporation models (which are summarised by their mass-loss profiles in Figure 1.3) and thus to identify a way forward to producing a consensus.

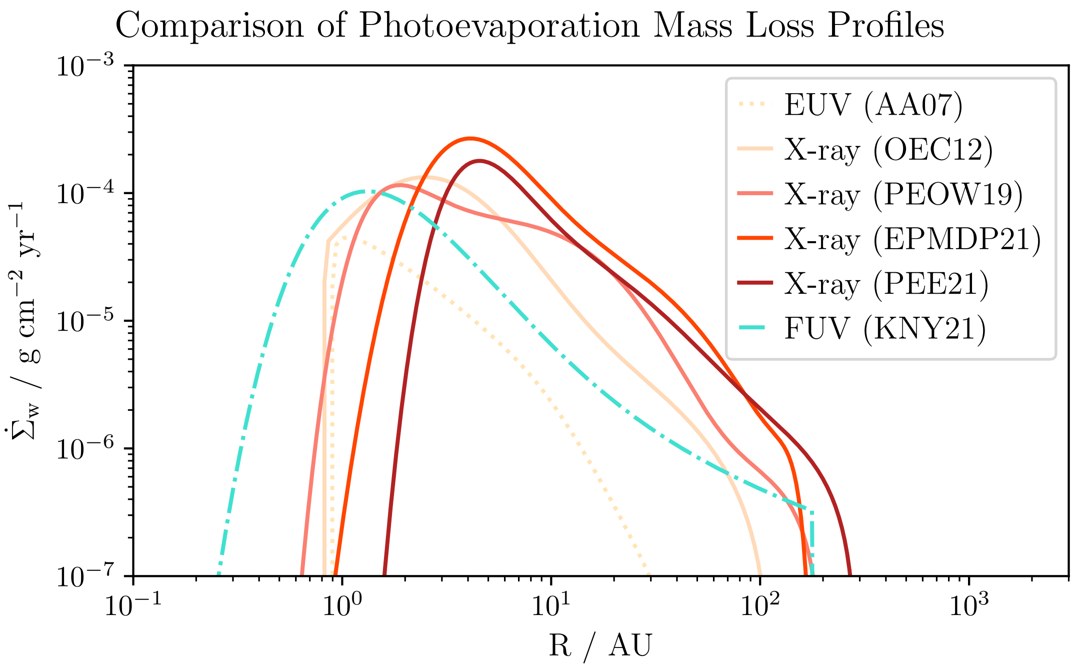

Fig. 1.3 A comparison of photoevaporation mass-loss profiles. The EUV profile of Alexander & Armitage (2007) ($\Phi = 10^{42}$) provides a low mass-loss rate peaking at small radii. The FUV profile of Komaki et al. (2021) (1 $M_\odot$) provides a higher mass-loss rate, with a more extended component over the disc. The X-ray prescriptions of Owen et al. (2012); Picogna et al. (2019); Ercolano et al. (2021); Picogna et al. (2021) ($L_X = 2 \times 10^{30}$ erg s^{-1}/1 $M_\odot$) provide the highest mass-loss rates and peak somewhat further out than the UV models.

Directly irradiated discs

Another important case is when stellar radiation, especially the EUV, is incident directly on the bulk of the disc, rather than just its upper layers. This happens once a sufficiently large and evacuated cavity has opened up (for example after the action of the UV switch, see Section 1.4.1). Alexander et al. (2006a) first modelled this, finding that the direct EUV field (which is much larger than the diffuse field as it is directional) lead to a much more significant wind, helping expedite the outer disc's dispersal. Significant mass loss from the inner edge in discs with inner cavities is also found in X-ray models (Owen et al., 2010, 2011b, 2012; Picogna et al., 2019). Owen et al. (2012, 2013) also put forward a rapid disc dispersal mechanism termed "thermal sweeping" in which the direct X-ray heating destabilises the inner hydrostatic disc, however Haworth et al. (2016) presented an improved criterion for the onset of this instability in which the process happens less readily.

1.2.7 Dust entrainment

The importance of dust to the thermodynamics and ionisation, particularly of FUV-driven winds, makes it important to establish how much dust is entrained in the wind. This is also of potential observational consequence (Owen et al., 2011a; Franz et al., 2022a,b), as well as an additional sink of dust mass.

Not all grains can be entrained in the wind, only those that are small enough to be lifted by drag forces. This size naturally depends on the wind's strength, but typical maximum sizes are in the range of $1 - 10$ μm (Hutchison et al., 2016; Franz et al., 2020). Hutchison & Clarke (2021) and Booth & Clarke (2021) showed that a more stringent limit is set by which grains could be advected to the wind base by the flow that feeds the wind (which can more easily supply grains than turbulent diffusion); this criterion is equivalent to the largest size for which the upward drag force on a stationary grain below the base can overcome the gravity. Since these sizes are much smaller than those to which grains are typically understood to grow, a small fraction $\lesssim 10\%$ of the dust mass can enter the wind (Franz et al., 2022a).

1.3 The Competition for Disc Dispersal

Photoevaporation does not occur in isolation to disperse discs, but as aforementioned, other processes including accretion, dust evolution, and magnetically-driven winds can all compete or act in concert so in this section I discuss each in turn.

1.3.1 Accretion

The Stresses Driving Accretion

Astrophysical fluid flows may in general be viscous and magnetised are so governed by the magnetohydrodynamic Navier-Stokes equations; these may be written in conservative form as the response of the momentum density to a range of stresses

$$\frac{\partial}{\partial t}(\rho u_i) = -\frac{\partial}{\partial x_j}(T_{ij}^{\mathrm{ram}} + T_{ij}^{\mathrm{th}} + T_{ij}^{\mathrm{M}} + T_{ij}^{\nu}) - \rho\nabla\Phi, \tag{1.31}$$

which are are the ram pressure T_{ij}^{ram}, thermal pressure, T_{ij}^{th}, Maxwell (magnetic) stress, T_{ij}^{M} and viscous stresses, T_{ij}^{ν}.

Radial gas motions will result from a change in angular momentum due to the torques imparted by these stresses. We thus take the azimuthal component of this equation

$$\frac{\partial}{\partial t}(\rho u_\phi) = -\frac{\partial T_{R\phi}}{\partial R} - \frac{1}{R}\frac{\partial T_{\phi\phi}}{\partial \phi} - \frac{\partial T_{z\phi}}{\partial z} - \frac{2}{R}T_{R\phi} \tag{1.32}$$

and average over azimuth, finding that

$$\begin{aligned} \frac{\partial}{\partial t}(\rho\langle u_\phi\rangle) &= -\frac{\partial\langle T_{R\phi}\rangle}{\partial R} - \frac{\partial\langle T_{z\phi}\rangle}{\partial z} - \frac{2}{R}\langle T_{R\phi}\rangle \\ &= -\frac{1}{R^2}\frac{\partial R^2\langle T_{R\phi}\rangle}{\partial R} - \frac{\partial\langle T_{z\phi}\rangle}{\partial z}. \end{aligned} \tag{1.33}$$

Thus the $T_{R\phi}$ and $T_{z\phi}$ components may drive accretion.

Although some vertical shear does exist in isothermal discs (Nelson et al., 2013), it will be symmetric about the midplane, resulting in viscosity having no net effect through $\langle T_{z\phi}^{\nu}\rangle$. Thus, the action of viscosity, which depends on orbital shear, is purely in the $R-\phi$ direction:

$$\begin{aligned} \langle T_{R\phi}^{\nu}\rangle &= \eta\frac{\partial\langle u_\phi\rangle}{\partial R} - \eta\frac{\langle u_\phi\rangle}{R} \\ &= \eta R\frac{\partial\langle\Omega\rangle}{\partial R}. \end{aligned} \tag{1.34}$$

By decomposing the velocity components as an average plus a fluctuation - $u_i = \langle u_i \rangle + \delta u_i$ - we can write the ram pressure contributions as due to bulk velocities plus a Reynolds stress:

$$\langle T_{R\phi}^{\mathrm{ram}} \rangle = -\langle \rho \rangle \langle u_R \rangle \langle u_\phi \rangle - \langle \rho \delta u_R \delta u_\phi \rangle. \tag{1.35}$$

Likewise, the Maxwell stress may be written as

$$\langle T_{R\phi}^{\mathrm{M}} \rangle = \frac{1}{4\pi} \langle B_R \rangle \langle B_\phi \rangle + \frac{1}{4\pi} \langle \delta B_R \delta B_\phi \rangle, \tag{1.36}$$

however is unclear to what extent net magnetic fields $\langle B_R \rangle, \langle B_\phi \rangle \neq 0$ occur.

Fluctuating velocities and magnetic fields can originate from a range of hydrodynamic and magnetohydrodynamic instabilities. In the case that the R and ϕ components are uncorrelated, the azimuthal average would give 0, but for correlated fluctuations, we can find non-zero $T_{R\phi}^{\mathrm{ram}}$ and/or $T_{R\phi}^{\mathrm{M}}$. For example, the magneto-rotational instability (MRI) of Balbus & Hawley (1992), may be one process capable of generating such correlated fluctuations that drive accretion (Balbus et al., 1994).

In the steady state, we thus have an equation for the mass flux

$$\frac{\partial}{\partial R} \left(R^2 \langle \rho \rangle \langle u_R \rangle \langle u_\phi \rangle \right) = \tag{1.37}$$

$$R \langle \rho \rangle \langle u_R \rangle \frac{\partial}{\partial R} \left(R \langle u_\phi \rangle \right) = \frac{\partial}{\partial R} \left(-R^2 \langle \rho \delta u_R \delta u_\phi \rangle + \frac{R^2}{4\pi} \langle \delta B_R \delta B_\phi \rangle + \eta R^3 \frac{\partial \langle \Omega \rangle}{\partial R} \right). \tag{1.38}$$

Assuming axisymmetry in the density, vertically averaging and writing the magnetic terms in terms of the Alfvén velocity $\mathbf{u_A} = \frac{\mathbf{B}}{\sqrt{4\pi\rho}}$, we find

$$\overline{\langle u_R \rangle} = \left(2 + \frac{\partial \ln \Omega}{\partial \ln R} \right)^{-1} \frac{1}{\Sigma R^2 \Omega} \frac{\partial}{\partial R} \left(\Sigma R^2 \left(\overline{\nu} \Omega \frac{\partial \ln \Omega}{\partial \ln R} - \overline{\langle \delta u_R \delta u_\phi \rangle} - \overline{\langle \delta u_{\mathrm{A},R} \delta u_{\mathrm{A},\phi} \rangle} \right) \right). \tag{1.39}$$

The $T_{z\phi}$ stress may also cause accretion. This is most commonly considered in the context of net vertical magnetic fields threading the disc: $T_{z\phi} = T_{z\phi}^{\mathrm{M}} = \frac{1}{4\pi} B_z B_\phi$ (since viscosity does not contribute). Such fields are also connected to the existence of magnetically-driven winds, explored more in Section 1.3.3. In this case, the angular momentum, rather than being transferred between disc elements, is carried away by the wind.

Disc Viscosity Models

It is clear from Equation 1.39, that the Reynolds and Maxwell stresses can have similar actions to a viscosity. In order to be agnostic about the source of the accretion stresses, an effective viscosity may be defined (Shakura & Sunyaev, 1973):

$$\nu_{\rm eff} = \alpha c_{\rm S} H, \tag{1.40}$$

such that for $\alpha < 1$, this corresponds to subsonic turbulent motions contained within one scale-height of the midplane.

The value of α appropriate to protoplanetary discs is still a matter of some debate. While the MRI can produce values $\gtrsim 10^{-2}$ (Hawley et al., 1995), protoplanetary disc midplanes may be insufficiently ionised over a large range of radii - a region denoted the “dead zone” - to support this instability (Gammie, 1996), so the lower values produced by purely hydrodynamic instabilities (e.g. Pfeil & Klahr, 2019) may be preferred. The turbulent motions assumed in this model should be of order $\sqrt{\alpha} c_{\rm S}$; measurements of turbulent line broadening with ALMA have thus been used to infer values of $\alpha \lesssim 10^{-3}$ (Teague et al., 2016; Flaherty et al., 2017, 2020). This is in agreement with values of $\alpha \approx 10^{-3}$ inferred from observations of accretion rates and disc masses (Rafikov, 2017). Moreover, low values $\alpha \lesssim 10^{-3}$ are needed to explain disc flux-size correlations (Rosotti et al., 2019a) and even lower viscosities $\alpha \lesssim 10^{-4}$ are needed for hydrodynamical simulations to explain the multiple gaps in the AS 209 disc (Fedele et al., 2018).

In protoplanetary discs, a common model for the temperature structure is a vertically isothermal profile that depends on orbital radius only as a power law. In the absence of disc self-gravity, applying hydrostatic equilibrium allows the vertical structure of a Keplerian disc to be approximated as a Gaussian with scale height $H = c_{\rm S}/\Omega$. In the simple, approximate case of $T \propto R^{-1/2}$, it then follows that $c_{\rm S} \propto R^{-1/4}$, so $H \propto R^{5/4}$, and finally $\nu_{\rm eff} \propto R$.

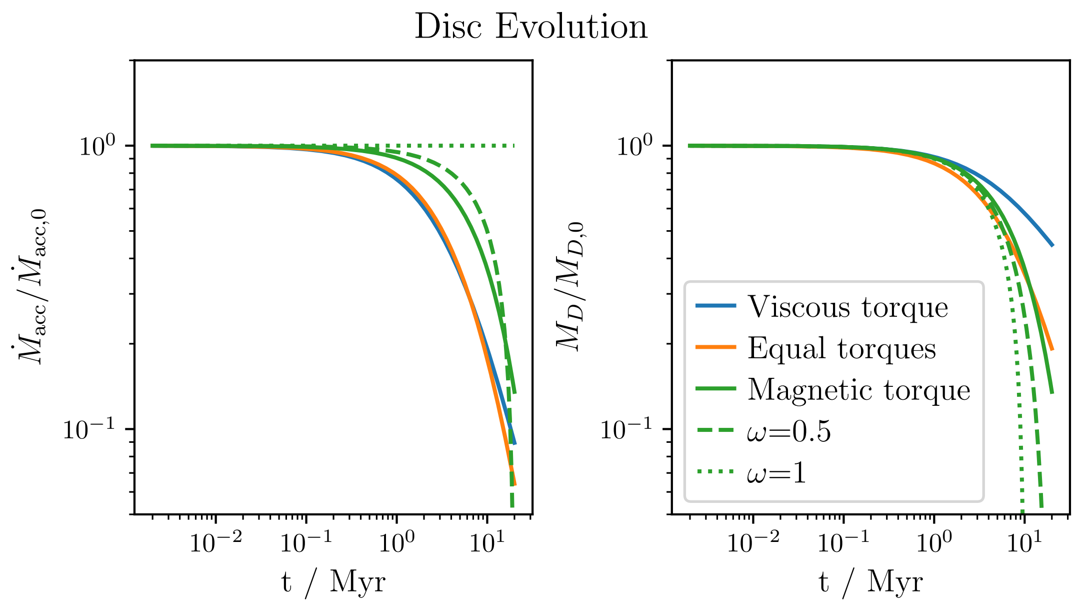

Fig. 1.4 The evolution of accretion rate and mass over time according to different viscous and/or wind-driven models (Tabone et al., 2022b).

Disc Evolution Equations

To obtain the discs's surface density evolution, we start from the vertically-integrated continuity equation

$$\frac{\partial \Sigma}{\partial t} + \frac{1}{R}\frac{\partial}{\partial R}(R\Sigma\overline{u_R}) = 0. \tag{1.41}$$

Substituting Equation 1.39 in the purely viscous case and evaluating for a Keplerian disc $\frac{\partial \ln \Omega}{\partial \ln R} = -3/2$ yields

$$\frac{\partial \Sigma}{\partial t} = \frac{3}{R}\frac{\partial}{\partial R}\left((R^{1/2}\frac{\partial}{\partial R}(R^{1/2}\nu_{\rm eff}\Sigma)\right). \tag{1.42}$$

Equation 1.42 is known as the *Viscous Diffusion Equation* since when recast with the transformed variable $x = R^{1/2}$ and using the common model $\nu \propto R$ (as motivated above), we find that $\frac{\partial x^{3/2}\Sigma}{\partial t} \propto \frac{\partial^2 x^{3/2}\Sigma}{\partial x^2}$. It is thus clear that (effectively) viscous terms arising from the $T_{r\phi}$ stresses have a diffusive quality and lead to the spreading of material both in and out - i.e. the inner regions will act as an accretion disc, while the outer regions where the density drops off serve as a decretion disc, where material moves outwards to conserve angular momentum.

Conversely, the vertically-integrated $T_{z\phi}$ stresses lead to the following form

$$\frac{\partial \Sigma}{\partial t} = \frac{2}{R}\frac{\partial}{\partial R}\left(\frac{R}{\Omega}[T_{z\phi}]^{+}_{-}\right). \tag{1.43}$$

Since this is a first order equation, it doesn't have the same diffusive quality, but will always drive accretion. Multiple works have put forward parametrizations of this regime including Armitage et al. (2013); Suzuki et al. (2016); Khajenabi et al. (2018); Chambers (2019); Tabone et al. (2022b).

When winds (whether responsible for driving accretion or not) remove material from the disc, these can be included in Equation 1.42 or 1.43 as a sink term (e.g. Equation 5.1).

Returning to the case of purely viscous evolution with general power-law viscosity $\nu \propto R^\gamma$, there are generally-attracting solutions to the viscous diffusion equation, meaning that no matter the initial conditions, after some time the disc profile will relax to the following form derived by Lynden-Bell & Pringle (1974):

$$\Sigma(R,t) = \frac{M_{\mathrm{disc},0}}{2\pi R_{\mathrm{C}}^2}(2-\gamma)\left(\frac{R}{R_{\mathrm{C}}}\right)^{-\gamma}\left(1+\frac{t}{t_\nu}\right)^{-\eta}\exp\left(-\frac{(R/R_{\mathrm{C}})^{2-\gamma}}{\left(1+\frac{t}{t_\nu}\right)}\right), \tag{1.44}$$

where $\eta = (5/2-\gamma)/(2-\gamma)$. Due to its simple, yet physically motivated, nature consisting of a power-law inner disc and an exponential cut-off, such profiles are commonly used for disc modelling. R_C may be interpreted as the disc's initial ($t = 0$) scale radius, which then expands over time proportional to $\left(1+\frac{t}{t_\nu}\right)^{1/(2-\gamma)}$ due to the spreading of the outer disc in order to conserve the total angular momentum. t_ν is the initial viscous timescale at R_C, with a typical value (for $\gamma = 1$) of:

$$\begin{aligned} t_\nu &= \frac{1}{3(2-\gamma)^2}\frac{R_{\mathrm{C}}^2}{\nu(R_{\mathrm{C}})} \\ &= 4.89\ \mathrm{Myr}\left(\frac{R_{\mathrm{C}}}{100\ \mathrm{au}}\right)\left(\frac{\alpha}{10^{-3}}\right)^{-1}\left(\frac{h_0}{0.033}\right)^{-2}\left(\frac{M_*}{\mathrm{M}_\odot}\right)^{-1/2}. \end{aligned} \tag{1.45}$$

From Equation 1.44 it can also be seen that the accretion rate onto the star $\dot{M} \propto \nu\Sigma$ is

$$\dot{M}_{\mathrm{acc}} \propto \left(1+\frac{t}{t_\nu}\right)^{-\eta}, \tag{1.46}$$

which integrates to

$$M_{\mathrm{disc}} \propto \left(1+\frac{t}{t_\nu}\right)^{1-\eta}, \tag{1.47}$$

where for the common $\gamma = 1$, $-\eta = -3/2$, $1-\eta = -1/2$. These solutions thus have an *accretion timescale* given by Lodato et al. (2017) as

$$t_{\rm acc} = \frac{M_{\rm disc}}{\dot{M}_{\rm acc}} \tag{1.48}$$

$$= 2(2-\gamma)(t+t_\nu). \tag{1.49}$$

Tabone et al. (2022b) found analytical solutions to the combined evolution under both viscous and magnetic wind stresses (i.e. the combined effects of equations 1.42 and 1.43). Parametrizing the ratio of magnetic and viscous torques as ψ and the efficiency of the wind as ξ, they find a steeper power law decrease with time

$$M_{\rm disc} \propto \left(1+\frac{t}{t_\nu}\right)^{(1-\eta)(1+\psi+2\xi)} \tag{1.50}$$

In the limit of pure wind-driving ($\psi \to \infty$), this becomes an exponential

$$M_{\rm disc} \propto e^{-\frac{t}{2t_{\rm acc,0}}}. \tag{1.51}$$

They also showed that magnetic wind stresses that increase with decreasing surface density as $\Sigma^{-\omega}$ cause runaway accretion (Armitage et al., 2013) in which the disc disperses in a finite time:

$$t_{\rm life} = \frac{2t_{\rm acc,0}}{\omega}. \tag{1.52}$$

1.3.2 Dust Evolution

The inclusion of dust results in the introduction of an additional dust-gas drag force. This is usually treated as being in the Epstein regime, where the dust grain is smaller than the mean free path for collisions between gas particles and the velocity slow compared to the thermal speed such that the drag results from the net impulse of all the individual collisions of gas particles swept up by the dust grain (Epstein, 1924).

The equation of motion for a dust grain with velocity $\mathbf{v}$ is

$$\frac{\mathrm{d}\mathbf{v}}{\mathrm{d}t} = \frac{v_\phi^2}{R}\hat{\mathbf{R}} - \frac{GM_*}{r^2}\hat{\mathbf{r}} - \frac{\mathbf{v}-\mathbf{u}}{t_{\mathrm{stop}}}, \tag{1.53}$$

while that of the gas (with velocity $\mathbf{u}$) can be approximated, neglecting viscous torques, as

$$\frac{\mathrm{d}\mathbf{u}}{\mathrm{d}t} = \frac{u_\phi^2}{R}\hat{\mathbf{R}} - \frac{GM_*}{r^2}\hat{\mathbf{r}} + \varepsilon\frac{\mathbf{v}-\mathbf{u}}{t_{\mathrm{stop}}} - \frac{1}{\rho}\nabla P. \tag{1.54}$$

The dust-gas drag force term is incorporated in terms of the stopping time, defined as the time taken for a constant drag force F_D to equalise the dust and gas velocities when they differ by Δv

$$t_{\mathrm{stop}} = \frac{m_{\mathrm{gr}}\Delta v}{F_D}. \tag{1.55}$$

The acceleration produced by this force on the gas is smaller than that produced on the dust by a factor of ε, the dust-to-gas ratio. While this dust feedback can be considered for higher accuracy (see Chapter 5), it can be neglected here for illustrative purposes.

Making the further assumption that $\frac{\mathrm{d}\mathbf{v}}{\mathrm{d}t} = \frac{\mathrm{d}\mathbf{u}}{\mathrm{d}t} = \mathbf{0}$, the radial components of these equations, evaluated at the disc midplane and neglecting the gas radial velocity, allow us to calculate the azimuthal velocity components:

$$v_\phi = v_K\left(1 + \frac{Rv_R}{t_{\mathrm{stop}}v_K^2}\right)^{1/2}, \tag{1.56}$$

$$u_\phi = v_K\left(1 + h^2\frac{\partial \ln P}{\partial \ln R}\right)^{1/2}. \tag{1.57}$$

We see that the gas orbits at a somewhat sub-Keplerian velocity due to the pressure support (Whipple, 1973). This creates a difference in orbital velocities between the dust and gas of approximately

$$v_\phi - u_\phi \approx \frac{v_K}{2}\left(\frac{v_R}{Stv_K} - h^2\frac{\partial \ln P}{\partial \ln R}\right), \tag{1.58}$$

where we have written $\Omega_K t_{\rm stop} = St$, the Stokes number. For the Epstein (1924) regime, this may be written using the grain radius a, grain internal density ρ_s and gas surface density Σ_G:

$$St = \frac{\pi}{2}\frac{\rho_s a}{\Sigma_G}, \tag{1.59}$$

illustrating that large grains have longer stopping times since they have larger momenta relative to the drag force they experience.

The headwind felt by the dust results in a drag force, and an associated negative torque that causes the dust to spiral inwards.

$$\frac{\mathrm{d}(Rv_\phi)}{\mathrm{d}t} = v_R \frac{\mathrm{d}(Rv_\phi)}{\mathrm{d}R} = -R\frac{v_\phi - u_\phi}{t_{\rm stop}}.$$

Approximating the left-hand side by its leading order term $\frac{1}{2}v_R v_K$, we can solve for v_R (Weidenschilling, 1977):

$$v_{R,\rm dr} = h^2 \frac{\partial \ln P}{\partial \ln R}\frac{v_K}{St + St^{-1}}. \tag{1.60}$$

Where the pressure gradient is negative, as is typical in a full disc where both the densest and hottest material is closest to the star, this represents an inward *radial drift* of dust grains. In the limit of small St, we have $v_R \propto St$ and a slow inwards drift at the terminal velocity (Whipple, 1973). In the limit of large St, we have $v_R \propto St^{-1}$, and a slow inwards drift for objects that have large inertia and are hard to torque inwards.

If we no longer neglect the gas radial velocity in Equation 1.56, then we find that an additional term arises for the radial motion of the dust representing its advection with the gas (Dipierro et al., 2018)

$$v_{R,\rm adv} = \frac{u_R}{1+St^2}. \tag{1.61}$$

For small Stokes numbers, the dominant term is this latter advection term, and the dust grains more or less perfectly follow the gas. As the Stokes number increases, not only does the advection term reduce as the coupling to the gas becomes more imperfect, but the radial drift from the azimuthal headwind drag torques increases. Given that $|u_R| \approx \alpha h^2 v_K$, the two terms become comparable when $St \sim \alpha$. Thus given the magnitude of α discussed in Section 1.3.1, dust with $St > 10^{-3}$ will decouple from the gas. Decoupled, drifting, dust grains with Stokes numbers in the range $\gtrsim 10^{-3}$ are often termed *pebbles* and their inward drift acts to deplete a disc of dust more rapidly than accretion alone. Equations 1.60 and 1.61, and the corresponding regimes, are indicated in Figure 1.5.

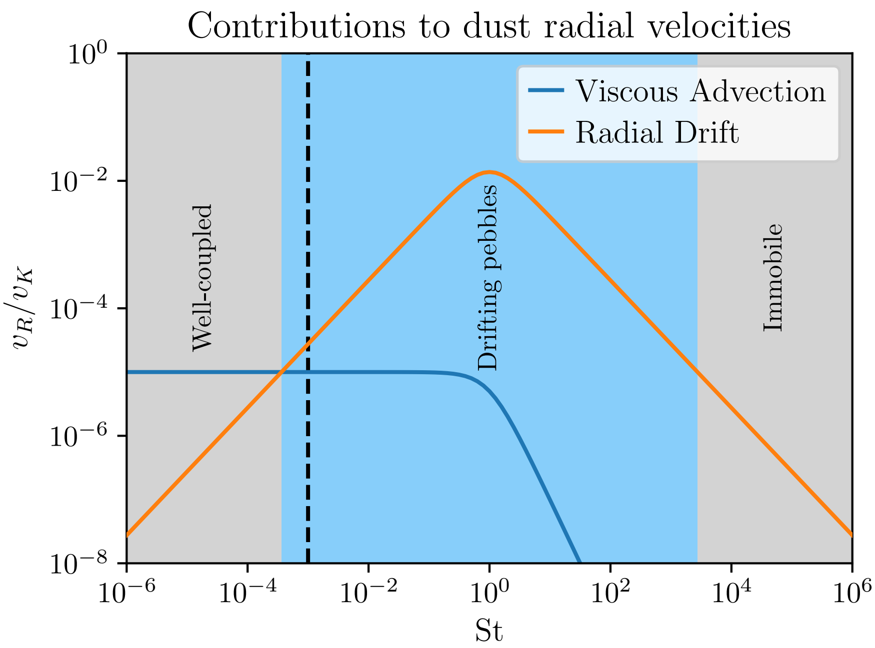

Fig. 1.5 Contributions to dust radial velocities. The radial drift velocity (orange) and velocity due to advection with the viscous flow (blue) are shown as a function of Stokes number. A value of $St = 10^{-3} = \alpha$ is indicated with the dashed line, illustrating that dust with Stokes numbers exceeding this - termed pebbles - are dominated by drift.

To make a simple estimate of how quickly radial drift can deplete a disc, we need to know how quickly grain growth can supply large enough grains to drift. The e-folding time for grain growth may be approximated as (Birnstiel et al., 2012)

$$t_{\rm grow} = \frac{1}{\varepsilon\Omega_K}. \tag{1.62}$$

Once grains grow large enough that their radial drift timescale $t_{\rm rd} \lesssim t_{\rm grow}$ they are removed from the disc before any further growth, thus limiting their size.

Considering a disc of age t, we expect that any grains that grew such that $t_{\rm rd} \ll t$ would rapidly drift, thus reducing ε and increasing $t_{\rm grow}$ and $t_{\rm rd}$. This means that we should expect the dust conditions to self-regulate such that $t_{\rm grow} \sim t$ (e.g. Powell et al., 2017, 2019). Thus, the dust-to-gas ratio may be expected to be

$$\varepsilon \sim \frac{1}{\Omega_K t}, \tag{1.63}$$

where Ω_K should be taken at some characteristic radius of the disc containing most of the mass. In other words, after an initial growth phase, the dust-to-gas ratio should drop approximately by a factor equal to the number of orbits completed in the outer disc.

Of course, the presence of inward radial drift at all is dependent on the negative pressure gradient. Should the pressure gradient become zero, then drift should cease and the grains get trapped. This may occur at a pressure bump such as might form on the outer edge of a gas gap such as that carved by large enough planets (Pinilla et al., 2012). Such pressure bumps are thought to be the origin of many of the dust rings observed with ALMA (e.g. Dullemond et al., 2018) and may prevent the catastrophic loss of dust predicted by Equation 1.63 and indeed most dust evolution models (Takeuchi & Lin, 2005).

However, the lack of radial drift at a pressure bump doesn't mean that grains here can grow arbitrarily large. Rather, since larger grains do not have their relative velocities damped as effectively by the gas (Ormel & Cuzzi, 2007), their collisions are more likely to lead to fragmentation, thus limiting further growth. Fragmentation-limited conditions may also occur in the inner disc, which is not only more turbulent (Birnstiel et al., 2012), but where grains are warmer and ice-free and therefore more prone to fragmentation as they are less "sticky" (Blum & Wurm, 2008; Gundlach & Blum, 2015)[4].

Pebbles may be consumed by the formation of larger bodies. One mechanism is for a clump of pebbles to collapse under its own self-gravity and form planetesimals. To generate sufficiently high pebble densities, a process that concentrates them is needed. The leading candidate is the streaming instability (Youdin & Goodman, 2005; Johansen et al., 2007, 2014), an instability resulting from dust-gas interaction that is triggered once the dust-to-gas ratio exceeds unity. This in turn requires some initial level of concentration perhaps in pebble traps (Johansen et al., 2014; Carrera et al., 2021), at the water snowline (Schoonenberg & Ormel, 2017; Drążkowska & Alibert, 2017), or at the dead zone inner boundary (Chatterjee & Tan, 2014; Hu et al., 2018).

Moreover, planetary embryos that grow beyond $10^{-4}\ M_\oplus$ (Liu & Ji, 2020) have large enough gravitational spheres of influence that pebbles take longer than a stopping time to cross them. This enables significant drag-assisted deflection of pebbles onto the planet, resulting in a regime of *pebble accretion* that efficiently grows planetesimals and planets. The pebble flux created by radial drift resupplies pebbles for the planet to accrete, allowing it to consume a much larger fraction of the disc's solid material.

[4]Though the increased resistance of icy grains to fragmentation has been called into question by more recent experiments at lower temperatures (Gundlach et al., 2018; Musiolik & Wurm, 2019).

1.3.3 Magnetically-driven Winds

Equation 1.43 demonstrates that $T_{z\phi}$ stresses may also drive accretion. Thus, large-scale magnetic fields threading the disc can apply net torques on disc material, which, generally speaking, is weakly ionised (meaning non-ideal effects are important). Electrons are the most mobile species affected by magnetic fields and thus are most strongly coupled to the magnetic fields; they then transfer momentum to the ions, and these to the neutral bulk, through collisions.

At the disc midplane, the magnetic field is frozen into the electrons, its outwards curvature provides magnetic tension that causes them to orbit more slowly than the neutral bulk. Consequently, the collisions remove angular momentum from the bulk material, driving accretion. Moving upwards, the orbital angular frequency of the magnetic field - and anything frozen to it - does not change, but the approximately Keplerian orbital frequency of the neutral bulk reduces. At some point the magnetic field ends up rotating faster than the neutral bulk and transfers angular momentum to it. This angular momentum provides an additional centrifugal acceleration, helping to unbind material in the upper layers and driving a wind to escape outwards. Angular momentum continues to be added roughly until the material crosses the Alfvén surface; material that became super-Keplerian at a distance R_0 and super-Alfvénic at a distance $R_{\rm A}$ has its angular momentum boosted by a factor $\lambda = \left(\frac{R_{\rm A}}{R_0}\right)^2$, known as the magnetic lever-arm parameter.

Classic cold magnetocentrifugal winds are only launched if $\lambda \geq 3/2$ due to energy conservation (Blandford & Payne, 1982; Ferreira, 1997) - in such systems, the energy needed to accelerate and unbind the wind comes from the potential energy lost by the accretion flows. For the potential energy surfaces to be favourable, the magnetic field inclination must be $> 30^\circ$ from the rotation axis. However, a further intermediate class of winds are magnetothermal winds (Bai, 2017), in which some angular momentum is extracted due to magnetic fields, but where the wind energetics are contributed to by the enthalpy term (which drives photoevaporative winds): hot winds are more easily unbound due to their thermal energy. Since magnetic winds are, energetically speaking, driven by a combination of effects, they can launch from region in the inner disc where material is too tightly bound in the stellar potential to be liberated by thermal energy alone.

Disc evolution models that include these winds as sinks of mass frequently do so following Suzuki et al. (2010) by normalising the mass-loss rate to midplane quantities $\dot{\Sigma} = C_w \rho_{\rm mid} c_{S,{\rm mid}}$). Following Suzuki et al. (2016), C_w is limited by the energetics to either all the liberated gravitational potential energy due to both $R-\phi$ and $z-\phi$ stresses (the strong wind case) or some small fraction of the total energy loss including the viscous dissipation (the weak wind case). An alternative approach (e.g. Tabone et al., 2022b) is to normalise

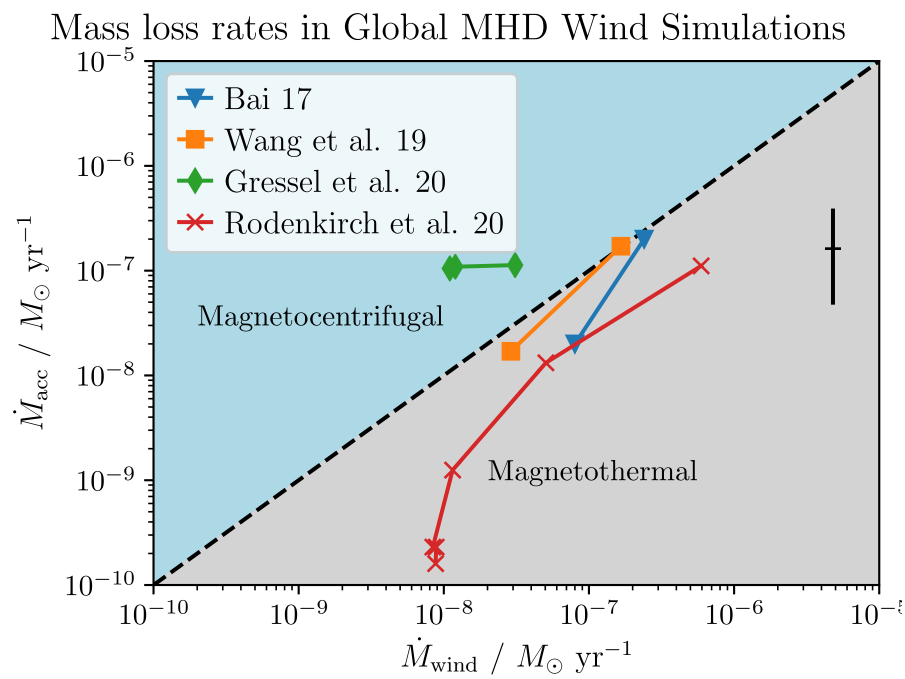

Fig. 1.6 Comparison of wind and accretion mass-loss rates in global simulations of magnetically-driven winds (Bai, 2017; Wang et al., 2019; Gressel et al., 2020; Rodenkirch et al., 2020). Observed rates for HD 163296 (Wichittanakom et al., 2020; Booth et al., 2021) are shown for comparison with the black marker (but note the stellar mass is 1.9 $M_\odot$ whereas the simulations all assumed a solar-mass star).

the mass-loss rate using the efficiency of angular momentum extraction given by λ (where $\lambda < 3/2$ describes magnetothermal winds with mass loss aided by thermal energy input while $\lambda \gg 3/2$ corresponds to the weak wind case).

For many of the same reasons as photoevaporation, as well as the additional details of non-ideal magnetohydrodynamic terms and the unknown strength and evolution of the magnetic flux, there is a lot of model uncertainty about magnetic winds and the degree of mass-loading and the efficiency with which angular momentum is extracted. For example, although recent global simulations (Wang et al., 2019; Gressel et al., 2020; Rodenkirch et al., 2020) do conduct more detailed thermochemical modelling than their predecessors (which assumed a temperature transition at some fixed height (Bai, 2017) or column density (Béthune et al., 2017)), they are still limited in their treatment of the high-energy spectrum and available coolants. Consequently, the mass-loss rates of magnetically-driven winds, as well the accretion rates they can drive, are still debated; Figure 1.6 shows the values obtained by several recent global simulations.

1.3.4 Environmental Effects

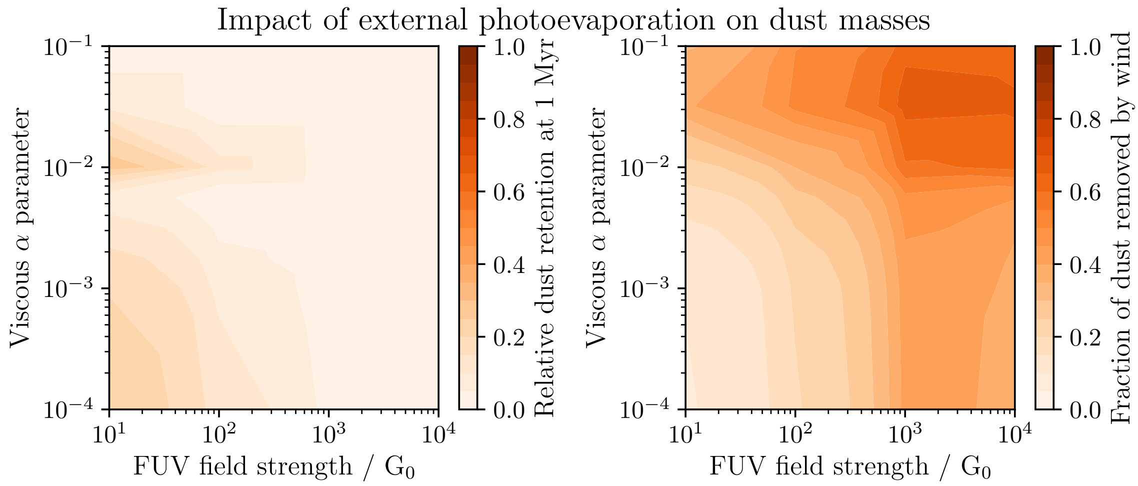

Fig. 1.7 Adapted from Sellek et al. (2020a), the impact of external photoevaporation on dust masses (for a initially 100 M_J, 100 au disc). L: the mass of dust present at 1 Myr as a fraction of that for an equivalent model with no photoevaporation. R: the fraction of the initial dust that was removed by the wind at the end of the model.

When a star-disc system has a neighbouring massive (O/B type) star, photoevaporation can also result, as evidenced by cometary-shaped ionisation structures known as "proplyds" first observed in the Orion Nebula Cluster. In this case, the hot neighbouring star has a photospheric spectrum that includes a considerable amount of FUV. Although intervening cluster gas may shield the disc (see Qiao et al., 2022; Wilhelm et al., 2023, for simulations accounting for this), if sufficient FUV reaches the disc, it may heat the outer regions sufficiently to launch a wind (with sigificant mass loss even for discs smaller than r_G Adams et al., 2004). The mass loss leads to truncation of the discs (Clarke, 2007)[5].

Significant loss of gas can result from external photoevaporation for many discs - not just those in the largest O/B star-hosting clusters - since the median cluster FUV radiation field is around 1000 times stronger than the current solar neighbourhood (Fatuzzo & Adams, 2008). Moreover even low FUV fields may drive a wind from sufficiently extended discs (Facchini et al., 2016; Haworth et al., 2017). Using tabulated mass-loss rates (the FRIED grid, Haworth et al., 2018), Sellek et al. (2020a) showed that the dust is also strongly affected as illustrated in Figure 1.7: for the first ~ 0.1 Myr while the dust is still small and growing it can be removed by the wind; after this time, it also grows large enough to drift inwards away from the wind base. However, the wind's truncation of the disc means that there is no dust at larger radii to resupply the drifting dust and consequently the dust abundance drops rapidly throughout the disc even when the wind only removes a small fraction.

[5] In cluster environments, dynamical encounters can also truncate discs, but on a statistical level this is always less significant than external photoevaporation (Winter et al., 2018, 2020; Wilhelm et al., 2023).

1.4 Observational Support for Photoevaporation

1.4.1 Constraints on Timescales and Progression of Disc Dispersal

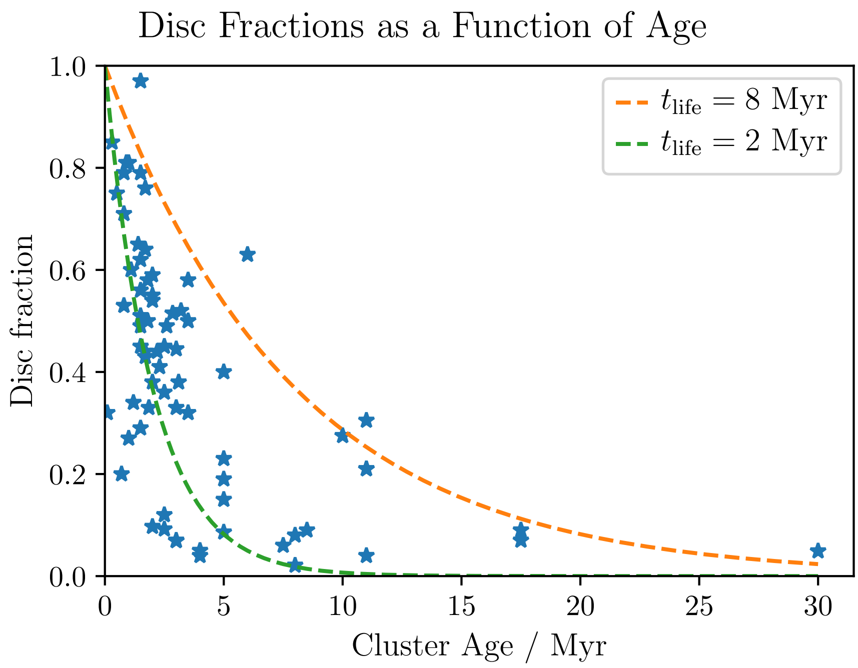

Fig. 1.8 Fraction of stars hosting discs as a function of region age using the sample collated by Pfalzner et al. (2022). The orange and green dashed lines show an exponentially decaying fraction according to the rough upper and lower lifetimes amongst literature estimates.

To estimate the rate at which discs must be dispersed, one may begin with simple estimate of their lifetime. Disc lifetimes are usually inferred from fits to disc fractions across regions of different ages, a version of which is shown in Figure 1.8. This process is complicated by several factors including the difficulty of determining the ages of each region (Pecaut & Mamajek, 2016), the stellar mass range considered (Ribas et al., 2015), the wavelength used to probe the disc emission (Ribas et al., 2014), which objects are members of any given region (with false-positives often reduced by looking only at central regions, which introduces its own bias Pfalzner et al., 2014), and indeed which regions are included in the estimate (Michel et al., 2021; Pfalzner et al., 2022). Thus, while many estimates tended to imply average lifetimes of $2-3$ Myr (Haisch et al., 2001; Richert et al., 2018; Briceño et al., 2019) these were biased towards denser, shorter-lived, clusters and more massive stars with shorter-lived discs as a result of brighter limiting absolute magnitudes for further clusters. Nearby, low-density, environments have disc lifetimes closer to $5-10$ Myr range.

The observed stellar Initial Mass Function suggests that the number of stars formed at a given mass increases with decreasing mass (e.g. Chabrier, 2003), at least as far as the Hydrogen Burning Limit that separates stars from brown dwarfs at $0.064-0.087\ M_\odot$ (Auddy et al., 2016). We therefore take $0.1\ M_\odot$ as the mass of a typical star. It is typically assumed that once a disc reaches a disc-to-star mass ratio of ~ 0.1, it will become gravitationally unstable. In this phase, gravitoturbulence may be driven, leading to high accretion rates that quickly lower the mass (Lin & Pringle, 1987). Thus, the gravitationally unstable phase is likely short and we may assume a typical initial disc-to-star mass ratio of 0.1.

The disc masses are challenging to measure directly - dynamical measurements are only now becoming possible for the most massive discs (Veronesi et al., 2021; Lodato et al., 2023, where disc-to-star mass ratios have been measured at 0.1-0.35). Moreover, most disc mass is in H_2 which emits only poorly, though its deuterated isotopologue HD has been used in a small number of cases (e.g. Kama et al., 2020). Therefore, many other molecules are used as mass tracers - with the total disc mass inferred based on some assumed abundance of the species - but this can lead to a large spread in mass estimates due to their more complicated chemistries (Miotello et al., 2022). Even CO, an abundant and well-studied gas tracer, has uncertainties due to isotopic-selective processes (Miotello et al., 2014, ^{12}CO is optically thick so more optically-thin tracers like ^{13}CO and C^{18}O are typically used) and C/H ratios that are altered by carbon depletion (Sturm et al., 2022). Another popular approach is to use dust continuum emission at mm wavelengths and, following the approach of Hildebrand (1983), infer the emitting dust mass assuming optically thin emission at some typical temperature (typically 20 K) and opacity (Beckwith et al., 1990). The gas mass is then determined as 100 times this value, based on ISM dust mass fractions:

$$F_\nu = \frac{1}{d^2}\int_{R_{\rm in}}^{R_{\rm out}} 2\pi R B_\nu(T)(1-e^{-\tau_\nu})\mathrm{d}R \tag{1.64}$$

$$\begin{aligned} F_\nu &\approx \frac{B_\nu(T_{\rm dust})\kappa_\nu}{d^2}\int_{R_{\rm in}}^{R_{\rm out}} 2\pi R\Sigma_{\rm dust}\mathrm{d}R \qquad (\tau_\nu = \kappa_\nu\Sigma \ll 1) \\ &= \frac{B_\nu(T_{\rm dust})\kappa_\nu}{d^2} M_{\rm d,obs}. \end{aligned} \tag{1.65}$$

The assumptions made above - particularly in relation to the opacity which varies with dust grain size, composition, and porosity - also introduce a large degree of uncertainty into the measurement. However, the simplicity of this approach and the brightness of the continuum emission, make this the most suitable approach for surveying large populations of discs with ALMA (Ansdell et al., 2016; Barenfeld et al., 2016; Pascucci et al., 2016; Ansdell et al., 2017; Eisner et al., 2018; Ansdell et al., 2020; van Terwisga et al., 2020; Grant et al., 2021; van Terwisga et al., 2022). These studies reveal evolutionary trends with age and cluster environment, but the most massive discs typically have dust masses on the order of 100 $M_\oplus$ corresponding to total disc masses $\approx 0.03\ M_\odot$.

Overall, this means that with disc masses of $\gtrsim 0.01\ M_\odot$ and lifetimes of $\lesssim 10$ Myr, discs must lose mass at an average of $\langle \dot{M} \rangle \gtrsim 10^{-9}\ M_\odot\ \mathrm{yr}^{-1}$.

Such rates are indeed typical of accretion. These rates are measured by estimating the accretion luminosity and converting it according to

$$\dot{M}_{\mathrm{acc}} = (1 - R_*/R_{\mathrm{in}}) \frac{L_{\mathrm{acc}} R_*}{G M_*}, \tag{1.66}$$

where $R_{\mathrm{in}}/R_* \approx 5$ is typically assumed. The luminosities themselves are derived either directly from the UV continuum excess (Bertout et al., 1988; Valenti et al., 1993; Gullbring et al., 1998; Herczeg & Hillenbrand, 2008) over some template for the photosphere (usually derived from observations of WTTSs of a similar spectral type Manara et al., 2013). Alternatively, the luminosity of individual emission lines may be used so long as a calibration to the total accretion luminosity is known (Natta et al., 2004; Calvet et al., 2004; Alcalá et al., 2014). Surveys of young star forming regions suggest that accretion rates lie in the range $10^{-11} - 10^{-7}\ M_\odot\ \mathrm{yr}^{-1}$ with a strong dependence on stellar mass (Rigliaco et al., 2011; Alcalá et al., 2017; Manara et al., 2017, 2020).

However, in the paradigm of viscous accretion (see Section 1.3.1), a steady, power-law decline in accretion rate occurs (Hartmann et al., 1998) and so the disc dissipates in an infinite amount of time. Rather, accretion signatures have a finite lifetime, with the fraction of discs exhibiting them declining on a similar - albeit slightly faster - timescale to the dust signatures (Fedele et al., 2010; Briceño et al., 2019) although detection thresholds make intepreting the distribution of low accretion rates somewhat challenging (Clarke & Pringle, 2006). A relatively small fraction of discs have a gap in their SED and are classified as *transition discs* - classically seen to be actively dispersing their material - with most systems showing either a full primordial disc, or a remnant debris disc. A picture thus emerges whereby after a slow steady phase of evolution, a rapid phase of clearing happens on the timescale of $0.1 - 1$ Myr (Skrutskie et al., 1990; Simon & Prato, 1995; Wolk & Walter, 1996), termed the *two-timescale behaviour*.

One early attraction of photoevaporation was that it solves this problem by means of the *UV switch* (Clarke et al., 2001). Using an EUV photoevaporation model, it was shown that once the accretion rate through the disc becomes less than the photoevaporation rate then accretion can no longer resupply the regions which are losing mass to the wind. Consequently, the wind can open a gap on scales of a few au, the isolated inner disc accretes onto the star on its short viscous timescale, and finally the outer disc is rapidly eroded by the direct radiation

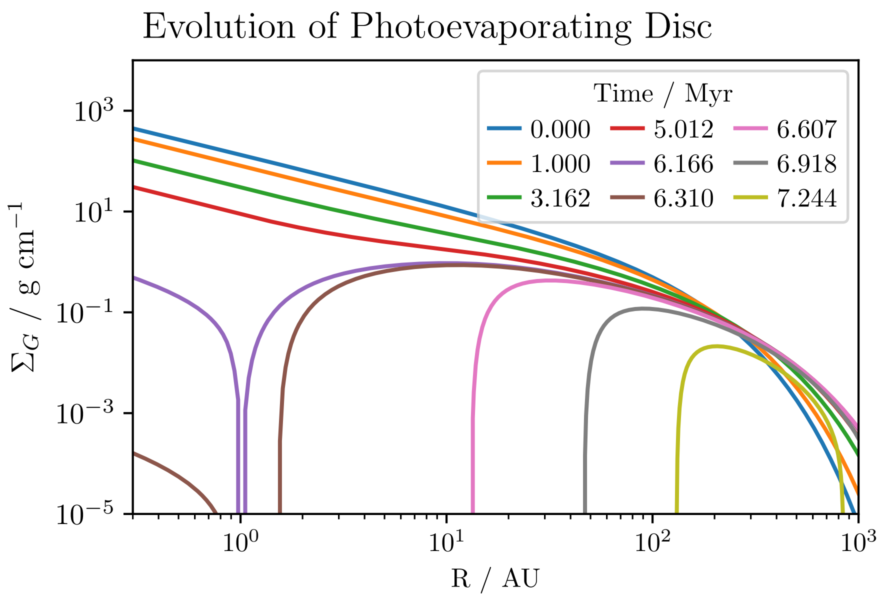

Fig. 1.9 Evolution of the gas surface density in a disc undergoing internal photoevaporation by EUV showing the opening of a gap, accretion of the inner disc onto the star, and inside-out dispersal of the outer disc.

field (Alexander et al., 2006a,b). This progression is illustrated in Figure 1.9. Thus, in this paradigm, disc dispersal happens from the inside out, a hypothesis which is supported by the relative disc lifetimes at different wavelengths (Ribas et al., 2014) and their evolutionary loci in colour-colour space (Koepferl et al., 2013) which imply the loss of the warmer inner material - which emits at shorter wavelengths - first.

In this case, the disc lifetime is set by the initial accretion rate $\dot{M}_{\mathrm{acc},0}$, how fast it declines (the viscous timescale t_ν) and the photoevaporation rate $\dot{M}_{\mathrm{PE}}$. In the limit where $t_{\mathrm{life}} \gg t_\nu$ this may be written as (Clarke et al., 2001):

$$t_{\mathrm{life}} \sim t_\nu \left(\frac{\dot{M}_{\mathrm{acc},0}}{\dot{M}_{\mathrm{PE}}} \right)^{2/3} . \tag{1.67}$$

In the more general case, one may alternatively use the same model to argue that

$$\dot{M}_{\mathrm{PE}} = \langle \dot{M} \rangle \frac{t_{\mathrm{life}}}{2t_\nu} \left(1 + \frac{t_{\mathrm{life}}}{t_\nu} \right)^{-3/2} ,$$

for which it can be shown that $\dot{M}_{\mathrm{PE}} < 3^{-3/2} \langle \dot{M} \rangle$. Thus, long-lived, low-mass, discs should have photoevaporation rates $\lesssim 2 \times 10^{-10}\ M_\odot\ \mathrm{yr}^{-1}$, though shorter-lived, higher-mass, discs may accommodate somewhat higher rates. The power-law decline in accretion rate means that discs spend longest at the accretion rates shortly before they are dispersed i.e. just above the photoevaporation rate. The dependence of the minimum observed accretion rates on stellar mass may therefore reflect that of the photoevaporation rates (Ercolano et al., 2014).

The picture established by the UV switch is consistent with the concept of transition discs as those where the diminished flux in the near infrared is indicative of a cavity in the inner disc. While such a cavity may be opened by photoevaporation, it is important to emphasise that transition discs are not a homogeneous class of objects when one considers their accretion rates (Sicilia-Aguilar et al., 2006) and mm-fluxes (Owen & Clarke, 2012) so this may not be the case for all transition discs. Indeed, many discs seem to remain bright and actively accreting with large cavity sizes, in contrast with the non-accreting relic discs predicted by photoevaporation models (Owen et al., 2011b, 2012; Picogna et al., 2019). Gaps created by massive planets are therefore often invoked to explain the actively accreting discs, although models which combine photoevaporation with a dead zone, such that the inner disc has a low accretion rate and takes a long time to disperse, mean that photoevaporation remains a viable candidate for at least some (Gárate et al., 2021; van der Marel et al., 2022). Moreover, effects including high inclination or dust growth may also lead to diminished emission in the NIR and so not all SED-selected transition discs are actually discs with cavities (van der Marel et al., 2022).

Coleman & Haworth (2022) combined models of internal and external photoevaporation and found that inside-out clearing occurs so long as the mass loss from external photoevaporation is not too large (otherwise the disc is progressively truncated from the outside in). They also show that if the internal photoevaporation rate is large and the α viscosity small enough, the timescale to accrete the inner disc can be long enough to avoid the relic discs.

Nevertheless, photoevaporation models can generally explain the observed decrease in inner disc lifetimes with increasing stellar mass (Komaki et al., 2021; Picogna et al., 2021). One may obtain this trend by converting the disc fractions in the λ Orionis region (Bayo et al., 2012) to lifetimes assuming an age of 5 Myr. Then, by combining in Equation 1.67 the dependence of the initial disc mass and accretion rate on stellar mass with the dependence of the mass-loss rate (on mass or accretion rate) measured from radiation hydrodynamical simulations of photoevaporation, one obtains a predicted lifetime trend.

Somigliana et al. (2022) discuss how to obtain these initial dependences $M_{\rm disc} \propto M_*^{\lambda_{m,0}}$ and $\dot{M}_{\rm acc} \propto M_*^{\lambda_{a,0}}$. Under viscous evolution the exponents evolve towards to $\lambda_m = \lambda_a = 1.5\lambda_{m,0} - 0.5\lambda_{a,0} := \lambda$. They use this to argue that the steepening slopes with time fitted by Ansdell et al. (2017) ($1.7 < \lambda_m < 2.4$) and Testi et al. (2022) ($1.3 < \lambda_m < 2.2$ and $1.5 < \lambda_a < 2.3$) imply $\lambda_{a,0} < \lambda_{m,0}$ where $1.2 < \lambda_{m,0} < 2.1$ and $0.7 < \lambda_{a,0} < 1.5$.

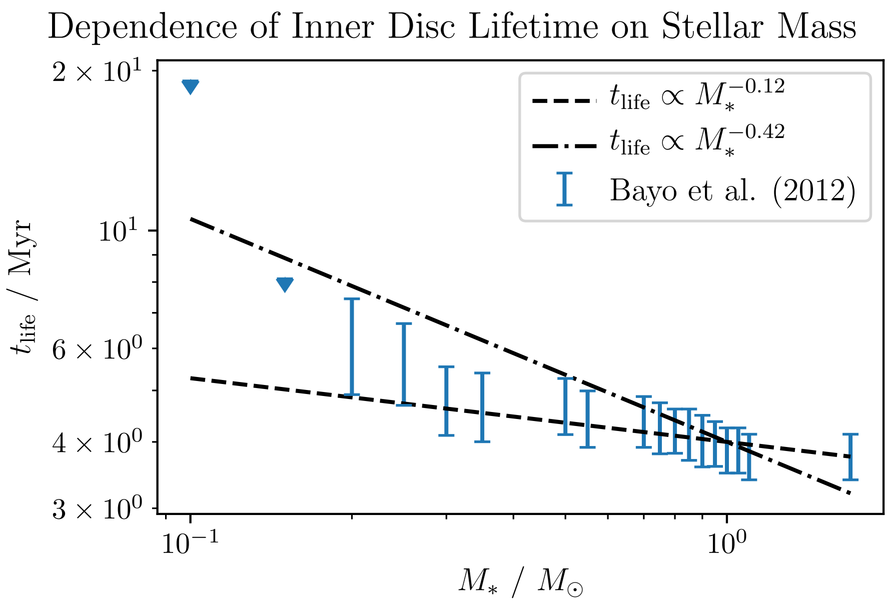

Fig. 1.10 The dependence of the inner disc lifetime on stellar mass. The data inferred from disc fractions in the λ Orionis region (Bayo et al., 2012) are compared to the trends that result from the scalings adopted by Picogna et al. (2021) (dashed) and Komaki et al. (2021) (dot-dashed).

In these terms, the inner disc lifetime scales as

$$t_{\mathrm{life}} \propto M_*^{\lambda_{m,0}-\lambda_{a,0}/3-2\lambda_w/3} \tag{1.68}$$

$$\propto M_*^{2/3(\lambda-\lambda_w)}, \tag{1.69}$$

where λ_w is the photoevaporation rates' mass dependence. As a simple example, in the X-ray–driven models of Picogna et al. (2021), the photoevaporation rate scaled roughly linearly with stellar mass ($\lambda_w = 1$). Assuming a constant initial disc-to-star mass ratio ($\lambda_{m,0} = 1$) and an accretion rate that scales as $\lambda_{a,0} = 1.37$ (Alcalá et al., 2017, although this may steepen for $M_* \leq 0.2M_\odot$), then one finds a decreasing $t_{\mathrm{life}} \propto M_*^{-0.12}$. This is compared to the Bayo et al. (2012) data in Figure 1.10.

The FUV-driven case of Komaki et al. (2021) is complicated by the weakening of photoevaporation over time since it is powered by the accretion luminosity. Their photoevaporation weakens more slowly than accretion (scaling close to $\dot{M}_{\mathrm{PE}} \propto \dot{M}_{\mathrm{acc}}^{1/2}$), so can still disperse the disc in a finite time. While in general this alters Equation 1.68, one can conduct a similar analysis resulting in a rough scaling of $t_{\mathrm{life}} \propto M_*^{-0.42}$.

1.4.2 Direct Tracers of Winds

Emission lines from atomic and/or molecular species in outflows have been detected from discs across all stages of evolution (Pascucci et al., 2022). In the protostellar stages, jets and wide-angle molecular winds are frequently spatially resolved with ALMA (e.g. Klaassen et al., 2016), and their kinematics may also be measured, typically revealing “onion-like” nested velocity structures. Similar outflows are also resolved for a handful of Class II systems (Güdel et al., 2018; Louvet et al., 2018; Booth et al., 2021), but for a majority of systems, the emission is spatially unresolved. However, these emission lines may be spectrally resolved and many studies have relied on this to understand the kinematics.

In particular, in the low-density environments surrounding discs, atomic forbidden transitions can be reasonably effective emitters. Many optical and infrared forbidden emission lines show blueshifted profiles (where the blueshift increases with decreasing critical density of the tracer, implying the outward acceleration of the outflow Hartigan et al., 1995). Table 1.1 summarises many lines that have been used for this purpose and some key information - the best-studied two are the [O I] 6300 Å and [Ne II] 12.81 μm lines.

The origin of the [O I] 6300 Å line has been something of a conundrum as it requires low ionisation (which implies an X-ray wind) but high gas temperatures (which imply an EUV wind). Font et al. (2004) produced the first hydrodynamic model for the Hartigan et al. (1995) emission as originating in a thermal wind: while several lines from *ionised* species could be explained by an EUV-driven wind, there was insufficient O I to explain its observed line luminosities. Ercolano & Owen (2016) reconciled this picture by showing that [O I] emission can originate in the inner region of a X-ray–driven wind, where the EUV can still penetrate and heat the gas sufficiently. Thus, the [O I] luminosity is determined by the size of the EUV-heated region which in turn depends on Φ. Since their accretion spectrum has a strong EUV component (though Alexander et al., 2004a, argue that as for stellar atmopsheres, the Lyman continuum should be strongly absorbed by H I, and the accretion streams will further attenuate the EUV from the spectrum that reaches the disc/wind, such that accretion should not contribute to Φ), they reproduce the observed correlation of [O I] fluxes with the accretion luminosity (Rigliaco et al., 2013; Nisini et al., 2018).

Outflows can also be traced in atomic absorption in Lyman α (Arulanantham et al., 2021, 2023), C II 1335 Å (Xu et al., 2021), Mg II 2796 Å and 2804 Å (López-Martínez & Gómez de Castro, 2015) and He I 10830 Å (Edwards et al., 2006; Erkal et al., 2022). In this case, broad emission lines are created at accretion shocks, and intervening material produces absorption within these lines. The outflows they trace are likely mostly jets and stellar winds so these lines have limited usefulness in understanding photoevaporation.

Table 1.1 Commonly observed outflow-tracing atomic forbidden lines.
Key studies of these lines include H95 (Hartigan et al., 1995), L07 (Lahuis et al., 2007), P07 (Pascucci et al., 2007), E07 (Espaillat et al., 2007), H07 (Herczeg et al., 2007), P09 (Pascucci & Sterzik, 2009), vB09 (van Boekel et al., 2009), N10 (Najita et al., 2010), Sa12 (Sacco et al., 2012), Sz12 (Szulágyi et al., 2012), E13 (Espaillat et al., 2013), R13 (Rigliaco et al., 2013), N14 (Natta et al., 2014), R15 (Rapson et al., 2015b), S16 (Simon et al., 2016), F18 (Fang et al., 2018), M18 (McGinnis et al., 2018), B19 (Banzatti et al., 2019), P20 (Pascucci et al., 2020), W21 (Whelan et al., 2021) F23 (Fang et al., 2023a).

Species	Wavelength	Critical Density $n_{\rm crit}$ / $\rm cm^{-3}$	Einstein Coefficient A_{21} / $\rm s^{-1}$	g_2/g_1	Detections
O I	6300 Å	1.8×10^6	5.65×10^{-3}	5/5	H95, R13, N14, S16, F18, M18, B19, P20, W21, F23
O I	5577 Å	1.0×10^8	1.26	1/5	H95, N14, S16, F18
O II	3726 Å	3.8×10^3	1.75×10^{-4}	6/4	N14
S II	4068 Å	2.6×10^6	1.92×10^{-1}	2/4	N14, F18
S II	6716 Å	1.7×10^3	2.02×10^{-4}	6/4	H95, N14
S II	6731 Å	1.6×10^4	6.84×10^{-4}	4/4	H95, N14, S16, W21
N II	6583 Å	8.5×10^4	2.92×10^{-3}	5/5	H95, N14
Ne II	12.81 μm	5.0×10^5	8.59×10^{-3}	2/4	P07, L07, E07, H07, P09, vB09, Sa12, Sz12, E13, P20
Ne III	15.55 μm	3.6×10^5	5.84×10^{-3}	3/5	L07, N10, Sz12, E13, R15

Henceforth in this section, I consider in turn what three lines of evidence - a) the kinematics inferred from line profile shapes, b) trends in line properties with quantities that trace disc evolution, and c) spatial information from spectroastrometry and IFU imaging - tell us about the role photoevaporation plays in disc evolution and dispersal.

Kinematics from Line Profiles

The blueshifted profiles may typically be decomposed into different components. The High Velocity Component (HVC) has a centroid blueshift of > 30 km s^{-1}: speeds which greatly exceed the sound speed in photoevaporative winds and so indicate that it traces a fast magnetohydrodynamic jet launched from either the star or the star-disc interaction region. The Low Velocity Component (LVC) therefore has a centroid blueshift of < 30 km s^{-1} and likely traces disc winds of some kind. Gaussian profiles are widely used to fit each component; for some lines the LVC requires two Gaussians (Simon et al., 2016) - one to fit the narrow central peak (the Narrow Component, NC/NLVC) and a broader one to capture the line wings (the Broad Component, BC/BLVC) - though sometimes a Single Component (SC) LVC is a sufficient fit (these may have widths consistent with typical values for either a BC or a NC).

The line widths (specifically the Half-Width at Half Maximum, HWHM), may be used to understand the wind's kinematics. Under the assumption of Doppler-broadened (as opposed to thermally-broadened) lines, the line width is set by the fastest approaching and receding velocities along the line of sight. Although there may be gradients in the poloidal velocity, the typical assumption is that - especially at high inclinations - the azimuthal velocities dominate and are approximately Keplerian (so long as the emission comes from low down in the wind). Thus, an approximate launch radius may be determined using the following expression:

$$R_{\rm Kep} = GM_* \left(\frac{\sin i}{\Delta v_{\rm HWHM}} \right)^2 . \tag{1.70}$$

Inferred values from [O I], [Ne II], CO and H_2 are shown for different line components in Figure 1.11. For rather broad lines we may find that $R_{\rm Kep} \ll R_G$, implying that the outflow is inconsistent with a photoevaporative wind, while the narrower components are more promising. I now discuss each in turn.

Considering the well-studied [O I] 6300 Å line, which typically consists of a HVC as well as both BLVC and NLVC components, the Keplerian launch radius approach yields values in the range of $0.05-0.5$ au for the BLVC and $0.5-5$ au for the NLVC (Simon et al., 2016; McGinnis et al., 2018). Line profiles with single-component LVCs also appear to span the full range of launch radii of both broad and narrow components. Energetically, photoevaporative winds cannot launch within ~ 1 au, so the BLVCs (and broader SCs) must trace a magnetically-driven wind. While the NLVC and BLVC appear to originate in different locations, Banzatti et al. (2019) argued that since the kinematics of two were closely correlated across the full sample of discs, then both LVC components should originate in (two different regions of) the same radially-extended magnetically-driven wind.

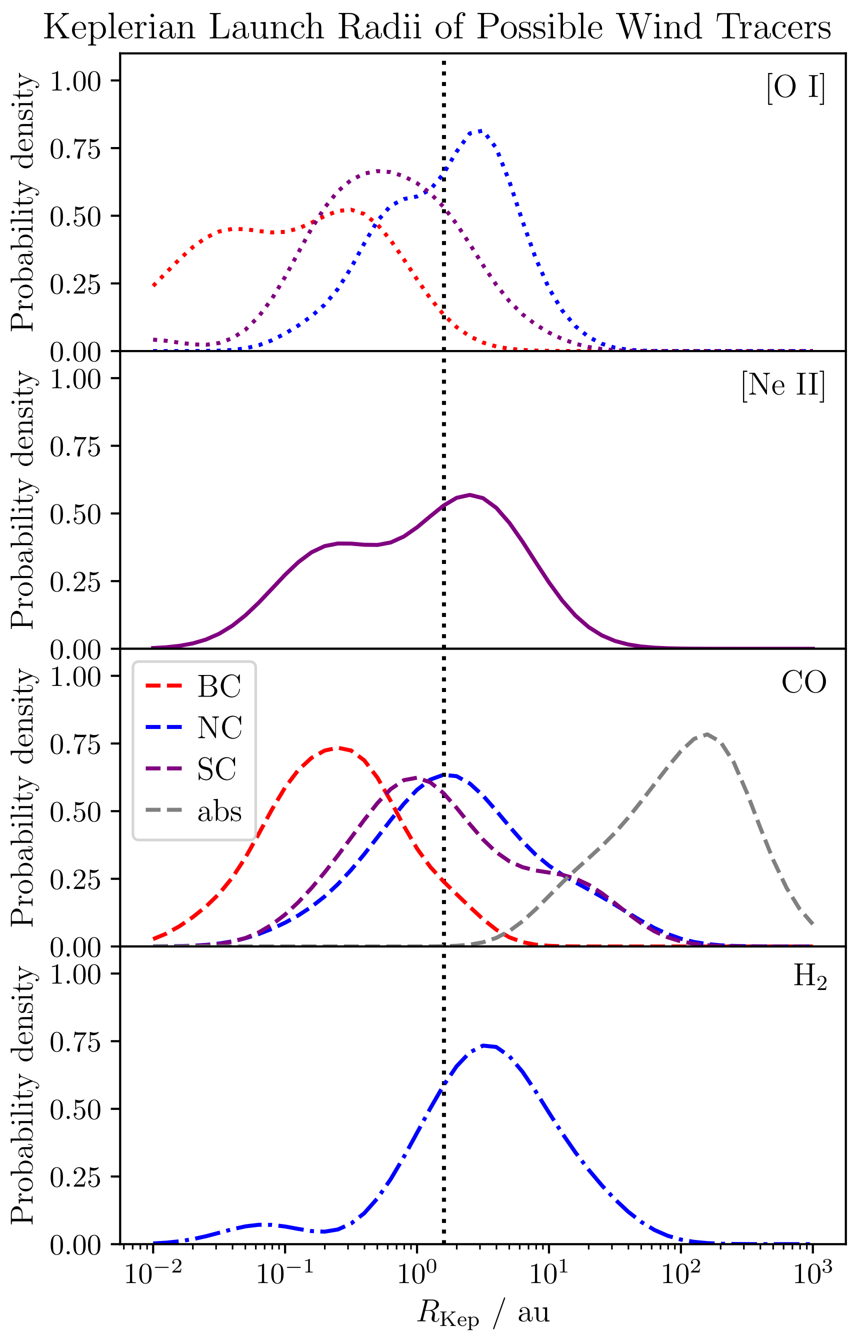

Fig. 1.11 Kernel Density Estimates of the distributions of radii inferred from line widths assuming Keplerian broadening. The data are from Banzatti et al. (2019); Pascucci et al. (2020) for [O I] and [Ne II], from Banzatti & Pontoppidan (2015); Banzatti et al. (2022) for CO and from Gangi et al. (2020) for H_2. The distributions are shown considering the designation of broad component (BC, red), narrow component (NC, blue), single component (SC, purple) and absorption (abs, grey) as determined by each work. The vertical dotted line indicates the critical radius of 0.2 r_G for the median stellar mass across the total sample ($\approx 0.9\, M_\odot$) assuming $c_S = 10$ km s^{-1}.

However, Weber et al. (2020) conducted forward modelling using simulations of both photoevaporative winds and MHD winds, finding that Gaussian decomposition doesn't necessarily trace physically distinct regions since projection effects result in each component being a superposition of emission from different parts of the flow. Nevertheless, photoevaporation models can match the FWHM and centroid shifts of the majority of NC profiles well; MHD models match the FWHM but tend to overestimate the shifts. Thus on the basis of NC profiles alone, photoevaporation is a viable explanation for the wind.

Weber et al. (2020) further argue that photoevaporation can produce all observed correlations of line strength, blueshift and width with accretion luminosity by means of larger emitting regions at higher $L_{\rm acc}$ (see also Ercolano & Owen, 2016) which probe regions of higher poloidal velocity (and therefore blueshift) and lower toroidal velocity (reducing the Keplerian broadening). Therefore the correlations between NC and BC properties can arise from common correlations with $L_{\rm acc}$ as a third variable. In MHD wind models, the accretion rate is correlated with the wind mass-loss rate and hence density, negating the ability of higher $L_{\rm acc}$ to penetrate further. Therefore this sort of MHD model seems unable to produce the observed kinematic correlations of the LVC components.

Further evidence against MHD models provided by Weber et al. (2020) is the widespread prediction of rarely observed Keplerian double-peaked profiles. This suggests the MHD wind models are not radially extended enough and may require some emission in a photoevaporative wind from the outer disc to fill in the troughs.

In contrast, the [Ne II] 12.81 μm line is usually fit with either an HVC or a single narrow LVC (Pascucci et al., 2020). While the modelling of this line has been less extensive, it doesn't yet seem able to discriminate between photoevaporation models as both EUV-driven (Alexander, 2008) and X-ray–driven models (Ercolano & Owen, 2010) can match the line shapes. The narrow LVC profiles can be consistent with either photoevaporative or extended MHD winds and there are no unequivocal correlations of the line fluxes, shifts or widths with properties such as luminosities (Güdel et al., 2010; Sacco et al., 2012; Pascucci et al., 2020).

Molecules emit a rich spectrum of (ro-)vibrational lines in the infra-red. CO line profiles may be roughly separated into two shapes: "double-peaked" (as expected for emission from a Keplerian disc) and "triangular" (Bast et al., 2011; Banzatti & Pontoppidan, 2015; Banzatti et al., 2022). These may be discriminated using the ratio of the line widths at 10% and 75% of the peak flux, with a value < 2.5 describing double-peaked profiles and > 2.5 triangular profiles. Like the atomic emission line LVCs, the triangular profiles may be split into broad and narrow components. Based on line ratios, the broad component shows vibrational excitation similar to the double-peaked profiles and likely also originates in the disc, while the narrow component is vibrationally colder implying this is an additional component with different excitation conditions. At the highest inclinations for triangular shape profiles, very narrow blueshifted absorption may be found with low vibrational excitation conditions (similar or even lower than the narrow component).

While the Doppler shifts found by Banzatti et al. (2022) are small - and often individually consistent with 0 given the uncertainties on the systemic radial velocity - overall the narrow component generally seems to be somewhat blueshifted implying an origin in a slow wind. The corresponding Keplerian radii for the narrow components are $1-20$ au, also consistent with an extended - potentially photoevaporative - disc wind (c.f. $\lesssim 2$ au for the broad component tracing inner disc gas). The narrow absorption would, in this scenario, result from self-absorption in the outermost part of the wind. Moreover, the line widths generally get narrower with increased inclination for both the double-peaked and triangular shapes in a way that is consistent with expectations for bound gas and winds respectively (Pontoppidan et al., 2011).

The H_2 quadrupolar transition at 2.12 μm has been observed for a few sources. For a sample of 17 discs with H_2 detections in Taurus and Auriga, Gangi et al. (2020) found the H_2 kinematics - particularly the centroid shifts - to be well correlated with those of the lowest velocity component of the O I emission. In only 7 of these sources, however, are there blueshifts that are inconsistent with the system velocity and suggestive of a wind; three have spatially resolved emission implying a wide-angle wind (e.g. DG Tau A, Agra-Amboage et al., 2014). The line widths are generally similar - thus implying a similar range of emitting distances from the star under the Keplerian assumption - though for the broadest [O I] lines, the H_2 lines are somewhat narrower (implying more extended H_2 emission) and H_2 is entirely undetected once the [O I] traces radii < 0.5 au.

Rab et al. (2022) post-processed the models of Weber et al. (2020) with the thermochemical code PRODIMO to determine the emitting regions of H_2 and O I. The hydrogen typically only survives where it can self-shield, limiting it to close to the wind base and generally to larger radii than the O I (though the emitting regions overlap), consistent with the observed line widths. They also predict that self-absorption should be seen when the lines are observed at inclinations of $i \approx 60^\circ$.

Comparing the inferred radii for the two atomic and two molecular tracers in Figure 1.11, we see that the broad components are typically on sub-au scales, while the narrow components all have their distributions peak around 3 au. Given a median stellar mass across the samples of $\approx 0.9 M_\odot$, this corresponds to around 0.4 r_G for a 10 km s^{-1} wind. Thus, the narrow components are consistent with the inner regions of a photoevaporative wind. The single components of [Ne II] also peak at this radius, though with a tail that lines up well with the broad components in CO and [O I].

Evolution of Line Strengths

As aforementioned, the [O I] line luminosity correlates with accretion luminosity (which is primarily in the UV) (Rigliaco et al., 2013; Nisini et al., 2018) and therefore evolves as the accretion rate declines over time (Hartmann et al., 1998). While it is tempting therefore to ascribe it to a UV-driven wind, or an accretion-powered (i.e. magnetically-driven) wind, Ercolano & Owen (2016); Weber et al. (2020) have shown how this naturally occurs due to the scaling of the EUV-heated volume even in a X-ray–driven photoevaporative wind. The less extended emitting volume as the accretion flux declines means that over time the [O I] LVC emission is skewed towards smaller radii and hence becomes more broadened as seen in the data (Banzatti et al., 2019).

Moreover, as the accretion luminosity declines, the HVC tends to become less strongly blueshifted, then vanishes entirely (Banzatti et al., 2019); HVCs are only found in discs with optically thick inner discs. The optical depth can be measured using spectral indices in the infrared (e.g. n_{13-31}): the loss of dust in the inner disc produces a drop in flux at shorter wavelengths and so an increase in the index. As spectral indices increase, indicating inside-out disc clearing, the HVCs first disappear, followed by the BCs - which trace material closer in - leaving only narrow SCs (McGinnis et al., 2018), which get narrower with increasing spectral index (Banzatti et al., 2019). The line luminosity also continues to fall.

Similar trends are identifiable between star forming regions of different ages. Fang et al. (2023a) surveyed [O I] emission for 115 disc-bearing stars in the older (5 – 10 Myr) Upper Sco region (previously surveyed regions - except the 3 – 5 Myr NGC 2264 (McGinnis et al., 2018) - have ages of 1 – 3 Myr)[6]. The detection rate is lower, in line with the weaker emission expected over time, with the fraction of sources with HVCs more than halving and the proportion of single component LVCs increasing. However, the blueshifts and line widths of the SCs are statistically indistinguishable between the younger and older samples.

With regards to the [Ne II], the HVC exists only for discs that appear young in the evolutionary sequence outlined above (i.e. those that have [O I] HVCs and lower infrared spectral indices). The LVC appears as discs clear and contrary to the [O I] actually grows in luminosity as the disc clears (Pascucci et al., 2020). For any given disc, the [Ne II] LVC also has a consistently larger blueshift and generally narrower width than its [O I] counterpart indicating an origin at larger radii outside the cavity (with the oxygen originating inside the cavity, where the redshifted emission from the disc's far side can also be seen, resulting in little overall blueshift).

[6]Due to the relatively longer lifetimes of inner discs around lower mass stars, the $\sim 20\%$ that retain discs are biased towards lower masses than in younger regions; no statistically significant difference in detection rate of the line was found between the earlier and later type stars however.

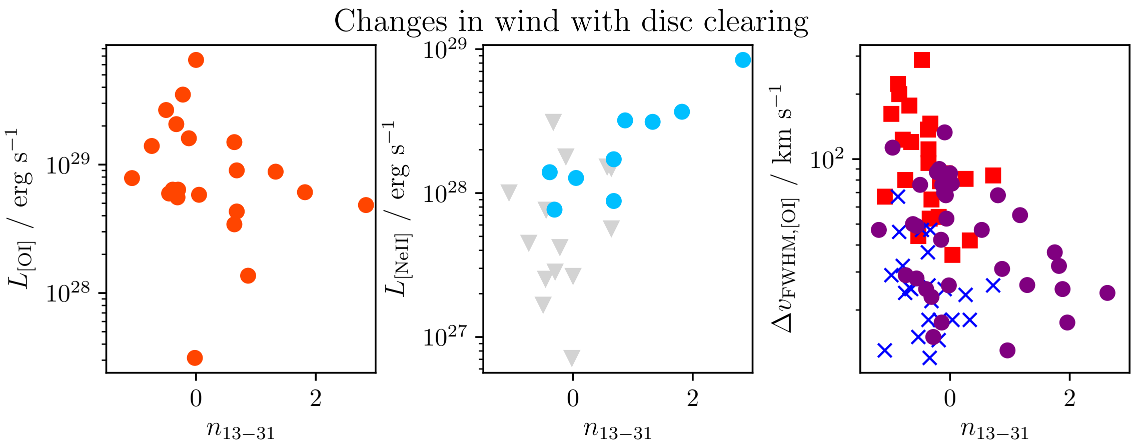

Fig. 1.12 The relationships between $L_{[\mathrm{O\,I}]}$, $L_{[\mathrm{Ne\,II}]}$ and $\Delta v_{\mathrm{FWHM},[\mathrm{O\,I}]}$ and n_{13-31} (Banzatti et al., 2019; Pascucci et al., 2020). The lines are separated by width into broad components (red squares), narrow components (blue crosses) and single components (purple circles).

Conversely, Banzatti et al. (2022) found triangular CO line profiles more often (though not exclusively) occurred in full discs without cavities. This suggests that the wind they trace is not considerably extended, more akin to a magnetically-driven wind from smallish radii.

These patterns suggest that the wind's nature may be changing significantly over the disc lifetime. The [Ne II] is the most robustly found at larger radii even as the disc clears and thus is now considered the leading candidate for an unambiguous tracer of an extended disc wind such as results from photoevaporation.

Spatial Information

While these observations are mostly spatially unresolved, recent years have seen increased attempts to obtain spatial information about the line emission. One promising technique deriving spatial information from the high spectral resolution data used to explore kinematics is spectroastrometry (Bailey, 1998; Whelan & Garcia, 2008). By calculating the centre of light at each velocity channel (which can be done with more spatial precision than the resolution), one can probe the emission's extent; the velocity gradients may also inform us about wind properties (Barrier et al., in prep.). Whelan et al. (2021) applied this to optical lines of O I and S II but Pascucci et al. (2011) detected no spectroastrometric signal for [Ne II] 12.81 μm . However, JWST's MIRI MRS IFU may be able to resolve [Ne II] emission from extended winds from nearby discs (Pascucci et al., 2021) and Chapter 4 explores this prospect. (Fang et al., 2023b) recently used the MUSE IFS to constrain 80% of the [O I] emission from TW Hya to inside 1 au.

1.5 Summary

In this introduction I have set the scene for the four following chapters:

- Chapter 2 regards self-similar models for the hydrodynamics of the wind as introduced in Section 1.2.2. This work was completed in an attempt to a) better understand what controls the velocity at which the wind is launched from the disc surface in radiation hydrodynamical models and b) produce some more accurate models (for example in terms of the wind base geometry) for use in forward modelling of wind observables (Section 1.4.2).

- Chapter 4 provides example applications of self-similar models for the exploration of the flux ratios and profiles of blueshifted emission lines (Section 1.4.2) and the creation of synthetic JWST IFU images. This helps test whether they do indeed trace photoevaporation and explores what their trends show in the context of protoplanetary disc evolution. We may also constrain debated properties including how the wind is heated and hence its extent and density (Sections 1.2.4 & 1.2.6). Understanding the mechanisms and cross-sections of X-ray photoionisation (Section 1.2.4) is crucial to interpreting the different behaviours of the [Ar II] and [Ne II] lines.

- Chapter 3 disentangles the effects of how thermochemistry has been modelled in different previous works on photoevaporation (Section 1.2.6). Specifically, I establish the important roles played by the X-ray spectrum shape (Section 1.2.4) and collisional cooling mechanisms (Section 1.2.5). These factors ultimately determine the wind's energetics (Sections 1.2.1 & 1.2.3), and so are responsible for the current theoretical uncertainty in the strength of photoevaporation.

- Finally Chapter 5 explores how photoevaporation interfaces with other processes - particularly gas accretion (Section 1.3.1) and dust radial drift (Section 1.3.2), by applying different previous prescriptions (Section 1.2.6) for photoevaporation mass-loss rates to a grid of disc evolution models. This supplements the body of existing work exploring how protoplanetary discs evolution and dispersal progresses (Section 1.4.1): by tracking how the inside-out clearing of discs appears in the plane of accretion rates and dust masses inferred from observations - and on what timescale this happens - I constrain the strength of winds in disc populations.

Chapter 2

The Self-Similar Hydrodynamics of Photoevaporative Winds

2.1 Motivation

As explored in the introduction, the kinematics of disc winds - and therefore information about their temperature, extent and driving mechanisms - may be constrained observationally through blueshifted emission lines. Modelling these observational diagnostics has typically required hydrodynamical simulations to self-consistently calculate the thermal structure and generate the streamline morphology (e.g. Font et al., 2004; Ercolano & Owen, 2010; Picogna et al., 2019) because in general no analytic solution exists. However including both radiative transfer and hydrodynamics makes such simulations expensive, which is compounded if one is interested in varying parameters to see their impact on line strengths and shapes in order to understand what can be inferred from observations.

A simple model for the winds which accurately captures their density and velocity structure without expensive hydrodynamical simulations is therefore useful for enabling the interpretation of observations. Moreover, verifying the agreement between such models and hydrodynamical simulations helps us to validate the salient physics that control conditions at key locations in the wind such as its launch base and sonic surface.

For this, we return to the concept of Clarke & Alexander (2016) introduced in Section 1.2.2 of neglecting effective gravity and thus establishing a self-similar solution in which streamline morphologies and quantities scale with power laws of the launch radius r_b and are independent of the gravitational radius r_G. Here, the streamline curvature is the salient effect controlling the sonic surface location in the manner of a transsonic nozzle flow. Ballabio et al. (2020) applied such solutions to model literature data for the blueshifted [O I] (Banzatti et al., 2019) and [Ne II] emission lines, and draw conclusions about, in particular, the sound speeds in the winds traced by these lines and therefore the likely radiation heating the wind. Knowing the wind's launch velocity is also crucial to determining which sizes of dust grains reach the wind launching region and thus constraining the likelihood of dust entrainment (Booth & Clarke, 2021); the self-similar solutions have also used to investigate this and to follow the subsequent grain trajectories in the wind (Hutchison & Clarke, 2021).

Clarke & Alexander (2016) made some simple assumptions that winds are a) isothermal (a decent approximation as while temperature gradients are found in simulations, they tend to be small, e.g. Nakatani et al., 2018a; Picogna et al., 2019) and b) launched perpendicularly from the disc midplane (simulations including those by Wang & Goodman, 2017; Picogna et al., 2019, show streamlines originating from elevated bases, sometimes at less than 90°). To obtain self-similar solutions, they found that all streamlines must launch at a common velocity $u_{\rm b}$. However for any given density profile, there were a range of self-consistent such solutions to their modified 'de Laval nozzle' problem, up to a maximum Mach number $\mathscr{M}_{\rm b,max}$ for which the solution could avoid encountering a singularity in the equation at some point along the streamline. When these solutions were benchmarked against scale-free 2D hydrodynamic simulations, they found that the solution adopted by the wind was in good agreement with the maximal allowed solution launched at $\mathscr{M}_{\rm b,max}$. Moreover, even when they reintroduced gravity and rotation into their hydrodynamical simulations, this solution was well-recovered at radii $r \gg r_G$ and was even a good description at radii as low as $0.5\ r_G$, so long as the streamlines' radius of curvature was small, thereby justifying neglecting gravity and rotation. Thus Clarke & Alexander (2016) concluded that one could model photoevaporative winds well using the solution for $\mathscr{M}_{\rm b,max}$.

If self-similar solutions are to be better understood - and used to approximate the results of radiation hydrodynamics simulations in interpreting observational data - the results of Clarke & Alexander (2016) must be tested with their key assumptions relaxed. In this chapter I thus aim to address the following questions:

- How may self-similar solutions for thermal winds be derived in the more general case of non-isothermal winds launched from an elevated base?
- Do the self-similar solutions with maximum allowable Mach numbers still correspond to scale-free hydrodynamical simulations in this generalised case and why?
- How do the non–scale-free effects of effective gravity and non–power-law density profiles affect the applicability of these generalised solutions?

2.2 Description of Variables and Wind Base

In the approximation described above, since gravity is neglected, then r_G cannot enter the solution - instead, the sole length scale is the radius at the base of each streamline, r_b, and so our solutions will be self-similar. This means any quantities with dimensions of length must scale linearly with r_b, for example the spherical radius, r, scales as $r = r_b\tilde{r}(\tilde{s})$ (where $\tilde{s}$ is the normalised arc length along the streamline). Similarly, since the problem we solve is a initial value problem, other quantities, including the density and velocity, are most sensibly expressed in terms of their values at the base i.e. $\rho = \rho_\mathrm{b}\tilde{\rho}(\tilde{s})$ and $u = u_\mathrm{b}\tilde{u}(\tilde{s})$ respectively.

Clarke & Alexander (2016) showed that for the *globally isothermal* case to display self-similarity, u_b must be the same for all streamlines. In this work we argue that more generally, when the sound speed (temperature) varies along the wind base, the *Mach number at the base* $\mathscr{M}_\mathrm{b} = u_\mathrm{b}/c_\mathrm{S,b}$ must be the same for all streamlines (see Section 2.3).

Geometry

To describe the wind geometry at the base, we first define the angle ϕ as the angle between a point on a streamline and the midplane

$$\tan(\phi) = \frac{z(\tilde{s}, r_b)}{R(\tilde{s}, r_b)} = \frac{\tilde{z}(\tilde{s})}{\tilde{R}(\tilde{s})}, \tag{2.1}$$

where R and z are the radial and vertical coordinates in cylindrical polar coordinates and $\tilde{R}$, $\tilde{z}$ are their equivalents normalised to r_b. ϕ_b is then the wind-base elevation. Since $\phi = \phi(\tilde{s})$, the solution at a given normalised arc length along the streamline could equally be thought of as the solution at given angle from the midplane.

Similarly, we define the angle θ (not to be confused with the colatitudinal angle of spherical coordinates, which here is equivalent to $\pi/2 - \phi$) as the angle between a streamline tangent and the midplane

$$\tan(\theta) = \frac{dz}{dR} = \frac{d\tilde{z}}{d\tilde{R}}, \tag{2.2}$$

and for ease further define the angle χ as

$$\chi = \theta - \phi, \tag{2.3}$$

such that $\chi_\mathrm{b} = \theta_\mathrm{b} - \phi_\mathrm{b}$ represents the angle with which the wind launches relative to its launch surface.

While Clarke & Alexander (2016) assumed $\phi_\mathrm{b} = 0^\circ$ and $\chi_\mathrm{b} = \theta_\mathrm{b} = 90^\circ$, simulations suggest that ϕ_b is larger for softer, lower luminosity spectra (Ercolano et al., 2021) and for discs around lower-mass stars (Picogna et al., 2021) and also depends on metallicity (Nakatani et al., 2018b) but typically lies in the range $20-50^\circ$. Although X-ray simulations tend to find $\chi_\mathrm{b} = 90^\circ$, Nakatani et al. (2018b) suggest this value could be as low as $\chi_\mathrm{b} = 30^\circ$. Therefore we explore a broad parameter space $0^\circ \leq \phi_\mathrm{b} \leq 72^\circ$ and $27^\circ \leq \chi_\mathrm{b} \leq 90^\circ$ to show how the launch Mach numbers $\mathscr{M}_\mathrm{b}$ depend on these parameters. For most of the chapter, I focus on a intermediate fiducial elevation $\phi_\mathrm{b} = 36^\circ$ - which is typical of photoevaporation models for solar-like stars (Wang & Goodman, 2017; Picogna et al., 2019) - and a launch angle $\chi_\mathrm{b} = 90^\circ$.

Imposed Profiles of Flow Variables

To obtain a self-similar solution, we require that the density at the wind base ρ_b is a power law (which has no characteristic scale) in base radius r_b:

$$\rho_\mathrm{b} = \rho_0 \left(\frac{r_\mathrm{b}}{r_0}\right)^{-b}. \tag{2.4}$$

where b is the power law index (for which Clarke & Alexander, 2016, consider values in the range $0.5-2$). We focus throughout much of this paper on $b = 1.5$ since this most closely resembles the density gradient at the base in Picogna et al. (2019) (though in the more recent simulations of Picogna et al., 2021, b is closer to 1), as well as the density profile for $r < r_G$ found by Hollenbach et al. (1994). This value also better reproduces the [Ne II] line luminosity Pascucci et al. (2011) measured for TW Hya (Ballabio et al., 2020). Since $\tilde{s}$ and ϕ are interchangeable, then at any fixed elevation ρ and u (or $\mathscr{M}$) should scale in the same way as at the base, e.g. $\rho \propto r^{-b}$.

We impose a fixed temperature at each location, i.e. use a locally isothermal equation of state $P = \frac{\mathscr{R}}{\mu}\rho T$ (this condition results from the balance of heating and cooling at each location, and *not* from the wind material being adiabatic with $\gamma \approx 1$, which would instead imply material kept the temperature at its base). For convenience, we express this temperature structure in terms of the isothermal sound speed; the sound-speed profile must also be scale free, meaning it can be written in a separable form in terms of r and ϕ, where the dependence on r is that of a power law:

$$c_\mathrm{S}^2(r,\phi) = c_\mathrm{S,b}^2(r_\mathrm{b})\tilde{c}_S^2(\tilde{r},\phi) = c_\mathrm{S,b}^2(r_\mathrm{b})\tilde{r}^{-\tau}\mathscr{C}(\phi). \tag{2.5}$$

where $c_\mathrm{S,b}^2(r_\mathrm{b}) \propto r_\mathrm{b}^{-\tau}$ and the angular dependence is normalised such that $\mathscr{C}(\phi_b) = 1$. τ is defined (analogously to b) as the power-law slope of the temperature profile. For *disc* temperatures, commonly used profiles have $\tau = 0.5$ (see Section 1.2.4). While the heating mechanisms are very different in the *wind*, the principles of geometric dilution (Owen et al., 2012) and disc flaring (Wang & Goodman, 2017) are still important and simulations suggest similarly modest radial temperature gradients (e.g. $0.28 < \tau < 0.4$ depending on the metallicity, Nakatani et al., 2018a). We thus investigate fiducial non-isothermal cases with $\tau = 0.25$ and $\tau = 0.5$.

We investigate two representative cases of these power law temperature profiles, where the temperature depends on either the spherical or cylindrical radius respectively as

$$c_{\rm S}^2 \propto r^{-\tau} \tag{2.6}$$

$$c_{\rm S}^2 \propto R^{-\tau} \propto \cos(\phi)^{-\tau} r^{-\tau}; \tag{2.7}$$

where $\mathscr{C}(\phi) = 1$ and $\mathscr{C}(\phi) = \cos(\phi)^{-\tau}/\cos(\phi_{\rm b})^{-\tau}$ respectively.

If the mass-loss rates $\dot{\Sigma}$ decline faster with radius than the disc surface density Σ, then the shortest depletion timescale is in the inner disc. In the scale-free models, $\dot{\Sigma} \propto \rho_{\rm b} c_{\rm S,b} \propto R^{-(b+\tau/2)}$ while gas surface densities are often assumed to be $\propto R^{-p}$; $p = 1 - 1.5$. Thus if photoevaporation indeed explains the inside-out clearing observed for protoplanetary discs, we expect that $b + \tau/2 \gtrsim 1$.

2.3 General Equations for Self-Similar Winds

We start from the momentum Equation 1.1 resolved parallel and perpendicular to the streamlines (see also Equation 1.16)

$$u\frac{\partial u}{\partial \tilde{s}} = -\frac{1}{\rho}\frac{\partial P}{\partial \tilde{s}} \tag{2.8}$$

$$\frac{u^2}{R_{\rm eff}} = \frac{1}{\rho}\hat{\mathbf{l}} \cdot \nabla P. \tag{2.9}$$

Our coordinates of the distance along the streamline $\tilde{s}$ and the base radius $r_{\rm b}$ are not orthogonal coordinates, therefore the perpendicular pressure gradient depends on them both and can be resolved in terms of changes between streamlines ($r_{\rm b}$) and along the streamlines ($\tilde{s}$)

$$\frac{1}{\rho}\hat{\mathbf{l}} \cdot \nabla P = \frac{1}{\rho}\frac{{\rm d}P}{{\rm d}l} = -\frac{1}{\rho}\left(\frac{1}{r_{\rm b}}\cot(\chi)\left(\frac{\partial P}{\partial \tilde{s}}\right)_{r_{\rm b}} + \frac{1}{\tilde{r}\sin(\chi)}\left(\frac{\partial P}{\partial r_{\rm b}}\right)_{\tilde{s}}\right), \tag{2.10}$$

where dl is an infinitesimal step in the perpendicular direction $\hat{\mathbf{l}}$.

The first term in Equation 2.10 (due to variation between points on a given streamline), is evaluated by eliminating $\left(\frac{\partial P}{\partial \tilde{s}}\right)_{r_{\mathrm{b}}}$ using Equation 2.8. The second term in Equation 2.10 (due to variation between streamlines) is evaluated by expanding the pressure as $\frac{\mathrm{d}P}{\rho} = c_{\mathrm{S}}^2 \mathrm{d}\ln(\rho) + \mathrm{d}c_{\mathrm{S}}^2$:

$$-\frac{1}{\rho}\frac{1}{\tilde{r}\sin(\chi)}\left(\frac{\partial P}{\partial r_{\mathrm{b}}}\right)_{\tilde{s}} = \frac{b+\tau}{r\sin(\chi)}c_{\mathrm{S}}^2. \tag{2.11}$$

Thus combining equations 2.9, 2.10, 2.11 and 2.8 and writing $r = r_{\mathrm{b}}\tilde{r}$, $R_{\mathrm{eff}} = r_{\mathrm{b}}\tilde{R}_{\mathrm{eff}}$, $u = \mathscr{M}_{\mathrm{b}} c_{\mathrm{S,b}} \tilde{u}$ and $c_{\mathrm{S}} = c_{\mathrm{S,b}}\tilde{c}_{\mathrm{S}}$ we get an equation relating the streamline curvature and the velocity gradients:

$$\frac{\mathscr{M}_{\mathrm{b}}^2 \tilde{u}^2}{\tilde{R}_{\mathrm{eff}}} = \frac{b+\tau}{\tilde{r}\sin(\chi)}\tilde{c}_S^2 - \mathscr{M}_{\mathrm{b}}^2 \tilde{u}\frac{\mathrm{d}\tilde{u}}{\mathrm{d}\tilde{z}}\cot(\chi)\sin(\theta), \tag{2.12}$$

The first term on the right-hand side is scale free and doesn't vary between streamlines. For this to be true of the other two terms we therefore see that $\mathscr{M}_{\mathrm{b}}$ is independent of streamline i.e. the wind launches with the same Mach number everywhere (this statement holds regardless of whether the wind is isothermal; the velocity however is only constant for isothermal winds).

To progress further, we relate the radius of curvature to the streamline morphology:

$$\frac{1}{\tilde{R}_{\mathrm{eff}}} = \frac{\tilde{R}''}{(1+\tilde{R}'^2)^{0.5}}, \tag{2.13}$$

where primes denote differentiation with respect to $\tilde{z}$. By Equation 2.2, $\tilde{R}' = \cot\theta$, while the second derivative may be related to the normalised area of a streamline bundle through differentiation of

$$\tilde{A} = \tilde{r}^2 \frac{\sin(\chi)\cos(\phi)}{\sin(\chi_{\mathrm{b}})\cos(\phi_{\mathrm{b}})}, \tag{2.14}$$

yielding

$$\tilde{R}'' = \frac{(1+\tilde{R}'^2)(\tilde{R}-\tilde{z}\tilde{R}')\tilde{R}'}{\tilde{R}(\tilde{z}+\tilde{R}\tilde{R}')} - \frac{(1+\tilde{R}'^2)^{3/2}}{\tilde{R}(\tilde{z}+\tilde{R}\tilde{R}')}\tilde{A}'\cos(\phi_{\mathrm{b}})\sin(\chi_{\mathrm{b}}). \tag{2.15}$$

Finally $\tilde{A}'$ is given by a normalised version of the nozzle Equation 1.15 (with $g_{\mathrm{eff}} = 0$) where we differentiate $\tilde{c}_S^2(\tilde{r},\phi) = \tilde{r}^{-\tau}\mathscr{C}(\phi)$ as:

$$\frac{\mathrm{d}\tilde{c}_S^2}{\mathrm{d}\ln(\tilde{r})} = \tilde{c}_S^2\left(-\tau + \frac{\partial\ln(\mathscr{C})}{\partial\phi}\tan(\chi)\right). \tag{2.16}$$

Combining everything we obtain an equation in $\tilde{u}$, $\tilde{R}$, $\tilde{z}$ and their $\tilde{z}$ derivatives:

$$\frac{\mathrm{d}\tilde{u}}{\mathrm{d}\tilde{z}} = \frac{g_1 + g_2}{f_1 + f_2} \tag{2.17}$$

$$f_1 = -\mathscr{M}_b^2 \tilde{u} \left(\mathscr{M}_\mathrm{b}^2 \frac{\tilde{u}^2}{\tilde{c}_S^2} - 1 \right) \frac{(\tilde{R} - \tilde{z}\tilde{R}')}{(1+\tilde{R}'^2)^{1/2}(\tilde{R}\tilde{R}' + \tilde{z})}$$

$$f_2 = \mathscr{M}_b^2 \tilde{u} \frac{\tilde{R}\tilde{R}' + \tilde{z}}{(1+\tilde{R}'^2)^{1/2}(\tilde{R} - \tilde{z}\tilde{R}')}$$

$$g_1 = (b+\tau) \frac{(1+\tilde{R}'^2)^{1/2}}{(\tilde{R} - \tilde{z}\tilde{R}')} \tilde{c}_S^2$$

$$g_2 = -\mathscr{M}_b^2 \tilde{u}^2 \frac{(\tilde{R} - \tilde{z}\tilde{R}')}{(1+\tilde{R}'^2)^{1/2}} \left(\frac{\tilde{R}'}{\tilde{R}(\tilde{R}\tilde{R}' + \tilde{z})} + \frac{1}{(\tilde{R}^2 + \tilde{z}^2)} \left(\tau - \frac{\partial \ln(\mathscr{C})}{\partial \phi} \frac{(\tilde{R} - \tilde{z}\tilde{R}')}{(\tilde{R}\tilde{R}' + \tilde{z})} \right) \right).$$

We will refer to f_2 and g_1 as pressure-related terms and f_1 and g_2 as curvature-related terms since they arise from the right- and left-hand sides of Equation 2.12 respectively. Compared to Clarke & Alexander (2016), f_2 is unchanged as it represents the change in pressure due to the Bernoulli effect, which is unaffected by geometry or temperature gradients. g_1 represents the radial pressure gradient and hence is affected by the additional radial temperature gradient τ and scales with the sound speed normalised to the base $\tilde{c}_S^2$. f_1 takes on a very different form - this is because we calculated $\tilde{A}'$ in a different way to Clarke & Alexander (2016). Finally g_2 picks up additional terms due to the variation of temperature with both radius and latitude. Note that this set of equations is independent of the geometric terms.

2.4 Numerical Solution of Scale-Free Problem

Clarke & Alexander (2016) calculated the maximum launch Mach numbers $\mathscr{M}_{\mathrm{b,max}}$ by numerically solving their equivalent to equations 2.17 using an Euler method, iterating to find solutions which avoided $f = f_1 + f_2 \to 0$. We apply the same method to investigate our generalised cases. At each point $\tilde{z}$ along the streamline, we track $\tilde{u}$, $\tilde{R}$ and $\tilde{R}'$. The velocity gradients are calculated using Equation 2.17. Then we can find the gradient of the area of a streamline bundle using Equation 1.15 and hence $\tilde{R}''$ from Equation 2.15. Finally, $\tilde{u}$, $\tilde{R}$ and $\tilde{R}'$ can be advanced to locate the next point on the streamline and its velocity:

$$\tilde{u}_{i+1} = \tilde{u}_i + \tilde{u}_i' \Delta\tilde{z} \tag{2.18}$$

$$\tilde{R}_{i+1} = \tilde{R}_i + \tilde{R}_i' \Delta\tilde{z} + \frac{1}{2}\tilde{R}_i''(\Delta\tilde{z})^2 \tag{2.19}$$

$$\tilde{R}_{i+1}' = \tilde{R}_i' + \tilde{R}_i'' \Delta\tilde{z} \tag{2.20}$$

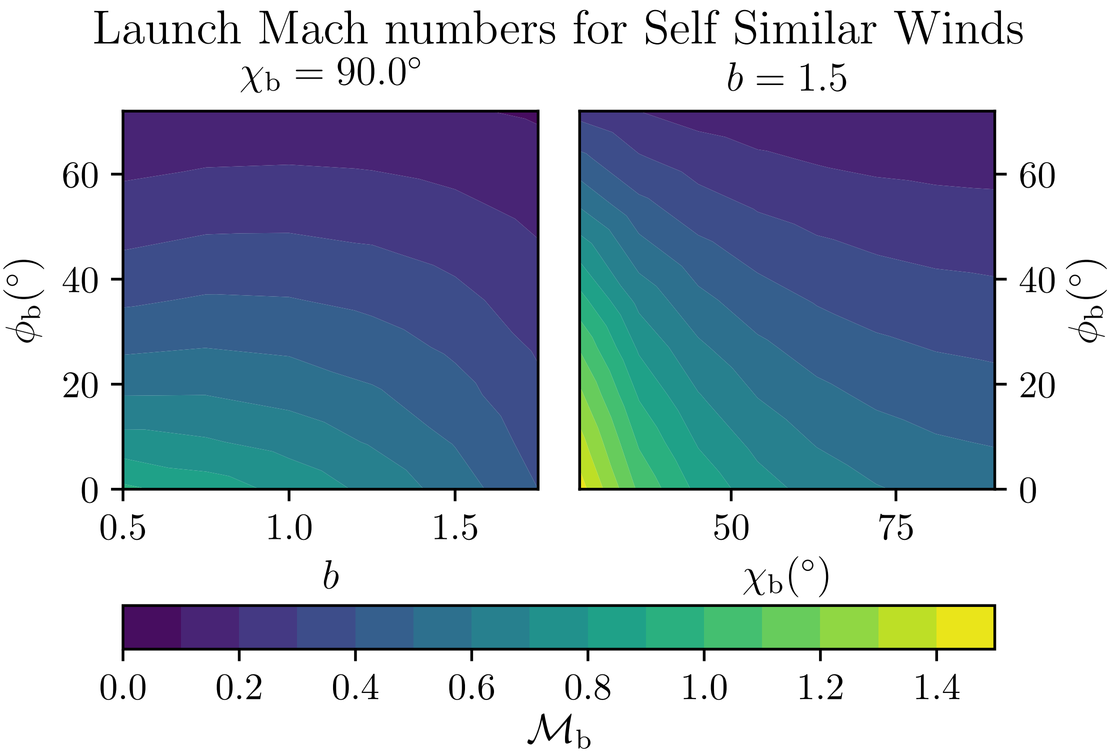

Fig. 2.1 The maximum allowed Mach number at the base $\mathscr{M}_{\mathrm{b,max}}$ as a function of the density power-law slope b, the wind-base elevation ϕ_{b} and the angle with which the wind is launched relative to this plane χ_{b}. The left-hand panel shows the dependence on b and ϕ_{b} for perpendicularly-launched winds, while the right-hand panel shows the dependence on the two angles for a fixed density profile with $b = 1.5$. The lighter, yellow colours at low b, low ϕ_{b} and low χ_{b} represent faster winds, while the darker blue colours represent slower velocities.

2.4.1 Launch Velocity in More General Geometries

We first consider isothermal winds, for which the maximum launch Mach numbers can now be a function of the angles ϕ_{b} and χ_{b} as well as the density gradient b. Hence we proceed to solve our revised differential equation to find $\mathscr{M}_{\mathrm{b,max}}(b, \phi_{\mathrm{b}}, \chi_{\mathrm{b}})$ on a regular grid covering density power-law slopes $0.5 \leq b \leq 1.75$, elevation angles $0° \leq \phi_{\mathrm{b}} \leq 72°$ and launch angles $27° \leq \chi_{\mathrm{b}} \leq 90°$.

For each model we integrate out to $\tilde{z} = 1000$; so long as we do not encounter $f \to 0$, we then increase the Mach number by 0.1 until such a singularity is encountered. Once this scenario arises, we then return to highest safe value and repeat, first increasing $\mathscr{M}_{\mathrm{b}}$ by 0.01 and then repeating a third time increasing by 0.001 such that $\mathscr{M}_{\mathrm{b}}$ is found to 3 decimal places. The results are presented as the contour plots in Figure 2.1.

The trends in Figure 2.1 can largely be understood by considering the relationship between $\mathscr{M}_{\rm b}$ and the (radius of) curvature at the base. Firstly, as found by Clarke & Alexander (2016), the Mach number at the base is generally a decreasing function of the density power-law slope b. A stronger pressure gradient provides a stronger force to push the streamlines over, meaning that they curve with a smaller radius of curvature; more strongly curved winds are associated with a slower velocity. Moreover, as we increase $\phi_{\rm b}$, there is a strong decrease in $\mathscr{M}_{\rm b,max}$. This is because the winds have to turn to become outward-flowing in a tighter space, meaning they must curve more strongly and consequently launch more slowly. Finally, as we decrease $\chi_{\rm b}$, such that the streamlines are flatter to the base, the flow is already more radial and does not have to turn so quickly, hence can launch faster. Since the streamlines are more closely aligned to the pressure gradients, the component of the pressure gradient acting to curve the streamline is less while the accelerating component is greater.

For most regions of $\phi_{\rm b} - b$ and $\phi_{\rm b} - \chi_{\rm b}$ parameter space in Figure 2.1, it is apparent that the launch Mach number depends most strongly on the wind-base elevation. For the range of $\phi_{\rm b}$ seen in simulations we expect typical Mach numbers of $\mathscr{M}_{\rm b} = 0.2 - 0.6$.

Figure 2.1 does not provide Mach numbers for $b \geq 2$ as we do not find a self-similar solution that avoids a singularity for these values. Clarke & Alexander (2016) found a value since when integrating a solution out to a finite distance, there is always some velocity for which the singularity lies beyond that point. However, for $b \geq 2$, the maximum velocity doesn't converge as one extends the domain of integration. Physically this occurs since if the density drops off as fast or faster than r^{-2}, then the wind must be diverging faster than spherical to ensure mass conservation, and thus would have to flow *into* the launch plane. I provide a more mathematical discussion in Section 2.6.

2.4.2 Launch Velocity for Radial Temperature Profiles

To explore winds with radial temperature profiles, we fix $b = 1.5$ and test for both midplane ($\phi_{\rm b} = 0^\circ$) and elevated launches ($\phi_{\rm b} = 36^\circ$). The resulting maximum Mach numbers are listed as the "predicted" values in Table 2.1. For comparison, we include the value for the isothermal case with the same b and $\phi_{\rm b}$. In each case the temperature gradient's effect is to lower the Mach numbers by no more than 10% when $\tau = 0.25$, and up to $10 - 20\%$ for $\tau = 0.5$. A decrease is to be expected - the temperature gradient at the wind base increases the outward pressure force, which makes the radius of curvature smaller and the velocities lower. Correspondingly, this effect is stronger for greater values of τ; additionally, we see stronger decreases when temperature scales with cylindrical radius than with spherical radius.

Table 2.1 The mass weighted average launch Mach numbers measured for a range of non-isothermal models.

		$\mathscr{M}_\mathrm{b}$			
ϕ_b ($^\circ$)	Temperature	Predicted	Isothermal	u constant	$\mathscr{M}$ constant
0	$r^{-0.25}$	0.522	0.555	0.528	0.522
0	$R^{-0.25}$	0.506	0.555	0.512	0.507
36	$r^{-0.25}$	0.322	0.327	0.330	0.329
36	$R^{-0.25}$	0.300	0.327	0.309	0.308
0	$r^{-0.5}$	0.472	0.555	0.495	-
0	$R^{-0.5}$	0.449	0.555	0.467	-
36	$r^{-0.5}$	0.305	0.327	0.318	-
36	$R^{-0.5}$	0.270	0.327	0.282	-

2.4.3 Streamline Morphology

The Mach numbers were interpreted above in terms of the curvature at the streamline base and the corresponding trends are indeed seen in the morphologies. At a given ϕ_b, shallower density/pressure gradients produce less curvature and hence have streamlines that are closer to vertical (Clarke & Alexander, 2016). While the effect of the elevated wind base is to decrease the launch velocities and hence increase curvature, since streamlines start off inwardly pointing they appear overall more vertical (Figure 2.2). Such considerations are critical for the determination of projected velocities, which can have a stark impact on the spectroastrometric signal (Barrier et al., in prep.).

The right-hand panel of Figure 2.2 shows the additional outward pressure gradient in the non-isothermal case results in more curved, less vertical streamlines (illustrated for the case of $\phi_\mathrm{b} = 36^\circ$, $T \propto R^{-0.25}$, for which $\mathscr{M}_\mathrm{b} = 0.300$). Nevertheless the effect is fairly minimal compared to that which results from variation with b.

By overplotting an isothermal streamline with the same $\mathscr{M}_\mathrm{b}$, we see that the effect of non-isothermality is almost completely explained by the (small) reduction in Mach number: the isothermal case does not seriously over-estimate the radius of curvature at the base, with deviations only setting in at quite large radii when the non-isothermal solution curls upwards relative to the isothermal streamline (in order to fill the spatial domain, c.f. Section 2.6).

Overall, we conclude that for realistic temperature variations, the impact on the launch Mach numbers and morphologies of the flow is rather small, and hence the validity of our results should be relatively insensitive to the heating and cooling uncertainties and thus the

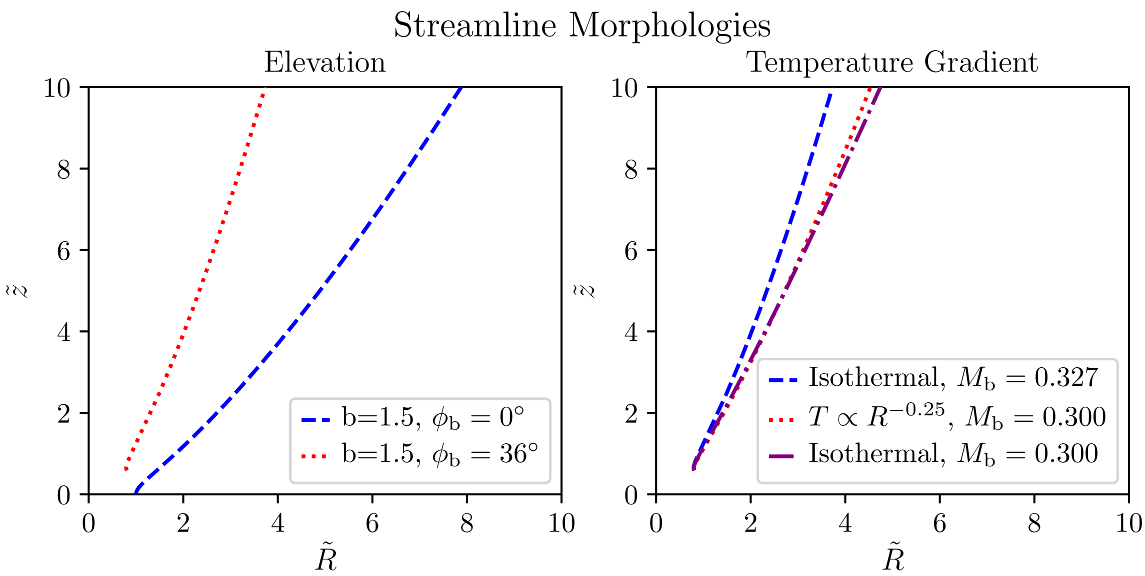

Fig. 2.2 Comparison of streamline morphologies. The left-hand panel shows the significant effect of the elevated base while the right-hand panel shows that the effect of a temperature gradient is weak. The right-hand panel additionally shows, as the purple dot-dashed line, the isothermal streamline for $\mathscr{M}_b = 0.300$.

finer picture of the wind's thermal structure (save for any role these processes play in setting the wind-base elevation).

2.5 Scale-Free Hydrodynamic Simulations

Having established predictions for the launch velocities of self-similar winds for more general base geometries and non-isothermal temperature profiles, we now benchmark these against hydrodynamic simulations using FARGO3D (Benítez-Llambay & Masset, 2016) .

2.5.1 Description of FARGO3D Setup

Since for a direct comparison we desire a scale-free scenario, our initial setup uses no gravitational forces, with the azimuthal velocity $v_\phi = 0$ to eliminate centrifugal forces.

We used a 2D spherical grid with 220 cells logarithmically spaced in r between $r = 0.01$ and $r = 10$ (since these simulations are scale free then these values have no particular meaning but are simply relative) and $50\,(1 - \phi_b/90°)$ cells spaced linearly between $\theta = 0°$ and $\theta = 90° - \phi_b$ (where θ is now the usual colatitudinal angle), such that the grid cells are approximately square with uniform angular resolution. While this is lower than the resolution of Clarke & Alexander (2016), we tested that this did not affect our results.

The launch plane at $\theta = 90^\circ - \phi_{\rm b}$ was treated by having constant perpendicular velocity across the boundary, with the parallel component set to 0 and the density set to $\rho = r^{-b}$. When $\chi_{\rm b} \neq 90^\circ$, the perpendicular velocity u_θ at the launch plane is still imposed to be constant across the boundary. We then use its value to set the parallel component $u_r = -u_\theta \cot(\chi_{\rm b})$ (the sign accounts for the positive θ direction being directed into the plane; we are interested in winds where $u_\theta < 0$, $u_r > 0$). At the polar axis, we used a reflecting boundary.

For both radial boundaries, we required that the components of Mach number should be constant across the boundary[1] and that the density follow the same imposed power-law slope as at the base. We argue that these are the correct boundary condition to use if we wish to seek perfect agreement with the self-similar solution since, as mentioned in Section 2.2, at a fixed angle we probe equivalent points on adjacent streamlines and so the density and velocity/Mach number should simply scale with the density and velocity/Mach number at their bases. We checked that our setup recovered the perpendicular, $\phi_{\rm b} = 0^\circ$, cases, and found that these boundary conditions have the effect of reducing the deviations from self-similarity near the boundaries (c.f. Clarke & Alexander, 2016, Figure 4). This is also apparent in Figure 2.3, where the Mach numbers remain exactly flat for all r.

As we use a fixed temperature profile, we used FARGO3D's locally isothermal equation of state. Here FARGO3D stores the sound speed, which it does not evolve in time, and calculates the pressure as $P = c_{\rm S}^2 \rho$. Its value is fixed via the initial conditions: for our globally isothermal cases (i.e. $\tau = 0$), we set $c_{\rm S} = 1$ everywhere, while for our power law temperature profiles, we follow Equation 2.5.

2.5.2 Generalised Geometry

In Figures 2.3 and 2.4, we examine the launch Mach number $\mathscr{M}_{\rm b}$ and streamlines respectively of winds launched from a base elevated by $\phi_{\rm b} = 36^\circ$ to the midplane. We focus on the three cases of b examined in Clarke & Alexander (2016): $0.75, 1.00, 1.50$. For $b = 1.5$ we also show in the right-most panel a model that is not launched perpendicularly; we choose an illustrative value of $\chi_{\rm b} = 45^\circ$, motivated by the approximate extreme value shown by the innermost streamlines in simulations (Wang & Goodman, 2017; Picogna et al., 2019).

It is apparent from Figure 2.3 that for all our elevated cases, the winds converge to the constant $\mathscr{M}_{\rm b}$ value corresponding to the $\mathscr{M}_{\rm b,max}$ from the self-similar models above (represented by the dark grey band) from the inside out on a timescale approximately proportional to r. Any small differences result from the simulation outputs plotted being derived at the centre of the grid cell closest to the base, when the base itself is at the imposed

[1] In the case of $\tau = 0.5$, a constant Mach number failed to reach a steady solution and so we had to use the less-accurate constant-velocity boundary condition.

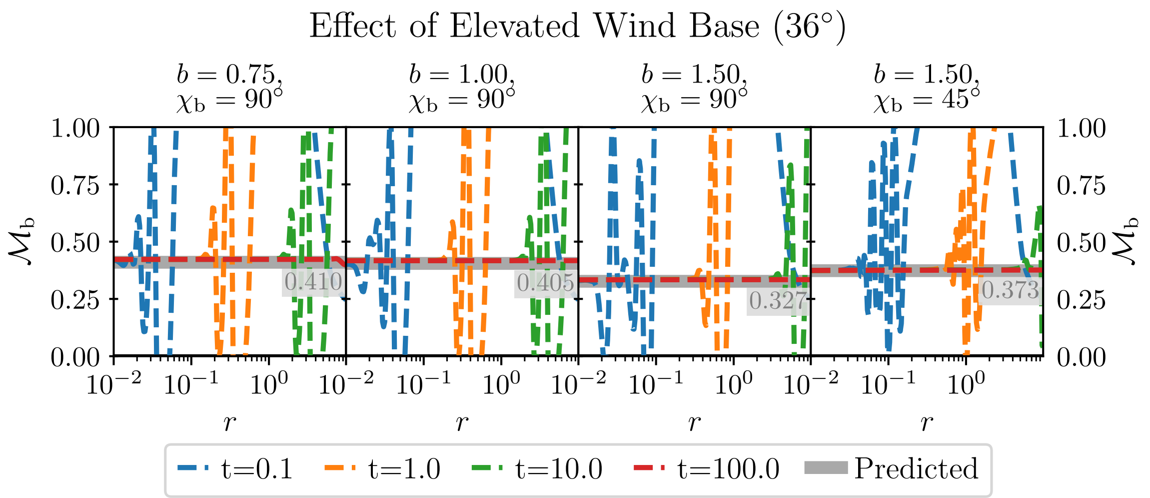

Fig. 2.3 Comparison of the launch Mach numbers $\mathscr{M}_b$ for scale-free wind models in our generalised geometry. From left to right: winds launched perpendicularly from elevated bases ($\phi_b = 36°$) with density power-law slopes $b = 0.75, 1.00, 1.50$, and a wind with $b = 1.5$ launched at $\chi_b = 0.25\pi$ from a base elevated by $\phi_b = 36°$. The coloured dashed lines indicate output hydrodynamic simulations at various times. The darker grey band represents the predicted $\mathscr{M}_{b,max}$ from the self-similar models and the grey label shows its value.

angle, which we confirmed by increasing the resolution and seeing that the $\mathscr{M}_b$ indeed converges more closely towards the predicted value. Moreover this agreement holds for the non-perpendicularly launched wind. For a direct comparison (and as would be relevant to interpreting mass-loss rates), we plot only the component of velocity perpendicular to the plane. Therefore though the Mach number is increased mildly above the $\mathscr{M}_{b,max}$ for the perpendicular case, the enhancement is smaller than would be immediately inferred from Figure 2.1, which shows the total velocity.

Moreover, in Figure 2.4 we show a comparison of the streamlines integrated from the same hydrodynamic simulations to those obtained in Section 2.4 (scaled by the base radius), for the appropriate $M_{b,max}$. The agreement is again excellent for all streamlines showing that the self-similarity is adopted throughout the domain. Moreover, the sonic surface is a surface of constant ϕ.

These results hold for the full range of ϕ_b and χ_b considered. Thus, the conclusions of Clarke & Alexander (2016) regarding the agreement between the predicted $\mathscr{M}_{b,max}$ and the $\mathscr{M}_b$ found in the hydrodynamic simulations for scale-free winds thus also apply to elevated bases and non-perpendicular launches: self-similar solutions with $\mathscr{M}_{b,max}$ are generally applicable for *any* scale-free isothermal wind, regardless of base geometry.

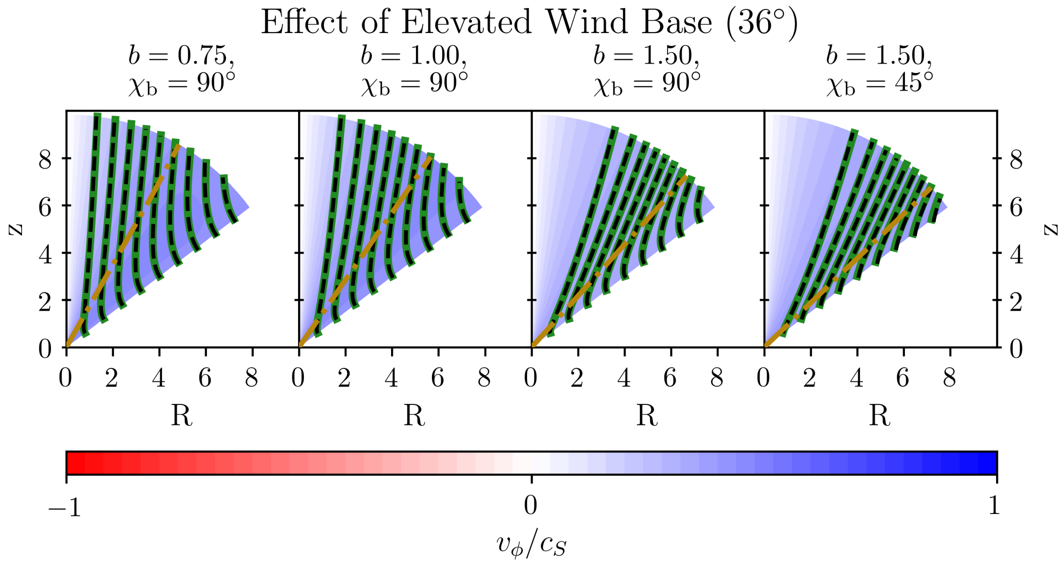

Fig. 2.4 Comparison of the streamline morphology for wind models in our generalised geometry demonstrating complete agreement of scale-free hydrodynamic simulations with self-similar solutions. From left to right: winds launched perpendicularly from elevated bases ($\phi_{\rm b} = 36°$) with density power-law slopes $b = 0.75, 1.00, 1.50$, and a wind with $b = 1.5$ launched at $\chi_{\rm b} = 45°$ from a base elevated by $\phi_{\rm b} = 36°$. The solid green lines are the streamlines retrieved from the final outputs of the hydrodynamic models, whereas the black dashed lines are those found by numerical integration of Equation 2.17 for $\tau = 0$, $\mathscr{C} = 1$. The gold dashed-dotted line shows the sonic surface. The background is coloured according to the velocity in the ϕ (latitudinal) direction.

2.5.3 Radial Temperature Profiles

We now turn our attention to the behaviour of temperature profiles that are power laws in either spherical radius (Equation 2.6) or cylindrical radius (Equation 2.7).

In Figure 2.5, we observe that when appropriate boundary conditions are used, the Mach number achieved in the simulations (measured with respect to the local sound speed) is indeed constant in radius - for both the spherical and cylindrical power laws - as we have argued is appropriate in the self-similar case. In the $\tau = 0.5$ case, since the constant-Mach-number boundaries did not achieve a steady solution, we resorted to constant-velocity boundary conditions. This causes a small increase of $\mathscr{M}_{\rm b}$ in the inner regions of the $\tau = 0.5$ simulations.

Moreover, the hydrodynamic simulations produce Mach numbers that are very close to the predictions of the corresponding non-isothermal analytic solutions (dark grey lines). To quantify the agreement further, we measure the mass-weighted average $\mathscr{M}_{\rm b}$ from each simulation and report the values for both sets of boundary conditions in Table 2.1; we also include values for winds with $\phi_{\rm b} = 0°$. The Mach numbers are generally within $0.01 - 0.02$

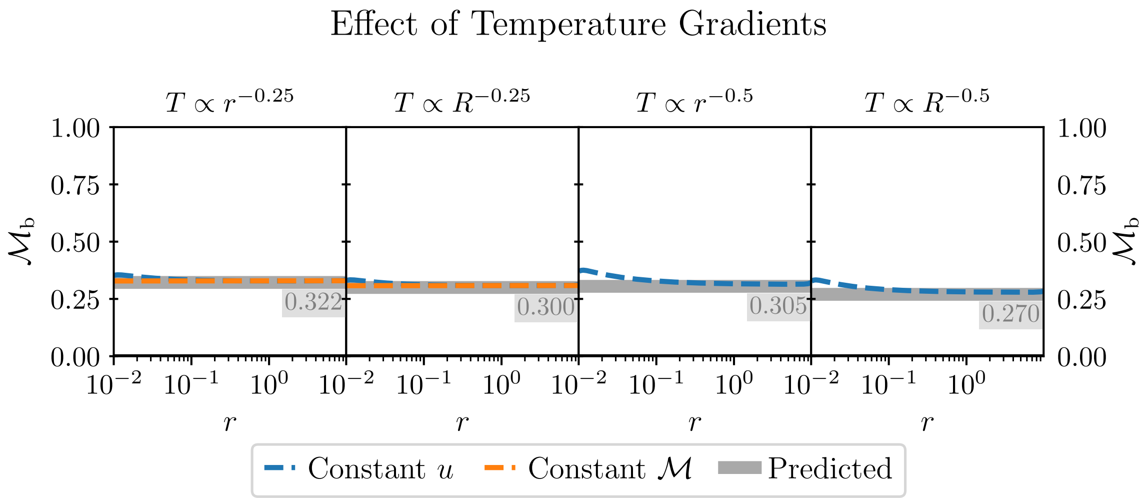

Fig. 2.5 Comparison of the launch Mach numbers $\mathscr{M}_{\rm b}$ (measured with respect to the local sound speed) for non-isothermal winds with density power law index $b = 1.5$ and temperature power law index $\tau = 0.25$ (first and second panels, spherical and cylindrical respectively) and $\tau = 0.5$ (third and fourth panels, spherical and cylindrical respectively) for discs with wind bases elevated by $\phi_{\rm b} = 36°$. The blue lines show simulations with constant velocity imposed at the radial boundaries; the orange lines use a constant Mach number. The darker grey band represents the predicted $\mathscr{M}_{\rm b,max}$ from the self-similar models.

of the predicted values. In Figure 2.6, we also confirm that in each case, the streamline morphology for our non-isothermal simulations is in excellent agreement with the model predictions.

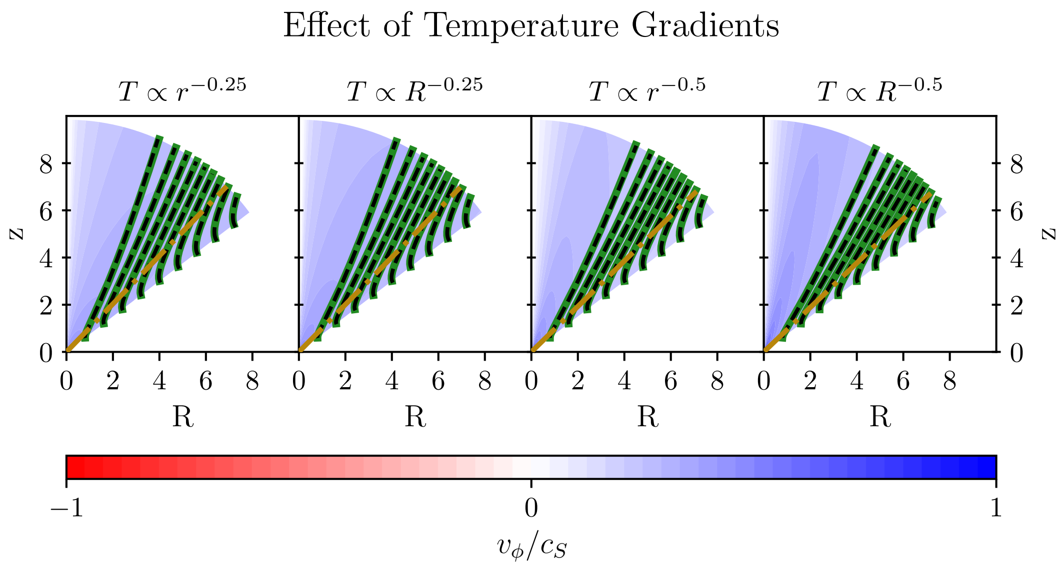

Fig. 2.6 As with the $b = 1.5$ case in Figure 2.4 but for the models in Figure 2.5 which include additional temperature gradients. The black dashed lines are the analytical streamlines for the corresponding Mach numbers reported in Table 2.1.

2.6 Domain Filling

In Section 2.5, we have seen that for self-similar winds, where the force balance involves pressure and curvature, that at a given pressure gradient, the curvature and launch Mach number are closely related. For example, the additional curvature at launch of the non-isothermal case could be captured well by simply a lower Mach number, and the elevated base led to lower Mach numbers because of the tighter curvature required. In this section, I explore how considering requirements on the curvature throughout the domain helps explain the behaviour of these winds.

In particular, we note that as $\tilde{r} \to \infty$, the angle with the midplane, ϕ, which is bound to lie between 0° and 90°, cannot change indefinitely. Hence, at large radii, we expect the streamlines to become asymptotically straight lines of constant $\phi = \phi_\infty$. The angle χ measures the angle between the streamline tangent and the radial direction, and is thus related to the change in ϕ by

$$\mathrm{d}\tilde{r}\tan(\chi) = \tilde{r}\mathrm{d}\phi. \tag{2.21}$$

Thus, we are interested in solutions that tend to $\chi \to 0$. Moreover, in the limit of straight streamlines, the radius of curvature $|\tilde{R}_{\mathrm{eff}}| \to \infty$.

Secondly, we argue that in both our simulations and those of Clarke & Alexander (2016), the correct limiting angle should be $\phi_\infty = 90^\circ$ as this is the computational domain's upper extent. Were all the streamlines to asymptote to $\phi_\infty < 90^\circ$, the wind could not fill the domain. The regions at $\phi > \phi_\infty$ would thus end up empty and provide no resistance to being filled by the wind: the resulting discontinuity in the density would create strong perpendicular pressure gradients at ϕ_∞ that would curve the streamlines upwards into the empty region. This runs contradictory to the fact that in the self-similar model in the limit that $|\tilde{R}_{\rm eff}| \to \infty$, the pressure gradient perpendicular to the streamlines (right-hand side of Equation 2.12) should be 0. Conversely, if the wind extends up to $\phi = 90^\circ$, there will by default be no perpendicular pressure gradient due to the symmetry about the z-axis.

Therefore, we seek to establish a connection between the Mach number of launch and the asymptotic angle ϕ_∞ of the streamlines with the base. By reversing our argument as for why in the more restricted domain for $\phi_{\rm b} > 0^\circ$ winds launch more slowly, we might expect that winds with a lower $\mathscr{M}_{\rm b}$ will not curve upwards so strongly and hence also inhabit a more restricted domain. As an illustrative example, in Figure 2.7 I show a model of a $\phi_{\rm b} = 0^\circ$ self-similar wind with $\mathscr{M}_{\rm b} = 0.4 < \mathscr{M}_{\rm b,max}$ for which the wind appears to only fill $\phi \lesssim 36^\circ$. It seems therefore that winds with $\mathscr{M}_{\rm b} < \mathscr{M}_{\rm b,max}$ do not fill the computational domain.

To progress further, we seek to mathematically describe the streamlines' approach to ϕ_∞. This will also allow us to extrapolate to a value of ϕ_∞ from our integrations which only cover a finite range (up to $\tilde{z} = 1000$).

We can work from Equation 2.12, and neglecting the curvature term require that

$$\frac{b+\tau}{\tilde{r}\sin(\chi)}\tilde{c}_S^2 = \mathscr{M}_{\rm b}^2 \tilde{u}\frac{{\rm d}\tilde{u}}{{\rm d}\tilde{z}}\cot(\chi)\sin(\theta). \tag{2.22}$$

By identifying $\cos(\chi) \approx 1$ and ${\rm d}\tilde{z} = {\rm d}\tilde{s}\sin(\theta) \approx {\rm d}\tilde{r}\sin(\theta)$, we can write this as

$$\frac{b+\tau}{\tilde{r}^{1+\tau}}\frac{\mathscr{C}(\phi_\infty)}{\mathscr{M}_{\rm b}^2} = \tilde{u}\frac{{\rm d}\tilde{u}}{{\rm d}\tilde{r}}, \tag{2.23}$$

which represents simply the radial acceleration due to the radial pressure gradient. In the case that $\tau \neq 0$, this integrates to show that the velocity tends towards a constant, while in the isothermal case its asymptotic form is

$$\tilde{u}^2 \sim \frac{2b}{\mathscr{M}_{\rm b}^2}\ln(\tilde{r}). \tag{2.24}$$

We proceed with the isothermal case here for simplicity, but this does not affect the validity of our argument.

Moreover, we know that along the radial direction, $\rho \propto r^{-b}$; in the isothermal case, we can use the Bernoulli function (Clarke & Alexander, 2016) to express the density in terms of

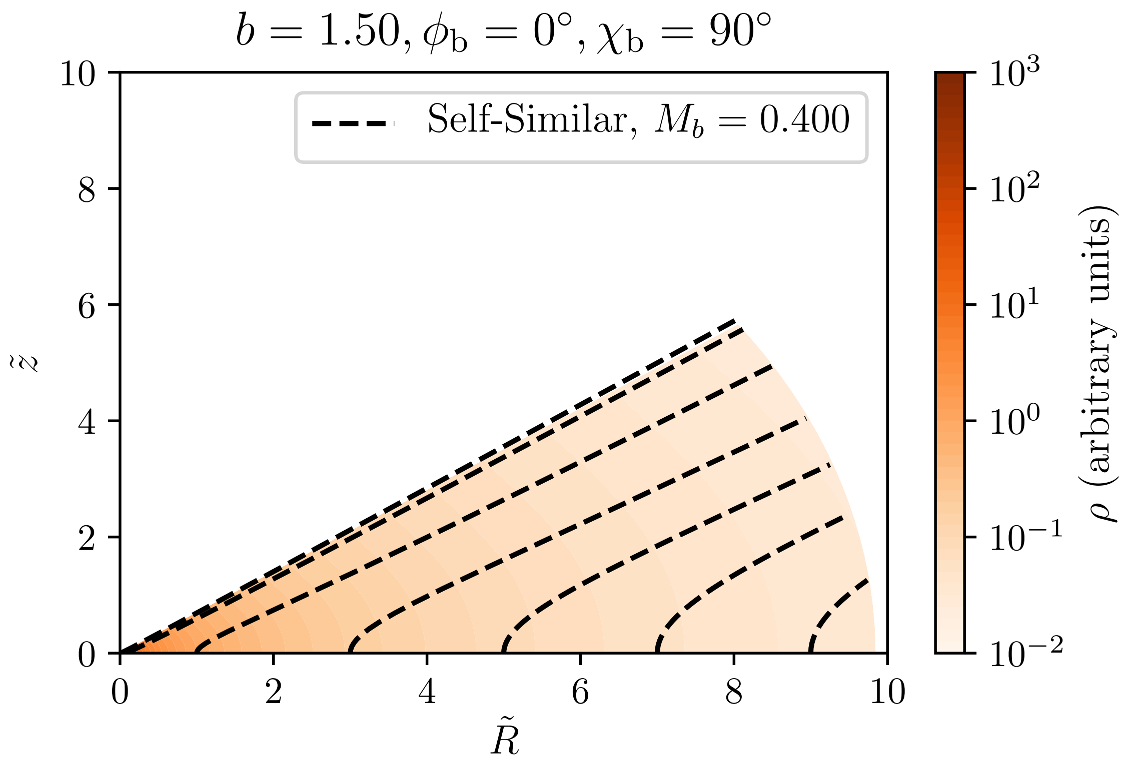

Fig. 2.7 The density contours inferred from a self-similar wind model which launches more slowly than the maximum Mach number, with various streamlines overplotted as the black dashed lines. The streamlines asymptote to an angle $\approx 36°$ with the midplane, leading to a sharp discontinuity in the density at this angle.

the velocity

$$\tilde{\rho} = \exp\left(-\frac{\mathscr{M}_\mathrm{b}^2}{2}(\tilde{u}^2 - 1)\right), \tag{2.25}$$

and hence deduce the scaling of

$$\tilde{\rho} \sim \exp\left(\frac{\mathscr{M}_\mathrm{b}^2}{2}\right)\tilde{r}^{-b}. \tag{2.26}$$

Finally, we can use Equation 2.14 to conclude that

$$\sin(\chi)\cos(\phi) \sim \sin(\chi_\mathrm{b})\cos(\phi_\mathrm{b})\frac{1}{\sqrt{2b}}\mathscr{M}_\mathrm{b}\exp\left(-\frac{\mathscr{M}_\mathrm{b}^2}{2}\right)\frac{\tilde{r}^{b-2}}{\sqrt{\ln(\tilde{r})}}. \tag{2.27}$$

Since $\cos(\phi)$ is bounded, to achieve $\sin(\chi) \to 0$, it is necessary to have $b < 2$ such that the right-hand side is a decreasing function of $\tilde{r}$ at large radii. This demonstrates why we cannot have self-similar solutions for $b \geq 2$: for such values, the streamlines cannot tend to be straight but must increase in curvature, which reinforces the physical argument made in Section 2.4 that they have to diverge to conserve mass when the density is dropping rapidly.

Moreover when this equation applies in the subsonic regime, $\sin(\chi) \propto \mathscr{M}_\mathrm{b} \exp\left(-\frac{\mathscr{M}_\mathrm{b}^2}{2}\right)$ is an increasing function of $\mathscr{M}_\mathrm{b}$. We therefore expect that ϕ changes more rapidly with increasing Mach number. Thus for lower $\mathscr{M}_\mathrm{b}$ than the maximum allowed, the rate of change of ϕ may become too small to reach $\phi = 90°$.

Approximating $\sin(\chi) \approx \tan(\chi) = \frac{\mathrm{d}\phi}{\mathrm{d}\ln\tilde{r}}$, we integrate Equation 2.27 (by substitution $t = \sqrt{(2-b)\ln(\tilde{r})}$) using the boundary condition $\phi \to \phi_\infty$ as $\tilde{r} \to \infty$ to find the polar equation of our streamlines at large radius in terms of the complementary error function erfc:

$$\sin(\phi) \sim \sin(\phi_\infty) - A\sin(\chi_\mathrm{b})\cos(\phi_\mathrm{b})\,\mathrm{erfc}\left(\sqrt{(2-b)\ln(\tilde{r})}\right), \tag{2.28}$$
$$A(b, \mathscr{M}_\mathrm{b}) = \sqrt{\frac{\pi}{2b(2-b)}}\mathscr{M}_\mathrm{b} \exp\left(-\frac{\mathscr{M}_\mathrm{b}^2}{2}\right).$$

Now, as desired, for any streamline calculated for a given value of $\mathscr{M}_\mathrm{b} \leq \mathscr{M}_{\mathrm{b,max}}$, we use Equation 2.28 to estimate $\sin(\phi_\infty)$ from the maximum $\tilde{r}$ and ϕ reached in our integration. The results for $\sin(\phi_\infty)$ are presented using triangle markers and solid lines in Figure 2.8 for isothermal cases with $b = 1.5$, $\chi_\mathrm{b} = 90°$ and $\phi_\mathrm{b} = 0, 36°$ in blue and orange respectively.

We see clearly that for both values of ϕ_b, as $\mathscr{M}_\mathrm{b}$ is reduced from its maximal permitted value, the ϕ_∞ reached by the streamlines decreases from 90° as expected, with $\phi_\infty = 90°$ if and only if $\mathscr{M}_\mathrm{b} = \mathscr{M}_{\mathrm{b,max}}$. That is to say that the slower the wind the lower (in ϕ) the surface to which it asymptotes.

If we have sufficiently slow/restricted solutions that they are expected to rapidly curve and reach the radial limit at $\tilde{r} \approx 1$, $\phi \approx \phi_\mathrm{b}$, then we can evaluate Equation 2.28 to find a relationship involving ϕ_∞, ϕ_b, χ_b, b and $\mathscr{M}_\mathrm{b}$.

$$\sin(\phi_\infty) = \sin(\phi_\mathrm{b}) + \cos(\phi_\mathrm{b})\sin(\chi_\mathrm{b})\sqrt{\frac{\pi}{2b(2-b)}}\mathscr{M}_\mathrm{b} \exp\left(-\frac{\mathscr{M}_\mathrm{b}^2}{2}\right) \tag{2.29}$$

This allows us to approximate the expected ϕ_∞ as a function of $\mathscr{M}_\mathrm{b}$ at a given b, ϕ_b and χ_b. Figure 2.8 shows examples of this expression for the two cases being considered as the black dashed lines; it provides a good estimate of the relationship between $\mathscr{M}_\mathrm{b}$ and ϕ_∞ in the case that the domain filled by the wind is sufficiently restricted, either because of an elevated base or a slow launch.

We can also use this framework to understand why the solutions fail above the Mach number for which solutions fill the domain. Given that χ is an increasing function of $\mathscr{M}_\mathrm{b}$, then for any faster launch the solution would try to curve up too steeply to reach impossibly large

$\sin(\phi) > 1$. Practically, these solutions must therefore break down; instead they encounter the critical point where $f_1 + f_2 = 0$ and the velocity gradient diverges (Clarke & Alexander, 2016).

This connection between $f \to 0$ and high $\sin(\chi)$ can be made explicit by considering an equivalent criterion expressed using the ratio of the two terms:

$$\mathscr{F} = \frac{|f_1|}{f_2} = (\mathscr{M}_b^2 \tilde{u}^2 - 1)\tan^2(\chi), \tag{2.30}$$

such that $\mathscr{F} \to 1$ represents the singularity. Note that since $\tilde{u}$ will be monotonically increasing (though potentially very mildly) then for $\mathscr{F}$ to remain less than 1, $\tan(\chi) = \frac{\mathrm{d}\phi}{\mathrm{d}\ln\tilde{r}}$ must be monotonically decreasing towards 0 - again we see the validity of the solution is determined by the streamlines becoming asymptotically radial.

For comparison therefore, we also plot the value of ϕ where these solutions with $\mathscr{M}_\mathrm{b} > \mathscr{M}_\mathrm{b,max}$ reach the singularity on the right-hand axis of Figure 2.8 using crosses and dotted lines. We see that indeed the faster the wind is launched, the larger $\sin(\chi)$ becomes and so the sooner the singularity is encountered (Clarke & Alexander, 2016).

2.6.1 Validation with Hydrodynamic Simulations

With the simulations presented so far, the winds must adopt $\phi_\infty = \pi/2$. However, if some external constraining pressure, for example from some separate magnetic or stellar outflow from smaller radii, is present, it may acts to constrain on the region occupied by disc winds. For example, Hollenbach et al. (1994); Richling & Yorke (1997) consider the effects of a strong stellar wind (as appropriate for O/B type stars) on the EUV irradiation - and consequent ionisation balance and wind base density profile. In this scenario, pressure equilibrium is established between the ram pressure of the stellar wind, and the pressure of the disc atmosphere/wind (Hollenbach et al., 1994).

To simulate such a scenario here we simply move our reflecting boundary in our FARGO simulations from the z-axis to some lower ϕ values $\phi_\mathrm{max} = 81, 72, 63, 54, 45, 36, 27, 18^\circ$, noting that this approach neglects any shear effects between the constraining region and the thermal wind; while this may not be entirely realistic, we use this to illustrate the validity of our interpretation of the slow winds using the most appropriate boundary conditions for the solutions. We assume winds launched from the midplane i.e. $\phi_\mathrm{b} = 0^\circ$. Otherwise this set of simulations are the same as those in Section 2.5. The values of $\mathscr{M}_\mathrm{b}$ that resulted (calculated as a mass-weighted average across the base) are shown as the green dots in Figure 2.8. These agree well for large enough ϕ_max, and apparently down to $\sin(\phi_\mathrm{max}) = 0.4 - 0.5$. Inspection of the simulations for $\phi_\mathrm{max} \lesssim 45^\circ$ shows they progressively deviate from steady, self-similar, solutions, and display oscillations at small radii. We were unable to bring these into agreement with the expected self-similar solutions by increasing the resolution in time or either spatial direction, nor find any critical angle or $\mathscr{M}_{\mathrm{b}}$, below which this behaviour manifests. Since it is not clear that such strongly restricted scenarios are realistic, we don't consider them any further.

We have thus shown that the solution with $\mathscr{M}_{\mathrm{b,max}}$ is a robust prediction for self-similar thermal winds, since it is the unique valid solution that fills the spatial domain (Figure 2.8). Only if the domain is reduced by somehow constricting the wind are self-similar winds expected to launch more slowly than $\mathscr{M}_{\mathrm{b,max}}$.

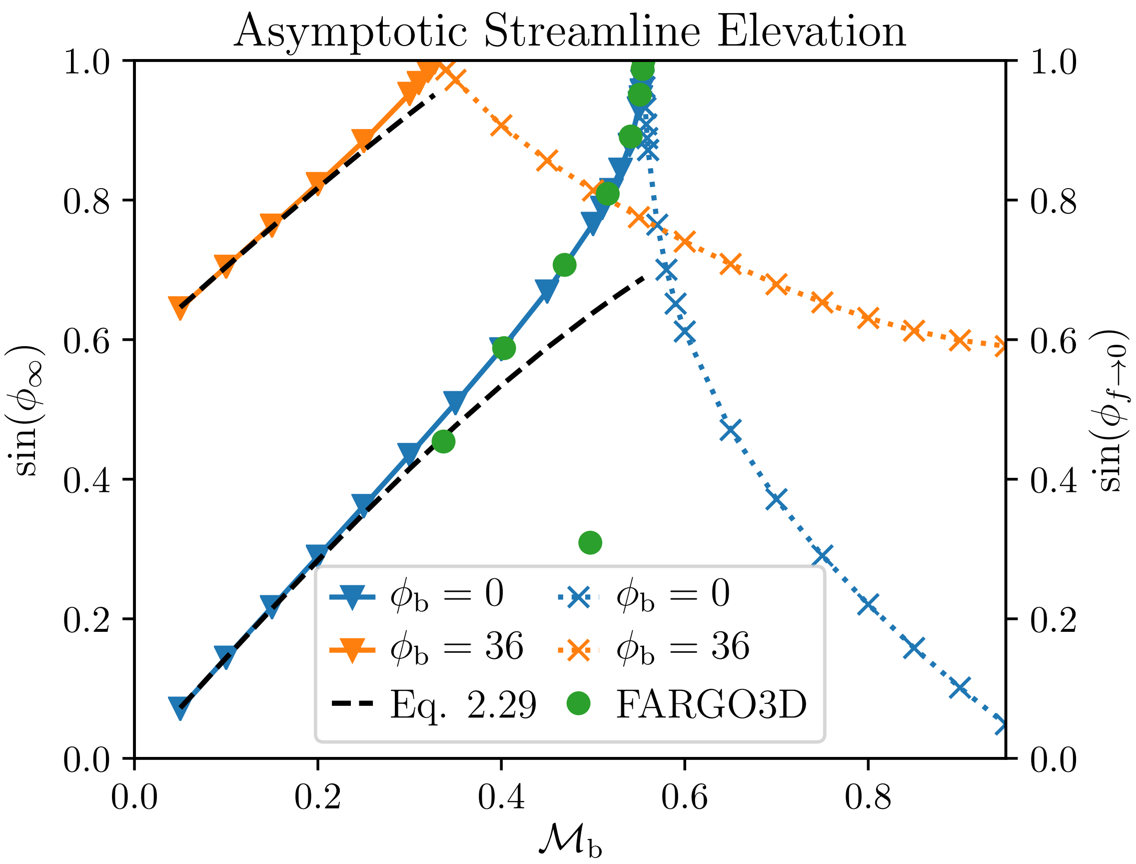

Fig. 2.8 The key angles describing the behaviour of self-similar wind solutions at large radius. The left-hand axis (solid lines, triangles) measures the angle to which the streamlines asymptote ϕ_∞ for self-similar midplane winds (blue), self-similar winds with $\phi_\mathrm{b} = 36°$ (orange) and winds in hydrodynamic simulations on a restricted domain (green circles) as a function of $\mathscr{M}_\mathrm{b} \leq \mathscr{M}_\mathrm{b,max}$. The right-hand axis (dotted lines, crosses) plots the angle $\phi_{f\to 0}$ at which self-similar solutions with $\mathscr{M}_\mathrm{b} > \mathscr{M}_\mathrm{b,max}$ encounter a singularity. The black dashed line represents a limiting expression (Equation 2.29) which approximates ϕ_∞ for winds with low $\mathscr{M}_\mathrm{b}$ (and thus works particularly well for $\phi_\mathrm{b} = 36°$).

2.7 Non-Scale-Free Hydrodynamic Simulations

2.7.1 Gravity and Centrifugal Force

Beyond the agreement of the scale-free simulations with the self-similar model with maximal $\mathscr{M}_\mathrm{b}$, which we have shown to apply to more general scale-free winds, Clarke & Alexander (2016) also demonstrated that this model provided a good prediction for the outer regions of discs even once gravity/centrifugal forces were included. We thus repeat the exercises from Section 2.5 with the gravitational potential included. Although we still assume axisymmetry and do not model the azimuthal direction, to provide the centrifugal force, we set the azimuthal velocity at the base equal to the Keplerian value at that cylindrical radius:

$$u_\mathrm{azimuthal} = R^{-1/2}. \tag{2.31}$$

This is applied regardless of the wind-base elevation since the corrections (Nelson et al., 2013) due to elevation above the midplane, which depend on the disc's density and temperature structure, are small. We use units where $GM_* = 1$ and $c_\mathrm{S}(r=1) = 1$, such that the radius is now expressed in units of r_G. In addition, to avoid spurious peaks in $\mathscr{M}_\mathrm{b}$ at small radii, we needed to use twice the resolution as in the previous section.

Elevated Bases

Figures 2.9 and 2.10 show the launch Mach numbers and streamlines respectively for elevated wind bases with $\phi_\mathrm{b} = 36°$. In all cases $\chi_b = 90°$. The simulation outputs are averaged over a range of times to average out small fluctuations.

Figure 2.9 illustrates that as found by Clarke & Alexander (2016) the launch Mach numbers are roughly constant in the outer disc where $r > r_G$ (i.e. $r > 1$ on the plots) with values that are well-predicted by $\mathscr{M}_\mathrm{b,max}$. Clarke & Alexander (2016) argued that the curvature dominates over gravity/centrifugal forces when $(r/r_G) \times r/r_\mathrm{eff} \gg 1$; consequently, we see the tightest agreement in the $b = 1.5$ cases where the wind is most strongly curved at the base. Moreover material continues to be launched somewhat inside the gravitational radius, albeit more slowly (Liffman, 2003; Font et al., 2004; Clarke & Alexander, 2016).

The self-similar streamlines continue to provide a good model for the streamline morphology in Figure 2.10, especially in regions of high curvature. Equation 2.31 strictly balances centrifugal force with gravity at the midplane. As z is increased at the elevated wind base, gravity weakens slightly but the centrifugal force is not affected. Thus centrifugal force dominates over gravity at our wind base, resulting in a net outward force. For the low b

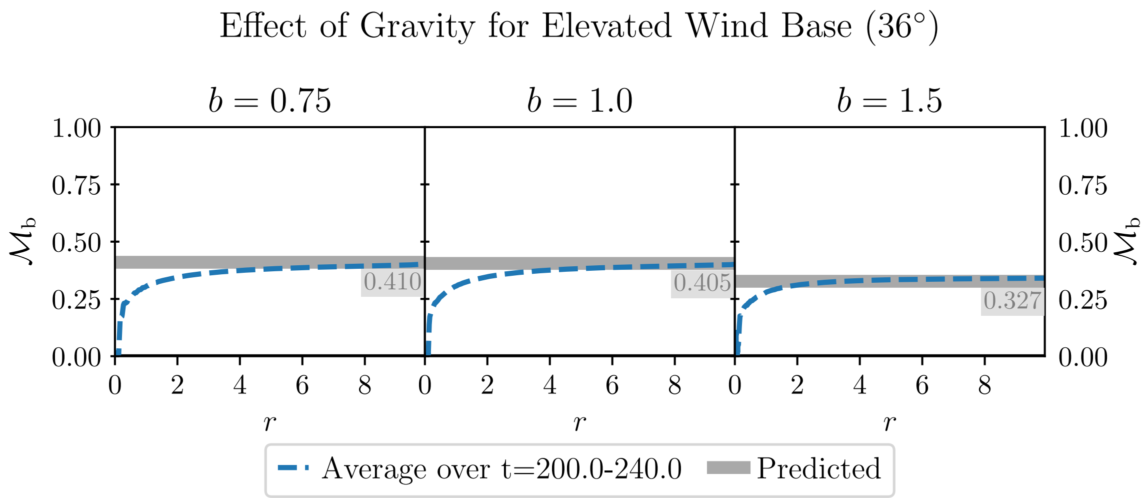

Fig. 2.9 Comparison of the launch Mach numbers $\mathscr{M}_\mathrm{b}$ as a function of radius (in units of the gravitational radius) for winds (with gravity/centrifugal forces included) launched perpendicularly from a base elevated by $\phi_\mathrm{b} = 36°$ with density power-law slopes $b = 0.75, 1.00, 1.50$ from left to right. The blue dashed lines indicate the output from hydrodynamic simulations averaged over a range of times to smooth the effect of oscillations since the solutions are not perfectly steady, especially at small radii. The grey bands are as in Figure 2.3. Note the switch to a linear x-axis scale as per Clarke & Alexander (2016) since the solution is no longer scale-free, allowing us to highlight the region over which the self-similar solution is a good approximation.

winds, the streamline curvature is small so this net force has a more significant effect and pushes the streamlines to a larger $R(z)$.

In the $b = 1.5$ case this effect is subdominant to the existing curvature. Instead, since there is no flow from small r_b, the region near the z-axis is poorly supplied with material. Thus, there are much stronger density gradients in the ϕ direction, which cause the streamlines to curl upwards more strongly to fill the spatial domain.

In the simulations described above, we use boundary conditions designed to impose $u_r = 0$ such that the winds should launch perpendicularly. However just above the base, the flow develops non-zero u_r due to the streamline curvature. As $\mathscr{M}_\mathrm{b} \to 0$ for $r \ll r_G$, then at small radii, the angle the wind makes with the base $\chi_\mathrm{b} \to 0$ also. By $r \approx 0.2\ r_G$, the launch velocity drops sufficiently that (when measured just above the wind base) $\chi_\mathrm{b} \approx \pi/4$ which we deem sufficient to explain the non-perpendicular streamlines in the inner disc in the simulations of e.g. Picogna et al. (2019). For this reason, we do not further impose a non-perpendicular launch.

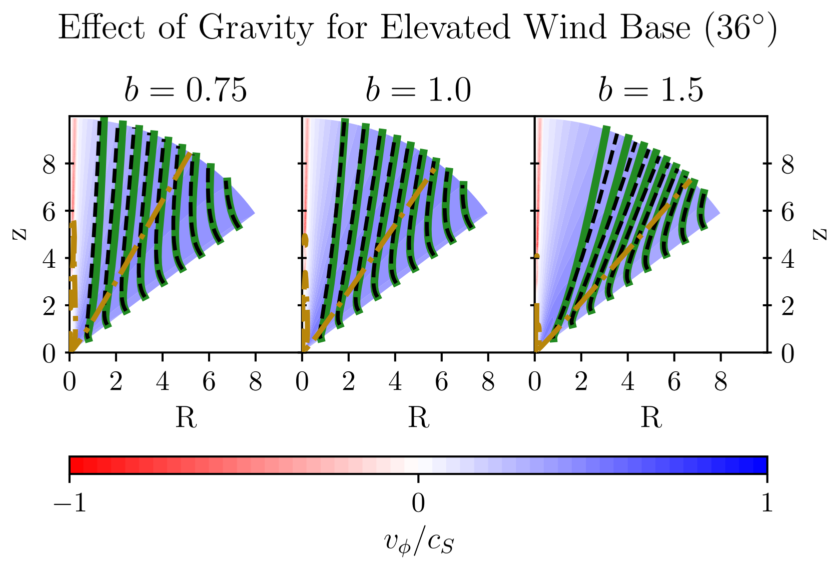

Fig. 2.10 As with Figure 2.4 but for the wind models in Figure 2.9 with gravity/centrifugal forces included. The hydrodynamic simulation outputs have been averaged over the same range of times as Figure 2.9. The self-similar solutions are still very decent representations of the streamline morphology.

Radial Temperature Profiles

We now present our most complete models by reintroducing non-isothermal effects. Since material is not launched from the inner grid anyway, it should not matter which boundary conditions are applied, so for consistency we use a constant velocity across the boundaries, rather than constant Mach number. We plot the Mach number at the base as a function of radius in Figures 2.11.

The resulting $\mathscr{M}_\mathrm{b}$ profiles are consistent with the previous results. The effect of gravity is still to stifle mass loss at small radii. However, when compared to the isothermal case, the wind is a little more readily launched from smaller radii for larger temperature gradients. This is because although the gravitational radius has been fixed, the ratio of thermal energy to gravitational energy declines more slowly (as $r_b^{1-\tau}$) with decreasing radius. Thus, the higher temperatures at smaller radii provide more thermal energy to drive the wind. Moreover, the reduced launch velocities mean that the radius of curvature is smaller, further pushing us into the regime where $(r/r_G) \times r/r_\mathrm{eff} \gg 1$ (Clarke & Alexander, 2016). Consequently, the profiles of $\mathscr{M}_\mathrm{b}$ are very flat, and in good agreement with the predicted values for non-isothermal winds (Table 2.1).

Thus, while the temperature gradients lower the launch velocities, they also have the effect of mitigating against gravity and centrifugal force, thus reducing the deviations from

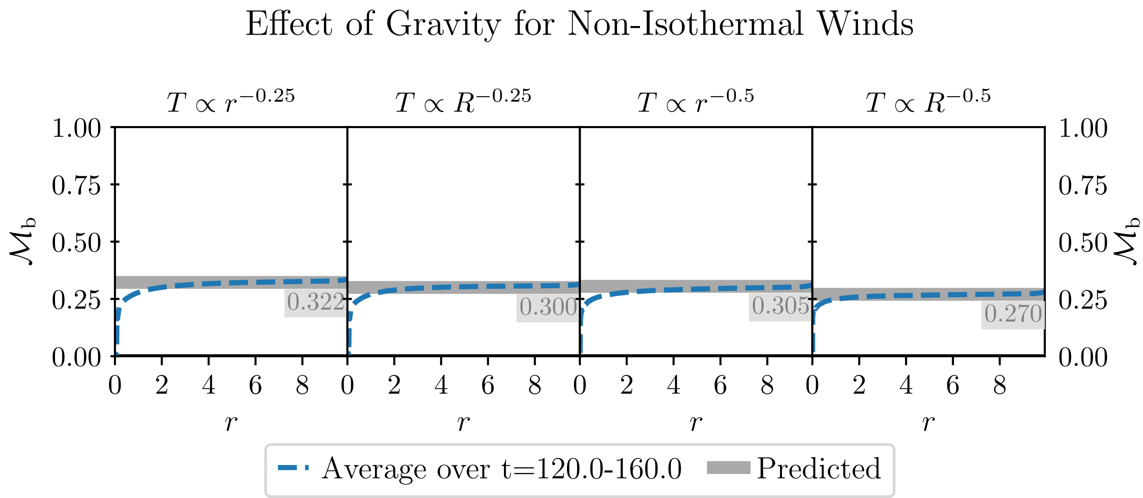

Fig. 2.11 As with Figure 2.5 but including gravity/centrifugal forces (hence r is in units of the gravitational radius). The blue dashed lines indicate the output from hydrodynamic simulations averaged over a range of times. The grey bands are as in Figure 2.5.

self-similarity. This can also be seen in the streamlines, which we plot in Figure 2.12. In particular, comparing the two left-most panels ($\tau = 0.25$) and the two right-most panels ($\tau = 0.5$), the steeper temperature gradients have closer agreement between the streamlines. Even the deviations at large radii are less apparent, because the additional thermal energy assisting the launch at small radii means that the region near the z-axis is no longer so depleted of material. Again, whether the temperature depends on the spherical or cylindrical radius has no bearing on the results.

Summary

We conclude that the effects of gravity/centrifugal forces do not strongly modify the launch velocities or streamlines at suitably large radii compared to r_G for elevated wind bases. At small radii, $\lesssim r_G$, it can become harder to drive an outflow and the launch velocities are lowered; correspondingly the winds no longer launch quite perpendicularly. This weakened flow from small radii does not impact on the validity of the self-similar solution outside the gravitational radius near the base, but can result in a stronger upward curvature at large radii in the case of weak temperature gradients. Thus as found by Clarke & Alexander (2016), the self-similar solutions have general applicability to describe the launch velocity and streamline structure of thermal winds when gravitational and centrifugal forces are included and this agreement is strengthened by introducing a moderate temperature gradient.

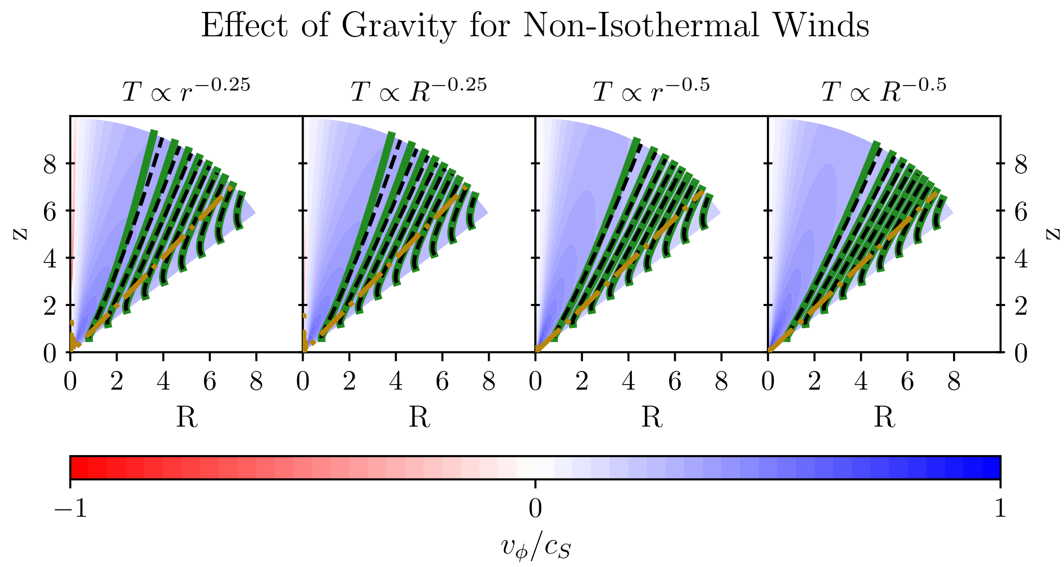

Fig. 2.12 As in the $b = 1.5$ panel of Figure 2.4, a wind launched from $\phi_b = 36°$ but including gravity, centrifugal force and temperature gradients of varying steepness and direction. Once again, the self-similar solutions are still very decent representations of the streamline morphology.

2.7.2 Double Power Laws

Our final consideration is that a power law of infinite extent will never completely describe the density at the wind base. Most simply, at some point, there must be a cut-off at the discs's outer edge. Moreover, the density structure at the wind base is dependent on the mechanics of the heating; for example Hollenbach et al. (1994)'s static models showed a transition from $b = 1.5$ at $r < r_G$ to $b = 2.5$ for $r > r_G$ (Section 1.2.6), although in other hydrodynamical simulations, such a transition to a steep $b > 2$ power law does not apparently occur at $r = r_G$ (Wang & Goodman, 2017; Yorke & Kaisig, 1995). Regardless of the reason for the transition, if a wind is described by different power laws at small/large radii, we expect the appearance of the transition radius r_t to break self-similarity, and this may affect the applicability of the self-similar solutions.

To see how these deviations from self-similarity manifest, we consider double power laws both of the form used by Font et al. (2004), and an inverse equivalent:

$$\rho \propto \left(\frac{2}{r/r_t{}^{5b_1} + r/r_t{}^{5b_2}} \right)^{1/5}, \tag{2.32}$$

$$\rho \propto \left(\frac{r/r_{\mathrm{t}}^{-5b_1} + r/r_{\mathrm{t}}^{-5b_2}}{2} \right)^{1/5}. \tag{2.33}$$

For clarity we will always choose $b_2 > b_1$; then the former of these profiles transitions to a steeper power law at large radii, whereas the latter transitions to a shallower power law.

We consider three combinations of b_{in} and b_{out}: $1.50/1.75$, $1.75/1.50$, $1.50/2.50$. In the first two cases (power law transitions to $b < 2$), we expect that on their own, both the inner and outer regions of the disc could launch a self-similar wind. In the latter case (power law transitions to $b > 2$), we would not expect a self-similar solution to exist for the outer disc. That said, a single power law with $b = 2.5$ may still permit a *non-self-similar* wind solution (Font et al., 2004); in particular the requirement for such a case to be diverging faster than spherical may be circumvented by suppressing the contribution from streamlines with small r_{b}; contributions to this in Font et al. (2004) include gravity impeding the launch for $r_{\mathrm{b}} < r_G$, and their use of a reflecting inner boundary condition which prevents material launched from $r_{\mathrm{b}} < r_{\mathrm{in}}$ entering the simulation domain.

In each case, we will assume $r_{\mathrm{t}} = 1$: firstly without gravity (where there is no physical significance to this value), and with gravity for the case with $b_2 = 2.5$ (using units of r_G such that $r_{\mathrm{t}} = r_G$). We use a grid that now extends from $r = 0.01$ to $r = 100$, in order to have an equal two decades in radius either side of the transition; this is enough to ensure that in all cases the slope of the density profile at the grid edges differs from the relevant limiting value by less than 1% of the difference in b values.

Power Law Transitions to $b < 2$

First, we consider two cases where in either extreme, the density profile permits a self-similar model: one that scales like $r^{-1.5}$ in the inner disc and $r^{-1.75}$ in the outer disc (steepening case), and one where these values are reversed (flattening case). The Mach numbers at the base are shown in Figure 2.13 for the elevated base with $\phi_{\mathrm{b}} = 36°$.

In both the steepening and flattening cases, Figure 2.13 shows that for radii $r \lesssim 1$ the launch Mach numbers (blue lines) are those that we would expect given the density gradient at these radii. Beyond $r = 1$, the velocities smoothly transition towards the value appropriate for the outer disc, reaching it at $r \gtrsim 30$. Regardless of whether the inner or the outer disc is the steeper, there is an asymmetric behaviour about the transition point between the two regimes of the density profile, with the launch velocity relatively unaffected within the inner disc, but the outer disc feeling the effects over 1 to 2 orders of magnitude.

We also show the Mach number that would be expected for the local density gradient $b_{\mathrm{eff}} = -\frac{\partial \ln(\rho_{\mathrm{b}})}{\partial \ln(r_{\mathrm{b}})}$ as the green dotted line. This shows a very similar shape to the Mach

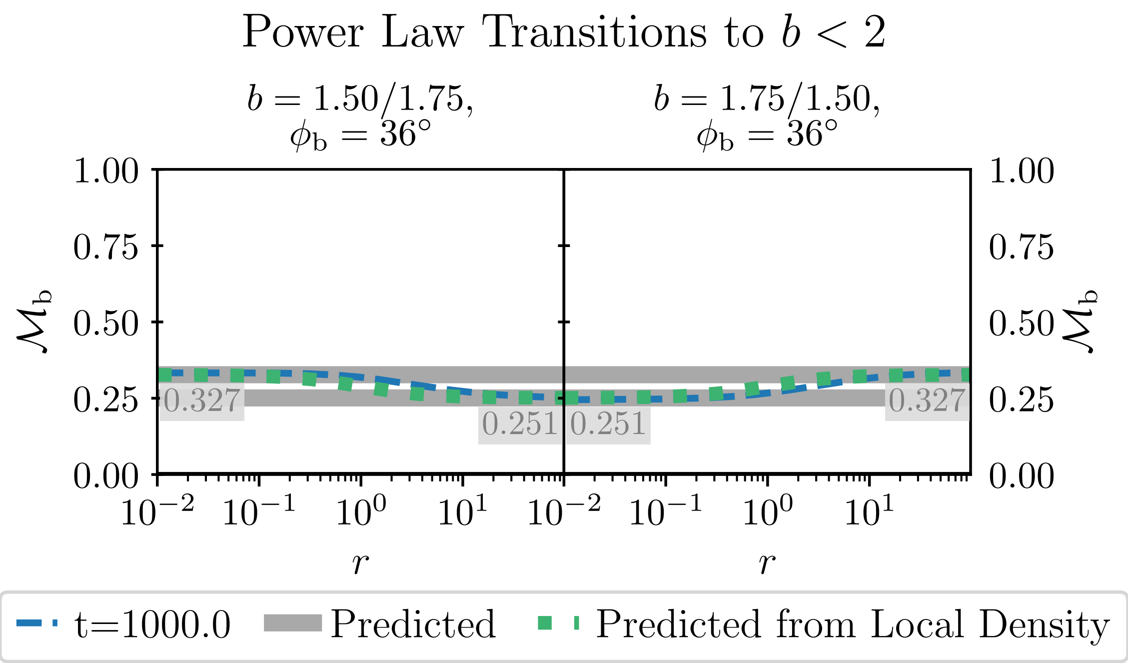

Fig. 2.13 As with Figure 2.3 but for a double power law density profile with $b_1 = 1.5$, $b_2 = 1.75$ in both the steepening and flattening cases. The two dark grey bands now represent the expected value of the Mach number for a self-similar wind with $b = 1.5$ or $b = 1.75$. In addition, the green dotted line shows the Mach number that would be expected for the local density gradient $b_{\mathrm{eff}} = -\frac{\partial \ln(\rho_b)}{\partial \ln(r_b)}$.

numbers that result in the hydrodynamic simulation, but the simulation profile is shifted to higher radii by a factor of roughly $3-4$. This suggests a picture of outwardly-directed causality: the streamlines from smaller radii are what provide the pressure constraining the outer disc streamlines. In the flattening case, the inner disc streamlines are more curved: for the outer disc streamlines to 'fit' underneath, they would have to launch more slowly than expected as per Section 2.6; conversely for the steepening case, the outer disc streamlines find themselves with a lower constraining pressure and more space to uncurl and therefore can launch somewhat faster than expected. However, in each extreme, particularly in the inner disc, the self-similar model becomes applicable.

Power Law Transitions to $b > 2$

Now we consider a base density profile described by Equation 2.32 with $b_1 = 1.5$ and $b_2 = 2.5$, i.e. the same case studied by Font et al. (2004) following Hollenbach et al. (1994). This scenario has a suitable density gradient in the inner disc for being described by a self-similar model. In the outer disc, the density gradient is too steep for our self-similar models, but as discussed above, may still permit a wind to be launched; Font et al. (2004) find there is some contribution to the wind from this region, though mass is mostly lost from inside the transition. We consider both the case without gravity (equivalent to the extreme limit of $r_t \gg r_G$) and a case where the transition radius r_t corresponds to r_G.

We investigate this scenario using two sets of boundary conditions. First we allow for a free perpendicular inflow or outflow at the launch plane. The Mach numbers at the base are shown in the left-most panel of Figure 2.14 for the gravity-free case. At small radii $r < r_G$, the flow adopts the expected value from the self-similar solution, in line with the two-regime winds studied above where the inner disc is not strongly affected by the outer disc. The transition from $b = 1.5$ to $b = 2.5$ is centred on $r = 1$ (at which location $b_{\rm eff} \equiv -\frac{\partial \ln \rho_b}{\partial \ln r_b} = 2$); in the vicinity of this point, the flow feels the effect of the more strongly declining density and begins to deviate from self-similarity with $\mathscr{M}_b$ dropping off rapidly. Thus, at radii $r \gtrsim 1.9$, the velocities change sign and there is a flow back into the launch plane. While this flow is subsonic, its velocities are still on the order of the sound speed.

Since we do not model the underlying disc, it is unclear how much resistance it might provide to such a back flow. We therefore also consider the extreme opposite situation (such that our two boundary conditions ought to bracket the "true" behaviour), where for $r > 1.9$[2], the launch plane becomes reflecting to prevent this flow back into the disc. The resulting Mach numbers for this "semi-reflecting" setup are shown in the second panel of Figure 2.14; the inner disc is unaffected by this change in boundary conditions while in the outer disc the flow instead becomes radial along the disc surface. While the small velocities in the outer region are not perfectly steady, the oscillations are very small and average out smoothly. We also attempted to set the boundaries self-consistently using a diode based on the sign of the velocities but found this was unstable and showed large deviations from the steady state.

Having established that a wind is only possible within $r \lesssim r_t$, we reran the models with both boundary conditions now including gravity and centrifugal force - the Mach numbers are shown in the third and fourth panels of Figure 2.14 respectively. In the inner disc, the Mach numbers greatly resemble the trends observed in the case of a single $b = 1.5$ power law when gravity is included (right-hand panel, Figure 2.9), in that there is no outflow inside $r \approx 0.1$, and the velocities rise in the range $0.1 - 1.0$, beginning to flatten off as $r \to 1$ though not quite yet reaching the self-similar value of 0.327. Beyond $r \approx 2$, the behaviour appears identical to the left-hand panels of Figure 2.14 and we find either a strong and smooth flow back into the disc, or no flow depending on our boundaries. Thus, here the wind only originates from a very limited range of radii in the vicinity of r_t. This is in agreement with

[2]We tested other locations in the range $1 \leq r \leq 2$ for the change in boundary conditions and found that $r = 1.9$ reduced any overshooting of the velocities near the change.

the results of Font et al. (2004) who found that the mass loss in such a scenario mostly comes from $0.1 < r/r_G < 2$.

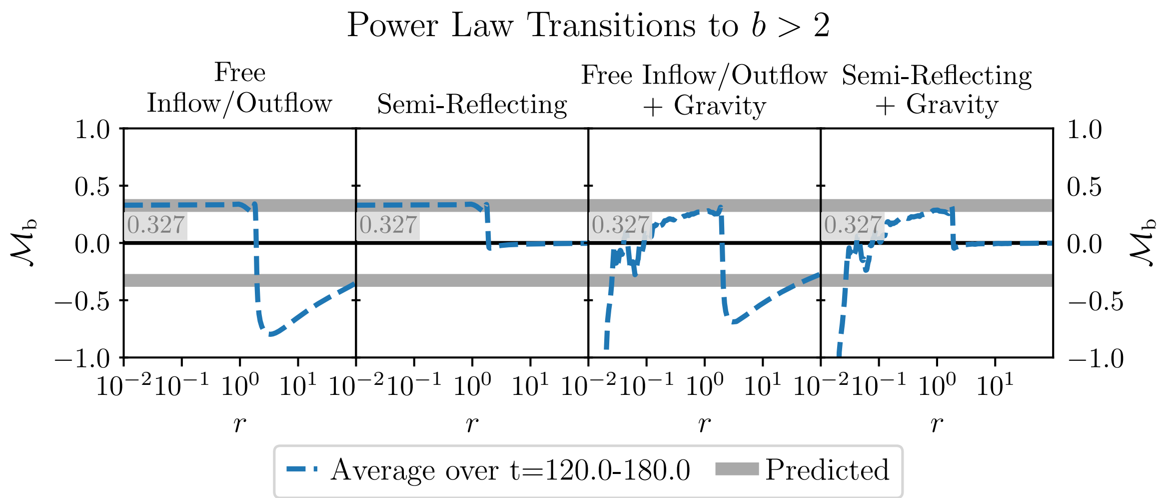

Fig. 2.14 Comparison of the launch Mach numbers $\mathscr{M}_b$ for a double power law density profile with $b_1 = 1.5$, $b_2 = 2.5$ launched from $\phi_b = 36°$. The odd panels have a free outflow/inflow at the launch plane while the even panels have a reflecting boundary to prevent inflow for $r > 1.9r_G$. The dark grey bands represent $\pm$ the predicted $\mathscr{M}_{b,max}$ from the self-similar models with $b = 1.5$ and the grey label shows its value.

The large-scale morphology of these winds should be very different from the self-similar models since either a radial flow or a flow back into the disc occurs at large radii. This means a lack of supply of material to provide pressure support to the streamlines from underneath. Thus the streamlines instead curl back towards the base. To emphasise this behaviour, Figure 2.15 shows the streamlines in polar coordinates i.e. ϕ as a function of r.

For the models without gravity, the innermost parts of the streamlines near their bases agree well with the self-similar models and the morphology is independent of the boundary condition choice at larger radii. Somewhere near $r = 1$, they begin to flatten off and the elevation peaks in the range $1 \lesssim r \lesssim 3$. Beyond this point there are two possible fates. In the case of free outflow, the elevation decays - most rapidly for the lower streamlines and more slowly for the higher streamlines, until they reintercept the launch plane. When the boundaries are reflecting, the streamlines cannot cross it, and the material following them remains in the grid. This provides an additional upwards pressure gradient, reducing the downward velocities of the wind and resulting in the elevation of each streamline levelling off again such that they become radial. A whole range of asymptotic elevations are possible, so not all material returns near to the base. Moreover the wind has no particular opening angle and the density contours are roughly spherical in agreement with Font et al. (2004).

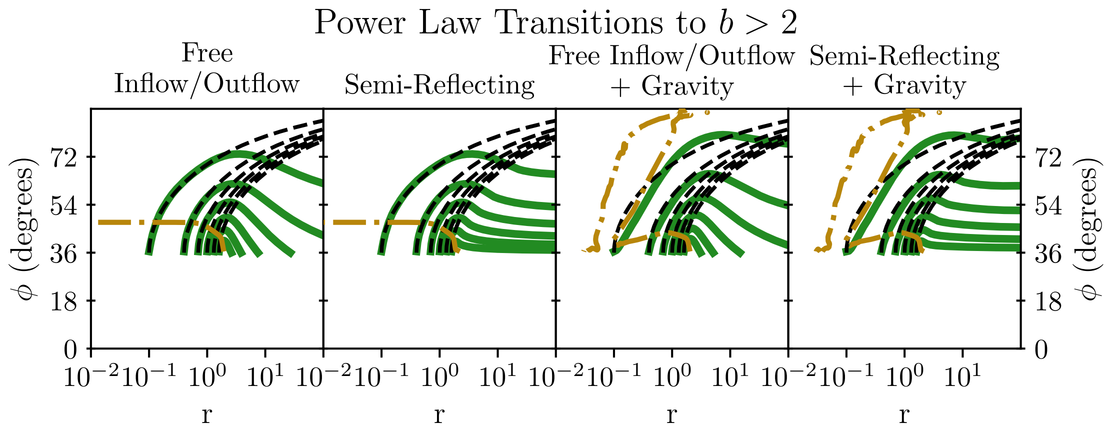

Fig. 2.15 The elevation ϕ (degrees) of the streamlines as a function of radius for the 'single-regime' models shown in Figure 2.14. The streamlines are shown for $r_\mathrm{b} = 0.1 - 1.6$ in steps of 0.3. It is apparent that due to the steep density drop-off, larger deviations between the self-similar solutions and the FARGO3D results are present than for winds with base densities described by single power laws as the wind curves back towards its base. The gold dot-dashed line shows the sonic surface, demonstrating that the wind remains supersonic in this region at $r \gtrsim r_G$; hence the material here is unbound.

In both cases the streamlines are concave upwards. Despite these differences close to the midplane, the qualitative picture of declining ϕ holds for both boundary conditions. Thus we expect to see streamlines curling back towards the disc regardless of where the correct boundary conditions lie relative to the two extremes shown here and can be confident that the "true" behaviour is reasonably well captured by these models.

The polar streamline plots in the presence of gravity (right-hand two panels of Figure 2.15) illustrate that as seen in the launch velocities, the large scale morphology at $r > r_G$ is little affected by gravity. The streamlines do reach slightly higher elevations - analogously to the upward curling seen at large radii in the $b = 1.5$ models with gravity.

In the particular example given, where $r_\mathrm{t} = r_G$, this implies that the self-similar solution is only approximately valid over a factor 3 in radius around $r_\mathrm{t} = r_G$, with deviations at small radii caused by the role of gravity and at large radii by the transition to a steeper density profile. More generally, the self-similar solutions can describe the region $r_G \lesssim r \lesssim r_\mathrm{t}$; we emphasise that although (Hollenbach et al., 1994) argued that $r_\mathrm{t} = r_G$ for EUV-driven photoevaporative winds, the location of any turnover in the density profile is sensitive to details of the radiation transfer and hydrodynamics with simulations (e.g. Richling & Yorke, 1997; Wang & Goodman, 2017) finding $r_\mathrm{t} > r_G$ and allowing a larger role for self-similar solutions in describing EUV-driven winds than our results would suggest.

2.8 Discussion of Applicability

The derivation of the self-similar solutions and their comparison to hydrodynamic simulations is motivated by both theoretical and observational considerations. For example, their relative ease of application allows us to interpret forbidden line spectra without needing dedicated radiation hydrodynamic simulations of photoevaporation (Ballabio et al., 2020); I explore observational applications in Chapter 4 so reserve the discussion here for their theoretical use in understanding photoevaporation simulations.

2.8.1 Comparison to Photoevaporation Simulations

Through simple hydrodynamic simulations, we have demonstrated that gravity and centrifugal force make only a small impact on the launch velocity and streamline morphology of thermal winds. Therefore, as long as, for example, the wind base isn't strongly flared, we should reasonably expect more detailed radiation hydrodynamic simulations including those of Wang & Goodman (2017); Picogna et al. (2019) to show velocities that agree with the self-similar models. The key determinant of $\mathscr{M}_\mathrm{b}$ is the wind-base elevation, with radial temperature gradients having an effect at no more than the $\sim 10\%$ level.

Wang & Goodman (2017) find that the wind launches from $z/R \approx 0.6$, corresponding to a launch plane at $\phi_\mathrm{b} \approx 30^\circ$. By inspecting Figure 2.1 we see that this corresponds to $\mathscr{M}_\mathrm{b} \lesssim 0.4$ (assuming $b \approx 1.5$ e.g. Hollenbach et al., 1994). In their Figure 2, Wang & Goodman (2017) also show the Mach number as a function of distance along streamlines originating from $R = 5$ and $R = 15$ au, which correspond to around 0.5 and 1.5 gravitational radii (Equation 1.9). In both cases, at the base the Mach number appears to be tending towards a value in the range $0.3 - 0.4$ in good agreement with our estimate.

Conversely, the simulations of Picogna et al. (2019) appear to agree with these predictions less well. Their wind base is well-fitted by $\phi_\mathrm{b} = 36^\circ$, with $\rho \propto r^{-1.5}$ but the average Mach number here is more like $\langle \mathscr{M}_\mathrm{b} \rangle = 0.1$ across a wide range of radii (R. Franz, Private Communication), whereas we would expect a value of 0.327. However, the Mach numbers quickly rise to around 0.3 within a couple of degrees of the base, much faster than they do in the self-similar solutions. This is due to their definition of the base placing it a region of steeply increasing vertical temperature gradient, which thus provides a pressure gradient against the direction of flow. Once the temperature gradients become smaller, the solution reverts to what we would expect would be appropriate to fill the domain.

Our "two-regime" models suggest that sufficiently outside a density transition, the wind forgets the inner disc conditions. We might therefore expect the self-similar solution to be a good approximation for the outer disc even in the case that a gas cavity has opened (as expected during inside-out clearing). Although a severely depleted inner disc is a much stronger deviation from the density profile than considered here, Alexander et al. (2006a) did note that there was no evidence for a strong radial dependence in the launch velocities of their directly EUV-irradiated discs, a feature seen in our models as a hallmark of self-similarity. This result is useful if we wish to apply self-similar solutions to discs undergoing clearing, which may be when photoevaporation is the most significant (Pascucci et al., 2020).

2.8.2 Interpreting Hydrodynamic Simulations

Owen et al. (2012) interpreted the results of their hydrodynamics simulations of photoevaporation using a similar theory of transsonic winds. They argued that at large radii in the wind, centrifugal force can be neglected in the effective gravity term which simply approaches the usual Newtonian $1/r^2$ force. Moreover, they suggest that at large distances, the divergence of the streamlines should be similar to the spherical case ($\frac{\mathrm{d}\ln A}{\mathrm{d}l} \to \frac{2}{r}$). Therefore, the terms become comparable to those in the classic spherical Parker wind (Parker, 1958) and we should expect that, up to a factor, $R_\mathrm{S} \sim r_\mathrm{s} = \frac{GM_*}{2c_\mathrm{S}^2}$. Inverting, they argued that at each radius R, the wind passed through the sonic point at a velocity $c_\mathrm{S} \sim \sqrt{\frac{GM_*}{2R}}$. Since in their simulations, temperature was prescribed as a function of density and distance from the star only, then immediately one can convert this into the density ρ_S at the sonic surface. One may finally integrate Equation 1.10 at the sonic surface to derive the mass-loss rate.

However, while this temperature gradient was a reasonable match to the simulations of Owen et al. (2012) within a factor ~ 2 of r_G, the agreement is much poorer when compared to Picogna et al. (2019) where the temperature profile is generally shallower and indeed seems to be independent of stellar mass. This is because the approach of Owen et al. (2012) is appropriate so long as the divergence terms are always of order $2/r$ such that the only way to achieve the singularity is the Parker case. However, here while $\frac{\mathrm{d}\ln A}{\mathrm{d}l} \to \frac{b}{r}$ at large radii, the streamline geometry may also permit, as discussed, a converging-diverging nozzle flow. In this case, the curved streamlines provide a $\frac{\mathrm{d}\ln A}{\mathrm{d}l} < 0$, where we have argued that the curvature term will dominate over gravity. Thus, at either limit of the streamline, the dynamics are dominated by the curvature/divergence terms. On coarse scales, the sonic surface location should therefore be primarily set by the nozzle condition, with gravity perturbing this position only slightly.

Therefore, while the temperature must, by definition, be roughly the Parker value in the vicinity of r_G where the self-similar geometry starts to break down (and a nozzle may no longer even be possible, thus potentially recovering the Parker-like case), in the outer disc, another consistent solution is allowed, in which at the sonic surface $\frac{\mathrm{d}\ln A}{\mathrm{d}l} \ll \frac{2}{r}$ and the temperature can therefore be very different to the Parker value. In conclusion, though it is certainly a permissable solution, the hydrodynamics do not generally limit the sound speed at the sonic point to take on any particular profile as a function of radius, but rather it is free to be set according to the thermochemistry.

2.9 Conclusions

In this chapter I extended the previous studies of self-similar solutions for thermal disc winds by Clarke & Alexander (2016) so as to derive a more general set of scale-free wind solutions. Specifically I relaxed the assumptions of isothermal gas and perpendicular launch from the disc mid-plane to obtain solutions for generalised launch geometry and power law temperature profiles. I validated these solutions using hydrodynamic simulations and furthermore used hydrodynamic simulations to explore non-scale-free conditions: the imposition of a disjoint power law for the wind base density profile and the inclusion of gravitational and centrifugal forces.

I analysed these models principally in terms of the streamline morphology and the Mach numbers with which the winds are launched (which control the mass-loss rates). In doing so I showed that self-similar solutions have widespread and general applicability to describing thermal winds launched from discs at reasonably large radii (beyond the gravitational radius). This is appropriate for protoplanetary discs where outflows consistent with thermal winds are seen to originate in the outer disc (Pascucci et al., 2020). This is important for works which seek to apply self-similar models - for example to interpret line spectra (Ballabio et al., 2020) or study dust transport (Hutchison & Clarke, 2021) - as well as for understanding the hydrodynamic properties of winds (such as launch velocity profiles and sonic surface locations) that result from more sophisticated radiation hydrodynamics simulations.

In particular, I found that:

1. Scale-free temperature profiles, including radial temperature gradients, still permit self-similar solutions which have a constant Mach number at the base, the value of which depends on the imposed profile. However, for temperature scaling as $r^{-0.5}$, the Mach number is decreased by only around $10-20\%$ compared with the isothermal case.

2. The parameter which most strongly influences the wind's launch velocity is the wind-base elevation to the midplane. The higher the winds originate, the more rapidly they must curve and so the more slowly they are launched.

3. Scale-free hydrodynamic simulations adopt the maximum Mach number at the base for which the solution avoids any singularities in the fluid equations (Clarke & Alexander, 2016) even when the winds are launched from elevated bases, non-perpendicularly to their base or in the presence of temperature gradients.

4. This preference for a maximal launch Mach number may be explained by the inability of solutions with lower Mach numbers to fill the computational domain. In that scenario, the region near the z-axis would become inaccessible to the wind and provide no resistance to the pressure in the wind region; the streamlines would spread out to fill it, allowing the wind to launch faster. However, if a reflecting boundary, representing some other constraint on the wind, is placed at lower latitude, then simulations adopt a lower launch velocity commensurate with a self-similar solution which asymptotes to the angle set by the reflecting boundary.

5. When gravity and centrifugal force are included, the streamlines and $\mathscr{M}_{\rm b}$ predicted by self-similar models remain a good approximation to the true streamlines, particularly at large radii or when the radius of curvature is small. Introducing temperature gradients improves the agreement because these solutions have a smaller radius of curvature and therefore pressure plays a more important role compared to gravity and centrifugal forces.

6. The predictions of self-similar winds may also describe the launch velocities of density profiles which are double power laws. The velocities vary smoothly between the values appropriate to the density gradient in each limit of the profile, with the launch velocity from inner disc unaffected by the changes in density at larger radius. However, when the density gradient steepens beyond $b = 2$ in the outer disc, an outflow is largely prevented: the region of wind launching extends by no more than a factor ~ 2 beyond the radius where the density profile attains this limiting gradient. Instead, streamlines originating from the inner disc curl down towards the wind base at radii beyond the transition radius.

Chapter 3

The Driving Thermodynamics of Photoevaporative Winds

3.1 Motivation

In the Introduction (Section 1.2.6) I explored the history of photoevporation models with particular emphasis on key methodological differences and how these manifest in divergent results within the current generation of models (with distinct conclusions about the driving radiation and orders of magnitude uncertainty in the mass-loss rates). This chapter focuses on comparing the temperatures calculated by different codes with a view to disentangling which differences are most critical and identifying a comprehensive methodology that will produce accurate mass-loss profiles in a range of scenarios.

I first review in more depth the microphysics controlling thermal balance and the contributions that atoms and molecules make to cooling. I then use MOCASSIN (Ercolano et al., 2003, 2005, 2008a) to calculate the temperatures for a static density grid taken from Wang & Goodman (2017), identify potential origins of the differences compared to Wang & Goodman (2017) and interpret our results in the context of an X-ray radiative-equilibrium model. Finally, I use these insights into the key heating and cooling processes to configure PRIZMO - a new thermochemisty code for protoplanetary discs presented by Grassi et al. (2020) - and verify its behaviour in the low ionisation parameter regime by applying it to a low-density EUV wind (Wang & Goodman, 2017). This is done to prepare PRIZMO for application to its first scientific use case, a coupling with the hydrodynamics code PLUTO (Mignone et al., 2007) that will perform radiation hydrodynamics with one-the-fly thermochemistry/photochemistry calculations.

3.2 Further Microphysics

3.2.1 Forbidden and Permitted Lines

Energy state transitions are typically classed as either *forbidden* or *permitted*. Forbidden lines are disallowed under the selection rules governing atomic transitions, for example requiring that parity change during a transition. Instead, they can only occur due to higher order terms in the expansion of the perturbation (for example the electric quadrupole). This makes the transition rates slow i.e. leads to lower A_{21} values than for permitted lines. This results in low critical densities, but nevertheless the conditions in winds are such that the collider densities may be below the critical density and the lines may be efficiently emitted.

Conversely, permitted lines undergo transitions at a much higher rate, this means they have much higher probability of being excited by absorbing radiation, resulting in a large cross-section for absorption. These lines may therefore become optically thick and there is a large chance of any emitted photon being reabsorbed and exciting another atom, for no net change in the occupation of the upper level: only a fraction β (where β is a function of optical depth e.g. Kwan & Krolik, 1981) of the photons which are emitted escape. When an atom's energy levels are in local thermodynamic equilibrium (i.e. their population is simply proportional to a Boltzmann factor), then this can limit the overall number of escaping photons and therefore the cooling rate. However, when collisional de-excitation is rare, i.e. the gas is sufficiently below the critical density ($n_{\mathrm{coll}} < \beta n_{\mathrm{crit}}$), then the reabsorbed photons can increase the population of the upper level as $n_2 \propto 1/\beta$. Thus, the number of photons emitted is higher by a factor $1/\beta$ and the same net number of photons escape. Although in this case, the material is optically thick, the line radiation is effectively thin.

The relevant atomic permitted lines are the Lyman series of hydrogen, particularly Lyman α for which spontaneous emission happens at a rate $A_{21} = 6.3 \times 10^{8}\ \mathrm{s}^{-1}$. Collisional de-excitation mainly occurs to the 2s subshell at a rate $1.8 \times 10^{-4}\ \mathrm{cm}^{3}\ \mathrm{s}^{-1}$ (Dennison et al., 2005) corresponding to a critical density $\sim 3 \times 10^{12}\ \mathrm{cm}^{-3}$. Thus, at typical wind electron densities $\lesssim 10^{5}\ \mathrm{cm}^{-3}$, no more than 1 in $\sim 3 \times 10^{7}$ Lyman α photons are collisionally destroyed per absorption, making it a rare process (Dijkstra, 2017).

The photons can escape two main ways. One is through the optically thin line wings. This occurs via a double-diffusive process whereby through successive re-absorptions photons perform a random walk in frequency (as well as space) due to the random Doppler boosting they receive each time (Avery & House, 1968; Dijkstra, 2017); the average frequency change is thus one Doppler width (Osterbrock, 1962). The line will have a Voigt profile consisting of a thermally broadened Gaussian core and naturally broadened Lorentzian wings. Given a thermal breadth $\Delta v_{\mathrm{th}} \approx 10\ \mathrm{km\ s}^{-1}$ and a natural breadth $\Delta v_{\mathrm{nat}} \sim \lambda A_{21} \approx 10\ \mathrm{m\ s}^{-1}$, the core will extend to $\Delta\nu \approx 3\Delta\nu_{\rm th}$. The line centre cross section is given by $\sigma_{\rm Lya} = \frac{\lambda^3 A_{21}}{8\sqrt{2}\pi^{3/2}\nu_{\rm th}} \approx 5\times10^{14}$ (Osterbrock & Ferland, 2006); assuming typical EUV wind properties - density $n \sim 10^5$ cm^{-3} (Equation 1.25), lengthscale $L \sim r_G \approx 10^{14}$ cm and neutral hydrogen fraction $f = 10^{-2}$ - the line centre optical depth is $\tau \sim nf\sigma L \approx 10^3$. Therefore $\tau = 1$ is achieved at $x := \Delta\nu/\Delta\nu_{\rm th} = \sqrt{\ln 10^3} \approx 2.6$, within the Gaussian core. Given the diffusive nature, roughly x^2 scatterings will be needed to populate this part of the line, after which time a fraction $1/\mathrm{erfc}(x)$ of the photons will be able to escape. Thus, per absorption, 1 in $2.6^2/\mathrm{erfc}(2.6) \approx 3\times10^4$ photons escape: a much higher rate than collisional destruction.

The photons could also be absorbed by dust and re-emitted at longer, optically-thin, wavelengths (Cohen et al., 1984). This happens every 1 in $\sigma_{\rm Lya}/\sigma_{\rm d,H} \approx 10^8$ collisions where $\sigma_{\rm d,H} \approx 3\times10^{-22}$ for the dust model shown in Figure 1.2. While here estimated to be the slowest of the three processes, it can dominate in very optically thick winds (where more scatterings are needed to escape in the line wings) with fewer colliders (either more tenuous or more neutral).

Although more detailed calculations are conducted by many of the works referenced here, overall, the result remains that the cooling rate matches the optically thin case (Hollenbach & McKee, 1979): the escape fraction matters for calculating the flux and shape of the Lyman alpha line reaching the observer, but not the degree of cooling it can provide.

3.2.2 Cooling from Atomic Fine Structure Lines

For single atoms (including ions), the different energy states correspond to different arrangements of electrons. Each arrangement consists of a *configuration* - denoting the number of electrons in each (sub)shell - and a *term* - denoting the way electrons in the partially-filled subshells align their spins and orbital angular momenta.

For each electron in an atom, the energy is principally determined by the Coulomb interaction, whose strength depends on its principal quantum number $n = 1,2,3...$, with the next order effect being corrections due to the orbital angular momentum quantum number $0 < l < n$. Therefore at this level, each configuration may have multiple degenerate terms. However, spin-orbit coupling breaks this degeneracy, causing the energy to depend on the alignment of the spin and orbital angular momenta: this is termed the energy level's *fine structure*.

Since fine structure is a relatively small correction compared to changing configuration, the fine structure transitions are, energetically speaking, the most easily excited. However, since these transitions happen without any change in the electronic configuration, they all have the same parity, making them forbidden transitions.

In multi-electron atoms, Russell-Saunders coupling is used as an approximation in order to determine the possible total spins and orbital angular momenta that determine a configuration's possible terms. First the possible total spins S are found by summing (vectorially) the spins of electrons in open subshells. Likewise the orbital angular momenta may be summed to give the possible total orbital angular momenta L. For S and L combinations that are allowed by symmetry considerations, then the total angular momentum lies in the range $|L-S| < J < L+S$. For example, for the two 2p electrons in neutral carbon, the possibilities are $S = 0,1$ and $L = 0,1,2$. Symmetry requires that S and L are either both even or both odd and so the allowed terms are $S = 1, L = 1 \implies J = 0,1,2$, $S = 0, L = 0 \implies J = 0$ and $S = 0, L = 2 \implies J = 2$. The ground configuration of neutral carbon thus encompasses 5 terms corresponding to 10 potential fine structure transitions.

Lower spin terms result from cancelling spins which allow electrons to share orbitals, making electron-electron repulsion stronger; thus the highest spin terms are the lowest in energy. The next most important contribution to the energy of the fine structure lines is the total L while J contributes only weakly. Thus, the fine structure terms come in multiplets of given S and L consisting of the lower of $2S+1$ or $2L+1$ members. The terms within a multiplet are separated by small energy differences, corresponding to transitions that emit radiation at 10s or 100s μm. The multiplets are separated by wider energy differences, corresponding to transitions in the optical. Since a higher energy state may (barring selection rules) transition to any of the closely-spaced terms in a given multiplet, the optical lines may occur in groups of closely-spaced lines (also called multiplets) with well-defined ratios.

For our example of C I, we have a triplet of low energy $S = 1, L = 1$ terms, where the only difference is the degree of alignment between S and L - this gives emission at 609 μm, 370 μm and 230 μm. The two further states each have a somewhat higher energy - corresponding to transitions that emit optical radiation: a triplet at $9808, 9824, 9850$ Å from the $S = 0, L = 2$ state to the $S = 1, L = 1$ states; a doublet at $4622, 4627$ Å from the $S = 0, L = 0$ state to the $S = 1, L = 1$ states (one transition doesn't occur) and finally a 8727 Å singlet from the $S = 0, L = 0$ state to the $S = 0, L = 2$ state.

Thus while in low temperature environments, C I may be treated as a 3-level system, winds from protoplanetary discs may reach temperatures $T \sim 10^4$ K, which corresponds to a wavelength $\lambda = \frac{hc}{k_B T} \approx 1$ μm and hence the optical transitions can be excited. It is thus important that the optical transitions are considered as coolants so a 5-level system encompassing all the terms in the ground configuration is necessary for winds. O is another important atomic coolant: O I has a low energy triplet and two higher energy singlets and O II has a low energy singlet and two higher-energy doublets in their respective ground configurations - both should therefore be treated with 5-level systems.

Previous photoevaporation simulations have varied in their treatment of fine structure lines. Nakatani et al. (2018a) include cooling from O I as a 5-level system and from C II as a 2-level system. Wang & Goodman (2017) include only a select few following Tielens & Hollenbach (1985): all relatively low-energy transitions in the IR which are excited at fairly low temperatures, making them the dominant coolants at the modest temperatures of a photodissociation region (PDR), which is a reasonable description of the underlying disc only. As argued above, this will be insufficient at wind temperatures when optical lines (particularly the O I 6300 Å) can be excited. The set of atomic collisionally excited lines used by MOCASSIN (used by Owen et al., 2010; Picogna et al., 2019; Ercolano et al., 2021; Picogna et al., 2021) is by far the more extensive as it is based on atomic data tables from CHIANTI (Dere et al., 1997; Landi et al., 2006) (though as noted by Wang & Goodman, 2017, some species including neutral sulfur are missing from its database).

3.2.3 Cooling from Molecular Rovibrational Lines

Molecules have extra degrees of freedom associated with the positions of each atom; under the Born-Oppenheimer approximation, the Hamiltonian describing their energy can be split into not only electronic motions about nuclei as in atoms, but also oscillations of the nuclei about the equilibrium bond length, and solid-body rotations of the molecule. This leads to a rich spectrum of vibrational and rotational transitions as well as electronic transitions analogous to those of atoms.

The typical spacing of vibrational energy levels is $\lesssim 0.5$ eV (corresponding to $\lambda \gtrsim 2\ \mu$m) and that of rotational energy levels $\lesssim 0.1$ eV (corresponding to $\lambda \gtrsim 10\ \mu$m). This leads to a hierarchy of *band systems* corresponding to transitions between electronic states, within which there are several *bands* corresponding to vibrational transitions each containing individual *lines* due to rotational transitions. For H_2, the band systems corresponding to the first and second excited electronic states consist of the Lyman bands and Werner bands respectively. However, H_2 lacks a permanent dipole meaning that its purely rovibrational transitions are forbidden and hence slow, making it a poor coolant compared to CO and H_2O.

It would usually be impractical to include every line individually in a thermochemical code so instead fits to the total cooling rates from all bands are typically used. For example, Neufeld & Kaufman (1993) tabulate fits for the total cooling rate

$$L = \left(\frac{1}{L_0} + \frac{n_{H2}}{L_{LTE}} + \frac{1}{L_0} \left[\frac{n_{H2}}{n_{1/2}} \right]^{\alpha} \left(1 - \frac{n_{1/2} L_0}{L_{LTE}} \right) \right)^{-1} \tag{3.1}$$

where the parameters are functions of temperature and column density, thus capturing the optically thin, effectively thin and optically thick regions. L_0 is the low-density limit, while the high-density (LTE) limit is given by $L = L_{LTE}/n_{H2}$. In a two-level system, these terms would be sufficient to be exact; the final term approximates the more gradual, transitional behaviour at intermediate densities in multi-level systems (where many lines contribute and reach LTE progressively at different densities). This fit is designed to be exact in both the high- (LTE) and low-density limits as well as at the average critical density, and the fractional error at other densities is nearly always $< 10\%$.

Wang & Goodman (2017) use Neufeld & Kaufman (1993)'s parametrizations of H_2, H_2O, OH and CO cooling, while Nakatani et al. (2018a) treat only H_2 and CO following Galli & Palla (1998) and Omukai et al. (2010) respectively.

3.2.4 Thermal Equilibrium in X-ray Heated Regions

Assuming that all X-ray radiation absorbed goes into heating the gas, the heating rate per unit volume can be written in terms of the geometrically diluted and attenuated X-ray flux, local gas density, n and photoionisation cross-section, σ_ν:

$$\Gamma_\nu = f_\mathrm{X} F_\nu n \sigma_\nu \tag{3.2}$$

$$F_\nu = \frac{L_\nu}{4\pi r^2} e^{-N\sigma_\nu}, \tag{3.3}$$

For these purposes we may assume that σ_ν is independent of temperature (though in practice it depends weakly on temperature through the gas' ionisation equilibrium). We include a factor f_X to represent the X-ray heating efficiency: as discussed in the introduction, the photoelectron energy is partially lost to effects including collisional ionisation and excitation before it can thermalise (Maloney et al., 1996; Shull & van Steenberg, 1985). The photon's energy is also partially used overcoming the ionisation energy of each photoelectron (of which the Auger effect may produce several).

Most atomic coolants have critical densities on the order of 10^6 cm^{-3}, on the order of maximum wind densities. Therefore, cooling through collisional excitation mostly happens as a two-body process, with each collision resulting in radiative de-excitation. The cooling rate per unit volume for each transition can be written as $n^2\Lambda_{n,i}(T)$ (where the subscript n here indicates that Λ is per particle per number density), and hence the total cooling rate is of the same form $n^2\Lambda_n(T)$ ($\Lambda_n(T) = \sum_i \Lambda_{n,i}(T)$).

Assuming radiative thermal equilibrium, we may equate the heating (integrated over frequency) and cooling, and rearrange to find

$$\Lambda_n(T) = \frac{f_X}{4\pi}\frac{L_\mathrm{X}}{nr^2}\int \frac{L_\nu}{L_\mathrm{X}}\sigma_\nu e^{-N\sigma_\nu}\mathrm{d}\nu = \frac{f_X \xi}{4\pi}\int \frac{L_\nu}{L_\mathrm{X}}\sigma_\nu e^{-N\sigma_\nu}\mathrm{d}\nu, \tag{3.4}$$

where we demonstrate that this expression can be written using the ionisation parameter (Tarter et al., 1969; Owen et al., 2010):

$$\begin{aligned} \xi &= \frac{L_\mathrm{X}}{nr^2} \\ &\approx 10^{-3}\frac{L_\mathrm{X}}{2\times 10^{30}\ \mathrm{erg\ s^{-1}}}\left(\frac{n}{10^5\ \mathrm{cm^{-3}}}\right)^{-1}\left(\frac{r}{10\ \mathrm{au}}\right)^{-2}\ \mathrm{g\ cm^3\ s^{-3}}; \end{aligned} \tag{3.5}$$

the second line normalises to the typical L_X of a solar-mass star, the maximum density of an EUV wind (Equation 1.25) and r_G for a 10 km s^{-1} photoevaporative wind in the solar mass case - EUV winds can therefore access $\xi \gtrsim 10^{-3}$.

By inverting the relationship expressed in Equation 3.4, one can see that at a given column density (Picogna et al., 2019) and for a particular spectrum (Ercolano et al., 2021), we can find the temperature as a function of the ionisation parameter $T = T(\xi; N, L_\nu/L_\mathrm{X})$. This allows one to precompute the relationship between the two variables, which can then be used in hydrodynamical simulations - where in each cell the distance r and density n are known - to determine the temperature at a given L_X. This is inexpensive compared to conducting radiative transfer and calculating thermochemical balance on the fly, so was the approach adopted by previous X-ray photoevaporation studies (Owen et al., 2010, 2011b, 2012; Picogna et al., 2019; Ercolano et al., 2021; Picogna et al., 2021), which all used MOCASSIN to provide the equilibrium $\xi - T$ relationship.

In this chapter we will be interested in determining the most important parts of the spectrum to the heating. These will be the frequencies that contribute most strongly to the frequency-dependent terms $L_\nu \sigma_\nu e^{-N\sigma_\nu}$, which depends on the contribution of each frequency to the spectrum as well as the efficiency (not to be confused with f_X) with which each frequency can heat the gas at a given column:

$$\varepsilon_\nu := \sigma_\nu e^{-N\sigma_\nu}. \tag{3.6}$$

This efficiency is maximised by radiation for which $\tau = N\sigma_\nu = 1$. More energetic radiation is more deeply penetrating (lower σ) so is simply not absorbed well enough locally to deposit much energy into the material. Conversely, less energetic radiation is more easily absorbed and so has been too strongly attenuated by the time is reaches the column N.

In the next section I will use this formalism to interpret the differences between the role of X-rays in previous works.

3.3 Disentangling the Origin of Model Discrepancies

In this section we seek to explore the impact of the methodological differences set out in the introduction. We address this by investigating whether, if we take the conditions of a low-density EUV-driven wind, an X-ray wind would result if the tools used for X-ray winds are applied to recalculate the temperatures. We therefore irradiate the Wang & Goodman (2017) density grids with MOCASSIN. Then, by varying the treatment of the cooling processes and spectrum we investigate the impact of any modelling decisions made in each.

Firstly, the approach to radiative transfer and thermal equilibrium differs between the works in a way that we cannot test with MOCCASIN. Wang & Goodman (2017) conducted radial ray tracing to calculate an attenuated flux in each cell in their simulations using the optical depth provided by a range of photoreactions. This process ignores the potential for scattering of radiation, the diffuse EUV field produced by recombinations, and the ability of these processes to change the frequency of radiation. However, it provides a relatively inexpensive way of estimating the radiation field, allowing them to avoid assuming thermal equilibrium but instead update the ionisation states of material and perform photoionisation heating (and radiative cooling) after each hydrodynamical timestep. That is to say, the thermal evolution of the disc/wind material is calculated by operator splitting, with atomic and molecular heating/cooling in one substep, and the hydrodynamical terms - adiabatic cooling by PdV work and advection of thermal energy (hereafter collectively hydrodynamical cooling) - in the other.

Conversely, MOCASSIN adopts a Monte Carlo approach closely following Lucy (1999) to calculating the radiation fluxes. A number of packets of fixed energy (each representing a large number of photons, avoiding the expense of following them individually) are released into a fixed density grid at frequencies randomly sampled from the input spectrum. A key feature of the Lucy (1999) algorithm is that the absorption of energy packets is checked on a cell-by-cell basis by randomly drawing an optical depth (assuming that cumulative distribution function $1-e^{-\tau}$ is uniformly sampled) and absorbing the packet only if this is smaller than the optical depth across the cell. This approach provides a vast speed-up over the main alternative, which is to similarly draw an optical depth to absorption but then determine the distance at which this absorption occurs, as it avoids repeatedly calling the bisection algorithm locating the cell containing the point of absorption. Unabsorbed packets are moved to the cell boundary and a new optical depth to absorption sampled; as the expected path to absorption is always the same, this repeated sampling introduces no bias. If the packet is absorbed in the cell, it is then re-emitted in a random direction at a frequency randomly sampled from the local emissivity (according to the current temperature and ionisation balance), but with the same total energy (therefore now representing a different number of photons). This process inherently conserves energy in the radiation packets and so requires an assumption of thermal equilibrium between radiative heating and cooling processes. This second key feature of the Lucy (1999) algorithm also helps make it faster than alternative methods, where the *energy* of the packet is determined by the local temperature, which only conserve energy once equilibrium has been reached. Finally, once the packets have passed through the grid, the local radiative intensity can be estimated. To account for potentially complicated 3D geometries, this step also follows Lucy (1999) and derives the radiation field from the energy density by considering the time that the energy packets of each frequency spend on path segments passing through the volume contained by the cell (rather than from a measure of the flux through a particular surface). The temperature and ionisation balance in each cell are then updated iteratively until they result in equal local heating and cooling rates. The whole procedure - releasing packets into the grid, following their absorption and re-emission, estimating the radiation field, and finding corresponding equilibrium temperatures and ionisation balances - is iterated until the solution converges. Although MOCASSIN was benchmarked against various problems, this doesn't guarantee its accuracy for our problem of interest, particularly given that it necessarily ignores hydrodynamic contributions to the thermal balance.

Another unique aspect of Wang & Goodman (2017) was their discrete spectrum. They use just 4 bands at 7 eV, 12 eV, 25 eV and 1000 eV - to represent FUV, FUV in the Lyman/Werner bands, EUV and X-ray respectively - with the luminosities of each chosen following Gorti & Hollenbach (2009). Although these values sound like sensible averages compared to a full spectrum (e.g. Ercolano et al., 2009) it is unclear a) whether using just the four bands to span the whole spectrum is sufficient to resolve the true behaviour (compared to MOCASSIN's 1396 energy bins spanning 11.27 eV to 12 keV), and b) if so, whether these really are a sensible choice. We will show that in fact the results are very sensitive to the energy of the X-ray bin in particular.

A final difference is that the density grid used by Wang & Goodman (2017) uses a larger inner boundary of 2 au compared to the works favouring X-ray photoevaporation which use 0.33 au. This could potentially be important if there is significant attenuation of the EUV at $\lesssim 2$ au. Nakatani et al. (2018b), who use an inner boundary of 1 au, report that varying their inner boundary to as little as 0.1 au made little difference to the heating and ionization rates in the outer disc as there was not sufficient shielding by the inner regions of the disc and its atmosphere. However, while this is therefore unlikely to drive a difference between previous works, attenuation by material closer to the star than the inner boundary, for example accretion columns, remains possible and could affect the spectrum irradiating the disc and wind (e.g. Alexander et al., 2004a).

3.3.1 Models

We carry out radiative transfer in MOCASSIN with conditions designed to replicate the approach of Wang & Goodman (2017) within its existing framework. The simulations are each labelled in the form K_Cooling representing the combination of a certain spectrum 'K' with a certain cooling model. The temperatures are completely calculated by MOCASSIN using its iterative proceedure i.e. unlike some previous works (e.g. Owen et al., 2010), we do not fix them to dust temperatures from D'Alessio et al. (2001) at high column densities. Each model was run for eight iterations with 10^9 photons and a final ninth iteration with 10^{10} photons, at which point they had all converged.

For each model we irradiate the same density profile for the wind and underlying disc derived from the fiducial model of Wang & Goodman (2017) and shown in Figure 3.1. Since MOCASSIN only accepts Cartesian grids, we interpolated onto a non-uniform Cartesian grid (designed to provide more resolution at smaller radii, as with the logarithmic grid of Wang & Goodman, 2017). The total grid is 321×321 cells, of which 97724, with radii spanning $r = 2 - 100$ au, are active.

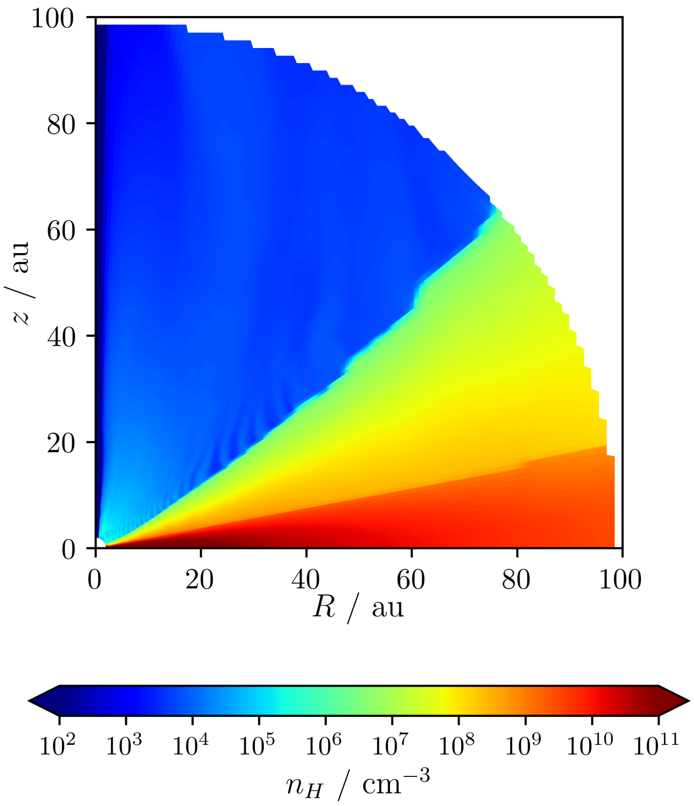

Fig. 3.1 The interpolated density profile from Wang & Goodman (2017) used for our calculations with MOCASSIN.

Table 3.1 Luminosity by band and associated energy for each spectrum tested. Units are ergs s^{-1}. The spectra are all discrete with a single energy bin per band (listed in brackets) except for E, which is continuous - in these cases the listed luminosity is that integrated over the range indicated.

Key	W	U	S###	E	X###
Description	Fiducial	UV only	Soft X-ray	Continuous	High L_X
Soft FUV	5.04×10^{31}	5.04×10^{31}	5.04×10^{31}	-	5.04×10^{31}
	(7 eV)	(7 eV)	(7 eV)		(7 eV)
Lyman-Werner	3.07×10^{29}	3.07×10^{29}	3.07×10^{29}	1.6×10^{31}	3.07×10^{29}
	(12 eV)	(12 eV)	(12 eV)	(11.27-13.6 eV)	(12 eV)
EUV	2×10^{31}	2×10^{31}	2×10^{31}	2×10^{31}	2×10^{31}
	(25 eV)	(25 eV)	(25 eV)	(13.6-100 eV)	(25 eV)
X-ray	2.56×10^{30}	-	2.56×10^{30}	1.6×10^{31}	1.6×10^{31}
	(1000 eV)		(### eV)	(100-12000 eV)	(### eV)

Spectra

For our fiducial model, we replicate the spectrum of Wang & Goodman (2017). We set the nearest frequency bin in MOCASSIN to have the same luminosity and all other bins to be zero. Note though that unlike in Wang & Goodman (2017), since MOCASSIN re-emits energy packets after interactions with atoms or dust, there will be secondary radiation at other energies. Since it follows Wang & Goodman (2017) we label this spectrum with the key **W**; its luminosity in each band is listed in Table 3.1. The X-ray luminosity L_X is similar to the median value for T Tauri stars (Preibisch et al., 2005; Güdel et al., 2007a).

In Section 3.3.2, we also consider several other spectra, including one with no X-ray and only UV (**U**), several with softer X-ray energy (**S###** where ### is the energy in eV from 100 to 900 in steps of 100), and the Ercolano et al. (2009) spectrum FS0H2Lx1 (**E**), which is a continuous spectrum (as opposed to the rest which all contain only discrete frequencies). We normalise spectrum E to have the same EUV luminosity to control for the location of the ionisation front; as a result it has higher FUV and X-ray luminosities than the other spectra. To allow us to isolate the effects of increased X-ray luminosity from X-ray spectral shape, we thus also consider discrete spectra with the X-ray luminosity enhanced by a factor 6.25 to match that of spectrum E (**X###**). All these spectra are also summarised in Table 3.1.

Cooling

We present simulations for two cooling models which we summarise in Table 3.2:

Table 3.2 Summary of radiative cooling processes included in our cooling models versus Wang & Goodman (2017).

Process	Full	IRFLNoH	Wang & Goodman (2017)
Lyman Alpha	Yes	No	Yes (escape probability)
Metal CELs	Yes	Yes (>10 μm only)	[C II] 158 μm, [O I] 63 μm, [S I] 25 μm, [Si II] 35 μm, [Fe I] 24 μm, [Fe II] 26 μm
Recombinations	Yes	Yes	Yes
Molecules	No	No	H_2, OH/H_2O and CO rovibrational

- **Full**, which includes all the mechanisms inherent to MOCASSIN. We also added atomic data for S I and the first 30 energy levels of Fe II (enough to include the most accessible states) from CHIANTI (Dere et al., 1997, 2019) so that collisionally excited forbidden line radiation (CELs) from these species is included, in particular the transitions producing the [S I] 25 μm and [Fe II] 26 μm lines included by Wang & Goodman (2017) (though they only found the former to be particularly significant).
- **IRFLNoH**, in which the only forbidden lines included are those longward of 10 μm - in order to eliminate cooling from optical and near infrared lines which Wang & Goodman (2017) did not model - and in which the cooling by the Lyman alpha and beta lines is also turned off in order to mimic a low escape fraction.

We expect the Full cooling to be a better representation of the physical reality, while the more restricted IRFLNoH is an exercise designed to bring the MOCASSIN treatment closer to that of Wang & Goodman (2017). Nevertheless, both models still exclude some processes - in particular molecular cooling and hydrodynamical cooling - which are not implemented within MOCASSIN. We discuss the potential impact of these in Section 3.3.4.

Dust and Gas Composition

We use include the same elements and abundances considered by Wang & Goodman (2017)[1], with all other elements set to zero. For the elements that overlap with Ercolano et al. (2009) (H, He, C, O, Si, S) the abundances are identical; in addition Wang & Goodman (2017) include Fe but not N, Ne or Mg. There can be reasonably significant, observable, emission

[1] $\mathrm{He/H} = 0.1$, $\mathrm{C/H} = 1.4 \times 10^{-4}$, $\mathrm{O/H} = 3.2 \times 10^{-4}$, $\mathrm{Si/H} = 1.7 \times 10^{-6}$, $\mathrm{S/H} = 2.8 \times 10^{-5}$, $\mathrm{Fe/H} = 1.7 \times 10^{-7}$.

from the omitted elements: we tested the difference including them would make to our results, ultimately finding it made qualitatively little difference to the overall conclusion.

Assuming an atomic/ionic composition, the gas' mean molecular weight μ can be calculated as

$$\mu = \frac{\sum_i m_i A_i}{\sum_i A_i + n_\mathrm{e}/n_\mathrm{H}}, \tag{3.7}$$

where m_i are the atomic masses relative to hydrogen, A_i are the atomic abundances relative to hydrogen and $n_\mathrm{e}/n_\mathrm{H}$ is the ratio of the free electron density to the hydrogen density. For a neutral atomic gas of our adopted composition, $\mu = 1.287$, though the value can be lower in regions of significant ionisation.

We assume a single grain population of 5Å and dust-to-gas mass ratio of 7×10^{-5}, with the "Car_90" composition from MOCASSIN's library of dust datafiles which represents a neutral carbon grain in the form of a PAH/graphitic solid, the closest available to the PAH assumption of Wang & Goodman (2017).

3.3.2 The Importance of Optical Coolants - A Practical Demonstration

We first demonstrate the effect of the two cooling models on the resulting temperature profiles when we employ the same input spectrum (i.e. EUV, FUV and 1000 eV X-rays). In Figure 3.2 we therefore show the temperature structure, and the error compared to Wang & Goodman (2017), for the W_Full and W_IRFLNoH models. Based on the penetration of different radiation (indicated by the dot-dashed lines) we can then delineate the resulting temperature structure into three broad regions - the wind, the warm disc and the cold disc - which we discuss in turn before demonstrating how we use the temperatures to determine where a wind can be launched.

In the models of Wang & Goodman (2017), the wind and disc are divided by an ionisation front (IF) where a sharp density contrast is seen (Figure 3.1). The locations of our IFs agree well with Wang & Goodman (2017), indicating that the Monte Carlo radiative transfer solution by MOCASSIN is consistent with the ray tracing conducted by Wang & Goodman (2017). This can be seen through the penetration depth of EUV, with the $\tau = 1$ surface marked in each case with the light dash-dotted line. The EUV-driven wind's low densities and high levels of ionisation are key to allowing the EUV to reach this far, in contrast to the higher density X-ray–driven winds into which the EUV does not penetrate very far (Owen et al., 2012).

The wind region penetrated by the EUV is hot and approximately isothermal: for the Full cooling model at around 10^4 K and for the IRFLNoH cooling model at around 3×10^4 K. The latter model yields temperatures that are close (within around 30%) to those obtained by

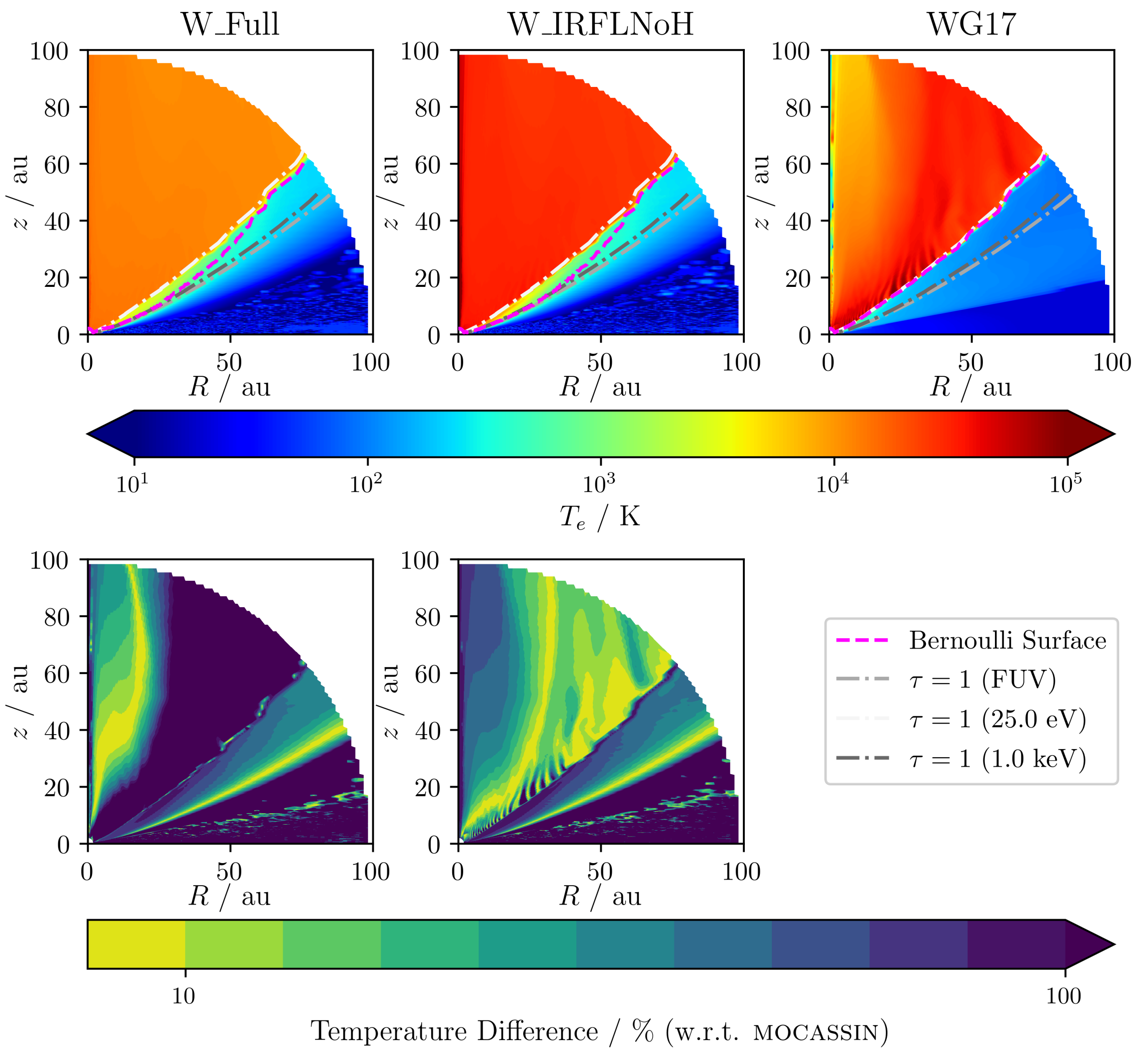

Fig. 3.2 Comparison of the temperature structure obtained using MOCASSIN with that of Wang & Goodman (2017). The left-most column shows the full cooling model, while the central column shows the restricted 'IRFLNoH' model in which cooling from Lyman lines and optical/NIR collisionally excited lines are turned off. The top row shows the temperatures, while the second row illustrates the percentage difference between the fiducial model of Wang & Goodman (2017) and our simulations. In the bulk of the wind region the IRFLNoH cooling model has smaller temperature differences as indicated by the lighter colours. The pink dashed line indicates the surface where the Bernoulli function becomes positive while the dot-dashed lines (clockwise from the z axis) are the $\tau = 1$ surfaces for EUV, X-ray and FUV respectively.

Wang & Goodman (2017); this is as expected given that the model omits cooling processes also omitted by Wang & Goodman (2017). We also tried to achieve agreement with the hot temperatures of Wang & Goodman (2017) by more measured means such as removing only a) the Lyman lines, b) certain metals or c) even individual lines from the cooling, but only the IRFLNoH model containing a total lack of NIR/optical/UV coolants produced the $\sim 3\times10^4$ K wind temperatures. The cooling from the mid-far IR lines included by Wang & Goodman (2017) will largely saturate for $T \gtrsim 10^3$ K as the Boltzmann factor in the collisional excitation $\rightarrow 1$ above this point. Optical lines start to become excited as temperatures approach 10^4 K causing the cooling rate to rapidly increase here; this effectively limits the temperatures to be $\lesssim 10^4$ K. Any sufficiently strong contributor to the optical spectrum should be able to provide this limit, though they will of course be somewhat more strongly limiting when several such lines act in concert. Hence, the 3×10^4 K temperatures of Wang & Goodman (2017) require the absence of all effective optical coolants to produce.

However within $R \lesssim 20$ au and at $z \gtrsim 20$ au, we see that Wang & Goodman (2017) find a cooler lobe of temperatures much closer to the 10^4 K of the Full Model. We suggest in Section 3.3.4 that the origin of these cooler temperatures is adiabatic cooling which is neglected in our (radiative equilibrium) models.

In principle hotter wind temperatures could act to make the wind more highly ionised and therefore more transparent to radiation. However we find little impact on the location of the ionisation front as the wind is already very highly ionised; moreover it is primarily photoionised rather than thermally ionised so the hotter temperatures make little difference to its transparency.

The X-ray and FUV penetration depths are sufficiently large that any modification to the neutral column in the EUV-heated wind region will have negligible effect on the volume they can heat; therefore beyond the ionisation front both simulations have broadly the same appearance. First we come to a warm ~ 1000 K region heated by both FUV and X-ray. We see that this region is generally warmer than it was found to be by Wang & Goodman (2017) by a few 100 K; this implies our models either have some additional heating or are missing some cooling - we suggest in Section 3.3.4 that this is likely the result of molecular cooling. There is little difference between the cooling models as these temperatures are not generally warm enough to significantly excite the optical lines that are turned off in the IRFLNoH model.

The soft FUV has an opacity largely dominated by dust absorption (Figure 1.2), and for the grains in question, can penetrate a column of roughly 2×10^{22} cm^{-2}, while the high energy 1 keV X-rays can reach around 10^{22} cm^{-2}. Therefore, the FUV and X-ray reach similar depths. Beyond this point the temperatures appear to decline and tend towards better agreement with Wang & Goodman (2017). The disc midplane is dark to all the bands of radiation included and hence cold.

In summary then, our IRFLNoH model, which turns off a number of atomic cooling channels, reasonably reproduces the temperature structure found by Wang & Goodman (2017), albeit with slightly warmer conditions below the ionisation front. However the Full model would be a more realistic description of the temperatures in the hot wind itself.

So, far we considered the effect of these coolants in the wind region itself, but what of their effect for which bands of radiation can, energetically speaking launch a wind? We can determine this using the Bernoulli function approach set out in Section 1.2.1. Following on from Equation 1.5, we can define the Bernoulli surface as the location where

$$T = T_{\mathrm{Bern}} := \frac{1}{5}\frac{GM_*\mu m_H}{k_B r} \approx 27600\ \mathrm{K}\left(\frac{r}{\mathrm{au}}\right)^{-1}\frac{\mu}{1.287}, \tag{3.8}$$

assuming that the wind is mainly atomic and so $\gamma = 5/3$ and where the typical value is given assuming a star of 1 $M_\odot$. We can then assess whether each cell in our simulations has a temperature exceeding T_{Bern} (using the local value of μ calculated as per Equation 3.7). Note that we are not saying that the wind's temperature must follow a $1/R$ profile (see discussion in Section 2.8.2), rather that it must just exceed it (in which case there will be a large temperature gradient near the base).

The Bernoulli surface is plotted as the magenta dashed line on Figure 3.2. In the case of Wang & Goodman (2017)'s temperature profile it lies along the ionisation front, coincident with the $\tau = 1$ surface of EUV. This is strongly indicative of an EUV-driven wind. In our simulations, for $R \gtrsim 50$ au, we also see a good agreement between these two, though the temperature gradient at this location is less sharp so there is a small difference. Within $10-50$ au, the Bernoulli surface dips down below the ionisation front, implying that in our simulations, the combination of FUV and X-ray is capable of heating the material to a hot enough temperature to drive a wind (though only at relatively low columns and not all the way down to their $\tau = 1$ surfaces). In the IRFLNoH case, this dip extends to slightly smaller radii due to the reduced cooling around the higher inner-disc T_{Bern}. Viewed another way, the innermost limit is on the order of the gravitational radius $r_G = \frac{GM_*}{c_S^2}$, which is smaller for the hotter wind temperatures. Therefore, over much of the disc the presence or lack of optical coolants shouldn't affect the ability of each radiation to launch a wind, but it will affect the wind's innermost extent.

Our MOCASSIN simulations with input spectrum matching that of Wang & Goodman (2017) thus produce thermal structures that corroborate the conclusion of Wang & Goodman (2017) that 1000 eV X-rays cannot drive a wind from the outer disc regardless of any differences in cooling processes. In the inner disc, the simulations indicate a possible minor role for FUV/X-ray wind launching but the Bernoulli surface is only modestly below the ionisation front. Therefore, we should next also explore what role how Wang & Goodman (2017) treated the X-ray spectrum plays in producing these results.

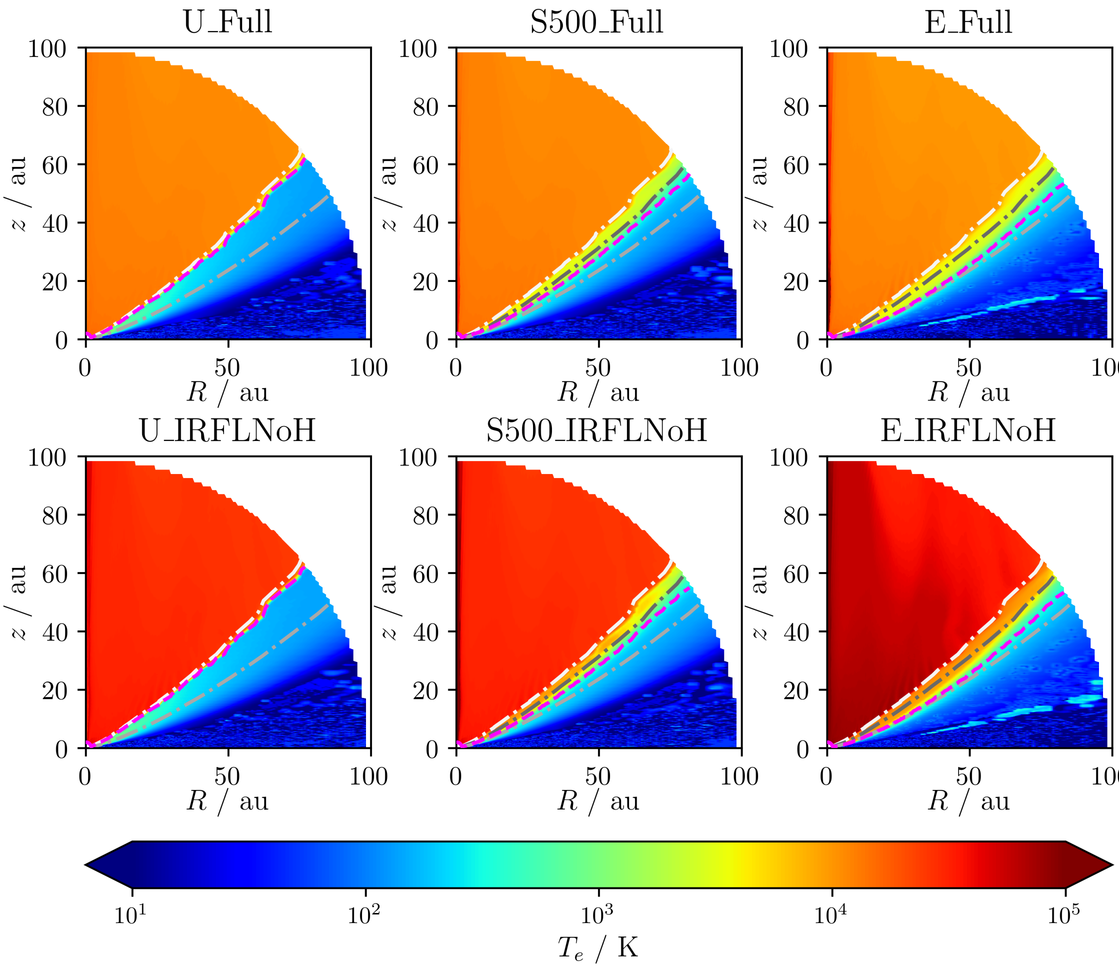

Fig. 3.3 Comparison of the temperature structure obtained for different combinations of spectrum and cooling model. From left to right: the UV-only spectrum, a spectrum with 500 eV X-ray and the spectrum of Ercolano et al. (2009). In each case the pink dashed line indicates the surface where the Bernoulli function becomes positive while the dot-dashed lines represent $\tau = 1$ surfaces for EUV, 500 eV X-ray and FUV.

3.3.3 The Importance of X-ray Frequency

Before exploring different X-ray frequencies, we first run a pair of simulations with the X-rays removed that is UV-only (simulations U_Full and U_IRFLNoH) as a control and present their temperature profiles in the first column of Figure 3.3.

Removal of X-rays makes fairly little difference to the overall picture of a 10^4 K (3×10^4 K) wind for the Full (IRFLNoH) cooling model. Conversely, we see cooler temperatures below the ionisation front, with the remaining heating provided mainly by FUV photoionisation of carbon. The difference to the fiducial simulations confirms the role of X-ray photoionisation heating in this region in our earlier models. Nevertheless while closer to those found by Wang & Goodman (2017), the temperatures are still a little too hot, strengthening the argument for missing coolants in that region (as opposed to say, uncertainties in X-ray heating efficiency). These temperatures are, however, sufficiently low that the Bernoulli surface no longer dips down but follows the ionisation front at all radii. Therefore at these luminosities, FUV alone cannot drive a wind from below the ionisation front. That said, a higher FUV luminosity (e.g. Nakatani et al., 2018a,b), different FUV spectrum, different assumptions about the dust properties, or inclusion of pumping of H_2 may allow for more significant FUV heating, potentially sufficient to launch a wind. PRIZMO, which I set out in the next section, will allow us to explore the role of FUV more thoroughly.

Now we proceed to vary the X-ray energy from 100 eV to 900 eV in steps of 100 eV to determine the impact of the choice of a single X-ray energy on wind driving. We thus keep the luminosity constant while doing so. In the second column of Figure 3.3 we depict the temperature structure for the runs with 500 eV which present the largest contrast with the 1 keV results discussed hitherto. For both of our cooling models, X-rays of this energy can clearly heat material comfortably below the ionisation front to escape and thus drive a wind from all radii. It is therefore clear that the choice of X-ray frequency is a key parameter affecting whether X-rays can heat material beyond the EUV ionisation front sufficiently to drive a wind.

We quantify the effectiveness of the X-ray band in each S### simulation by determining the radial H I column density to the Bernoulli surface at 4 representative radii. We plot these values as a function of X-ray energy as the solid lines in Figure 3.4. In addition, the triangles of corresponding colour (plotted at 25 eV) mark the column at the Bernoulli surface at the same radii in our UV-only simulations and the circles (plotted at 1000 eV) likewise for Wang & Goodman (2017)'s fiducial model.

Firstly, observe that the Bernoulli surface in our UV-only simulations, despite lying very close to that of Wang & Goodman (2017), has a much higher column by up to $\sim 10\times$ at $1-5\times10^{20}$ cm^{-2} than found for the Wang & Goodman (2017) temperatures where it lies at

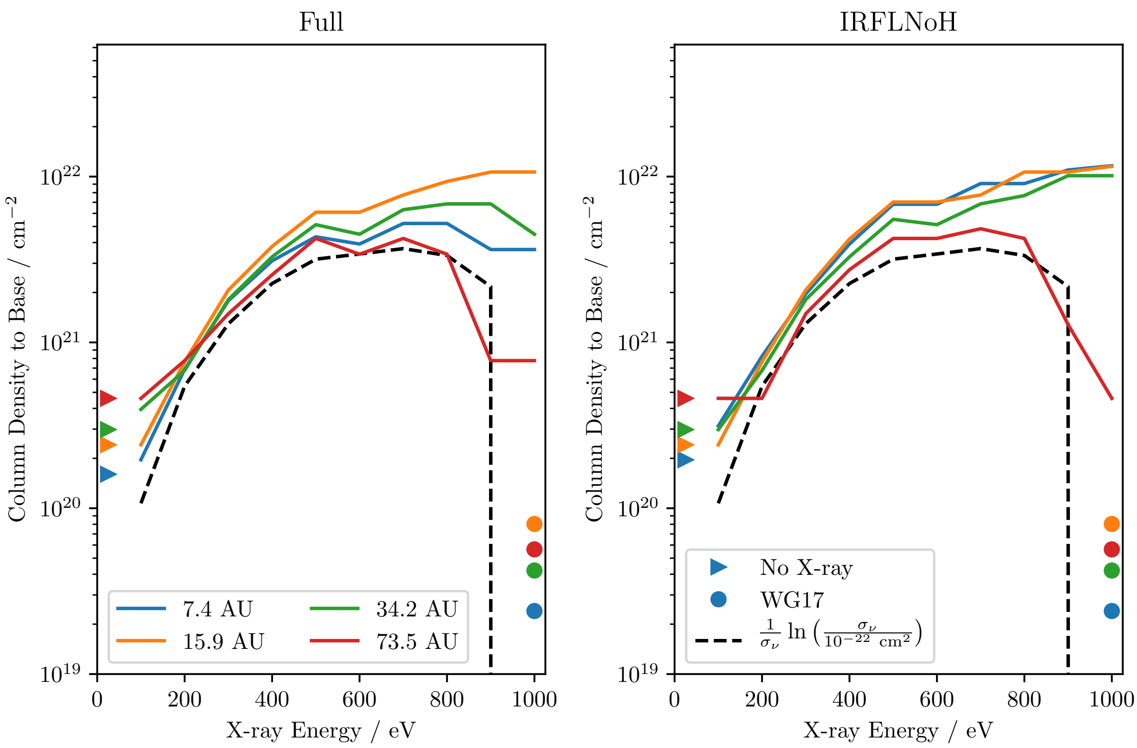

Fig. 3.4 The H I column to the Bernoulli surface for each energy of X-ray at selected radii (solid lines). Simulations with the Full cooling model are shown on the left-hand panel and the IRFLNoH cooling on right. In each case, the triangles and circles represent the corresponding values for the UV-only spectrum and Wang & Goodman (2017)'s temperature field respectively. The dashed line is equation (3.10) for $\varepsilon_c = 10^{-22}$ cm^2.

$2-8\times10^{19}$ cm^{-2}. The origin of this behaviour is that our UV-only simulations are hotter below the base than found by Wang & Goodman (2017). Although this effect is small enough that the Bernoulli temperature is reached at only a very a slightly lower height below the IF, since the base is only mildly flared, photons reach it at a very glancing angle - the distance travelled below the IF at $n_{\mathrm{H\,I}} \sim 10^6$ cm^{-3} is thus considerable.

Above 800 eV, the X-rays cannot heat a greater column at large radii than the UV alone. Moreover, for all radii, at the lowest energies, the column heated by the X-ray is not much greater than the EUV as these frequencies are quite strongly absorbed. The most effective choices for a single X-ray energy that will heat the largest column are those in the range $500-700$ eV, depending slightly on the radius in question.

The choice of cooling model makes fairly little qualitative difference to these results at most radii because the cooling rates between them are not so different for typical values of T_{Bern}. The biggest difference between the two panels of Figure 3.4 is seen for 7 au where $T_{\mathrm{Bern}} \approx 4000$ K is high enough for the omission or inclusion of atomic cooling channels to start to affect the temperature attained. For the higher X-ray energies, this affects the column to which they can penetrate and still heat to escape. This suggests that while the low energy X-rays are limited by their attenuation, the high energies are limited by the cooling. However, the (non-)inclusion of optical forbidden line cooling will only enter into this consideration at the smallest radii (which contribute only modestly to $\dot{M}$).

Thus we conclude that forbidden line cooling and Ly α (and β) cooling is not an important factor in determining the feasibility of X-ray–driven mass loss, despite being important for obtaining the correct temperatures in the wind itself. Instead we conclude that the limited role for X-rays relative to UV in the simulations of Wang & Goodman (2017), predominantly reflects the fact that 1000 eV X-rays are too hard - and so interact too weakly with the disc gas - to heat it sufficiently to drive a wind on their own, regardless of the differences in cooling processes.

Explanatory Model

In Section 3.2.4 we explored how thermal equilibrium is established in X-ray-heated regions. Since we consider only one X-ray frequency, we now take $L_\nu/L_\mathrm{X} = \delta(\nu-\nu')$.

Assuming that $\Lambda(T)$ is a monotonically increasing function of T, then the requirement that $T \geq T_\mathrm{Bern}$ in the wind gives us a requirement on the minimum total cooling - and hence in thermal equilibrium - the minimum total heating. Using Equation 3.4, this can be turned into a requirement on the X-ray efficiency (Equation 3.6):

$$\varepsilon_\nu \geq \varepsilon_c := \frac{4\pi\Lambda_n(T_\mathrm{Bern})}{f_X\xi}. \tag{3.9}$$

Given the X-ray luminosity L_X, stellar mass M_*, radius r, local density n and information about the ionisation states of each element (which controls $\Lambda(T)$ and f_X), we can determine a value for ε_c at each location in the density field. The X-ray luminosity, cooling rate and heating fraction have degenerate impacts on ε_c, and so each may be changed to similar effect. We discuss the first two in more depth in Sections 3.3.3, and 3.3.4 respectively.

From the definition of the efficiency, we can solve for the maximum column that radiation of a single frequency can heat to the required temperature

$$N_\mathrm{max} = \frac{1}{\sigma_\nu}\ln\left(\frac{\sigma_\nu}{\varepsilon_c}\right). \tag{3.10}$$

A necessary condition to have an X-ray wind is therefore that $N_\mathrm{max} > 0$, in which case our single choice of frequency must have $\sigma_\nu > \varepsilon_c$ since otherwise even completely unattenuated radiation of that frequency could not heat the wind. This imposes an lower bound on σ_ν and thus an upper bound on the X-ray energies that can heat the gas to the escape temperature. We thus see that indeed the high energy X-rays are prevented from launching a wind at $T_{\rm Bern}$ or above as they interact with gas too weakly and therefore heat it too inefficiently to overcome the expected cooling.

The highest column (at fixed ε_c) is heated by radiation with $\sigma_\nu = e\varepsilon_c$, such that $N = 1/\sigma_\nu = 1/(e\varepsilon_c)$. At larger still values of σ_ν, the column heated is moderately larger than $1/\sigma_\nu$ ($\tau \gtrsim 1$), but is nevertheless a decreasing function of σ_ν as the column that radiation can heat is strongly limited by its attenuation.

Correspondingly, the optical depth at the base is $\tau = 1$ for the most efficient radiation. Since they heat inefficiently, higher energies are required to be optically thin at the base, while the lower energies will be somewhat optically thick. Therefore for radiation effective enough to drive an X-ray wind, we expect order unity optical depth at the base. This means that the temperatures around the base are not declining purely due to increasing cooling from denser material but also by a decrease in heating as the radiation is attenuated too. This means that an optically thin prescription using a single $\xi - T$ relation (e.g. Owen et al., 2012) will generally be less accurate than an attempt to account for column density or attenuation of radiation (Picogna et al., 2019).

We now determine the ε_c (Equation 3.9) along the Bernoulli surface in the UV-only models and show this as a function of radius in Figure 3.5; to allow for comparison to Wang & Goodman (2017), we use $L_{\rm X} = 2.56 \times 10^{30}$ erg s^{-1}, and since this surface more-or-less coincides with the IF, we assume completely ionised gas with $f_X = 1$. The right-hand axis equates values of ε_c with the X-ray photon energy for which ε_c equals the cross-section of neutral gas according to Verner & Yakovlev (1995); Verner et al. (1996) (as per Figure 1.2), this being the maximum energy for which heating to $T_{\rm Bern}$ would be possible in the case of no attenuation.

Except in the disc's innermost parts, the values for ε_c derived are in the range $10^{-22} - 10^{-21}$ cm^2 and reach a minimum around $10 - 20$ au. These correspond to the photoionisation cross-sections of photons in the range $400 - 1000$ eV. The shallow increase to larger radii is due to the effects of geometric dilution weakening the irradiating flux, though this is largely offset by the material being less tightly bound (with a lower $T_{\rm Bern}$ at which the cooling rates to be overcome are lower) and less dense.

Thus over much of the disc outside $\gtrsim 40$ au, 1000 eV acting alone should not be able to launch an X-ray–driven wind, though it can marginally do so around ~ 20 au. Indeed, this is what was discussed in Section 3.3.2 and illustrated in Figure 3.4 where the Bernoulli surface dips below the IF. It is likely that in practice the ability of these harder X-rays to launch a

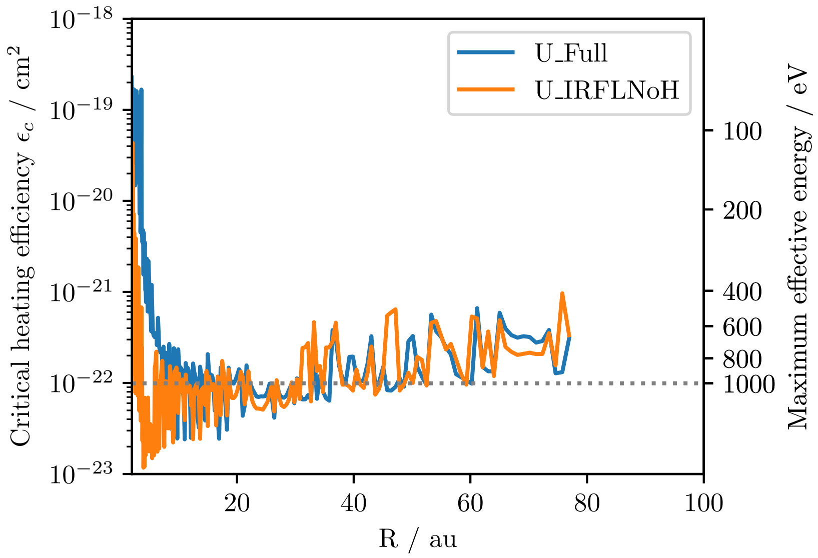

Fig. 3.5 The critical efficiency required to overcome the local cooling along the Bernoulli surface in the U_Full (blue) and U_IRFLNoH (orange) simulations as a function of radius assuming $L_X = 2.56 \times 10^{30}$ erg s^{-1} (Wang & Goodman, 2017) and $f_X = 1$. The right-hand axis calibrates this scale in terms of the X-ray energy with cross-section equal to this value - any higher energy will have too low a cross-section to achieve the required efficiency. The maximum energy that is effective on its own at this luminosity is similar between the cooling models except for the inner 20 au. 1000 eV as used by Wang & Goodman (2017) is marked with the dotted line for reference.

wind a bit beyond this was assisted by the presence of FUV which has a similar cross-section for absorption and thus is contributing to the heating at these columns.

Conversely, in the optically thin limit, energies $\lesssim 600$ eV can launch an X-ray–driven wind from the entire disc as was the case for the 500 eV example shown in Figure 3.3. Once attenuation is considered, then assuming a best-case scenario that a low efficiency of $\varepsilon_c \sim 10^{-22}$ cm^2 is sufficient, we should expect that the highest column achieved is $N \sim \frac{1}{e \times 10^{-22}\ \mathrm{cm}^2} \sim 4 \times 10^{21}$ cm^{-2} for an energy of ~ 700 eV.

Based on these results we adopt a fiducial value of $\varepsilon_c = 10^{-22}$ cm^2 and use equation (3.10) to calculate the maximum penetration depth as a function of energy, shown as the black dashed line in Figure 3.4. We can see that this excellently captures the shape, normalisation and maximum of the simulation curves. This validates our model and explains why the efficacy of wind driving is such a strong function of energy. In particular it demonstrates why 1000 eV X-rays (employed by Wang & Goodman (2017) are too weakly interacting to heat material to T_{Bern}, whereas energies of $500-700$ eV are most potent. That this model so well captures the dependence across a range of energies - which penetrate to depths with different densities and thus different associated cooling rates - despite its simplicity suggests that it is largely the attenuation of radiation that determines the base - this is in line with our earlier discussion of the assumption of optically-thin heating being insufficient.

This model also captures the small differences between the Full and IRFLNoH models. We see in Figure 3.5 that ε_c only diverges as T_{Bern} becomes larger in the inner disc (due to the reduced cooling of the IRFLNoH model at such temperatures). This makes it easier to heat a larger column and drive a significant wind at small radii in the disc, but the largest radii with the coldest T_{Bern} are essentially unaffected.

Impact on Mass-Loss Rates

We cannot directly measure mass-loss rates from our models as we have not performed hydrodynamic simulations to adapt the density and velocity fields to be consistent with our different temperatures. However since the amount of mass loss determines how much material the radiation has to pass through to reach the wind base, it is reasonable to assume that $\dot{M} \propto N$ (i.e. we are assuming that $N \propto n_{\mathrm{base}}$ and $\dot{M} \propto n_{\mathrm{base}}$).

Therefore, we would expect the higher columns in the UV-only simulations to translate into a similar factor ~ 10 boost in the mass-loss rates. We ascribe this difference to additional cooling in the model of Wang & Goodman (2017); indeed, when they produced a setup closer to Owen et al. (2010) (their OECA analog) by turning off some of this cooling, they did see a mass-loss rate that was higher by a factor of $4-5$.

Moreover, in the 1000 eV X-ray case, since they cannot heat a larger column than the EUV in the outer disc, which typically dominates the mass-loss rates, we would expect the total photoevaporation rate to be only marginally higher than an UV-only one, as observed by Wang & Goodman (2017). However, we estimate that were a single X-ray energy of ~ 500 ev used instead, it could increase the mass-loss rate by a factor $\sim 4-6$ over that found in a simulation driven by UV-only.

Exploring Different Spectra

One of the degenerate factors in Equation 3.9 was the X-ray luminosity. The spectrum of Wang & Goodman (2017) has relatively less X-ray compared to its UV flux than that of (Ercolano et al., 2009); therefore as well as the choice of the single X-ray band, the relative luminosities could also be acting to diminish or enhance the role of X-ray between these studies.

Figure 3.6 therefore shows the column density to the Bernoulli surface for each energy for our X### simulations which have 6.25 times the X-ray luminosity of the S### simulations and which therefore reproduce the ratio of $L_X/L_{EUV} = 0.8$ in the multifrequency input spectrum employed by Ercolano et al. (2009).

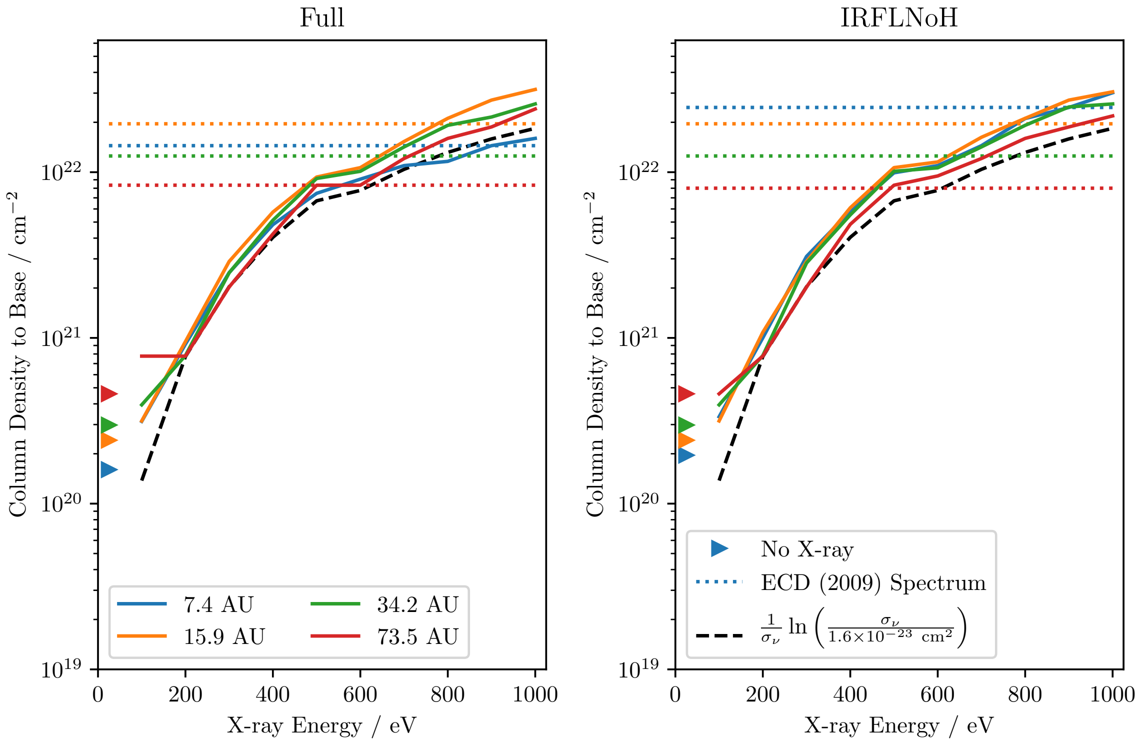

Fig. 3.6 As Figure 4 but for an increased X-ray luminosity $L_X = 1.6 \times 10^{31}$ erg s^{-1}. The coloured dotted lines are the values obtained using Ercolano et al. (2009)'s spectrum. The dashed line is equation (3.10) for $\varepsilon_c = 1.6 \times 10^{-23}$ cm^2.

At the low-energy end, where the optical depths are high, this has relatively little effect on the columns reached. Greater difference is seen as we move to higher energies, where the column no longer peaks around $500 - 700$ eV; indeed among those frequencies tested, 1000 eV was the most effective. This is in line with our explanatory model - since $\varepsilon_c \propto 1/\xi \propto 1/L_X$, then the appropriate $\varepsilon_c \sim 1.6 \times 10^{-23}$. With this lowered ε_c, our model (black dashed line) remains an excellent fit and we would expect the highest column to be reached for X-ray energy of around 1350 eV.

Thus, by making more energy available in the X-ray, the ability of X-rays, in particular the harder bands, to drive a wind can be improved. Nevertheless, the choice of frequency still has a strong effect on the outcome. Since the X-ray luminosity is an inherently variable quantity (and closely tied to the stellar mass), the notion of the most effective energy for driving the wind will be linked to stellar properties.

In reality both the EUV luminosity and X-ray luminosity are likely to vary between stars. In models of EUV-driven winds under direct irradiation, the wind densities scale with the number of ionising photons as $n_{\rm base} \propto \Phi^{1/2}$ (e.g. Hollenbach et al., 1994; Tanaka et al., 2013) which can be understood from a simple Strömgren-volume approach. The ε_c to be overcome in order for X-ray to heat below the EUV-heated base therefore also scales as $\Phi^{1/2}$; thus we could get the same result as here by lowering the EUV luminosity by two orders of magnitude. Moreover if the X-ray luminosity scales more strongly than $\Phi^{1/2}$ (as found by Chadney et al., 2015; King et al., 2018), then ε_c becomes a decreasing function of $L_{\rm X}$ and so higher luminosity sources will be more likely to host X-ray-driven winds, while sufficiently low $L_{\rm X}$ would lead to EUV-driven winds; these trends would be reversed if $L_{\rm X}$ is a relatively weak function of Φ.

A simplification in the above arguments is that heating is assumed to be driven by only one frequency of radiation. A realistic X-ray spectrum would have a range of bins with different efficiencies and weights in the spectrum all working together. As an illustrative example, Figure 3.6 thus shows, as dotted lines, the column achieved by Spectrum E at each radius.

The heated column is somewhat intermediate between that at low energies and 1000 eV since more energy is present in the effective bands than in the most soft extremes but it is not all concentrated there. Spectrum E nevertheless heats a substantially higher column than any of the monochromatic spectra in our S### series (see Figure 3.4). This is mainly because the spectrum of Ercolano et al. (2009), when normalised to the same EUV flux, has almost an order of magnitude higher X-ray luminosity than Wang & Goodman (2017). Therefore the relatively high EUV flux may be a further key reason why Wang & Goodman (2017) did not find that an X-ray driven wind was more effective.

To quantify what we would expect for a continuous spectrum, we can generalise our explanatory model by returning to using an integral over frequency (c.f. the attenuation factor of Krolik & Kallman, 1983; Alexander et al., 2004b):

$$\varepsilon_{\rm eff}(N) := \int\limits_{E>100\ \rm eV} f_\nu \varepsilon_\nu d\nu \geq \varepsilon_c \tag{3.11}$$

where $f_\nu = L_\nu / L_{\rm X}$ and thus the effective efficiency $\varepsilon_{\rm eff}(N)$ is a flux-weighted average efficiency. We iteratively calculate $\varepsilon_{\rm eff}$ for increasingly large N until it no longer satisfies the inequality in equation (3.11); the maximum N will be our estimate of the heated column. We plot these values for each radius against against the column density to the Bernoulli surface for the E_Full and E_IRFLNoH models in the left-hand panel of Figure 3.7. There is a good agreement between the model and the true densities for most points at $\gtrsim 10^{21}$ cm^{-2} and so we conclude that our model can accurately explain full spectra.

Clearly, based on the arguments above, the most representative frequency is neither an ineffective one nor the most optimal one as much of the energy can be in less efficient bands. However, for a given combination of N and $\varepsilon_{\rm eff}$, we can ask what single frequency would produce the same efficiency at that column. There are two solutions, the lower and high energy ones having cross-sections $\sigma_1 = -\frac{1}{N}W_{-1}(-N\varepsilon_{\rm eff})$ and $\sigma_2 = -\frac{1}{N}W_0(-N\varepsilon_{\rm eff})$ where W_0 and W_{-1} are the two real branches of the Lambert W function. These energies are a function of column as higher columns will progressively attenuate the spectrum at its softer end, meaning that what reaches the base will be better approximated by harder energies.

For each radius in the simulations with spectrum E, the lower of these two energies is indicated on the right-hand panel of Figure 3.7, while the higher energy solution is generally not realistic for X-ray spectra of low-mass stars and so is not depicted. As usual, very little difference is seen between the cooling models outside ~ 10 au. The representative frequency changes with radius as the column to the Bernoulli surface changes with radius. Thus it is hard to reasonably pick a single frequency that would drive the wind everywhere with complete accuracy compared to a full spectrum. Nevertheless, for both cooling models, outside the innermost few au, the appropriate energies are always < 1000 eV, further suggesting that this choice by Wang & Goodman (2017) may not be an appropriate one anywhere. In the outer disc, the most representative energy is around 600 eV and would expected to drive an X-ray wind from the whole disc given the cooling rates assumed here.

More recent spectra as used by Ercolano et al. (2021) are somewhat softer, particularly for the lowest luminosity stars. These are therefore better represented by even softer energies from $400-800$ eV for $L_{\rm X} = 10^{31}$ erg s^{-1} to close to 100 eV for $L_{\rm X} = 10^{29} - 10^{30}$ erg s^{-1}. This may lead to less effective photoevaporation as these energies are less effective than ~ 600 eV due to their shallower penetration, though Ercolano et al. (2021) do still see a substantial X-ray–driven wind. Similarly, Nakatani et al. (2018b) used the TW Hya spectrum from Nomura et al. (2007) which is dominated by its soft X-ray excess; its representative energies should therefore be very low, which may be a factor in their result that X-rays are ineffective drivers of photoevaporation on their own.

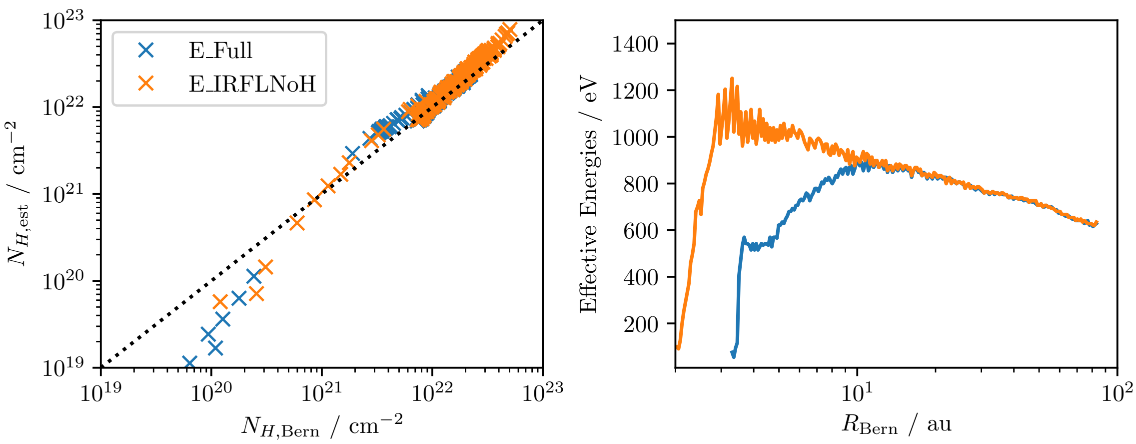

Fig. 3.7 Left: the column to the Bernoulli surface estimated from the cooling rates and spectrum using the toy model as a function of the true column to Bernoulli surface in the simulations with spectrum E - good agreement is seen especially at large columns. Right: the lower of the two energies with heating efficiency equal to the effective efficiency of the whole spectrum at the relevant column as a function of radius.

3.3.4 Discussion - Further Cooling

We have shown how the ability of harder X-rays to drive an extended wind depends on their ability to overcome the cooling at temperatures of $\lesssim 10^3$ K. We must therefore question more closely whether sufficient cooling channels are included at these energies under different approaches. To provide a baseline comparison, we first determine the dominant cooling channels (collisionally exited Lyman lines of H, collisionally excited forbidden lines of metals and recombinations, shown in Figure 3.8) in our models, before exploring the impact of the additional cooling channels discussed by Wang & Goodman (2017) as differences in methodology between their work and that of Owen et al. (2010): neutral sulfur, adiabatic cooling and molecular cooling.

For the Full cooling, the wind has fairly equal contributions to the cooling from Lyman radiation and metal CELs, with the former dominating slightly at larger radii and vice versa. Metal CELs are almost entirely responsible for cooling below the wind base, while recombinations play only a minor role in the wind and none below the base where the material is most neutral. For the IRFLNoH cooling, the Lyman lines have been switched off and play no part in the cooling. The metal CELs are still dominant below the base, but are heavily suppressed in the wind region as this contribution was largely down to optical lines. Instead, cooling in the wind is now almost entirely dominated by recombinations, which was the only significant non-adiabatic cooling found in this region by Wang & Goodman (2017) due to their cooling model.

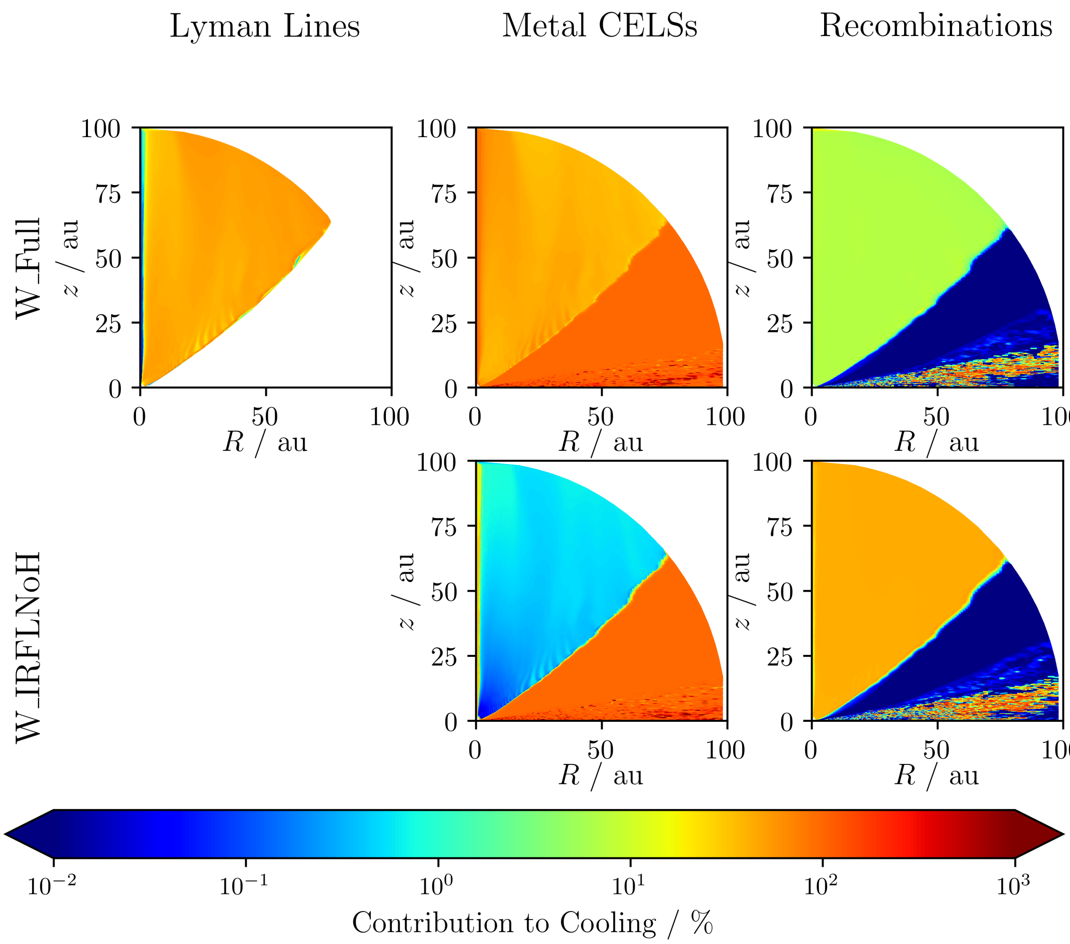

Fig. 3.8 The percentage contribution to the cooling from 3 key processes - permitted line Lyman radiation from collisionally excited H, forbidden line radiation from collisionally excited metals and recombinations - in the fiducial simulations. The top row shows the Full cooling model where cooling is dominated by Lyman lines and metal CELs. The bottom row shows the IRFLNoH model - here Lyman lines are switched off and the Metal CELs severely suppressed, increasing the role of recombinations in the wind region. Note that percentages greater than 100 are recorded near the midplane as MOCASSIN treats dust as a coolant but here it can become warmer than the gas and has a net heating effect i.e. a negative cooling contribution.

Sulfur

The coverage of infrared CELs in MOCASSIN is generally good, though the publically available version doesn't include neutral sulfur, which we added to enable a more direct comparison. This has little impact in the wind itself as the sulfur is easily ionised by the FUV to which the wind is transparent. Thus, neutral sulfur cooling only comes into play once the disc becomes optically thick to the FUV. While this is at a similar depth to penetration of 1000 eV X-rays, we expect an X-ray wind to be driven by softer frequencies and thus at lower columns. Since it was included anyway here and didn't stop X-rays launching a wind, we conclude this is not a critical cause of the differences between Wang & Goodman (2017) and Owen et al. (2010).

Moreover, the abundance of sulfur in these wind models (and therefore its contribution to cooling) may actually be overestimated. Although the ISM measurements of Savage & Sembach (1996) did not record a depletion relative to solar, it does appear to be depleted in discs (Kama et al., 2019, who propose this results from it becoming locked non-volatile FeS minerals). Consequently, although sulfur emission is also predicted to be bright in existing models (Ercolano et al., 2008b), detections of its lines is much rarer than expected (Simon et al., 2016; Fang et al., 2018; Pascucci et al., 2020).

Adiabatic Cooling

The potential for adiabatic cooling resulting from the expansion of gas was explored in Section 1.2.3. Figure 3.9 shows quantities relevant to this consideration for the W_Full simulation. Firstly, the left-most panel shows the divergence of the velocity field $\nabla \cdot \mathbf{v}$ from Wang & Goodman (2017) (since we do not recalculate this for our temperature field). Indeed over most of the wind volume, the velocity field is diverging which would result in cooling of the material. This is particularly strong in a column at $R \lesssim 20$ au as a result of a strong acceleration in the radial direction.

The net hydrodynamical cooling (adiabatic cooling less thermal advection) as a percentage of the non-adiabatic calculation from MOCASSIN (using the temperatures and cooling rates of the W_Full simulation) is shown in the middle panel of Figure 3.9. We can see that correspondingly, while in most of the volume, it can only account for around 10% of the cooling (similar to the value found by Owen et al., 2010, for material originating at $R \approx 20$ au) - making it a not insignificant (compared to recombinations) but nevertheless non-dominant contribution - adiabatic cooling is important at $R \lesssim 20$ au. This suggests that the cooler temperatures seen by Wang & Goodman (2017) in this region than in our W_IRFLNoH simulation are a result of additional adiabatic cooling. There are also a few hotspots where

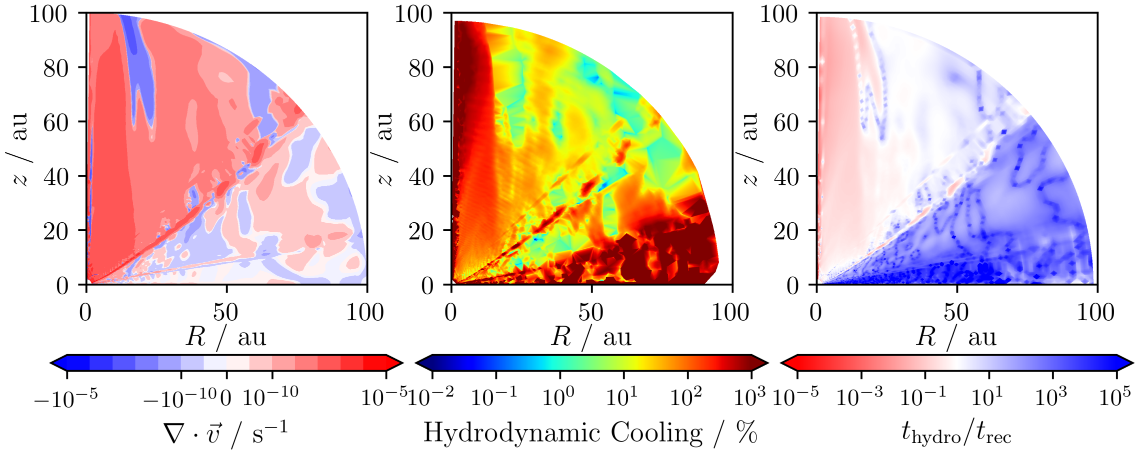

Fig. 3.9 Estimates of the significance of hydrodynamical cooling for simulation W_Full. The leftmost panel shows the divergence of the velocity grid from Wang & Goodman (2017) with diverging flows in red and converging flows in blue. The central panel shows the hydrodynamical cooling relative to the total MOCASSIN cooling expressed as a percentage. The large values near the midplane are likely an artefact of the low cooling rates there. The rightmost panel shows an estimate of the ratio between the hydrodynamic and cooling (recombination) timescales with red regions indicating shorter hydrodynamic timescales and blue indicating regions where the radiative equilibrium is reasonable to assume.

adiabatic cooling may be important near the wind base as the material is rapidly accelerated across it which may have some effect on the launching of the wind.

As a further check, the right-hand panel shows the ratio of the hydrodynamical timescale (estimated as $|\nabla \cdot \mathbf{v}|^{-1}$) and the recombination timescale ($1.5 \times 10^9 T_e^{0.8} n_e^{-1}$, which is usually the longest microphysical timescale Ferland (1979); Salz et al. (2015)). Again, the hydrodynamical timescale is around an order of magnitude longer nearly everywhere except for near the z-axis, and we can mostly safely assume radiative thermal equilibrium.

Nevertheless, these estimates of timescales are much more comparable than found by Picogna et al. (2019). On the one hand, the temperatures are a little higher here which increases the typical velocity ($c_S \propto T^{0.5}$) and hence decreases the hydrodynamical timescale, while the recombination timescale increases as the electrons are more energetic and harder to recapture. Moreover, the hydrodynamical timescale is independent of density, while the timescales of two-body non-adiabatic cooling processes are longer at the low densities of the EUV-driven density profile of Wang & Goodman (2017) compared to the higher densities in X-ray–driven winds.

We conclude that therefore the contribution from adiabatic cooling shown in Figure 3.9 probably represents an upper bound; this contribution should be less significant in the cooler, denser X-ray–driven winds which we argue should result from the use of a softer X-ray spectrum than that employed by Wang & Goodman (2017). Nevertheless, adiabatic cooling should probably be considered, particularly when modelling the inner wind regions and their tracers (e.g. O I 6300 Å Ercolano & Owen, 2016) or lower density winds (as might result at lower L_X).

Molecules

Molecules, likely to be present in the underlying disc, are the final missing piece of our model compared to that of Wang & Goodman (2017) (and also Nakatani et al., 2018b). In Section 3.3.2 we showed that irradiating Wang & Goodman (2017)'s density grids using MOCASSIN produced warmer temperatures below the IF and in Section 3.3.2 that this persisted once X-rays were removed entirely. This implies extra cooling is needed below the base to fully reproduce Wang & Goodman (2017): since sulfur is included in our models and adiabatic cooling is relatively negligible in this region the best candidate is molecular cooling; indeed Wang & Goodman (2017) find that H_2, H_2O and OH are the dominant coolants just below the base.

To demonstrate the possible effect of additional cooling, we can start by illustrating the impact of some representative increases in ε_c on the column that each X-ray frequency can heat (Equation 3.10) and which frequency is optimal for launching a wind in Figure 3.10. This shows that the curve of maximum heated column vs energy shifts down to lower columns and peaks at lower energies as ε_c is increased. An increase by a factor ~ 8 would be needed to prevent any X-ray from being able to heat a higher column than our UV-only simulations to $T_{\rm Bern}$ at large radii, and an increase by $\gtrsim 16$ would be needed to achieve this at all radii. In this limit, only very soft X-rays $200-400$ would have any significant heating effect. However, Wang & Goodman (2017) found even lower columns, which would require a larger increase in ε_c of more like $30-100\times$ to prevent any single X-ray from heating the wind. Therefore to significantly affect our conclusion about the viability of X-ray wind launching at softer energies, molecules would need to contribute at least an order of magnitude more cooling than the atomic processes here modelled.

These effects may not be uniform across all stars. Other spectra used in the recent literature (Nomura et al., 2007; Ercolano et al., 2021) are softer than those used here so the representative energies are more robust against being rendered ineffective by additional cooling since they lie in the attenuation-limited (optically thick) regime (whereas additional cooling progressively limits the effect of harder energies). Conversely, higher luminosity spectra, despite being harder, would increase ε_c and thus have an additional "head start" against the effects of additional cooling.

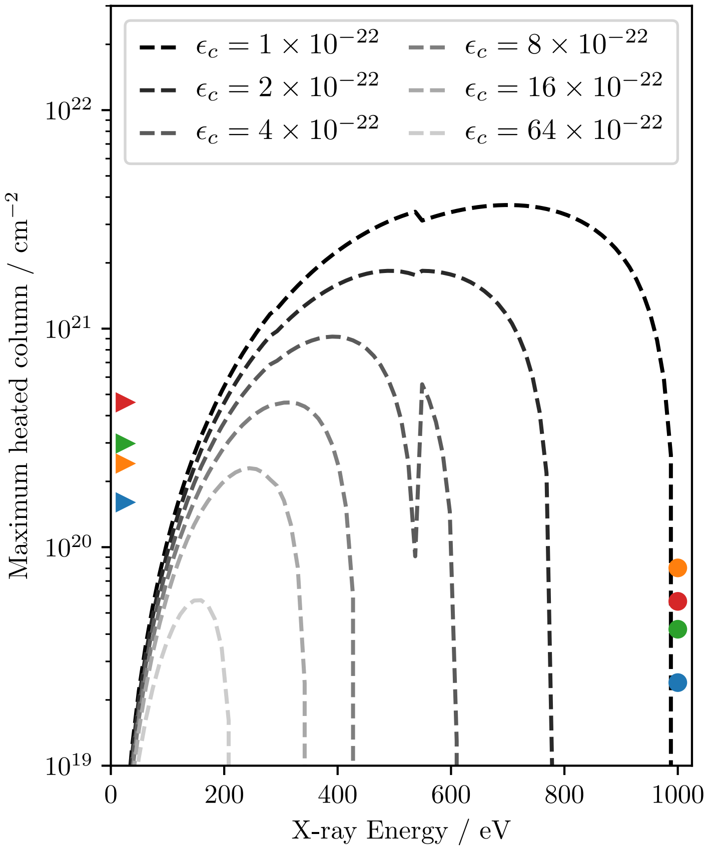

Fig. 3.10 Effect of additional cooling on the maximum column that can be heated to T_{Bern}. Additional cooling is parametrized as an increase in ε_c and represented by increasingly light colours. The kinks in some curves are because of a non-monotonicity in the photoionisation cross-section due to inner-shell ionisation of oxygen. The coloured triangles represent the column reached in our UV-only model for the same range of radii as in 3.4.

We now estimate the upper limit on how much additional cooling molecular rovibrational transitions can provide over atomic fine structure along the Bernoulli surface from the U_IRFLNoH model using the tabulations for H_2, H_2O and CO from Neufeld & Kaufman (1993) and compare them to the above requirements. We choose to match the initial molecular abundances of Wang & Goodman (2017) and in each case assume that the wind base is optically thin and set the optical depth parameter to its minimal tabulated value. The calculated cooling rates are shown alongside those from the U_Full and U_IRFLNoH simulations in the left-hand panel of Figure 3.11.

The most significant cooling typically comes from water, which under these assumptions can indeed contribute more than an order of magnitude more cooling than the atomic processes thus suggesting a potentially important role for molecular cooling in the framework

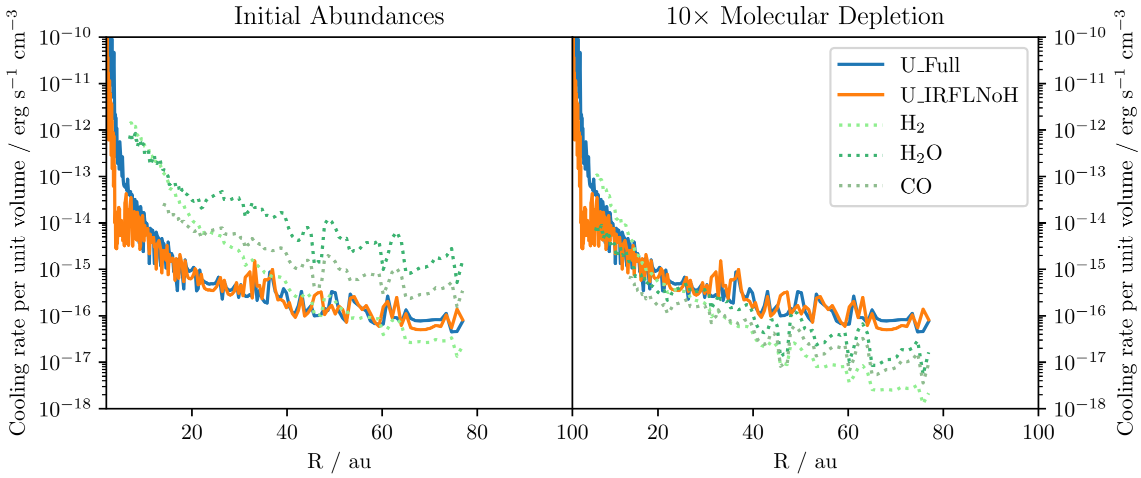

Fig. 3.11 Cooling rates per unit volume for the U_Full (blue) and U_IRFLNoH (orange) simulations at the Bernoulli surface. The dotted lines show the possible contribution of additional molecular cooling from H_2, H_2O and CO, on the left-hand panel with maximal abundances assuming all atoms are in molecules and on the right-hand panel with molecular abundances depleted by 10 times from the maximal values.

set out above. Thus between them, molecules may contribute roughly enough cooling to have the potential to change the picture set out in this work and to entirely prevent X-ray photoevaporation.

An important caveat here is the generous abundance of molecules that we assumed. In reality molecular abundances are likely to be somewhat lower than this at the base: since FUV is generally more penetrating than EUV or soft X-rays, the base will be optically thin to FUV which will lead to molecular dissociation (so long as the conditions are not such that self-shielding sets in). Moreover, protoplanetary discs' warm upper layers are frequently observed to be depleted in volatile molecules such as H_2O by a couple of orders of magnitude (e.g. Du et al., 2017) due to freeze-out onto ice grains that settle to the midplane. The right-hand panel of 3.11 demonstrates that an order of magnitude depletion in all molecular abundances near the base would be sufficient to make them subdominant coolants to atoms.

A further caveat is that this only considers the role that molecules can play in cooling. Whereas, FUV pumping and photodissociation (Section 1.2.4) can result in heating contributions by molecules, particularly H_2; a significant contribution from these processes is seen by Wang & Goodman (2017). Thus it is not clear that even if abundant, molecules lead to *net* cooling in the quantity required to prevent X-ray photoevaporation, although since Wang & Goodman (2017) find lower temperatures than us below the base, they likely do at least produce a net cooling effect. A self-consistent calculation of molecular abundances along with both molecular heating and cooling, and photoionisation heating from realistic X-ray spectra is needed to more accurately determine molecules' role in competing against X-ray heating.

3.3.5 Conclusions

In this section I have explored the relative ability of different bands of radiation to drive a thermal wind by irradiating the density grid of Wang & Goodman (2017) using MOCASSIN.

Fixing the EUV luminosity to be the same, we find that this approach gives a consistent prediction for the EUV-heated region's extent and can thus conclude that the implementation of radiative transfer is not a key contributor to the divergent results between current generations of photoevaporation models.

The ability of X-rays to heat a higher column than the EUV and hence launch an X-ray–driven wind is a strong function of frequency. At low energies, this is driven by attenuation. At higher energies this becomes limited by cooling, since the column over which the X-rays dissipate their energy increases until they do not provide enough heating locally to offset the cooling that would result at the temperatures required of a thermal wind. The most effective frequency, which balances these effects, is ~ 500 eV - within the soft part of the X-ray spectrum - for typical cooling rates and luminosities. We regard the critical reason that Wang & Goodman (2017) were unable to produce an X-ray–driven wind as due to 1000 eV being too high energy to produce enough heating; a lower value would likely have enabled X-ray-driven winds.

However, over much of the disc, molecular cooling can be relevant near the temperatures at which material becomes unbound. This manifests in our simulations, which lack molecular cooling, as hotter temperatures below the base than found in Wang & Goodman (2017). If generous assumptions are made about molecular abundances, molecular cooling - particularly from water - could play an important role in reducing the maximum column heated by X-rays and further preventing hard frequencies from having sufficient heating effect to launch a wind (but is not required to reproduce the lack of X-ray wind seen by Wang & Goodman, 2017). However it is likely somewhat more challenging for it to completely invert our conclusion that winds should be X-ray–driven, especially once molecular heating is also considered.

In order to calculate correct wind temperatures in the wind itself - that are limited to no more than $\sim 10^4$ K (and therefore avoid winds launching from unphysically small radii), it is crucial to include sufficient optical lines such as the [O I] 6300 Å and the Lyman series of H. Wang & Goodman (2017) neglect these coolants, or suppress them with an escape probability formalism that does not apparently account for the possibility of the lines being optically thick but effectively thin.

Adiabatic cooling is a modest contributor to thermal balance over most of the grid compared to emission line radiation once all such sources are accounted for. It may be most significant in regions of high acceleration such as in the low-density column near the z axis. However, its significance would likely be lower in a cooler, denser, X-ray–heated wind at least for the $> 10^{30}$ erg s^{-1} luminosities considered here.

Finally, we emphasise that it is not possible to define a single representative X-ray frequency in general terms since this changes as a function of column density and radial distance to the star. However, 1000 eV is not a very representative energy anywhere or for any of the spectra considered. It is therefore important to use a larger number of X-ray energies, especially in order to be robust against variation in the shape or luminosity of the spectrum.

3.4 Towards Comprehensive Thermochemistry of Photoevaporation with PRIZMO

The last section highlighted the need for an approach to photoevaporation modelling which a) uses a broad, detailed, spectrum for the radiation, b) includes sufficient atomic transitions to provide cooling regardless of temperature (and ionisation), c) includes cooling of molecules with abundances calculated in a self-consistent way given the radiation field, d) is done on the fly with hydrodynamics to avoid assuming radiative thermal equilibrium in the regions where adiabatic cooling may be prevalent.

To do so thus requires a fast code that can solve the *thermochemistry* - a term here used to describe collectively the heating and cooling that results from the chemical composition of the gas and interactions between its constituents - across molecular and atomic regimes and can be called as a library by hydrodynamics codes. Ultimately, this must include both gas-phase chemistry (typically two-body reactions) - and *photochemistry* - reactions such as photoionisation and photodissociation of a single atom/ion/molecule induced by the local radiation field - in order to know the gas composition.

For this purpose Grassi et al. (2020) presented PRIZMO. PRIZMO includes a python preprocessor which reads input files containing atomic data, a list of (photo)chemical reactions with rates, dust optical constants, and a spectrum. For a given number of frequency bins, it arranges the bins to capture important spectral features accurately and then tabulates photochemical cross-sections and dust opacities (which it integrates over a grain size distribution) at these energies allowing it to perform photochemistry using the local radiation field (rather than assuming rates based on a standard field). It also tabulates the total collisional (de-)excitation rates of each atomic species due to each collider as a function of temperature according to fits provided in the atomic data file. Finally, it updates the module files for PRIZMO with functions describing the rate of each reaction and matrix coefficients for calculating the level populations, ready for compilation into the main program (or as part of a hydrodynamics code).

Model Description

In order to build a sufficient network to accurately capture the fine structure line cooling, we first inspected the results from our MOCASSIN models from Section 3.3. Focusing on the wind region, in the W_Full model, 23 (44) lines contribute more than 1% (0.1%) to the cooling: 7 (8) lines of S II, 7 (8) lines of O II, 3 (5) lines of O I, 2 (3) lines of C III, 2 (5) lines of C I, 1 (6) lines of C II, 1 (1) line of Si II, 0 (3) lines of S I, and 0 (5) lines of Fe II. Therefore, except for a single Si line, only S, O and C contribute at more than the percentage level and will be the most important elements. However, the correct abundance of

S is somewhat uncertain, so we decide to keep it out of the network for now. Moreover, the lines of C III are not fine structure lines but involve configuration changes. By comparing the specific line list to the fine structure levels, we concluded that treating each of O I, O II, C I, and C II as a five-level system should be enough to provide fine structure line cooling accurate at roughly the percentage level across different temperature regimes and levels of ionisation, beyond which we start to become dominated by the uncertainty in the lack of species included rather than a lack of levels.

In these early applications, we therefore use a network - based on PDR chemistry - in which the only elements are H, He, C and O. Our network also includes the singly-ionised versions of each atom, electrons, 22 neutral/ionised gaseous molecules and finally CO and H_2O ices, all for a total of 33 species. While not all significant in their own right, several molecules are important intermediaries, for example CH_2^+ and CH in CO production. A total of 290 reactions are included covering two-body gas-phase reactions, photoionisation, photodissociation, cosmic-ray-induced reactions, formation of H_2 on dust grains, and freeze out/thermal desorption of CO and H_2O onto/from dust grains. Table 3.3 summarises the species included and the number and type of reactions in which they participate as reactants/products.

The default PRIZMO data file treated O I and O II only as three-level systems, which would be insufficient to capture the optical coolants required for our purposes; we therefore updated these species to five-level systems using energies and spontaneous transition rates from the NIST database (Kramida et al., 2022). This means that we will be able to provide atomic cooling in both ionised and neutral regions at all temperatures of $\leq 10^4$ K. For the collisional (de-)excitation rates of these transitions by electrons, we turn to Draine (2011, Appendix F) where fits to these rates as a function of temperature are provided for both O I (Pequignot, 1990; Bell et al., 1998) and O II (Tayal, 2007). In order to have a homogeneous set, we exclusively use these for electrons, replacing the previous PRIZMO data. Draine (2011) also provides fits for excitation of O I by H (Abrahamsson et al., 2007; Krems et al., 2006).We use these to supplement PRIZMO's existing data for excitation of O I by H^+ (Glover & Jappsen, 2007). Finally, though Draine (2011) provides fits for the excitation of O I by H_2 (in both its ortho- and para- spin isomers), inspection of these fits showed that these - in particular excitation of the $J = 1 \rightarrow 0$ transition by ortho-H_2 - were not well-behaved. Therefore we refit the data from Jaquet et al. (1992) on which these were based, obtaining much better fits (Table 3.4 and Figure 3.12).

Due to the availability of collision strengths for the higher energy states, we currently still treat C I and C II as a three-level and two-level system respectively, but plan to extend

Table 3.3 The species included in our fiducial network for use with PRIZMO and the number of each type of reaction in which they participate.

Molecule	Gas-phase reactions	Photo-ionisation/ -dissociation reactions	Cosmic-ray-induced reactions	Grain-surface reactions
H	60	11	3	1
H^+	21	3	2	
He	24	1	1	
He^+	24	1	1	
C	35	3		
C^+	19	2		
O	50	5		
O^+	19	1		
e^-	34	8	4	
H_2	71	1	3	1
H_2^+	22	1	1	
H_3^+	12			
CH	42	3		
CH^+	31	3		
CH_2	40	2		
CH_2^+	26	1		
CH_3	27	3		
CH_3^+	23	1		
CH_4	36	1		
CH_4^+	16			
CH_5^+	16			
CO	36	1		2
CO^+	26			
CO ice				2
H_2O	37	2		2
H_2O^+	27	1		
H_2O ice				2
H_3O^+	20			
OH	62	2		
OH^+	24	1		
O_2	26	2		
O_2^+	17	1		
HCO^+	27			
Total	259	21	5	5

Table 3.4 Fits to the rates of collisional de-excitation of O I by H_2 from Jaquet et al. (1992) in the form $k_{\mathrm{ul}} = a \times T_2^{b+c\ln T_2} \times 10^{-10}$ cm^3 s^{-1}, where $T_2 = \frac{T}{100\ \mathrm{K}}$.

Transition	Energy Levels	Wavelength / μm	a	b	c
para-H_2					
$^3P_0 \rightarrow ^3P_1$	$E_2 \rightarrow E_1$	145	0.0162	1.811	-0.205
$^3P_1 \rightarrow ^3P_2$	$E_1 \rightarrow E_0$	63	1.50	0.344	-0.013
$^3P_0 \rightarrow ^3P_2$	$E_2 \rightarrow E_0$	44	2.40	0.342	-0.026
ortho-H_2					
$^3P_0 \rightarrow ^3P_1$	$E_2 \rightarrow E_1$	145	0.0225	1.679	-0.174
$^3P_1 \rightarrow ^3P_2$	$E_1 \rightarrow E_0$	63	1.39	0.389	-0.005
$^3P_0 \rightarrow ^3P_2$	$E_2 \rightarrow E_0$	44	2.26	0.405	-0.026

this in the near future. Again for homogeneity we update/supplement the data for collisions with H, ortho-H_2 and para-H_2 with those from Appendix F of Draine (2011).

Lyman cooling is included and assumed to be effectively thin as discussed earlier in this chapter (Spitzer, 1978).

For molecular cooling, the present version of PRIZMO uses tables computed from Omukai et al. (2010) for CO cooling and from the piecewise functions of Glover & Abel (2008); Glover (2015) for H_2 cooling. Heating is included from H_2 photodissociation and pumping, proportionally to the photodissociation rate calculated by the chemical network. With this architecture it would be relatively simple to extend to include rovibrational cooling and photodissociation heating contributions from other molecules, such as H_2O, which may be the dominant molecular coolant if abundant (see previous section).

Benchmarking using photoevaporation models

To benchmark the results of PRIZMO with other codes, we repeat the basic tests from Section 3.3 by calculating the equilibrium temperature for the density grid of Wang & Goodman (2017). The results of these tests are compared to Wang & Goodman (2017)'s temperatures and the MOCASSIN calculations in Figures 3.13 and 3.14 for spectra W and E respectively.

In both cases, the wind temperatures calculated by PRIZMO seem to be in good agreement with those from MOCASSIN at $\sim 10^4$ K, implying that we have indeed captured the radiative heating and cooling well for this high ionisation parameter regime.

Conversely, near the midplane, PRIZMO's temperatures are generally cooler than either Wang & Goodman (2017) or MOCASSIN. This results from the high optical depth to the star which prevents the dust from being effectively heated when radial ray tracing is used; in MOCASSIN, the Monte Carlo approach allows some photons to be scattered towards the

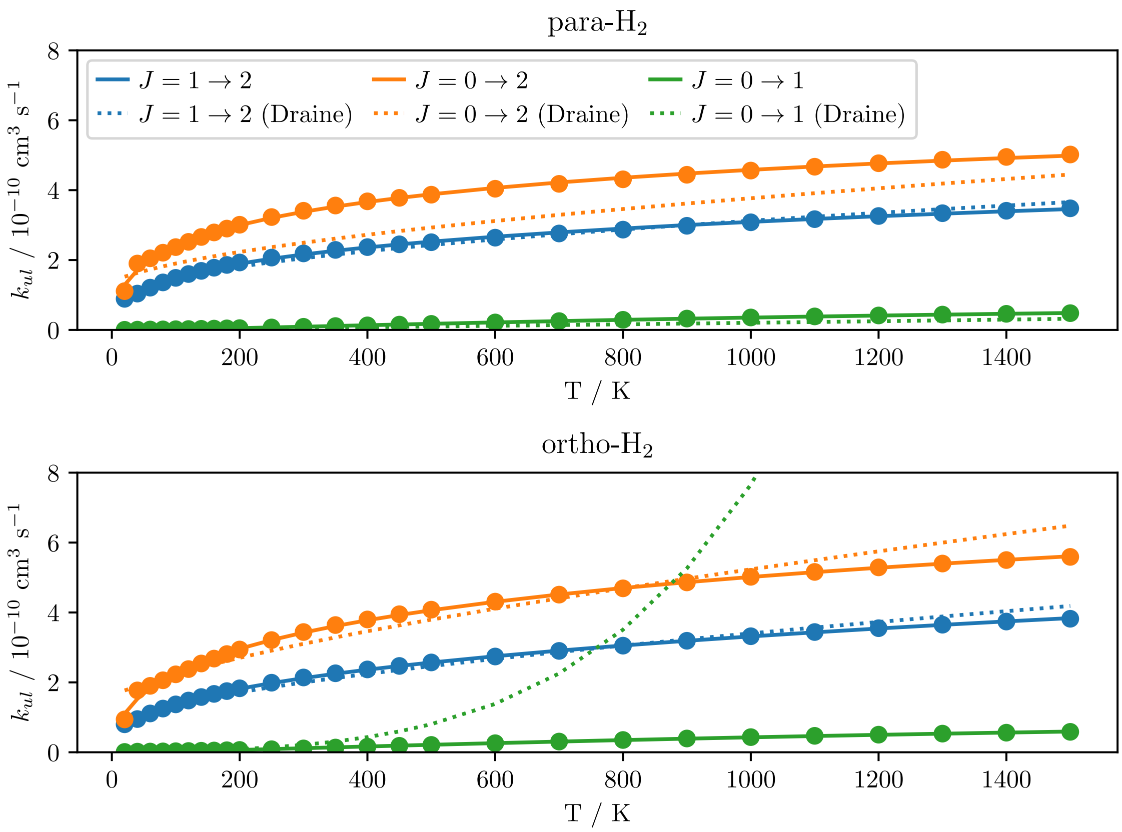

Fig. 3.12 Our fits (solid) to the tabulated de-excitation rate of Jaquet et al. (1992) (dots) for O I by para-H_2 (top) and ortho-H_2 (bottom). The fits by Draine (2011) are included as the dotted lines.

midplane, somewhat alleviating this problem, while Wang & Goodman (2017) fix their temperatures to have a floor given by the model of Chiang & Goldreich (1997). These differences will matter to the hydrostatic structure of the disc once PRIZMO is applied in hydrodynamics codes; to avoid the disc shrinking to be incredibly thin, we will therefore need to fix the temperatures at high column density, while still allowing the chemistry to evolve (because this breaks the interdependence of the calculations of temperature and chemical abundances, this also significantly helps the calculation speed in high-density cells).

Our PRIZMO models are slightly warmer below the ionisation front than Wang & Goodman (2017), as were those from MOCASSIN, and as before this region is larger for spectrum E than spectrum W, reaffirming the result that a more realistic X-ray spectrum provides more effective heating than the single 1 keV bin used by Wang & Goodman (2017).

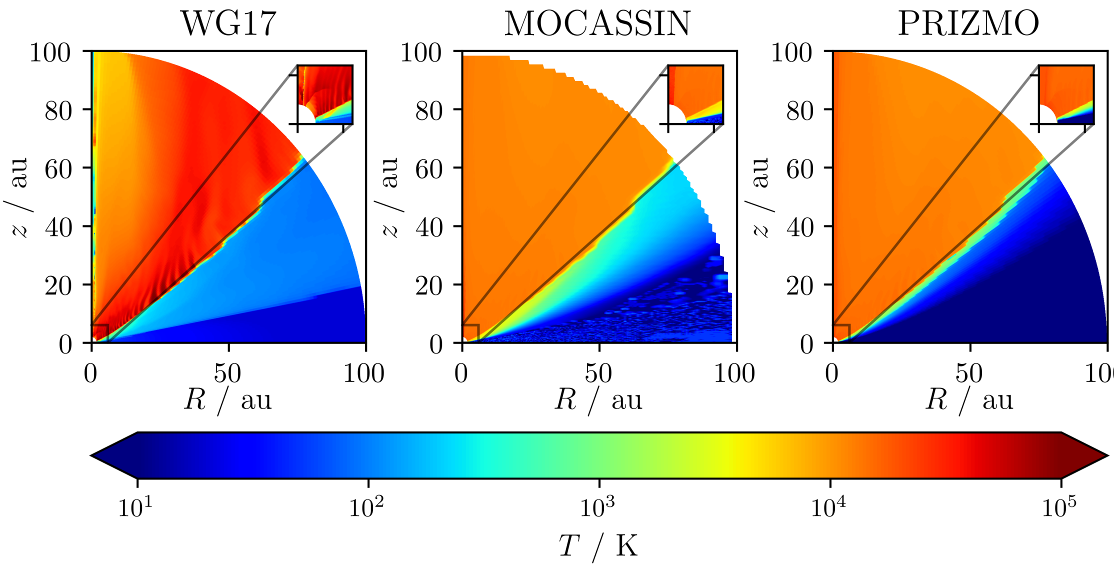

Fig. 3.13 The temperatures calculated by Wang & Goodman (2017), MOCASSIN model W_Full (Section 3.3) and PRIZMO for the same spectrum as used by Wang & Goodman (2017).

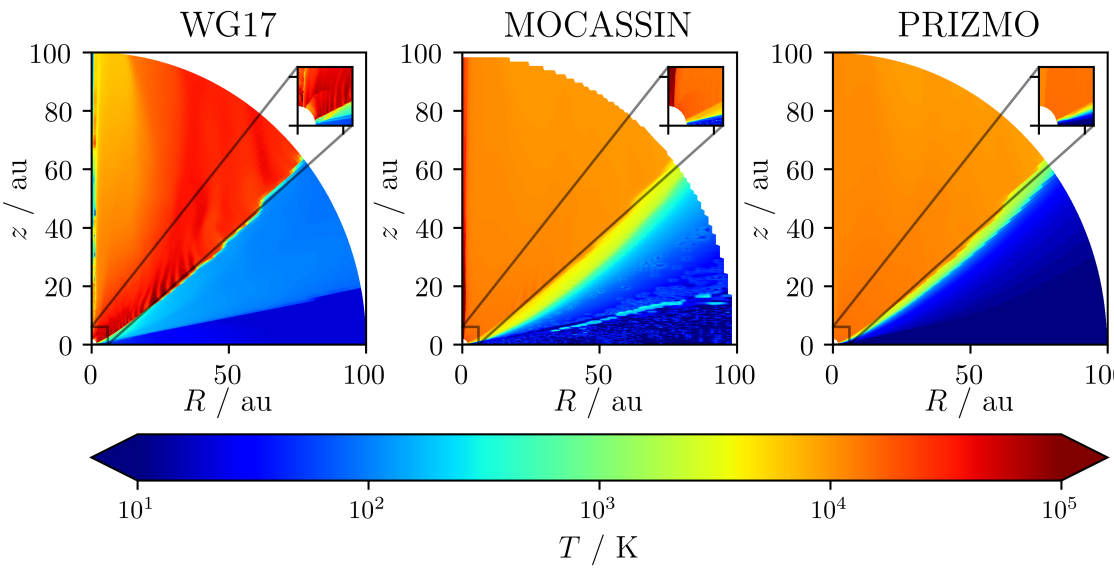

Fig. 3.14 The temperatures calculated by Wang & Goodman (2017), MOCASSIN, model E_Full (Section 3.3) and PRIZMO for the same spectrum from Ercolano et al. (2009).

Moreover, this suggests that the current level of molecular cooling is not drastically preventing the heating of this layer by X-rays and may still permit an X-ray–driven wind. CO is playing very little role in these models as where the disc is optically thin to our spectrum, it may be dissociated, while where the disc is optically thick to our spectrum, it is frozen-out. A spectrum containing a more realistic optical/near UV component from the stellar photosphere would provide somewhat warmer temperatures below the CO dissociation front. Similarly, H_2O is either frozen-out or dissociated so never reaches the levels where its cooling would become important. Conversely, there is a thin layer around the H_2 dissociation front where H_2 becomes an important coolant. However in this layer there is also a strong contribution to heating via its photodissociation and pumping. Figure 3.15 shows the relative magnitude of these heating and cooling mechanisms (with the H_2 mass fraction and its percentage contribution to the cooling also shown for reference). At high column densities near the midplane, there will be little FUV field to provide any heating, so H_2 has a net cooling effect. However, at heights such that the disc becomes more optically thin to FUV, heating starts to become more important, thus increasing the temperature. As the temperature rises, this in turn excites more cooling transitions such that in the region where H_2 cooling is important, it actually more or less balances the heating. Thus, in these tests we don't see any evidence that molecules provide enough net cooling to change the conclusions of the previous section.

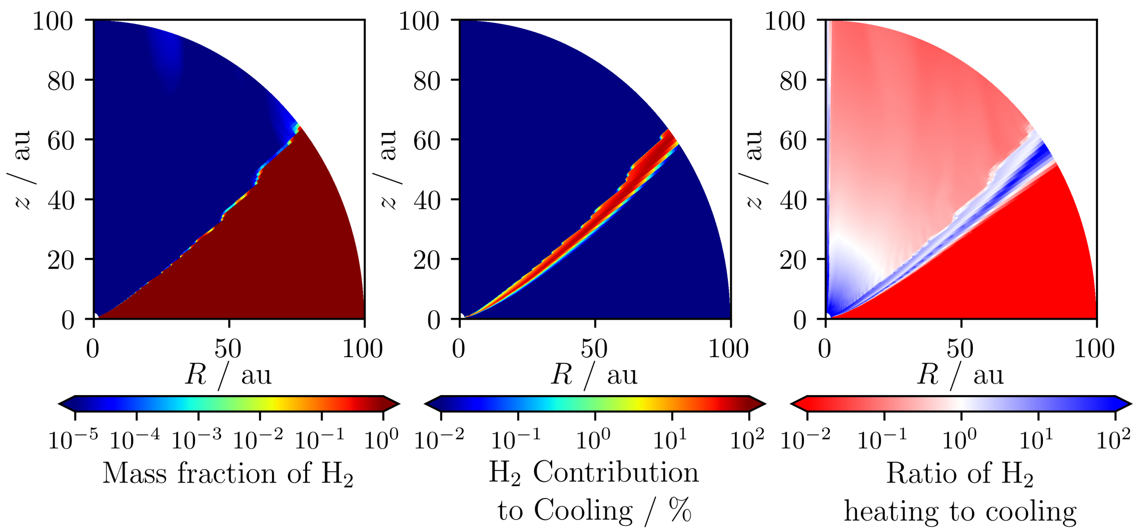

Fig. 3.15 Maps of the mass fraction of H_2, the percentage contribution of H_2 to cooling and the ratio of the heating and cooling rates due to H_2 in our PRIZMO models with the Ercolano et al. (2009) spectrum.

3.4.1 Conclusions

Motivated by the results of Section 3.3 I have discussed how we have configured PRIZMO such that it contains a set of atomic coolants that allow for accurate determination of temperatures in photoevaporative winds of various temperatures and compositions. I have then shown that PRIZMO produces accurate results when compared to MOCASSIN, which currently suggest that although molecules can provide significant additional cooling channels, they do not necessarily lead to a strong net cooling below the wind base. Once further tests and any necessary modifications are complete, PRIZMO will be a comprehensive thermochemical solver that will enable radiation hydrodynamical simulations of winds with a variety of well-resolved spectra. This should allow us to conclusively resolve the current divergent pictures of photoevaporation.

Chapter 4

The Forbidden Line Appearance of Photoevaporative Winds

4.1 Motivation

As discussed in Section 1.4.2, forbidden emission lines, particularly those of O I and Ne II, may be used to trace wind material. Since different types of wind are predicted to have different kinematics and spatial extents then by determining the sound speed and emitting region, observations can attempt to discriminate between scenarios.

While fitting Gaussian components and inferring Keplerian radii from their widths has been widely used to provide simple estimates, the presence of emission from different disc regions that overlap spectrally means that this process isn't always very informative (Weber et al., 2020). Post-processing of simulations can go some way to rectifying this (e.g. Ercolano & Owen, 2010; Picogna et al., 2019; Rab et al., 2022), but it is expensive if a large sample of parameters is to be studied, and in any one study the investigation will be limited to a particular type of wind (for example X-ray–driven).

The self-similar solutions of Clarke & Alexander (2016) and Sellek et al. (2021) discussed in Chapter 2 offer a solution to this as the velocity and density fields may be easily generated for various parameter combinations and then scaled according to a choice of normalisation - typically of the sound speed and integrated mass-loss rate. Such an approach was first carried out by Ballabio et al. (2020) to model the [O I] 6300 Å emission line sample observed by Banzatti et al. (2019), as well as various literature data for [Ne II] 12.81 μm. To convert the densities provided by self-similar models to line profiles they assumed spatially constant abundances, ionisation fractions and temperatures. They then normalise their profiles to avoid the uncertainty introduced by the unknown magnitudes of these quantities.

The results of Ballabio et al. (2020) suggest that the two key line profile parameters - the centroid shift and the FWHM - are highly sensitive to the wind's sound speed. The centroid is almost entirely insensitive to the density gradient in the wind (b, see Equation 2.4) and $\dot{M}$ though the FWHM shows more dependence, especially at high inclination (higher b and lower $\dot{M}$ shift the location where the density exceeds the critical density inwards thus resulting in emission more strongly dominated by small radii with strong Keplerian broadening). Moreover, both parameters are sensitive to the inner and outer radii assumed for the calculation, illustrating the advantage of potentially being able to tailor these parameters to an individual disc using the self-similar model.

Comparing to the observed data, Ballabio et al. (2020) found that the [Ne II] centroids and FWHM both preferred a fast wind with $c_S \sim 10$ km s^{-1} as appropriate to an EUV wind, the [O I] centroids were more consistent with a slower wind with $c_S \sim 3-5$ km s^{-1}. This supports the hypothesis of different origins for the [Ne II] and [O I] emission (Pascucci et al., 2020). However, a key limitation was the use of $\phi_b = 0^\circ$ in contrast with more realistic values of $20-50^\circ$. With the generalised models derived in Chapter 2, we are in a position to assess the impact of this choice in Section 4.2.

A second limitation is the lack of knowledge of the relevant elements' degree of ionisation and therefore of the overall luminosity, which makes it hard to study the trends outlined in Section 1.4.2. Moreover Ercolano & Owen (2016) showed that some regions, even of an X-ray wind, may be EUV-heated and therefore hotter and more ionised, which will skew the emission towards different regions of the wind. Therefore in Section 4.3, I post-process self-similar density structures of winds using MOCASSIN which calculates the emission for a large number of atomic transitions. I conduct a parameter investigation using different self-similar models, as well as various spectra, in order to understand the factors controlling line ratios, luminosities, and shapes.

Since (Pascucci et al., 2020) argue [Ne II] 12.81 μm is the most promising candidate for tracing photoevaporation, I focus this application of MOCASSIN to understanding this line in particular, along with a small sample of other lines that when considered in combination with [Ne II], reveal the physical conditions in the wind. In particular, I model the transition discs around T Cha and V4046 Sgr as these are part of an ongoing JWST Cycle 1 program to observe this line (GO 2260 Pascucci et al., 2021). Both discs have large cavities in mm continuum observations (Francis & van der Marel, 2020) (consistent with their large infrared spectral index values). Yet, the LVCs have net blueshifts, implying that wind emission from the disc's far side - which would be redshifted - may be mostly obscured by the dust disc in our line of sight. Thus it can be argued that the emission originates outside the cavity and therefore far enough from the star to potentially be resolvable using the MIRI MRS IFU. Having selected models that best reproduce existing observations, I then produce synthetic emission maps for comparison with the data.

4.2 Line profiles of Winds from Elevated Launch Plane

4.2.1 Calculation of Luminosities

The luminosity per unit volume of a collisionally excited line is given by the product of the Einstein coefficient for spontaneous emission (i.e. we ignore stimulated emission), the number density of atoms/ions in the upper energy level and the transition's energy difference:

$$L(\mathbf{r}) = A_{21}\Delta E_{12} n_2(\mathbf{r}). \tag{4.1}$$

By solving the equation of detailed balance with electrons as the colliders and assuming that the escape fraction $\beta = 1$, following Glassgold et al. (2007); Ballabio et al. (2020):

$$n_2 = f_2 X_j A_i n \tag{4.2}$$

$$f_2 = \left(1 + \frac{g_1}{g_2}\exp(\Delta E_{12}/k_B T)\left(1 + \frac{n_{\mathrm{crit}}}{n_{\mathrm{e}}}\right)\right)^{-1}, \tag{4.3}$$

where A_i and X_j are the abundance of element i and the fraction of its atoms in the ionisation state j respectively and f_2 is the fraction of those atoms in the upper energy level. For [Ne II] 12.81 μm emission, $g_1/g_2 = 2$.

The total luminosity is then

$$L = \int L(\mathbf{r})\mathrm{d}V. \tag{4.4}$$

However, since here we do not calculate the gas' thermochemical state, we do not know the relevant ions' abundances relative to that of the electrons. We thus proceed by assuming that X_j and A_i have constant but unknown values and renormalise our line profiles in terms of their peak luminosity. In Section 4.3 we avoid this issue by calculating $L(\mathbf{r})$ using the Monte Carlo photoionisation code MOCASSIN.

4.2.2 Calculation of Line Shapes

For the line shape, at each location we use a thermally-broadened Gaussian centred on the line of sight velocity v_{los} (Ballabio et al., 2020)

$$L(\mathrm{v};\mathbf{r}) = \frac{1}{\sqrt{2\pi}\mathrm{v}_{\mathrm{th}}}\exp\left(-\frac{(\mathrm{v}-\mathrm{v}_{\mathrm{los}})^2}{2\mathrm{v}_{\mathrm{th}}^2}\right)\mathrm{L}(\mathbf{r}) \tag{4.5}$$

where $v_{\rm th} = \sqrt{m_H/m_i} c_{\rm S}$ and

$$\begin{aligned} v_{\rm los} =& (-\sin(\theta)\cos(\phi)\sin(i) - \cos(\theta)\cos(i))v_r \\ &+ (-\cos(\theta)\cos(\phi)\sin(i) + \sin(\theta)\cos(i))v_\theta \\ &+ \sin(\phi)\sin(i)v_\phi. \end{aligned} \tag{4.6}$$

v_r and v_θ are obtained from the self-similar models. We set the azimuthal component to the Keplerian velocity $v_\phi = v_{\rm K}$ at the base and assume angular momentum conservation along the streamline.

The contributions from all cells which are visible at the relevant inclination are then summed to give the line profile. In the disc, dust provides the dominant source of opacity and blocks the receding (redshifted) wind, resulting in observations with net blueshifts [Ne II] (Pascucci et al., 2011, 2020). For simplicity, we assume that the disc midplane is completely opaque (and all other material is optically thin) when determining which parts of the wind are visible at any inclination. The disc has finite extent equal to the outer radius of our wind region. Practically, all cells with $z > 0$ are therefore visible, while for $z < 0$, whether they are visible is determined by tracing each cell back to the midplane along the line of sight; those that are visible are those satisfying

$$(R\cos(\phi) - z\tan(i))^2 + (R\sin(\phi))^2 > R_{\rm out}^2 \tag{4.7}$$

The profile is then convolved with a Gaussian of width 10 km s^{-1} to degrade the profile to the spectral resolution ($R = 30000$) of the observations.

4.2.3 Results

In order to compare our results to Ballabio et al. (2020), we also calculate our line profiles on a spherical grid spanning radii $r = [0.03, 10] r_G$ and elevations $\phi = \pm[\phi_{\rm b}, 75°]$. The density at $(r, \phi) = (r_G, \phi_{\rm b})$ is normalised to the same number density $n_G = 2.8 \times 10^4$ cm^{-3}. This relatively low value probably best represents an EUV-driven wind, in which a typical density gradient is $b = 1.5$. We calculate our profiles at 801 velocities spanning $v = [-40, 40]$ km s^{-1}. We present in Figure 4.1 emission profiles for the [Ne II] 12.81 μm line at different viewing inclinations and compare directly winds launched from the midplane with those launched from $\phi_{\rm b} = 36°$ (a typical value found in photoevaporation simulations). The solid lines indicate the true line profile, while the dotted lines indicate the effect of the Gaussian convolution to the typical spectral resolution of the observations.

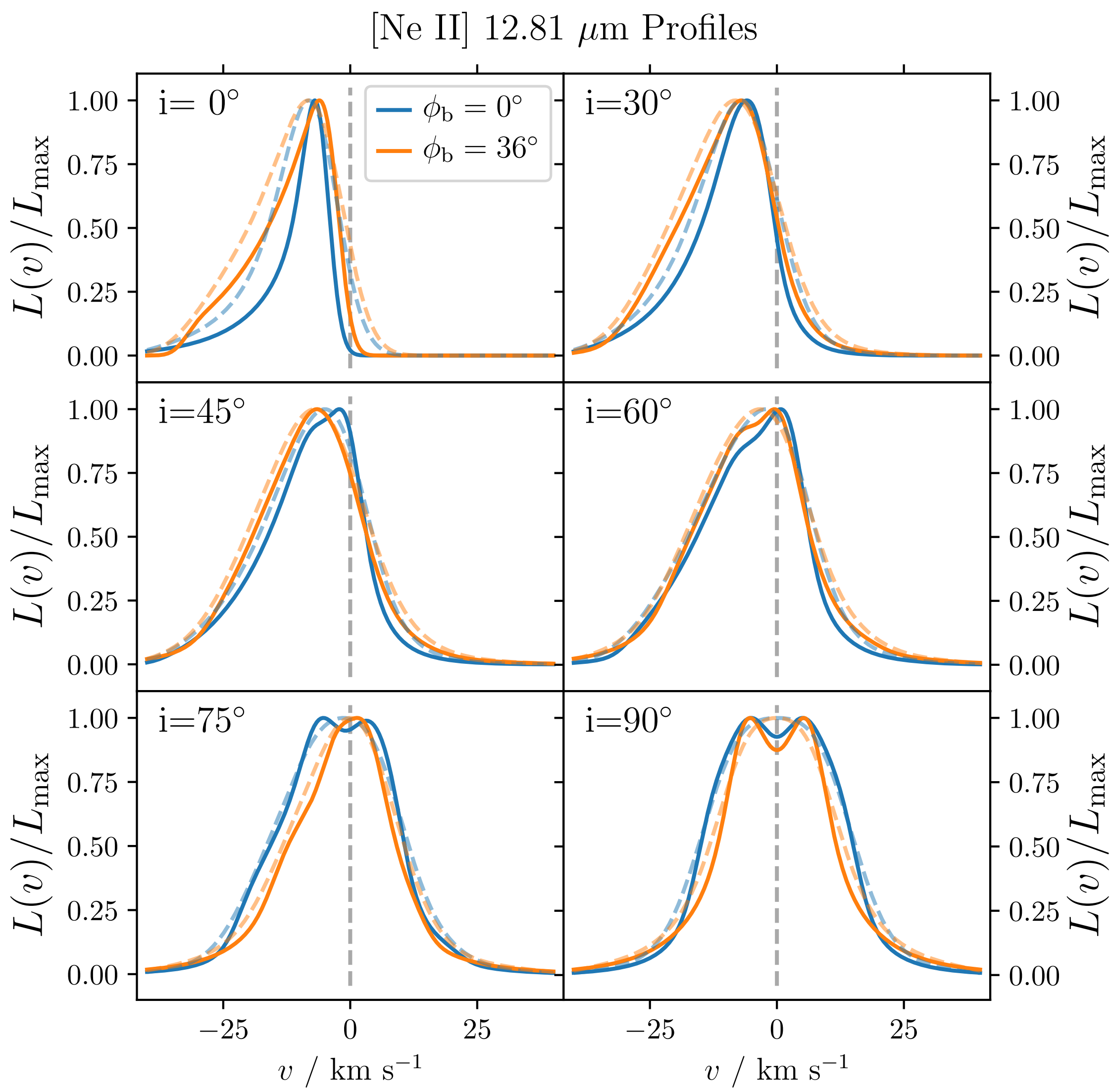

Fig. 4.1 Normalised line profiles for photoevaporative winds launched from $\phi_b = 0°$ and $\phi_b = 36°$. The fainter, dashed lines indicate the profiles after convolution of a Gaussian with width 10 km s^{-1}.

As expected, for face-on discs, the material is flowing towards the observer and so we see lines with very little red wing emission. Conversely in edge-on discs, we see emission from both above and below the midplane and which is dominated by Keplerian broadening; therefore we see symmetric, double-peaked profiles. At the limited spectral resolution of current observations, however, this double-peaked profile can no longer be resolved, though the lines are still obviously less sharply peaked.

At small inclinations, the lower launch velocities of the $\phi_b = 36°$ models and the inclination of their streamlines to the line of sight at the base (where densities are highest) results in a small redwards shift of the line peak (although the effect is reduced at finite spectral resolution). This is consistent with previous expectations that launch from an elevated base reduces the line peak blueshift by ~ 1 km s^{-1} (Pascucci et al., 2011; Ballabio et al., 2020).

The more striking effect is on the FWHM: the line width when the base is elevated is greater for discs which are viewed face-on, but the lines become narrower at high inclinations; this largely wipes out the dependence of the FWHM on viewing inclination predicted for winds launched from the disc mid-plane (Ballabio et al., 2020). This occurs since the streamline morphology is more vertical when the base is elevated (e.g. Figure 2.2), meaning that near the base the velocity vectors are directed more along the polar direction ($i = 0°$) than towards high inclinations ($i \lesssim 90°$). Thus for discs seen at low inclination, where the width is largely determined by poloidal velocities, the line profile is better able to trace the full velocity gradient along the streamlines. Whereas for discs seen at high inclination where the width is largely determined by azimuthal velocities, there is less of an additional contribution from the poloidal velocities. For discs observed close to face-on, the blue wing itself has an absolute luminosity which is fairly insensitive to the launch base. This is because the highest velocity material is in the limit given by Equation 2.24 and is insensitive to the launch speed. Conversely, the lowest velocity material is found near the base; the reduced wind volume (due to $0° \leq \phi < \phi_b$ being excised) therefore mostly affects luminosities near $v = 0$.

4.2.4 Discussion

Though fractionally smaller than the unconvolved case, the difference in FWHM is still seen between the convolved line profiles since it is typically a few km s^{-1} and thus only slightly less than the spectral resolution of 10 km s^{-1}. Moreover, the error bars on [Ne II] FWHM data tend to be comfortably $\lesssim 5$ km s^{-1}. Therefore these effects are not totally negligible and should be taken into account in future analyses for a more accurate interpretation of the FWHM as a function of inclination, particularly as future improvements in instrumentation lead to higher resolution spectra.

In Chapter 2 I showed that these solutions describe winds well throughout a large region. At low densities as considered here, the wind's ionisation level is fairly uniform as they are EUV-heated throughout. Therefore, small radii, where the wind deviates most strongly from the self-similar solution, contribute weakly due to their small volume. Thus the results are robust to the inclusion of gravity and centrifugal force.

The more significant caveat is if the wind is not isothermal. Although this only weakly modifies the launch velocities and streamline morphologies, it will have more significant effects on the overall velocity scale through the local sound speed (which is the dominant factor in setting the blueshift and width of the lines Ballabio et al., 2020). Moreover, it will affect the population of the excited energy state of the transition as a function of radius. Therefore, rather than adopt the approach used here to investigate these effects, in the next Section I use MOCASSIN to calculate them self-consistently for different density profiles.

4.3 Simulating [Ne II] Emission from Transition Discs

4.3.1 T Cha and V4046 Sgr

Simulating the wind emission from the discs around T Cha and V4046 Sgr requires knowledge of the properties of the central stars and their discs in order to scale the self-similar solution's densities and velocities. These are summarised in Table 4.1.

The most critical lengthscale when it comes to photoevaporation is the gravitational radius. Since each system has a total stellar mass $> 1\ M_{\odot}$, the r_G (assuming 10 km s^{-1}) are $10-20$ au. Moreover, both discs have ~ 30 au ($2-3\ r_G$) dust cavities according to high resolution ALMA imaging (Francis & van der Marel, 2020). However launching a wind inside this point is not precluded as neither disc shows evidence for a deep gas cavity (Wölfer et al., 2023). Similarly, the *small dust* may extend some way interior to 30 au. Estimates for V4046 Sgr have ranged from 0.2 au, consistent with the central binary's tidal truncation radius (Jensen & Mathieu, 1997; Martinez-Brunner et al., 2022), to ~ 10 au in scattered light observations (Rapson et al., 2015a; Avenhaus et al., 2018). T Cha has a more significant cavity in small dust containing a very compact inner disc. This cavity is thought to extend from $0.1-0.2$ au to $7-30$ au (Brown et al., 2007; Olofsson et al., 2011, 2013; Pohl et al., 2017), although shadowing could hide significant amounts of dust in the cavity that wouldn't be detectable through SED modelling or interferometry (Olofsson et al., 2013). JWST observations point a highly variable infrared SED (Xie, in prep.), which may influence the uncertainty in these values.

Moreover, we need to provide the MOCASSIN code with a spectrum. The X-ray luminosity has been reported for V4046 Sgr by Sacco et al. (2012) and for T Cha by Güdel et al. (2010), while Pascucci et al. (2014) provided upper limits on their EUV photon fluxes based on free-free emission at centimetre wavelengths. For our fiducial spectrum we use the Ercolano et al. (2009) model FS0H2Lx1 - which contains both EUV and X-ray components - normalised to the observed X-ray luminosities. This produces an EUV flux slightly (25%) in excess of the Pascucci et al. (2014) upper limit in V4046 Sgr, and comfortably below in the case of T Cha. Sacco et al. (2014) also performed an X-ray analysis of T Cha and provide two-temperature fits for two different abundance patterns, resulting in two possible spectra; though they differ slightly in their hardness, the most important difference is the higher luminosity of the S14_B10C spectrum compared to the S14_sol08 spectrum, with the ratio of EUV and X-ray luminosities being similar ($L_{\rm X}/L_{\rm tot} = 82\%$ and 84% respectively).

For T Cha we therefore also investigate the results of using these alternate spectra. We also create an additional version of each including an EUV component scaled to match the Pascucci et al. (2014) upper limit such that we can bracket the possible contributions from

EUV. Details of the spectra, which we produce using PINTOFALE (Kashyap & Drake, 2000), are given in Table 4.2.

4.3.2 Methodology

We use the self-similar solutions of Sellek et al. (2021), described in Chapter 2 to produce models of the wind's density and velocity structure. These depend on four key parameters:

- **The slope of the density at the wind base, $\rho \propto r^{-b}$.** In such a model, the column density is accumulated at small radii for $b > 1$ and large radii for $b \leq 1$. While we focus on $b = 1.5$, a value motivated both by theory/simulations (Hollenbach et al., 1994; Picogna et al., 2019) as well as previous comparisons to observations of TW Hya (Pascucci et al., 2011; Ballabio et al., 2020), we briefly also consider $b = 1.0$, which matches some more recent simulations (Picogna et al., 2021), as this may change where the ionising radiation is absorbed and consequently where Ne II emits.

- **The slope of the temperature profile in the wind, $T \propto r^{-\tau}$.** We assume this to be $\tau = 0$, i.e. an isothermal case (as arises for an EUV-heated wind). Typical temperature gradients are small (Nakatani et al., 2018a) and only weakly affect the density and velocity structure (Sellek et al., 2021, see 2.4). The results of our MOCASSIN calculations indeed show fairly small temperature gradients throughout most of their volume; therefore neglecting $\tau \neq 0$ is a small source of uncertainty.

- **The wind base elevation above the midplane ϕ_b.** The elevation of base is largely controlled by the underlying disc's aspect ratio (Picogna et al., 2021), and accordingly scales similarly. A good approximation to their results (which effectively assumes the temperature is independent of stellar mass e.g. Sinclair et al., 2020) is

$$\phi_b(r; M_*) = 8.5^\circ \left(\frac{r}{\mathrm{au}}\right)^{1/4} \left(\frac{M_*}{M_\odot}\right)^{-0.5}. \tag{4.8}$$

  At $r \geq r_G$, we thus expect $\phi_b \gtrsim 13^\circ$ and so choose the 18° models of Sellek et al. (2021) for our analysis (the lowest pre-calculated ϕ_b models fulfilling this criterion). This is consistent with CO emission height observations of the bound disc around V4046 Sgr that place it below this at $z/r = 0.24$ (Law et al., 2022).

- **The wind launch angle with respect to the base χ_b.** This is assumed to be 90° given that we expect strong temperature jumps across the base.

Table 4.1 Properties of T Cha and V4046 Sgr systems. Where appropriate, values have been rescaled from the original references to use the Gaia DR3 distance.

System	$M_* \ / \ M_\odot$	Distance / pc	Inclination	$R_{\rm cavity}$ / au		$R_{\rm out}$ / au			r_G[a]/ au	$\dot{M}_{\rm acc}$ / $M_\odot$ yr^{-1}
				mm	μm	mm	μm	gas		
T Cha	1.5[b,g]	102.7 ± 0.3[c]	73°[d]	33[e]	20[f]	44[e]	58[g]	220[h]	13	$10^{-8.4}$[i]
V4046 Sgr	0.912 & 0.873[j]	71.48 ± 0.11[c]	35°	24[k]	0.2[k]	63[k]	300[l]	300[l]	16	$10^{-9.22}$[m]

[a] Assuming $c_S \approx 10^4$ km s^{-1}
[b] Olofsson et al. (2011)
[c] Gaia DR3 value (Gaia Collaboration et al., 2022)
[d] Hendler et al. (2018)
[e] Francis & van der Marel (2020)
[f] Xie (in prep.)
[g] Pohl et al. (2017)
[h] From 12CO, Huélamo et al. (2015)
[i] Cahill et al. (2019), using relationship between [O I] and accretion luminosity from Nisini et al. (2018).
[j] Stempels & Gahm (2004)
[k] Martinez-Brunner et al. (2022)
[l] From 12CO, Kastner et al. (2018)
[m] Curran et al. (2011)

Table 4.2 Properties of different spectra used in this work. Where given, EM_2/EM_1 is estimated from the plots of Preibisch et al. (2005) using the inferred L_X.

Name	Components	Composition	L_X / erg s^{-1} (band)	Φ_{EUV} / s^{-1}	L_{tot} / erg s^{-1}
E09_V4046Sgr	RS CVn template Ercolano et al. (2009) (peaks at $T = 1.8 \times 10^7$ K and $T = 10^4$ K)	$Z_\odot$	1.19×10^{30} $(0.3 - 10$ keV) Sacco et al. (2012)	5.2×10^{40}	4.66×10^{30}
E09_TCha	"	"	2.7×10^{30} $(0.3 - 10$ keV) Güdel et al. (2010)	1.2×10^{41}	1.06×10^{31}
S14_sol08	$T_1 = 0.9 \times 10^7$ K $T_2 = 2.7 \times 10^7$ K Sacco et al. (2014) $EM_2/EM_1 = 3$	0.8 $Z_\odot$	4.4×10^{30} $(0.15 - 8$ keV)	7.0×10^{39}	5.23×10^{30}
S14UV_sol08	" $T_3 = 10^4$ K $EM_3/EM_1 = 35.1$	"	"	4.1×10^{41} (Pascucci et al., 2014)	1.58×10^{31}
S14_B10C	$T_1 = 0.35 \times 10^7$ K $T_2 = 2.1 \times 10^7$ K Sacco et al. (2014) $EM_2/EM_1 = 10$	Brickhouse et al. (2010) Model C	3.7×10^{31} $(0.15 - 8$ keV)	8.6×10^{40}	4.52×10^{31}
S14UV_B10C	" $T_3 = 10^4$ K $EM_3/EM_1 = 7.3$	"	"	4.1×10^{41} (Pascucci et al., 2014)	5.38×10^{31}

Once these parameters are established and the scale-free solutions derived, the solutions' normalisation must be set. The wind's density normalisation is one of the most uncertain parameters and hence we therefore investigate several values, chosen to give certain overall mass-loss rates. Given $\tau = 0$ and $\chi_\mathrm{b} = 90°$, the relationship between the mass-loss rate $\dot{M}$ and the density at r_G, ρ_G, is

$$\dot{M} = \frac{4\pi \cos\phi_\mathrm{b}}{2-b} \mathscr{M}_\mathrm{b} \frac{G^b M_*^b}{c_S^{2b-1}} r_\mathrm{out}^{2-b} \rho_G, \tag{4.9}$$

assuming that $b < 2$ and $r_\mathrm{in} << r_\mathrm{out}$ (in which case, the mass-loss rate is dominated by the contribution from the outer disc at $\sim r_\mathrm{out}$). Therefore, the normalisation depends on both parameters of the self-similar model (b, ϕ_b) and parameters of the system, specifically the stellar mass and wind outer radius r_out, which we take to be the gas disc outer radius given in Table 4.1 though Ercolano et al. (2021) find the wind cuts off at only 120 au for the Ercolano et al. (2009) spectrum. Moreover, here, and when quoting inner radii in r_G, we choose an upper limit value for the sound speed of 10 km s^{-1}. Therefore while we quote our density normalisations in terms of a nominal value of $\dot{M}$, these may not correspond to the true $\dot{M}$, which for a fixed density normalisation is degenerate with the true outer radius and sound speed, such that it is likely to be somewhat lower by up to a factor $3-10$:

$$\dot{M}_\mathrm{true} = \dot{M}_\mathrm{nom} \frac{c_\mathrm{S,true}}{10\ \mathrm{km\ s^{-1}}} \left(\frac{R_\mathrm{out,true}}{R_\mathrm{out}} \right)^{2-b} \tag{4.10}$$

The theoretical value of the mass-loss rates has a large degree of uncertainty at present between various models as discussed throughout this thesis. As examples, Ercolano et al. (2021) and Picogna et al. (2021) would predict 4.0×10^{-8} $M_\odot$ yr^{-1} (for the E09_TCha spectrum) and 5.1×10^{-8} $M_\odot$ yr^{-1} (for a 1.3 $M_\odot$ star). Hence we investigate the effect of $\dot{M}$ values in the range $\dot{M}_\mathrm{PE} \in 10^{-10}, 10^{-9}, 10^{-8}, 10^{-7}$ $M_\odot$ yr^{-1} and thus spanning the limits set by many models. For comparison, the accretion rates of T Cha and V4046 Sgr are $10^{-8.4}$ $M_\odot$ yr^{-1} and $10^{-9.22}$ $M_\odot$ yr^{-1} respectively; if the photoevaporative mass-loss rates are on the order of or greater than these values then the wind is likely to carve out a gap at small radii and quickly halt accretion (the so-called UV switch of Clarke et al., 2001). Conversely, in magnetothermal models, the mass-loss rate in the wind may exceed the accretion rate by a larger factor (see Figure 1.6).

The resultant density grids are provided to MOCASSIN, truncated at a range of inner radii $r_\mathrm{in} \in 0.03, 0.1, 0.3, 1.0, 3.0$ r_G, and irradiated using the spectra from Table 4.2. While the smallest of these radii is comfortably inside what is expected for a photoevaporative wind, this allows us to crudely explore the signatures of winds launched further in (most likely MHD winds). MOCASSIN is run for eight iterations with 10^8 photon packets, plus a final ninth iteration with 10^{10} photon packets to reduce noisiness in the ionisation state, and outputs temperatures and line fluxes in each cell.

Line Profiles

From the MOCASSIN temperature outputs we can calculate a local sound speed in each cell. In practice the temperature gradients are sufficiently small that we may use isothermal self-similar models to calculate the Mach numbers at each location; these two quantities may be combined to determine the velocity components at each location. Then, as per Section 4.2.2, for each cell located at $\mathbf{r}$ we produce a thermally-broadened line profile at the total luminosity for the line $L(\mathbf{r})$ calculated by MOCASSIN (rather than that calculated in Section 4.2.1.) Finally we sum the contributions of all cells to give the total line profile.

Synthetic Images

To produce synthetic JWST observations we use the MIRISIM python package (Klaassen et al., 2021). MIRISIM allows a "scene" to be built from several components. For each model we create four scenes: "line only" - containing only the line emission which we use to study the instrumental effects on our ability to resolve the emission; "full" - containing the line emission, disc and stellar continuum and background noise in order to test our ability to recover the line from the continuum; "continuum" - containing only the continuum emission which we can use to help correct for incomplete treatment of fringing in the JWST pipeline (see below); and "background" containing only the background noise to use for subtraction from the other scenes in the pipeline.

As it is the only one of GO 2260's two sources to yet be observed, we focus on creating these images for T Cha. For the line, we provide MIRISIM with a FITS file containing the $L(v;\mathbf{r})$, integrated along the line of sight and where the velocities are mapped onto wavelengths. To this, we to add a low level thermal background, as well as a point source with a 1.36 $L_\odot$, 5400 K blackbody to represent the star (Olofsson et al., 2011). Finally, we approximate the disc continuum as a Sersic disk with scale radius 50 au (Pohl et al., 2017) and index $n = 0.4$ (a by-eye fit to the continuum profiles of Huélamo et al., 2015). This 50 au scale is similar to the FWHM extent of the major axis of the observed JWST continuum (Bajaj, in prep.). There is a reasonable amount of variation in fits for the inner and outer radius of this disc with $R_{\rm in} = 7.5 - 30$ au (Olofsson et al., 2011; Pohl et al., 2017) and $R_{\rm out} = 25 - 300$ au (the latter largely depending on the steepness of the surface density profile assumed). Therefore we choose an intermediate $R_{\rm in} = 20$ au (which is consistent with

SED modelling of the observed JWST spectrum, Xie, in prep.) and do not assume an outer truncation radius, since it would anyway likely be in the tail of the tapered profile. For the disc component's SED we use Spitzer measurements of the continuum spectrum covering $9.9 - 36.9\ \mu$m (Lebouteiller et al., 2011).

MIRISIM (Klaassen et al., 2021) Version 2.4.2 is then used to simulate the illumination of the imaging detectors on JWST's Mid Infrared Instrument (MIRI) Medium-Resolution Spectrometer (MRS). MRS consists of IFUs covering 4 wavelength channels:

- Channel 1: $4.87 - 7.76\ \mu$m
- Channel 2: $7.45 - 11.87\ \mu$m
- Channel 3: $11.47 - 18.24\ \mu$m
- Channel 4: $17.54 - 28.8.2\ \mu$m

Each IFU performs image slicing: 12-21 slices (depending on the PSF size in the channel and its field of view) of the sky are taken along the IFU's β coordinate, which to within a few degrees corresponds to (the negative of) JWST's V3 coordinate (which is directed away from the sun shield and so must be maintained within 45° of the anti-sun). For simplicity we assume that the V3 axis is aligned parallel to the disc's major axis. The image slices are each passed through one of three dispersers (A: SHORT, B: MEDIUM, C: LONG) - corresponding to sub-bands of the channels - to create multiple long slit spectra. Finally the spectra are interleaved next to each other on one of two imaging detectors (one for channels 1 & 2 and the other for channels 3 & 4) to produce images in the plane of wavelength against spatial coordinate.

MIRISIM applies several distortions and transformations to the data, including the effects of both the optics and the detectors themselves, to produce detector images, which are suitable for import into the JWST Science Calibration Pipeline (Bushouse et al., 2022, we use Version 1.4.3). The pipeline reduces the observations in three stages: firstly detector-level corrections and read-outs yielding photon count rates, secondly calibrations of individual exposures for instrumental effects, and finally combinations of exposures into a final image cube (including background subtraction). For MIRI MRS, the second stage includes flat field corrections, stray light subtraction, fringing removal, flux calibrations, rectification of the 2D detector data into a 3D data cube and spectral extraction. However, MIRISIM doesn't yet model the contribution of stray light so we disable this step in our reduction. We also disable the "refpix" step in the first stage as there is a known inconsistency with the handling of reference pixels as of Version 2.4.2 of MIRISIM. The default fringing removal carried out in stage two only works well for uniform extended sources and leaves residual fringing. In the Pipeline version we used, this was not yet corrected in channels 3 & 4. Consequently we calculated the residual fringing effect ourselves using the continuum as a reference.

Table 4.3 JWST measurements of T Cha noble gas forbidden line fluxes

Ion	Wavelength / μm	Flux / erg s^{-1} cm^{-2}
Ne II	12.81	$(5.01 \pm 0.024) \times 10^{14}$
Ne III	15.55	$(0.474 \pm 0.097) \times 10^{14}$
Ar II	6.98	$(4.40 \pm 0.073) \times 10^{14}$
Ar III	8.99	$< 0.11 \times 10^{14}$

4.3.3 Noble Gas Line Ratios

We begin by considering what constraints may be obtained from the line luminosities alone. In order that initially we are not sensitive to overall scalings such as abundances, we thus compare [Ne II] 12.81 μm to [Ne III] 15.55 μm; we expect this to provide information about the levels of ionisation in the wind. As an independent constraint on ionisation, we also consider the ratio of [Ar III] 8.99 μm to [Ar II] 6.98 μm.

Among the sources with classified [Ne II] LVCs, two have a published [Ne III] measurement derived in the same work as a [Ne II] detection, both in Spitzer spectra: TW Hya (Ne III detection, Najita et al., 2010) and V4046 Sgr (Ne III upper limit, Rapson et al., 2015b). To these we may add T Cha, for which JWST GO 2260 observations have detected [Ne II], [Ne III] and [Ar II] and placed an upper limit on [Ar III] (Table 4.3).

In Figure 4.2, we compare the predictions of our models with these data; since it is the source with most data, we choose to show models relevant to T Cha. The equilibrium ionisation should result from balancing the rate of photoionisations (collisional ionisation is largely negligible at wind temperatures, Glassgold et al., 2007) - which depends on the spectrum - and the rate of recombinations or charge exchange to lower ionisation states - which depends largely on density. Therefore, each panel shows a different nominal mass-loss rate (density normalisation), while each series of points shows a different spectrum.

We first consider low mass-loss rates $\dot{M}_{\rm nom} \lesssim 10^{-9}\ M_\odot\ {\rm yr}^{-1}$, which correspond to EUV-driven winds (upper panels of Figure 4.2). These winds must by definition be wholly transparent to EUV so the ionisation balance will be between direct EUV photoionisation of Ne II to Ne III at rate Φ_{23} and recombination of free electrons with the ions at electron-density dependent rate $R^{\rm rec}_{32}$:

$$\frac{n_3}{n_2} = \frac{\Phi_{23}}{R^{\rm rec}_{32}}. \tag{4.11}$$

In these highly ionised environments, the electron fraction will more or less have saturated, so the ratio becomes simply a measure of the ionising photons: we see that the ratios predicted by the S14_sol08, E09_TCha and S14_B10C spectra are so arranged in order of their EUV

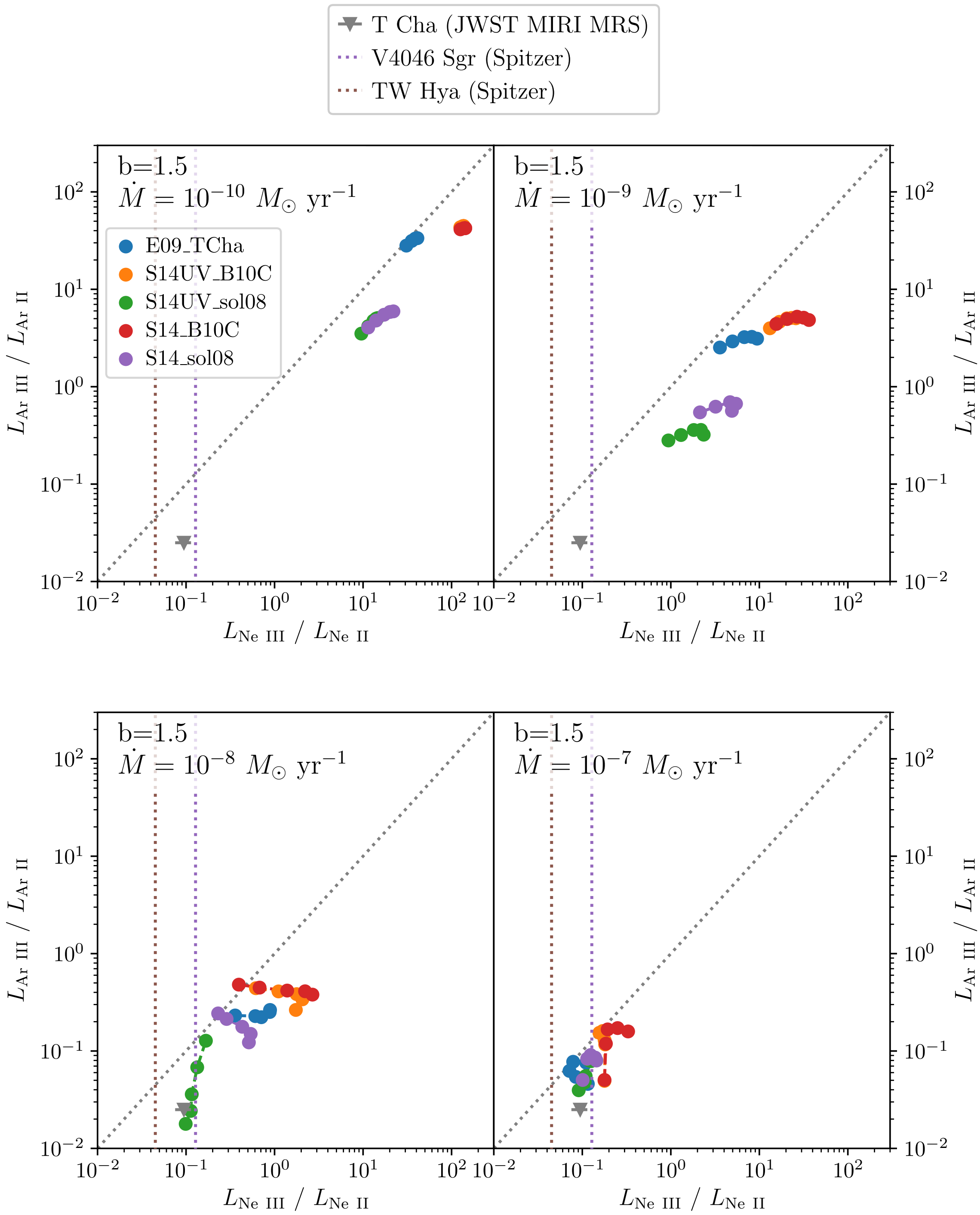

Fig. 4.2 Comparison of the ratio of the [Ar III] 8.99 μm and [Ar II] 6.99 μm lines to the ratio of the [Ne III] 15.55 μm and [Ne II] 12.81 μm. Each set of points of a given colour (connected by dashed lines) represents a particular one of the five T Cha spectra considered in this work and consists of five models with different inner radii. Results are shown for $b = 1.5$ and a differ $\dot{M}$ in each panel. JWST measurements for T Cha (which only have an upper limit for [Ar III]) are included for comparison (grey triangle) while the vertical dotted lines illustrate the [Ne III]/[Ne II] ratio for V4046 Sgr and TW Hya which as yet lack detections of the Ar lines.

photon fluxes. However, the $T_3 = 10^4$ K EUV component added to the S14UV_sol08 and S14UV_B10C spectra mostly contributes flux below 20 eV and so doesn't contribute to the secondary ionisation of Ne or Ar through the Φ_{23} term since their ionisation energies are 40.96 eV and 27.63 eV respectively. Nevertheless, for all these spectra $L_{\text{Ne III}}/L_{\text{Ne II}} > 1$ and $L_{\text{Ar III}}/L_{\text{Ar II}} > 1$, in complete contrast to all the data.

Henceforth we should therefore consider only winds with mass-loss rates $\gtrsim 10^{-8}\ M_\odot\ \text{yr}^{-1}$ as able to produce the line ratios that are remotely consistent with the observed range $0.045 < L_{\text{Ne III}}/L_{\text{Ne II}} < 0.13$. These will be X-ray–heated winds (though their innermost regions may be EUV–heated). In particular, $\dot{M}_{\text{nom}} = 10^{-7}\ M_\odot\ \text{yr}^{-1}$ models are favoured as they most closely cluster around the observed range although still overpredict T Cha's ratio of Ar lines. Indeed, the only combination able to reach sufficiently low $L_{\text{Ar III}}/L_{\text{Ar II}}$ is a $\dot{M} = 10^{-8}\ M_\odot\ \text{yr}^{-1}$ wind with the S14UV_sol08 spectrum (while on average the S14_B10C and S14UV_B10C spectra are the most likely to overpredict both ratios). This results from these winds now being in a partially-ionised X-ray regime. In this case, the S14UV_sol08 spectrum's significantly higher EUV flux raises the electron density (which scales as $\sqrt{\Phi}$ Glassgold et al., 1997; Igea & Glassgold, 1999; Glassgold et al., 2007), and thus the recombination rate of Ar III to Ar II.

We can now turn our attention to the absolute luminosities, focusing, as argued above, on higher (nominal) mass-loss rates. To understand the scalings seen here, we first consider the energies of absorbed X-rays. In the X-ray regime, multiply-ionised species are predominantly created via inner-shell ionisation due to the Auger effect rather than valence-shell ionisation; singly ionised species are then predominantly created by recombination (or charge exchange) of more highly-ionised species. In the case of Ne, the most important inner shell is the K (n=1) shell, with ionisation energy 870.1 eV while for Ar, it is the L (n=2) shell (the K shell of Ar being much more tightly bound) with an ionisation energy of 249.2 eV. Thus, the most relevant X-rays for Ne ionisation are at modestly higher energies than the most effective X-rays for heating (Section 3.3.2). Therefore X-ray–driven winds are likely to be modestly optically thin to these X-rays; we can also see this by calculating the column density of a self-similar wind model by integrating:

$$N(\phi) = \int_{r_{\text{in}}}^{r_{\text{out}}} n_G \tilde{n}(\phi) \left(\frac{r}{r_G}\right)^{-b} dr \tag{4.12}$$

$$\propto n_G r_{\text{out}}^{1-b} - r_{\text{in}}^{1-b}. \tag{4.13}$$

Substituting Equation 4.9 and assuming $b = 1.5$:

$$N = 1.6 \times 10^{20}\ \mathrm{cm}^{-2} \left(\frac{\dot{M}}{10^{-8}\ M_\odot\ \mathrm{yr}^{-1}}\right) \frac{1}{\mathscr{M}_\mathrm{b} \cos(\phi_\mathrm{b})} \left(\frac{r_\mathrm{out}}{100\ \mathrm{au}}\right)^{-1/2} \left(\frac{r_\mathrm{in}}{1\ \mathrm{au}}\right)^{-1/2}, \quad (4.14)$$

where the amount of ionising X-ray absorbed scales as $L_\mathrm{X}(1-e^{-\tau}) \sim L_\mathrm{X}\tau \propto L_\mathrm{X}N \propto L_\mathrm{X}\dot{M}$.

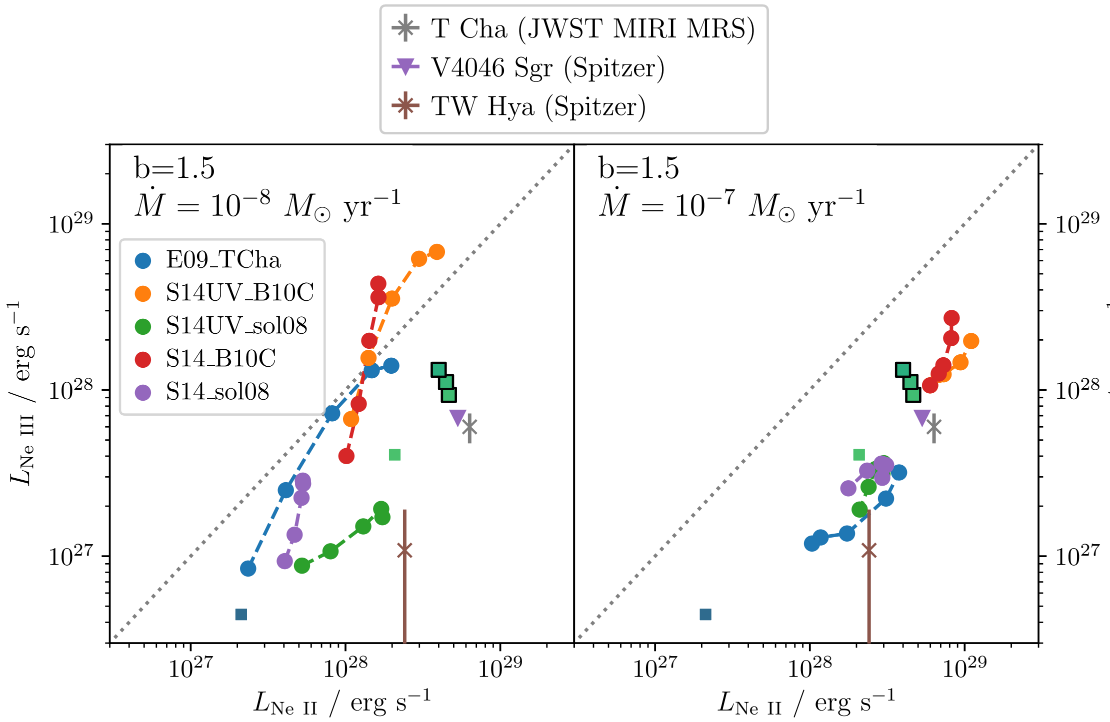

Fig. 4.3 Comparison of the [Ne III] 15.55 μm and [Ne II] 12.81 μm luminosities for each of the different T Cha spectra considered in this work. Results are shown for $b = 1.5$ and for the two highest $\dot{M}$: $10^{-8}\ M_\odot\ \mathrm{yr}^{-1}$ (left) and $10^{-7}\ M_\odot\ \mathrm{yr}^{-1}$ (right). Included for comparison are the models of Ercolano & Owen (2010) (squares) and JWST/Spitzer measurements for T Cha, TW Hya and V4046 Sgr (upper limit). Note that the errorbars on the [Ne II] luminosity are too narrow to be visible.

Consequently, comparing the panels of Figure 4.3, we see that the $10^{-7}\ M_\odot\ \mathrm{yr}^{-1}$ models are more luminous in [Ne II] than the $10^{-8}\ M_\odot\ \mathrm{yr}^{-1}$ models. While the most luminous of the latter do approach the [Ne II] luminosity of T Cha, they do so at much too high a [Ne III] luminosity. Thus, we are more or less forced to favour $10^{-7}\ M_\odot\ \mathrm{yr}^{-1}$ as the only models capable of reaching the observed [Ne II] luminosity of T Cha.

Comparing the performance of the different spectra, we can see that the observed value is straddled by the higher luminosity spectra S14_B10C and S14UV_B10C and the other, lower luminosity spectra. This suggests that a key component of a favoured model is a high

L_X as found in the S14_B10C or S14UV_B10C spectra. Although not tuned for the other systems, this set of high $\dot{M}_{\rm nom}$ is also broadly consistent with the [Ne II] and [Ne III] fluxes for V4046 Sgr and TW Hya, though taken at face value, the later would appear to require a lower luminosity spectrum.

For each spectrum we show models with five different inner radii; increasing $r_{\rm in}$ has a strong positive effect on the luminosity at 10^{-8} $M_\odot$ yr^{-1} but less at 10^{-7} $M_\odot$ yr^{-1} (there is also a slightly higher dependence the more EUV the irradiating spectrum has relative to X-ray). This reflects the contribution from the EUV-heated innermost regions of the wind (which is relatively larger in the lower $\dot{M}$ case). As the inner radius grows, the EUV-heated region moves outwards and its volume increases, which results in a brighter EUV-induced contribution to the emission. However, despite the strong dependence, we cannot really therefore use Ne line luminosities alone to constrain the wind's inner radius as whether a large or small radius is preferred depends on whether the wind spectrum has a low or high L_X respectively, and there is enough observational uncertainty in this value.

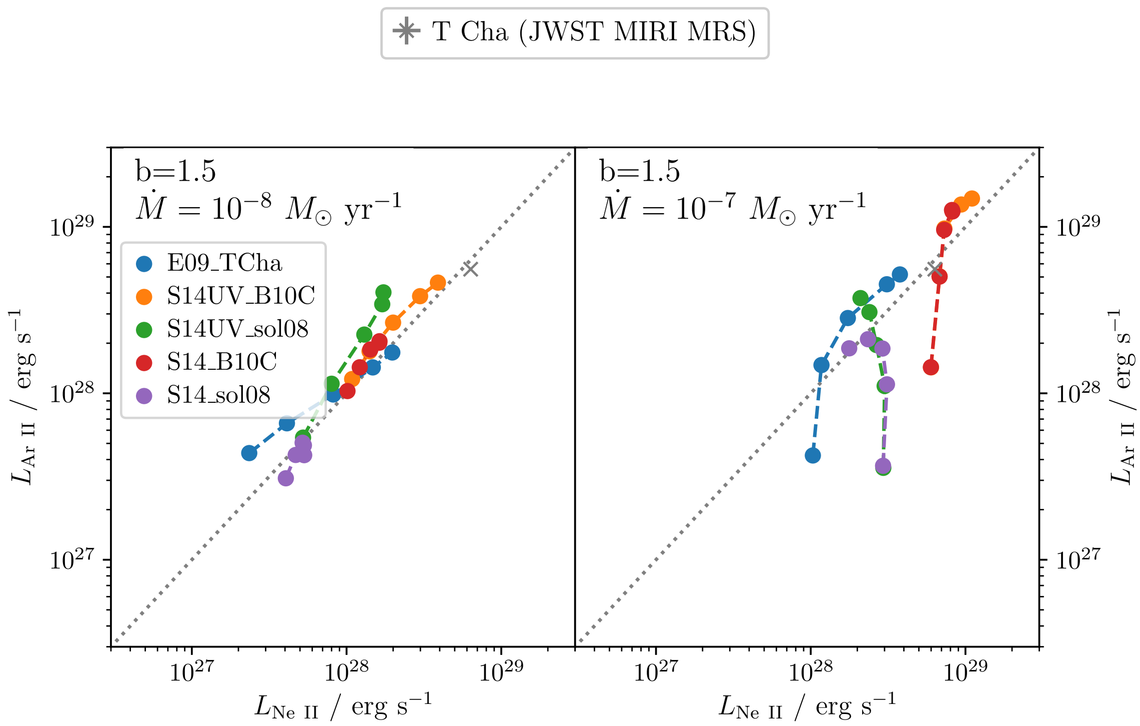

Fig. 4.4 As with Figure 4.3 but comparing the [Ar II] 6.99 μm and [Ne II] 12.81 μm luminosities. JWST measurements of [Ar II] for T Cha are included for comparison.

We can get a better constraint by comparing the [Ne II] and [Ar II] luminosities. At $\dot{M}_{\rm nom} = 10^{-7}$ $M_\odot$ yr^{-1}, we see a much stronger dependence on the inner radius for the [Ar II] than for the [Ne II] as the Ar ionisation energies are much lower (249.2 eV for L shell ionisation) and so these winds are moderately optically thick to the Ar-ionising radiation and thus benefit from a larger emitting volume with increased inner radius. Thus, for our high L_X spectra, we find that the [Ar II] fluxes taken in combination with the [Ne II] suggest an inner radius of around 0.1 r_G. Lower luminosity spectra with large inner radii would tend to overpredict [Ar II] relative to [Ne II].

For comparison, we also include in Figure 4.3 the luminosities calculated by Ercolano & Owen (2010) from the radiation-hydrodynamic simulations of both primordial and inner-hole discs. While the inner-hole discs are designed to be appropriate models for transition discs such as T Cha, they imply significant emission near the midplane from the flow emanating from the directly irradiated cavity rim. Since we do not include this region in our models - and T Cha is not thought to have a significant gas cavity (Wölfer et al., 2023) - the most relevant comparison is to the $L_X = 2 \times 10^{30}$ erg s^{-1} primordial disc, with $L_{\mathrm{Ne\ II}} = 2.08 \times 10^{28}$ erg s^{-1} and $L_{\mathrm{Ne\ III}} = 4.08 \times 10^{27}$ erg s^{-1} (indicated by the green, borderless, square in the figures). We see that this point lies between the models with nominal mass-loss rates $10^{-8} - 10^{-7}$ $M_\odot$ yr^{-1} for the E09_TCha spectrum (close to a line joining models with $r = r_G$), putting it in good agreement with our models. Although the mass-loss rate of the Ercolano & Owen (2010) model is 1.36×10^{-8} $M_\odot$ yr^{-1} and yet it is closest to our 10^{-7} $M_\odot$ yr^{-1} model, the stellar mass, sound speed and disc extent in their models are somewhat less than those assumed in our model, resulting in the two having comparable densities.

Discussion of Best-Fitting Model

Thus our single best-fitting model would appear to be $\dot{M}_{\mathrm{nom}} = 10^{-7}$ $M_\odot$ yr^{-1} (such that the ionisation level is low), with a high luminosity (S14_B10C/S14UV_B10C spectra) and relatively small inner radius ~ 1.3 au $= 0.1$ r_G. The greatest weakness of such a model is that it somewhat overpredicts the amount of emission from doubly ionised species relative to their singly ionised counterparts.

Such high mass-loss rates are achievable with X-ray–driven winds for very high L_X (which we find to be the best fit), but not EUV-driven winds. The nominal mass-loss rate is substantially more than the accretion rate of T Cha, though since this disc may be undergoing dispersal, this could be a selection effect (although there is no gas cavity Wölfer et al., 2023). Moreover, the modelled densities should correspond to a lower photoevaporation rate in reality (Equation 4.10) given that the sound speed in such a dense wind would likely be lower than assumed in calculating the mass-loss rate, and given that the wind may not launch from all radii. Alternatively, these mass-loss rates can also be achieved via magnetically-driven winds (Figure 1.6).

Moreover, since photoevaporative winds, energetically speaking, should not launch within these sorts of radii (especially considering that, for the $\dot{M}$ that we prefer, $c_S < 10$ km s^{-1} and so 13 au will be an underestimate of r_G) this potentially implies that the nature of the wind traced by the [Ne II], at least for T Cha, is that of an inner, MHD-driven, wind.

4.3.4 [Ne II] Line Shapes

As a further constraint, we consider line profile shapes; we shall see that the conclusions are broadly consistent with those drawn from luminosities alone. We compare to [Ne II] line profiles from the VISIR spectrometer on the VLT for T Cha and V4046 Sgr (Sacco et al., 2012; Pascucci et al., 2020). The centroid shifts are derived relative to the systemic velocity, which is usually determined by fitting a variety of photospheric absorption lines; comparing the results from various lines suggests that the typical error in the centroid shifts is around 1 km s^{-1} (Pascucci et al., 2015). Since Sacco et al. (2012) provide uncertainties on their measurements that are consistent with this estimate, we use their values for the centroid shift and FWHM of [Ne II], noting that they are consistent within the error bars with the Pascucci et al. (2020) values (which were also derived by reanalysing the same dataset of Pascucci & Sterzik, 2009). For V4046 Sgr, Pascucci et al. (2020) fit the radial velocity using a precise measurement of the circumbinary CO disc, which reduces the error in the systemic velocity to just 0.01 km s^{-1}. As it is a differential measure of two velocities, the FWHM is not so sensitive to the wavelength calibration and hence typically has smaller error bars.

In Figure 4.5 we show the key summary statistics of our modelled line profiles for the E09_TCha and E09_V4046Sgr spectra, compared to that of the data. This includes the centroid shift and FWHM described above; we also measure the full width at the 10th percentile and 68th percentile of the line peak to determine how triangular or boxy the shapes are (analogously to Banzatti et al., 2022, though we find it advantageous to use a lower value of 68 rather than 75 to avoid noisier regions around the line peak).

For T Cha, all our models slightly underpredict the centroid shift of -4.7 km s^{-1}, although the profiles for higher mass-loss rates are consistent within the typical uncertainty. Moreover, none of them are quite broad enough to match the observed FWHM though the $\dot{M} = 10^{-8}\ M_{\odot}$ yr^{-1} models with $r_{\rm in} \leq 0.3\ r_G$ are broadest and in best agreement with the line shape; thus in the bottom panel of Figure 4.5, we compare our line profiles for $\dot{M} = 10^{-8}\ M_{\odot}$ yr^{-1} and $r_{\rm in} = 0.03 - 0.3\ r_G$ with the observed data. Overall, we see that the line shapes also prefer a small inner radius $\lesssim 0.3\ r_G$ that may be more consistent with an MHD-driven wind than photoevaporation. In the right-hand column of Figure 4.6 we show equivalent models for the S14UV_B10C spectrum (which were the best fit to the line

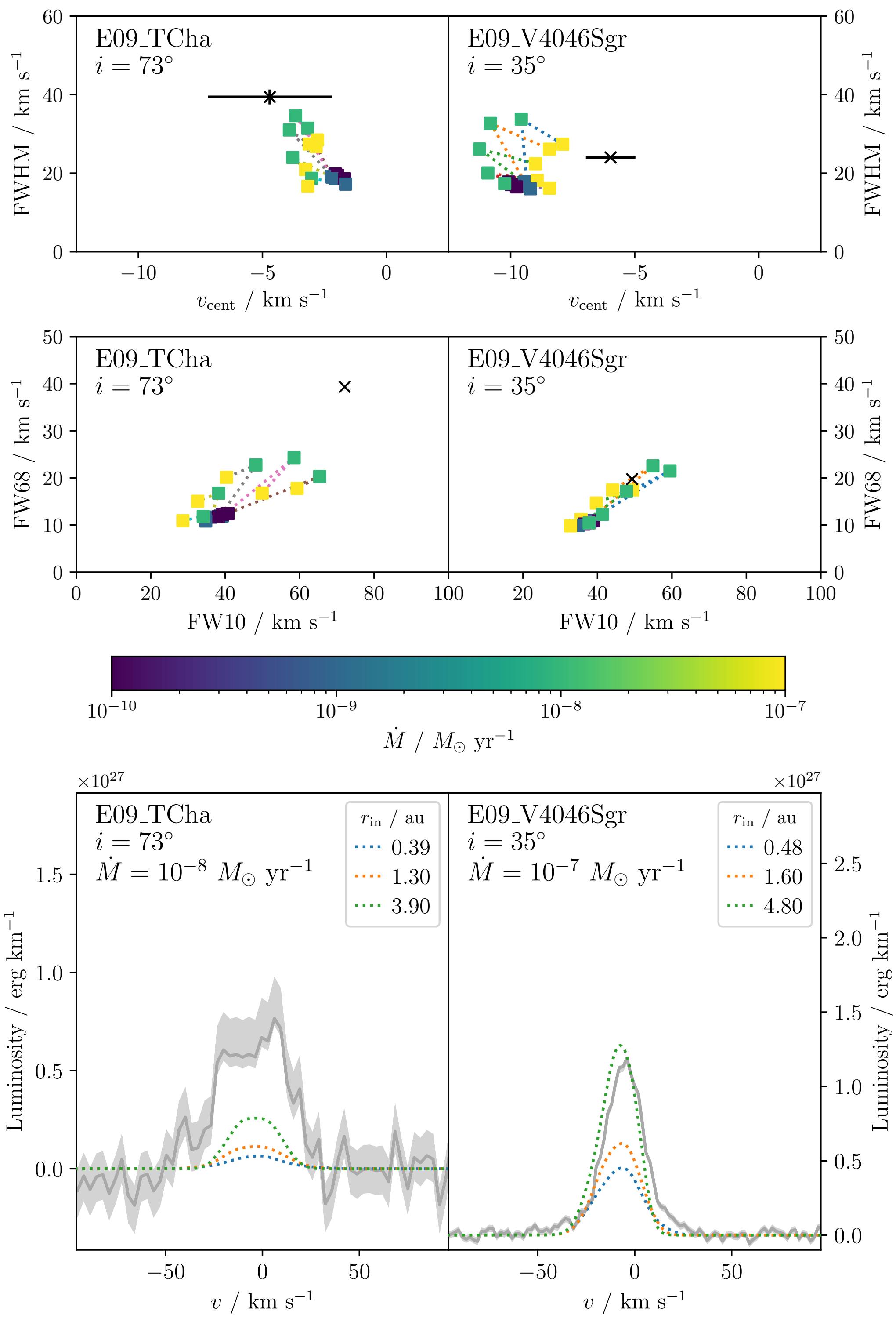

Fig. 4.5 The [Ne II] 12.81 μm line shapes for our E09_TCha and E09_V4046Sgr spectra compared to those of T Cha (left) and V4046 Sgr (right) respectively. The top panels compare the FWHM and centroid shift and the middle panels compare the full width at 68% and 10% of the maximum (an indicator of line shape). In each, dashed lines connect models with the same inner radius: 0.03 r_G (blue), 0.1 r_G (orange), 0.3 r_G (green), 1.0 r_G (red) and 3.0 r_G (purple), while the marker colour denotes the nominal mass-loss rate (see colourbar). The bottom panels show the predicted profiles for $r_{\rm in} = 0.03, 0.1, 0.3\ r_G$ overlaid on the observed profile for the $\dot{M}$ that appears to fit the shapes best in the upper panels. Since the shapes are relatively insensitive to the elemental abundances, for V4046 Sgr we show models with an elevated Ne abundance as this matches the luminosities best (Section 4.3.6).

luminosities). The spectrum does not affect the line shapes or the quality of their agreement with the data significantly.

Conversely, our models reproduce the shape for V4046 Sgr much better. Although we now overpredict the centroid shift, the models are nicely spread around the observed FHWM, as well as being clustered around the ratios of widths measured at 10% and 68% of the flux. Based on these parameters, there is a preference for $\dot{M} = 10^{-7}\ M_\odot\ \mathrm{yr}^{-1}$ and $r_{\mathrm{in}} = 0.1 - 0.3\ r_G$. In the individual line profiles, the overestimated blueshift can be seen in the location of the line peak, but we also seem to miss some flux on the red wing (which seems more extended than the blue wing). This could potentially be the contribution from a receding wind seen through a cavity, though from observations it is unclear how big such a cavity may be.

That we better reproduce the [Ne II] line profile for V4046 Sgr is consistent with the literature; although in part the large line width for T Cha results from its high inclination, we see in Figures 8 and 7 of Ballabio et al. (2020) and Pascucci et al. (2020) respectively that it lies some way above predicted trends with inclination that the other sources broadly seem to follow. We should be careful therefore that the conclusions we draw from T Cha about the origin of the [Ne II] emission may not be representative of transition discs as a whole.

Underpinning the results shown so far was the fact that X-ray–driven winds are modestly optically thin to the X-rays that ionise Ne via K shell ionisation. The total amount of ionised Ne, and thus the Ne luminosities, therefore depend on the amount of absorbed X-ray. According to Equation 4.13 this is largely controlled by the wind's inner radius for $b = 1.5$. However, for $b \leq 1$, the absorption shifts from being predominantly at small radii to large radii. We therefore briefly consider what the effect of a lower b on the shapes is in the left-hand panels of Figure 4.6. As found by Ballabio et al. (2020), a lower b predominantly results in narrower emission lines, thus worsening the agreement with the data. This is because the emitting material is shifted to larger radii; since T Cha is observed at such high inclinations, the line width is mainly due to Keplerian broadening which drops off as $R^{-1/2}$.

Effect of Slit Size

One limitation of the VISIR data is that the slit widths are quite narrow: the T Cha data were taken with a 0.4" slit, corresponding to around 40 au. By comparison to Spitzer values, Pascucci et al. (2020) concluded that the [Ne II] fluxes measured from these data may be lower than their true value by a factor ~ 2. We do not rescale the profiles here as this would likely not occur homogeneously across the line profile. Instead we now consider the effects of masking out cells in our models which would fall outside the slit.

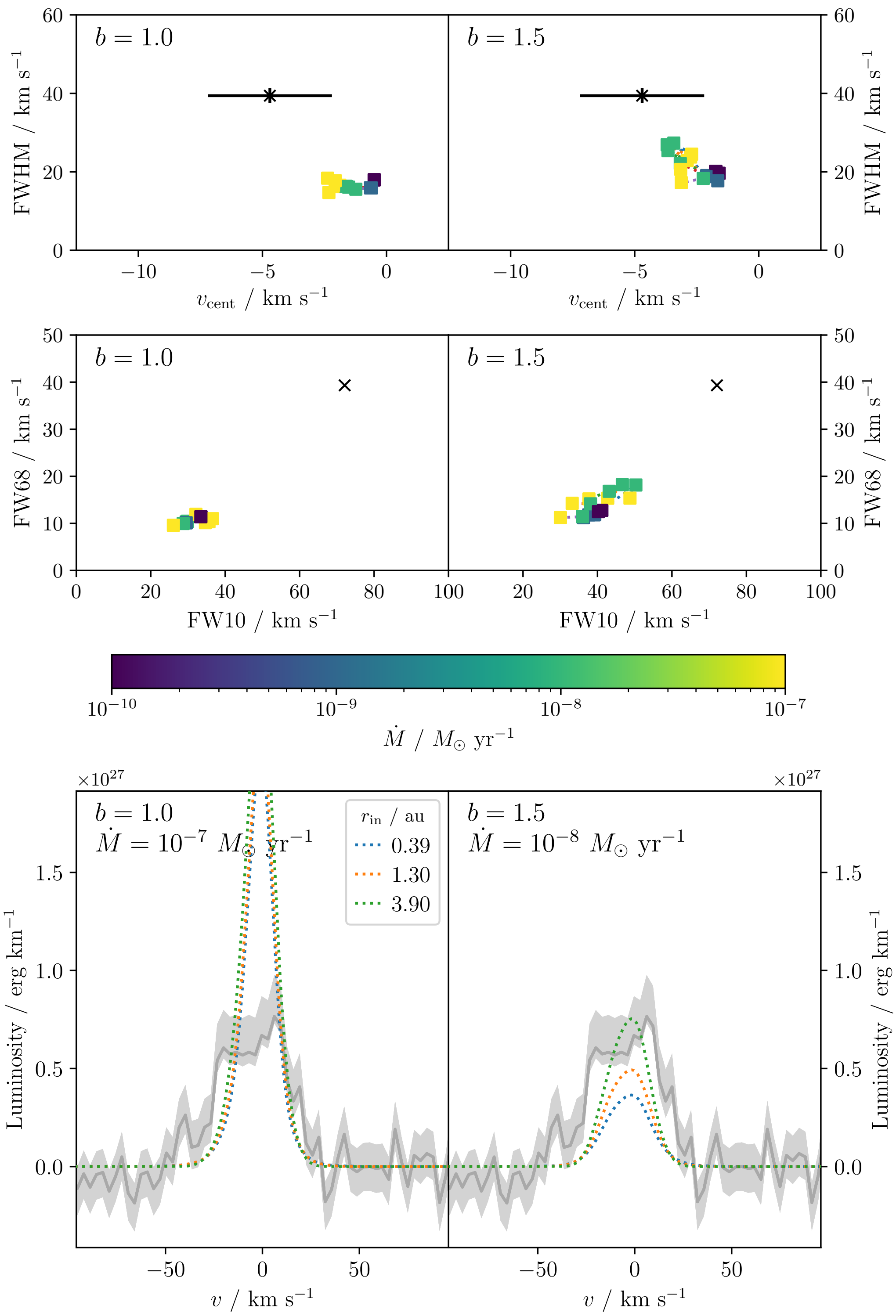

Fig. 4.6 [Ne II] line shapes as in Figure 4.5 but for the S14UV_B10C spectrum. $b = 1.0$ is shown in the left-hand column and $b = 1.5$ on the right. In both columns, the data are for T Cha.

We show these results in Figure 4.7 for the two slit position angles used to take the data (according to the ESO archive): 98° (left) and 172° (right) (which compare to a disc position angle of $113-114°$ Huélamo et al., 2015; Pohl et al., 2017). In either case, we lose flux from large radii, where the Keplerian broadening is weakest and consequently predominantly from the line peak (while the wings are relatively unaffected). This results in profiles with a flattened top that are less triangular. Moreover, since the flux at half maximum is reduced, the FWHM is increased. When the slit is taken at 98°, which is closer to alignment with the disc's major axis, we see that the net blueshift increases, implying that flux is preferentially lost from the redshifted line wing. Overall, the effects of the finite slit width marginally improve the agreement between our models and the data.

Cavities

As discussed, since a net blueshift is observed for the [Ne II] emission lines, it is generally understood that the redshifted emission from the receding wind on the disc's far side is hidden by optically thick micron-sized dust in the disc. However, as introduced in Section 4.3.1 T Cha has a cavity in small dust between $0.1-0.2$ au and $7-30$ au (Brown et al., 2007; Olofsson et al., 2011, 2013; Pohl et al., 2017). Since our best matching models have $r_{\rm in} = 0.39-3.9$ au, their inner radii likely lie within this cavity. Therefore the disc may not be optically thick to significant amounts of emission if it originates where our model suggests. We thus adapt Equation 4.7 and reanalyse our models by masking out only those cells lying between

$$R_{\rm cav}^2 < (R\cos(\phi) - z\tan(i))^2 + (R\sin(\phi))^2 < R_{\rm out}^2, \tag{4.15}$$

for the cases $R_{\rm cav} = 10$ au and $R_{\rm cav} = 30$ au

Comparing Figure 4.8 to Figure 4.6 shows that as one might expect, additional flux on the red wing from inside the cavity acts to lower the line centroid shift, while simultaneously broadening it; while these effects are slightly larger for the larger cavity, there is no significant qualitative difference between the two cases. Given that the fractional uncertainty in the centroid shift is larger, statistically speaking, this does improve the fit. In fact, in the case illustrated (albeit where $\dot{M} = 10^{-8}\ M_\odot\ {\rm yr}^{-1}$), the flux in the red wing is quite consistent with the data and the blueshifts of our models are limited by a lack of blue-wing emission, not by an excess of emission from the cavity. Moreover, given that the slit width effects increase FWHM and can increase the centroid shift, the two acting together may be able to provide the best fit to the line shape. Therefore, we conclude there is not strong evidence to exclude small $r_{\rm in}$ models on the basis that the emission would arise within a cavity.

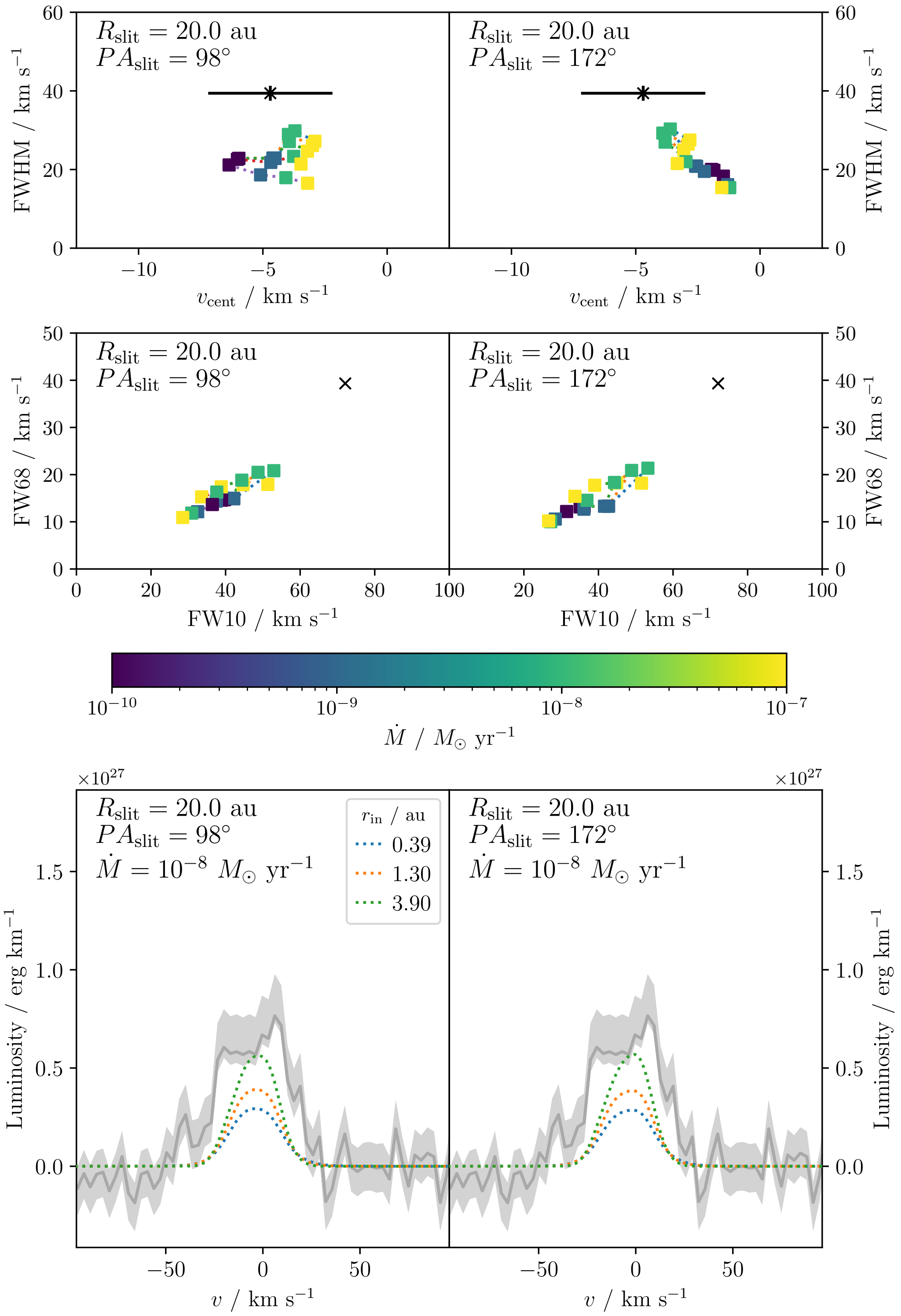

Fig. 4.7 [Ne II] line shapes for the S14UV_B10C spectrum as in Figure 4.6 but masking material which would fall outside the slits used for observations given position angles of 98° (left) and 172° (right). In both columns, the data are for T Cha.

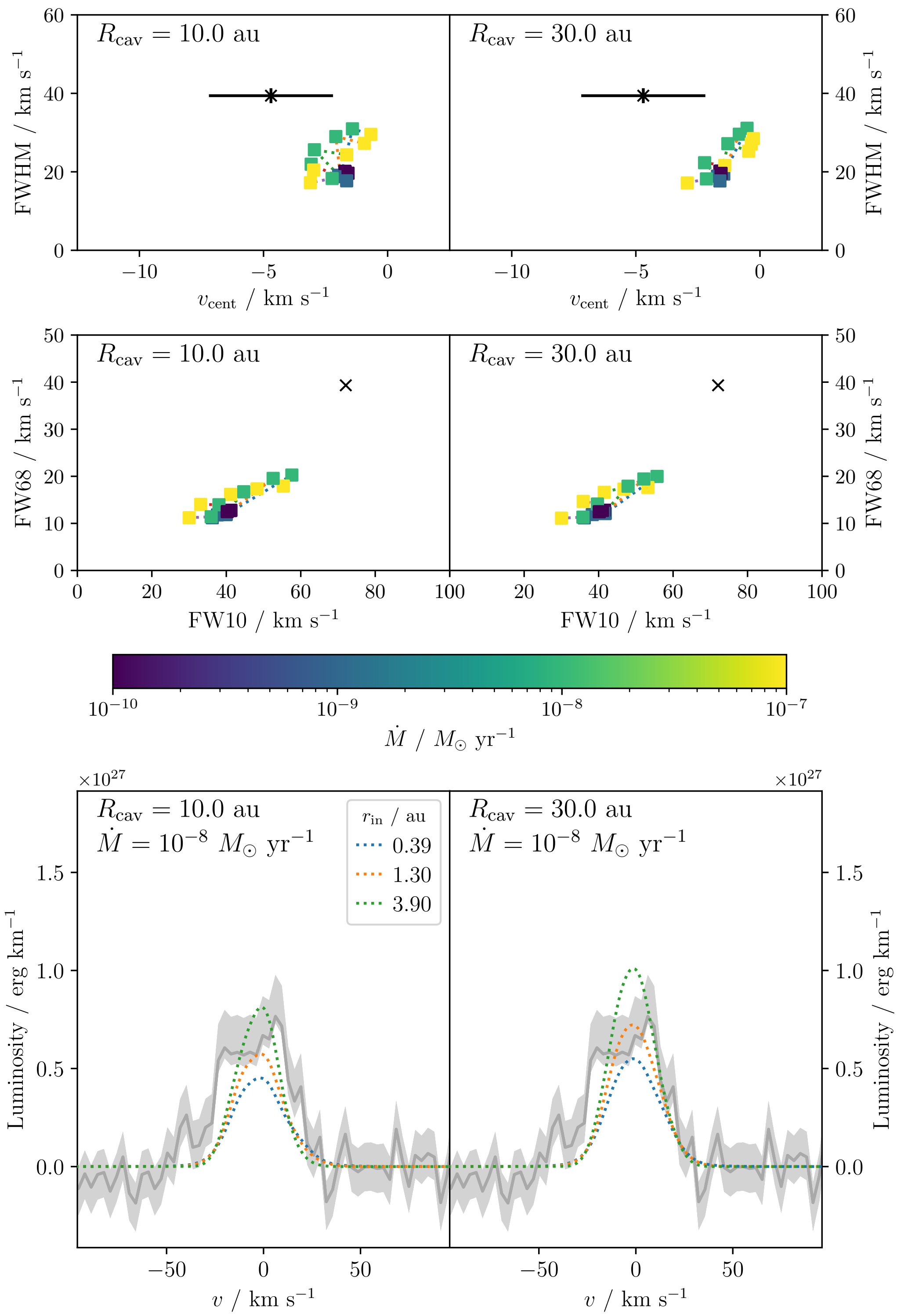

Fig. 4.8 [Ne II] line shapes for the S14UV_B10C spectrum as in Figure 4.6 but including a transparent cavity out to $R_{\rm cav=10}$ au (left) and $R_{\rm cav=30}$ au (right). In both columns, the data are for T Cha.

4.3.5 Synthetic JWST Imaging of T Cha in [Ne II] emission

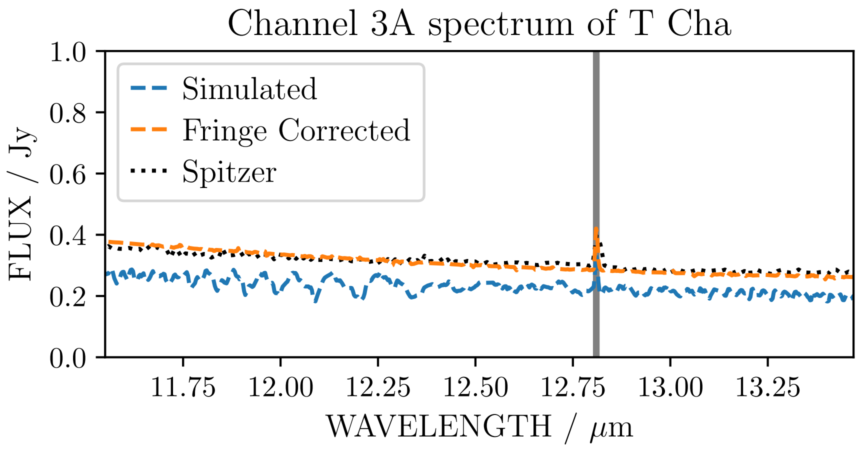

Fig. 4.9 The simulated MIRI MRS Channel 3A spectra before (blue) and after (orange) we apply the fringe correction. The [Ne II] 12.81 μm line can clearly be seen in the fringe corrected spectrum as well as the Spitzer spectrum and the grey bar highlights the region that we use to produce the images.

Having determined that the best fit to the observed line luminosities are $\dot{M} = 10^{-7}\, M_{\odot}\ \mathrm{yr}^{-1}$ models with the S14UV_B10C spectrum, we now proceed to produce synthetic images of them following the procedure outlined in Section 4.3.2. We do this for all the different r_{in}, despite the constraints we were able to put, as the aim is to see to what degree JWST will be able to measure the emission's extent. As aforementioned, we treat the residual fringing in the output spectrum using continuum-only models; this allows us to calculate the transmission for MIRISIM and the pipeline relative to the known continuum and then we divide our full model by this factor to recover the expected spectrum. The spectra before and after this procedure are compared to the Spitzer spectrum in Figure 4.9, where we also highlight the region of the spectrum around the line that we extract to produce the images (12.81 ± 0.005 μm - equivalent to ± 120 km s^{-1} about the line centre).

Figure 4.10 shows the full gallery of images we produce. In the left-most column we show the theoretical distribution of the emission. On the right-hand side of these plots, a faint region of the receding wind can be seen beyond the disc's edge. The black band running top-bottom is the cold and neutral - and therefore dark - disc material (which we do not simulate). The brighter left-hand side of the image shows the emission from the wind from the disc's upper surface. Little difference in morphology is visible for the three smallest radii - each has a bright core and an extended halo - though the halo gets a bit brighter as r_{in} increases. Once $r_{\mathrm{in}} = r_G$, we start to see a ring-like morphology emerge from the bright core, which can be seen most clearly at $r_{\mathrm{in}} = 3\ r_G$. This represents the wind's bright innermost

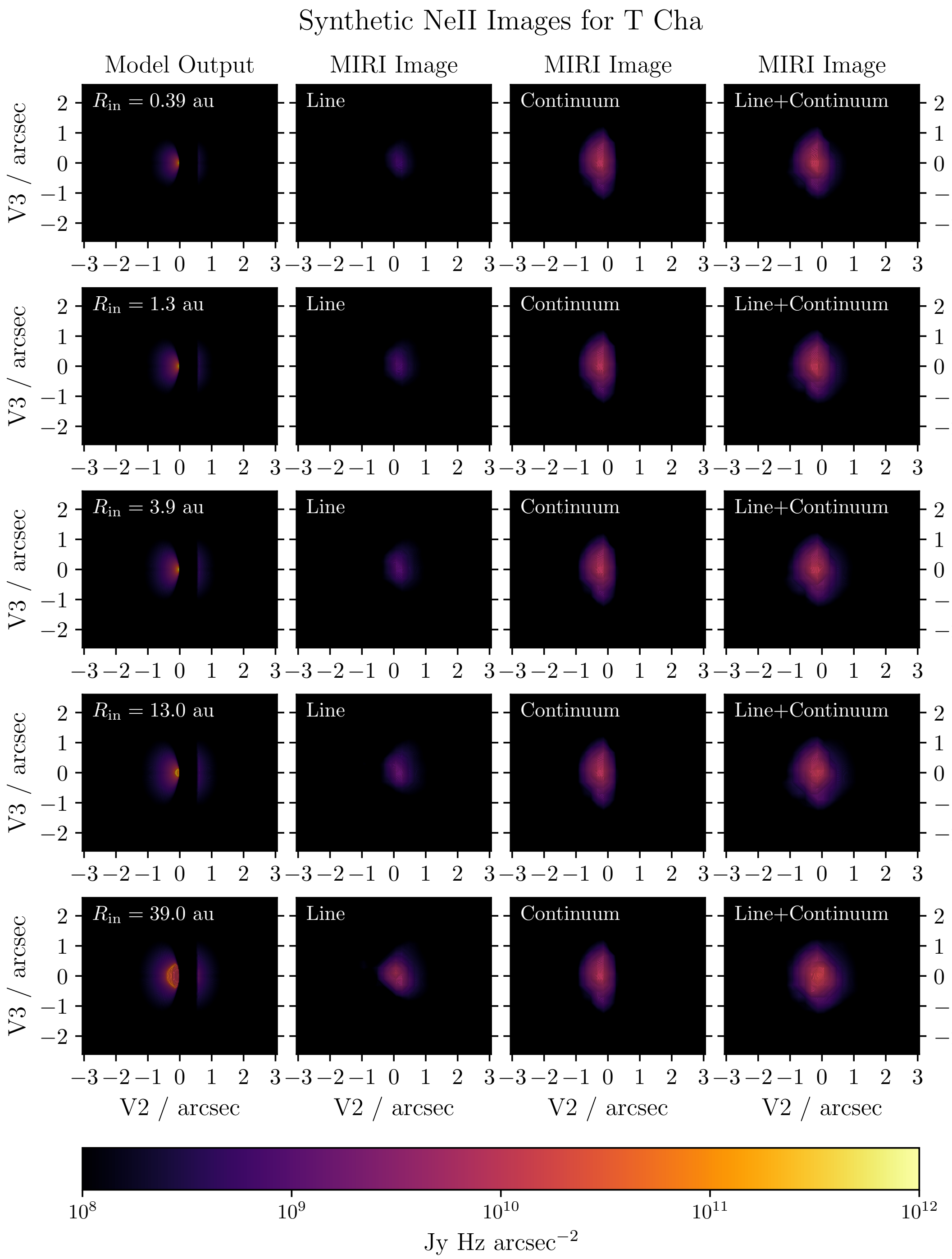

Fig. 4.10 Left-most column shows the theoretical distribution of [Ne II] at the full resolution of our simulations for the models with $b = 1.5$, $\dot{M} = 10^{-7}\ M_{\odot}\ \mathrm{yr}^{-1}$ using the S14UV_B10C spectrum. The other columns show synthetic images produced by MIRISIM and the JWST pipeline for scenes including the line only, the disc and stellar continua only and the full model including both. From top to bottom, each row shows the models with increasing $r_{\rm in}$.

edge, which is spherical in our model (and hence doesn't appear foreshortened by the disc's inclination). The second column shows how these morphologies would be resolved by MIRI MRS. Aside from a brightening with increasing r_{in}, there is no obvious variation except for the largest inner radius, where the bright ring leads to the emission becoming more extended along the V2 direction.

The third column shows the continuum distribution, which doesn't differ between models. It is clearly more extended in the V3 direction than the V2 direction and in each case appears brighter and more extended than the [Ne II] emission (although the V2 extents for $r_{\mathrm{in}} = 3\ r_G$ are more comparable). Consequently, in the full images in the final column it is impossible by eye to distinguish the [Ne II] emission, save for the largest inner radius where the total image begins to look more round.

Therefore, if the [Ne II] distribution is to be recovered in order to more directly measure the emitting region, careful continuum subtraction and extent fitting procedures will be needed. These are under preparation (Bajaj, in prep.) and once finalised we will apply them to the datacubes represented by these images to quantify JWST's ability to resolve Ne II emission. Most likely, given early indications from the data and the preference for smaller inner radii expressed here, we will be able to put an upper limit on the emission extent in T Cha, in which case we may be able to rule out photoevaporation if this is required to be very compact.

4.3.6 Exploring Neon to Oxygen ratios

Parameter Exploration

As introduced in Section 1.4.2, the [Ne II] 12.81 μm luminosity increases with the infrared spectral index n_{13-31}, while that of the [O I] 6300 Å appears to decrease, indicating changes as the inner disc clears (Pascucci et al., 2020). While we generally see increasing [Ne II] emission with increasing inner radius, since the discs in the sample are mostly not thought to have large gas cavities (Wölfer et al., 2023), it is unlikely that this is what influences the observed trend. Here we therefore discuss other possibilities using our models, including variations in the mass-loss rate, spectrum or elemental abundances.

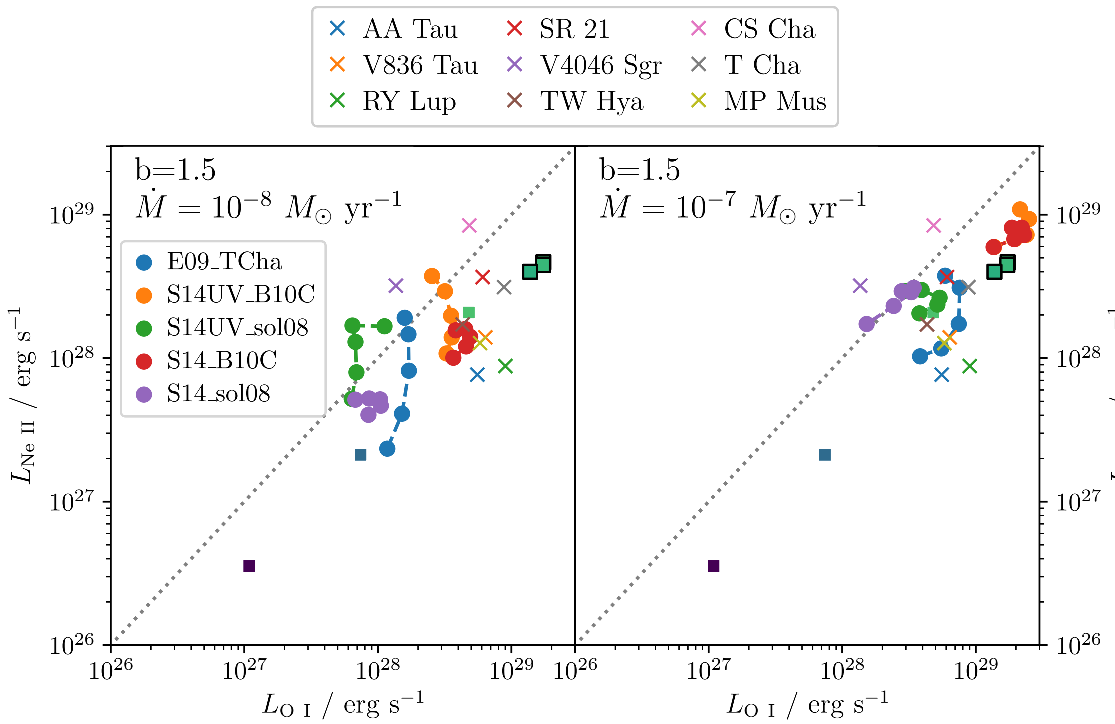

Fig. 4.11 As with Figure 4.3 but comparing the [Ne II] 12.81 μm and [O I] 6300 Å luminosities. Observational data are taken from the sample in Pascucci et al. (2020) where a [Ne II] LVC is detected. For a homogeneous sample we use their VISIR Ne II measurements but since we are more interested in the overall trends with model parameters rather than achieving a fit to any particular source, we do not attempt to correct the fluxes for slit loss.

Figure 4.11 shows the relationship between the Ne II and O I emission for each T Cha model spectrum. The figure includes data from the VISIR spectrometer; these [Ne II] fluxes may be lower than their true value by a factor ~ 2 (estimated by comparison to Spitzer values, Pascucci et al., 2020) due to the instrument's narrow slit.

Comparing the two panels, we see that at $\dot{M}_{\rm nom} = 10^{-7}\ M_\odot\ {\rm yr}^{-1}$, the ratios are nearly all such that $L_{\rm NeII} < L_{\rm OI}$ as seen in most observed data; at lower mass-loss rates some models start to stray into the regime of $L_{\rm NeII} > L_{\rm OI}$ and this would be expected to become even more significant at $\dot{M}_{\rm nom} \lesssim 10^{-9}\ M_\odot\ {\rm yr}^{-1}$ where the winds are essentially fully ionised and contain little O I (the degree of ionisation of O is closely tied to that of H via charge exchange). At higher densities, comparing for example the S14_sol08 and S14UV_sol08 spectra, we see that the additional EUV tends to boost the [O I] (and so lower the $L_{\rm NeII}/L_{\rm OI}$ ratio) by creating more gas that is sufficiently hot to excite optical lines (c.f. Ercolano & Owen, 2016). The effect is somewhat limited however as most of the extra photons are in the range $13.6 - 20$ eV where O I has a high photoionisation cross-section. Therefore, it is unlikely that changes in the spectrum alone could produce the variance seen in the [Ne II]/[O I] ratio. Moreover, lowering the wind's nominal mass-loss rate would generally appear to lower the line luminosities too much.

The unusual case of V4046 Sgr

There are only two sources in our sample which are brighter in the [Ne II] 12.81 μm line than in [O I] 6300 Å (in contrast to most of the models shown so far): CS Cha, which is a circumbinary disc (Guenther et al., 2007) with a gas cavity on the order of 10 au (Wölfer et al., 2023) and so could be explained by a large $r_{\rm in}$, and V4046 Sgr. In the left-hand panel Figure 4.12 we show that V4046 Sgr is something of an outlier when considering the trend of line luminosities with n_{13-31} (whereas CS Cha does have the largest n_{13-31}).

Unsurprisingly therefore, it is difficult to reproduce the [Ne II] and [O I] emission line strengths as shown in Figure 4.13 for the E09_V4046Sgr spectrum (shown as the blue "fiducial" model sets). The observed [O I] line luminosity seems to lie between that of our $\dot{M} = 10^{-8} - 10^{-7}\ M_\odot\ {\rm yr}^{-1}$ models, while both underpredict the [Ne II]. It is unlikely that V4046 Sgr could sustain such high photoevaporation rates for long; its accretion rate is only $10^{-9.22}$ and so its lifetime in this state would be exceptionally short. Moreover, over the 18 Myr estimated disc lifetime (the age of the β Pic moving group of which V4046 Sgr is a member, Miret-Roig et al., 2020), a $\dot{M} = 10^{-8}\ M_\odot\ {\rm yr}^{-1}$ wind alone would have removed nearly 0.2 $M_\odot$ of gas. Since any period with $M_{\rm disc}/M_\odot > 0.1 - 0.3$ should be short due to strong gravitoturbulent torques, the disc cannot have started much more massive than this.

Therefore, we could question the suitability of the abundances used here and whether alterations could address the challengingly high mass-loss rates required. We assumed that the disc gas inherits ISM gas-phase abundances from Savage & Sembach (1996), determined using absorption towards the star ζ Oph and tabulated as depletions/enhancements over solar (Anders & Grevesse, 1989; Grevesse & Noels, 1993). O appeared depleted (by -0.39 dex), likely due its inclusion in solid species, whereas Ne is assumed to be at solar levels. There is however reasonable uncertainty on the absolute solar Ne abundance due to a lack of suitable photospheric lines so it is usually derived with respect to O using solar energetic particles. For example, the development of 3D modelling lowered the estimated solar photospheric metallicity considerably from $Z = 0.0275$ to $Z = 0.0122$ (Asplund et al., 2005), with Ne simply reduced proportionally to O.

Ne does however have a plethora of lines at coronal temperatures. In using these, caution must be exercised as the coronae of active stars are subject to an inverse first ionisation potential (IFIP) effect where elements with high first ionisation energies are enhanced relative to those with lower ionisation energies (Brinkman et al., 2001; Audard et al., 2003). The same trend has been observed (Telleschi et al., 2007b) for T Tauri stars, which are very active. Ne has a higher ionisation potential than O and consequently in active stars may appear enhanced by a factor $2-3$ (Robrade et al., 2008).

However, for a small number of T Tauri stars, Ne enhancement relative to O above that achievable from the IFIP effect is seen. TW Hya (Kastner et al., 2002; Stelzer & Schmitt, 2004, Ne/O ~ 10) was the first identified, followed by none other than V4046 Sgr (Günther et al., 2006, Ne/O ~ 6). Conversely, for other sources - BP Tau (Drake et al., 2005), MP Mus (Argiroffi et al., 2007, 2009), and AA Tau (Schmitt & Robrade, 2007) - no additional enhancement is measured.

Drake et al. (2005) suggested that since TW Hya has an accretion signature in the X-ray, the anomalous enhancement may trace the composition of accreting material: an elevated Ne/O would result from the less-volatile O becoming locked in larger bodies (including planets and planetesimals) over time and thus depleted from the gas. Support for this scenario may come from evidence of Si depletion for both TW Hya and V4046 Sgr (Ardila et al., 2013), implying that less refractory material is making it onto the star.

If V4046 Sgr's wind consists of material of similar composition to the accretion streams, we might therefore also expect it to display an elevated Ne/O. Whether the wind should match the accreting composition depends on which bodies contribute most strongly to the oxygen depletion and where they accumulate relative to snowlines (where oxygen-bearing ices may sublimate back into the gas phase). Unfortunately, the sample for which both forbidden emission line luminosities and coronal abundances have been measured consists of only four discs, so while we compare these in the right-hand panel of Figure 4.12, we cannot draw any reasonable conclusions from it. However of these four, the two with elevated coronal Ne/O do also have a higher $L_{\mathrm{Ne\ II}}/L_{\mathrm{O\ I}}$.

Moreover, in the central panel of Figure 4.12, by eye there appears to be a decent correlation of the luminosity ratio with the factor by which Francis & van der Marel (2020) estimate the inner disc to be depleted of mm dust with respect to the outer disc. In these terms, V4046 Sgr is less of an outlier, implying that it could be the mm dust (which is more easily trapped) that is most important for explaining these trends. In this scenario, the wind could potentially originate anywhere inside the mm dust cavity ($\sim$ 30 au, Francis & van der Marel, 2020, and thus comfortably outside both the water snowline and r_G).

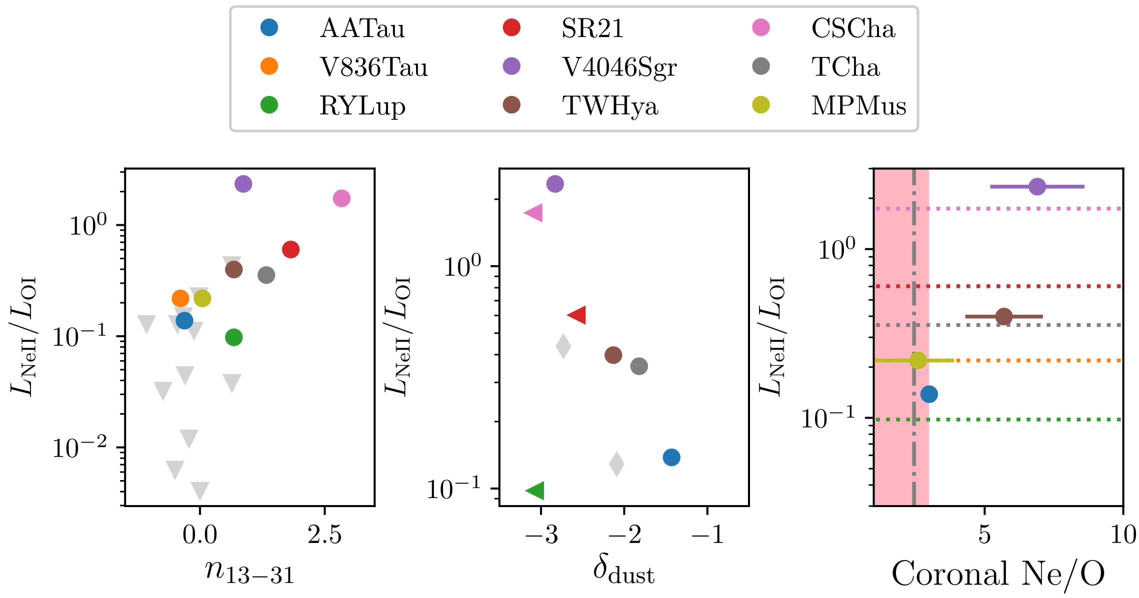

Fig. 4.12 Correlations involving the ratio of [Ne II] 12.81 μm and [O I] 6300 Å emission. The left-hand panel shows the known correlation with the 13 μm – 31 μm spectral index (Pascucci et al., 2020); sources with non-detections of Ne II are shown as downward pointing grey triangles. The middle panel shows a comparison to the $\delta_{\rm dust}$ measured by (Francis & van der Marel, 2020), the logarithm of the factor by which the inner disc is depleted in dust with respect to the outer disc based on ALMA observations. The triangles represent points for which [Ne II] is detected but no inner disc. The right-hand panel shows a comparison to X-ray measurements of coronal abundances taken from Günther et al. (2006) for TW Hya and V4046 Sgr, Argiroffi et al. (2009) for MP Mus and Schmitt & Robrade (2007) for AA Tau and renormalised to Asplund et al. (2005) solar abundances. The other Pascucci et al. (2020) discs with [Ne II] LVCs but without coronal abundance measurements are shown by horizontal dotted lines. The pink shaded area shows the coronal enhancement achievable by the IFIP effect while the vertical grey line shows that achievable by taking ISM gas-phase abundances rather than solar (Savage & Sembach, 1996).

An alternative way to achieve this ratio would instead be to boost the Ne abundance. Although Ne is highly volatile and not expected to freeze-out under protoplanetary disc conditions, Jupiter shows elevated abundances of other noble gases, similar to those observed for less-volatile heavy elements. Since the accretion of metal-rich solids is usually invoked to explain these abundances, Owen et al. (1999); Gautier et al. (2001) suggested that the noble gases were also delivered by planetesimals formed at temperatures low enough to trap volatile gases in amorphous ices or clathrates (< 30 K, though neon appears to require even lower temperatures Bar-Nun et al., 1985). Based on CO brightness temperatures, such conditions may be reached at > 100 au in V4046 Sgr (Law et al., 2022), well beyond the 63 au disc seen in mm emission (Martinez-Brunner et al., 2022). If icy solids did form at such distances, they have therefore presumably drifted inwards, potentially as far as the bright ring at $20-30$ au; any subsequent sublimation of Ne from the ices could have enriched this region of the disc, with interior regions becoming enriched as the accreting gas moves inwards. Assuming a $1/R$ surface density profile, there is approximately $300/63 \approx 5$ times more gas mass outside the mm-disc than within it, such that assuming a high efficiency of inward transport, there is enough material to raise the abundance of Ne by a factor of a few. Thus, on long enough timescales, the regions from which the wind is launching may feasibly have achieved a high Ne abundance through pebble drift *if* it can be effectively trapped.

Fractionation, the differential depletion of gaseous atoms based on their mass, has been suggested to operate during thermal winds driven from planets by stellar heating, including the solar system's rocky planets (e.g. Zahnle & Kasting, 1986). Since Ne is about 20 times heavier than H, it is potentially less susceptible to hydrodynamic escape and could thus become relatively enriched in the disc, thus providing an alternative mechanism for raising the neon abundance. However, if we follow the approach of Zahnle & Kasting (1986) to estimate the fractionation possible by a $\sim 10^{-8}\ M_{\odot}\ \mathrm{yr}^{-1}$ disc wind launched on scales $\sim r_G$, we find that the entrainment of Ne and H should differ by no more than 0.01% and we cannot consider this a viable way to enhance the Ne abundance in older discs.

In Figure 4.13 we therefore also show models where we additionally raise the Ne abundance or lower the O abundance by a factor 3 consistent with the factor (above the IFIP effect) needed to explain the coronal data (Günther et al., 2006). The effect is very simple: the Ne luminosities are scaled upwards by a factor 3 when it is enhanced and the O luminosities are scaled downwards by a factor 3 when it is depleted. For discs with larger $r_{\mathrm{in}} \gtrsim 0.3\ r_G$, this brings the $L_{\mathrm{Ne\ II}}/L_{\mathrm{O\ I}}$ ratio nicely into agreement with the observed ratio. For $\dot{M} = 10^{-8}\ M_{\odot}\ \mathrm{yr}^{-1}$ the absolute luminosities are still too low, though raising both abundances further may resolve this problem. The $\dot{M} = 10^{-7}\ M_{\odot}\ \mathrm{yr}^{-1}$ model with elevated Ne now overestimates the Ne luminosity so may need both abundances depleting somewhat. The

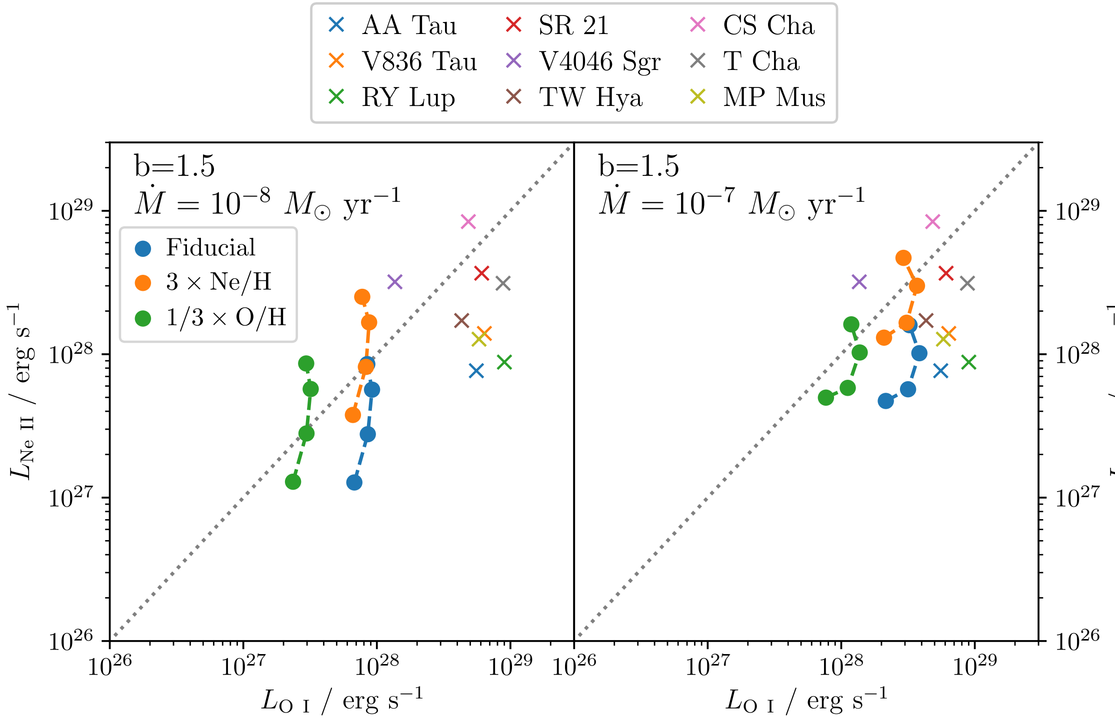

Fig. 4.13 As with Figure 4.11 but comparing models with the E09_V4046Sgr spectrum with ISM gas-phase abundances (Savage & Sembach, 1996) ("Fiducial") to those with elevated Ne/H or depleted O/H.

observed luminosities for V4046 Sgr sit on the locus joining the $\dot{M} = 10^{-8} - 10^{-7}\ M_\odot\ \mathrm{yr}^{-1}$ models for $r_{\mathrm{in}} = r_G$ and the elevated Ne abundance, so an intermediate mass-loss rate between the two would also reproduce the luminosities.

Moreover, we saw previously how the irradiating luminosity could strongly influence the emission. In particular, using the high L_X S14_B10C spectrum for T Cha boosted the [Ne II] luminosities; this spectrum was derived by Sacco et al. (2014) by assuming a coronal abundance pattern similar to that of TW Hya (Brickhouse et al., 2010). Since we know that V4046 Sgr has a similar pattern, then a thorough exploration of its X-ray spectrum may also yield a higher luminosity solution that assists in producing the required emission.

Unfortunately there is now too large a degenerate parameter space of abundances and spectra for us to make conclusive deductions here.

4.3.7 [O I] Line Shapes

Having explored the [O I] line luminosity, we briefly discuss its observed line profile for T Cha, shown in Figure 4.14. The observed line is negligibly blueshifted with $v_c = -0.4$ km s^{-1} while all our models tend to mildly overpredict the blueshift by around $1-3$ km s^{-1}, not much more than the typical uncertainty.

Much like all other constraints, the line shapes show a strong preference for high $\dot{M}$. In winds with $\lesssim 10^{-9}\ M_{\odot}\ \mathrm{yr}^{-1}$, the weak O I emission extends out to large radii with little Keplerian broadening and hence models predict much narrower lines than observed. At higher mass-loss rates, only the innermost regions are sufficiently heated to excite the [O I] transition so broader profiles are found; in particular, for $\dot{M} = 10^{-7}\ M_{\odot}\ \mathrm{yr}^{-1}$, inner radii of $0.03-0.1\ r_G$ straddle the observed FWHM of 46.8 km s^{-1}. The line shape also favours a high mass-loss rate: the observed ratio of the widths at 10% and 68% of the peak flux is ~ 2 and several models with $\dot{M} \gtrsim 10^{-8}\ M_{\odot}\ \mathrm{yr}^{-1}$ have $FW68/FW10 \gtrsim 2$. Once again the data seem to lie between the models with $\dot{M} = 10^{-7}\ M_{\odot}\ \mathrm{yr}^{-1}$ and inner radii of $0.03-0.1\ r_G$.

In the bottom panel of Figure 4.14, we show a comparison of our line profile for $\dot{M} = 10^{-7}\ M_{\odot}\ \mathrm{yr}^{-1}$ and $r_{\mathrm{in}} = 0.03-0.3\ r_G$ with the observed data. As expected from the summary statistics, a reasonably good match to the shape can be found. This adds to the weight of evidence - which we hope to confirm with the IFU imaging, that the disc wind from T Cha has a small inner radius.

4.3.8 Conclusions

In order to better understand what information about disc winds can be constrained by blueshifted forbidden emission line profiles, it is necessary to conduct forward modelling. I first showed that the elevation of realistic wind bases above the midplane has a small but non-negligible effect on emission line shapes, particularly on their FWHM: since winds with $\phi_{\mathrm{b}} > 0^{\circ}$ have lower opening angles, this enhances the poloidal velocity gradient - and therefore line width - seen at low inclinations, while decreasing it at high inclinations.

I then conducted a parameter study using the self-similar models. By irradiating the density structures using MOCASSIN, I determined ionisation fractions and temperatures that were consistent with the wind's density and radial extent, whereas previous applications of the self-similar solutions to forbidden emission line profiles (Ballabio et al., 2020) could only consider the shapes of normalised line profiles. This enables us to see how factors including the spectrum and the density control the line luminosities.

Crucially, although Ballabio et al. (2020) found that in general [Ne II] emission lines were best fit using a 10 km s^{-1} wind, characteristic of EUV photoevaporation, we find that

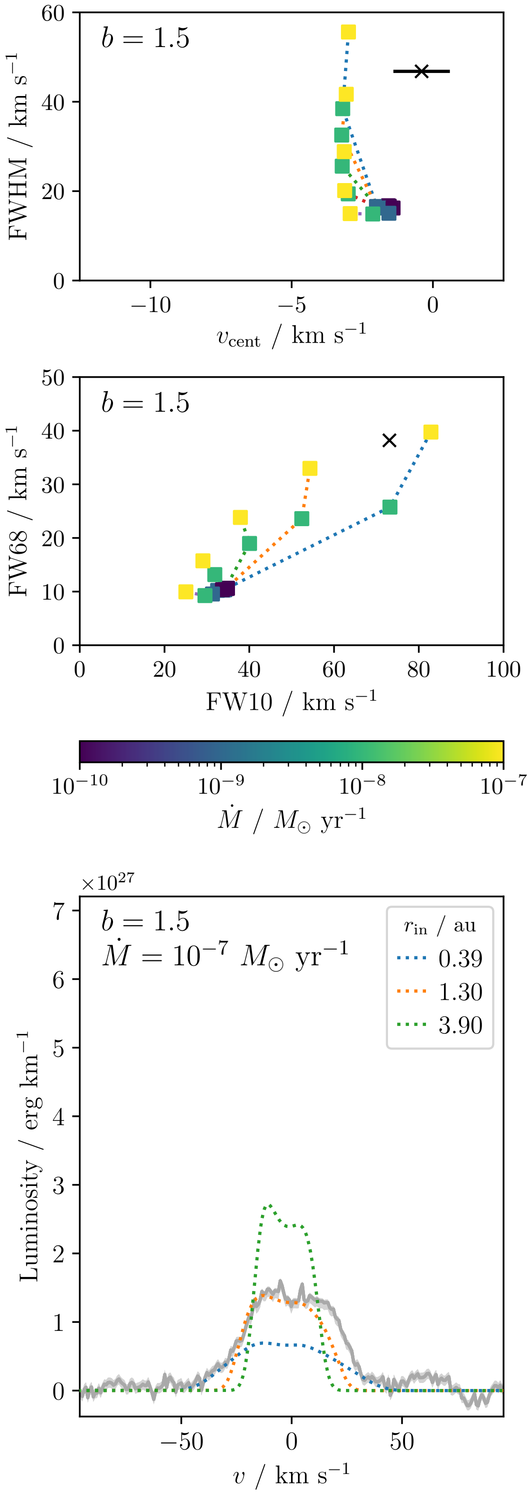

Fig. 4.14 The [O I] 6300 Å line shapes for our models compared to those of T Cha measured using high resolution spectra. The panels are as in 4.5.

winds of sufficiently low density to be EUV-driven would vastly overpredict the emission from Ne III relative to that from Ne II (where observations imply $L_{\rm NeIII}/L_{\rm NeII} \lesssim 0.1$). This is also consistent with the detection of emission from O I, which must come from relatively neutral gas. We therefore prefer a high mass-loss rate wind as might result from X-ray photoevaporation; moreover this is the only way that the wind absorbs enough X-ray to efficiently produce the high [Ne II] luminosities observed. Even then, we find that we need a relatively large X-ray luminosity to reproduce the observations.

Ballabio et al. (2020) found that in general higher sound speeds are needed to explain the [Ne II] compared to the [O I], and suggested a multi-phase wind may be responsible. While I did not directly model a combination of different winds for a single disc, we can capture modest temperature and ionisation gradients. However, we still underpredict the Ne II line width and blueshift, but not that of the O I (at least for T Cha) suggesting that our models have similar limitations. Moreover, to match the breadth of the lines observed for T Cha, we see that an inner radius $r_{\rm in} \sim 0.1\ r_G$ (as used by Ballabio et al., 2020) is needed, along with a relatively steep density profile at the base, such that there is sufficient material with a large degree of Keplerian broadening. Given that the critical radius for photoevaporation is often taken to be $\sim 0.2\ r_G$, it is not inconceivable that a photoevaporative wind could contribute, but would realistically be deviating strongly from the self-similar model in this region. Thus a magnetically-driven model may be a more promising explanation in this case. T Cha does, however, have unusually broad [Ne II] (especially since the elevated base should reduce the dependence of FWHM on inclination) so for other sources it is possible that a larger $r_{\rm in}$ compatible with photoevaporation would be more acceptable. Given these scales I expect that IFU imaging of [Ne II] emission will likely not be able to spatially resolve the emission for T Cha, however future comparisons of our models to the data using methods for recovering the [Ne II] that are still under development should at least allow us to more quantitatively constrain the emitting region's extent.

V4046 Sgr, which is closer, has a larger r_G, and appears not to be such an outlier in terms of its line breadth, may be a more promising target and is scheduled for MIRI MRS observations this Autumn. Though it also tentatively requires a larger $r_{\rm in}$ for the models to reproduce the observations, the less well-constrained high-energy spectrum and Ne abundance uncertainties make reproducing its line luminosities more of a challenge.

Chapter 5

The Evolutionary Impact of Photoevaporative Winds

5.1 Motivation

In the Introduction, I explored processes with which photoevaporation competes to drive disc evolution, including viscous accretion and the radial drift of dust. I discussed how the evolution of observables - particularly the disc dust mass and accretion rate onto the central star - is measured, and what these tell us about disc dispersal. Questions remain in this field about the origin of the accretion process: in particular whether it is viscous or wind-driven in nature, and in the former case, how large an α is approrpriate.

One way to investigate these processes is through the accretion timescale - as defined in Equation 1.49 - which is the ratio of the current disc mass and current accretion rate. This may also loosely be termed the "lifetime" of a disc (e.g. Lodato et al., 2017) as it represents the time taken to disperse the disc at a constant accretion rate. However in viscously evolving discs, the accretion rate declines over time and they evolve towards a value of $t_{\rm acc} \sim t$ i.e. it is a much better measure of the "disc age" (Jones et al., 2012). This limiting behaviour results from the disc spreading and represents the viscous timescale $t_{\rm visc}$ (Equation 1.45) at the outer edge. Consequently when disc radii are known, this quantity still holds information about the strength of the accretion torques acting to disperse the disc and has lead to measurements of α for individual discs of $\lesssim 10^{-2}$ (Rafikov, 2017; Ansdell et al., 2018).

A consequence of this behaviour where $t_{\rm acc} \rightarrow t$ is that disc evolution ends up in a self-similar regime which is independent of initial conditions. Correspondingly, for coeval disc populations, a linear relationship should develop between the accretion rate and disc mass. Manara et al. (2016) found the first evidence, in Lupus, of such a correlation between the accretion rates (measured by Alcalá et al., 2014, 2017) and the disc masses (measured from dust emission by Ansdell et al., 2016) with a power law slope of 0.7 ± 0.2, consistent with a simple linear relationship as expected from the viscous theory. 60% of discs were consistent with an accretion timescale of $1-3$ Myr, the age of the Lupus region; however, several sources had accretion timescales that were either too long (too low an accretion rate for their mass), or too short (too high an accretion rate for their mass) i.e. there was too large a spread in $t_{\rm acc}$. Equivalently, to be explained by the self-similar evolution, some discs had to be too old or too young compared to the age of Lupus.

The correlation between accretion rate and disc mass at a given age is expected to become tighter with age. Equation 1.49 implies that for a region with a given age, discs should show a spread in $t_{\rm acc}$ values owing to there being a range of initial viscous times t_ν, but the relative scatter should decrease with age (Lodato et al., 2017). The region Chamaeleon I does show a very similar range of disc masses and accretion rates to Lupus, as befits its similar age (Mulders et al., 2017). Conversely the Upper Scorpius region, which is $5-10$ Myr old (Pecaut & Mamajek, 2016; David et al., 2019) should show lower accretion rates at a given mass, as well as a tighter spread in $t_{\rm acc}$. However, Manara et al. (2020) found that the median accretion rates and spreads are not dissimilar to the younger regions, resulting in many discs which could only be explained by Equation 1.49 if they had very young ages (i.e. they exhibit very high accretion rates for their masses). The distribution also appears similar in Lynds 1641 (Grant et al., 2021), a 1.5 Myr-old cluster.

Consequently, it is natural to conclude that viscous accretion is not the only process driving disc evolution and determining the $t_{\rm acc}$ values. In the context of this thesis, we are interested in the role played by internal photoevaporation, which should mostly act to lower accretion rates late in a disc's evolution and should therefore increase $t_{\rm acc}$. A similar effect can result from the action of dead zones or planet formation (Jones et al., 2012; Rosotti et al., 2017). Conversely, *external* photoevaporation does reduce $t_{\rm acc}$ (Rosotti et al., 2017) and may be relevant in Upper Sco (Trapman et al., 2020), but is not thought to be a significant influence in Lupus: for example the trend observed between dust-disc radii and sub-mm flux (Tripathi et al., 2017; Andrews et al., 2018) precludes strongly photoevaporating discs (Sellek et al., 2020a).

A potentially greater caveat is that this analysis has been predicated on masses inferred from dust continuum observations with the canonical assumption that the gas-to-dust ratio retains its primordial value of 100. As discussed in the introduction, dust masses are often preferred to CO-based mass estimates due to uncertainty surrounding the latter's accuracy; indeed Manara et al. (2016) found no correlation between accretion rates and the latter. This prompts the question as to whether, as Manara et al. (2016) have argued, the dust masses' relative success in producing better agreement with the viscous predictions (despite the issues highlighted above) is a vindication of deriving disc masses from dust emission under standard assumptions. However, Mulders et al. (2017) found the agreement could be further improved by introducing an ad hoc elevation and scatter in the assumed gas-to-dust ratio.

The gas-to-dust ratio may deviate significantly from 100 due to effects including radial drift, dust trapping and internal or external photoevaporation (e.g. Takeuchi et al., 2005; Alexander & Armitage, 2007; Birnstiel et al., 2012; Sellek et al., 2020a). Moreover, models predict opacities and temperatures that vary with properties including grain size, composition and location, rather than the single values used by observational surveys in estimating dust masses from sub-millimetre fluxes. Discrepancies between the true and observed masses could also arise due to optically thick emission (Galván-Madrid et al., 2018). There is also observational evidence for this paradigm: by modelling the dust emission extent at different wavelengths and using dynamical arguments, Powell et al. (2019) derived mass estimates independent of any tracer-to-total mass conversion which implied gas-to-dust ratios of $10^3 - 10^4$.

However, prior to the work described in this chapter there have been no attempts to interpret the accretion rate - dust mass correlation using models for grain growth and evolution which, as discussed, predict a much more complex mapping between dust emission and total disc mass than is generally assumed; if we wish to isolate the role of internal photoevaporation, we must also take the dust evolution into account.

In this chapter I therefore begin by considering which parts of the $\dot{M}_{\rm acc} - M_{\rm dust}$ plane dust growth and drift models can reach and whether these are compatible with the observations. I use the dust model of Birnstiel et al. (2012) to compute the dust evolution in viscously accreting discs. From these models, I calculate a sub-mm flux density from which we may estimate an "observers' equivalent dust mass" in order to account for any differences between the true and observationally-inferred masses and hence study the evolution of discs in the same observational plane as the survey data. I then show that such models can better reproduce accretion rate and disc mass observations in both Lupus (representing a younger region) and Upper Sco (representing an older region).

I then turn my attention to how internal photoevaporation helps reach some of the remaining outliers at low accretion rates. In particular I compare the impact of EUV and X-ray models for a range of luminosities and at different stellar masses.

5.2 Model Description

In this work we build on the model of Booth et al. (2017), which solves the viscous diffusion equation for a Shakura & Sunyaev (1973) α viscosity model (Section 1.3.1) and includes a two-population dust growth model following Birnstiel et al. (2012). We add photoevaporation into the model; an almost identical model of viscous evolution, dust and photoevaporation was first used by Ercolano et al. (2017). In all cases, the evolution equations were solved on a grid with 5000 cells equispaced in $R^{1/2}$ between 0.025 au and 10000 au.

5.2.1 Gas Evolution

The viscous diffusion equation for the evolution of the gas surface density $\Sigma(R,t)$ is

$$\frac{\partial \Sigma}{\partial t} = \frac{3}{R}\frac{\partial}{\partial R}\left(R^{1/2}\frac{\partial}{\partial R}\left(\nu R^{1/2}\Sigma\right)\right) - \dot{\Sigma}_{\rm photo}, \tag{5.1}$$

where $\dot{\Sigma}_{\rm photo}$ represents the mass-loss due to internal photoevaporation. In our basic model we do not include any photoevaporation. However, in Section 5.4 we introduce models that use either the EUV prescriptions parametrized by Alexander & Armitage (2007, Equations A1-A5) or the X-ray prescriptions derived by Picogna et al. (2019, Equations 2-5) for $\dot{\Sigma}_{\rm photo}$; at the time this work was conducted, the latter were a recent update to the commonly-used Owen et al. (2012) prescriptions and were the best available X-ray photoevaporation rates. We discuss the potential impact of more recent prescriptions in Section 5.5.1.

Once photoevaporation opens a gap, and the column density to the outer edge of this gap is $< 10^{22}$ cm^{-2}, we switch from the 'Primordial disc' to the 'Inner-Hole disc' for $R \geq R_{\rm hole}$ while continuing to use the 'Primordial' profile at smaller radii to clear the remaining inner disc. The fit to the total mass-loss rate in the primordial case quoted by Picogna et al. (2019) is as follows, with an inner-hole disc sustaining a rate 1.12 times higher:

$$\log_{10}(\dot{M})) = -7.2580 - 2.7326 \exp\left[-\frac{(\ln(\log_{10}(L_{\rm X})) - 3.3307)^2}{2.9868 \times 10^{-3}}\right], \tag{5.2}$$

where $L_{\rm X}$ is the X-ray luminosity in erg s^{-1}. We take this expression at face value and assume all dependence on the star is through $L_{\rm X}$, as the explicit effect of stellar mass was then thought to be weak (Owen et al., 2012). However, we rescale the *profiles* provided by Picogna et al. (2019) radially with stellar mass according to Equations 5.3 and 5.4 (c.f. Equations B3, B6 of Owen et al., 2012) to account for the gravitational effect of masses different to their fiducial 0.7 $M_\odot$.

$$R' = R\left(\frac{M_*}{0.7\mathrm{M}_\odot}\right)^{-1}, \tag{5.3}$$

$$x' = (R - R_{\mathrm{hole}})\left(\frac{M_*}{0.7\mathrm{M}_\odot}\right)^{-1}. \tag{5.4}$$

We choose to neglect external photoevaporation as the typical FUV radiation fields are only $\sim 4\ G_0$ in Lupus (Cleeves et al., 2016). The typical FUV field strengths are likely higher in Upper Sco (Trapman et al., 2020), but still low in absolute terms, so we neglect them to enable a more direct comparison between our models at different ages.

We assume a standard $T \propto R^{-1/2}$ - with the normalisation set by imposing an aspect ratio (the ratio of the scale height over the radius) of 0.033 at 1 au - and a constant α value of 10^{-3}, such that $\nu \propto R$ ($\gamma = 1$). Although Lodato et al. (2017) preferred $\gamma > 1.2$ in order for the predicted t_{acc} to be low enough and as such chose a non-constant $\alpha \propto R^{1/2}$; the effect of dust is such that we no longer require this constraint.

Our surface density profile is therefore set up in the initial condition given by the Lynden-Bell & Pringle (1974) profile (Equation 1.44) for $\gamma = 1$ and $t = 0$. For the initial disc mass and radius we run a grid of different values. As discussed in the introduction, the most massive discs can be expected to have initial masses in the range $0.1 - 0.03\ M_\odot$. To bracket this range we thus use $M_{\mathrm{disc},0} = \{1, 3, 10, 30, 100\}\ \mathrm{M_J}$ (where $\mathrm{M_J}$ is the mass of Jupiter). We vary the initial scale radius in the range $R_{\mathrm{C}} = \{10, 30, 100\}$ au.

5.2.2 Dust Evolution

Key to this work (compared to other studies such as Appelgren et al., 2020, which use a single constant dust grain size) is that we use the two population model of Birnstiel et al. (2012) in which the maximum grain size varies with local conditions. It is important to know this size for two reasons. Firstly, it determines the dust dynamics and hence the evolution of the dust budget. Secondly, for comparison to observations, it is the largest grains that control the emissivity at mm wavelengths.

As discussed in the introduction, the dust dynamics are affected by drag and thus governed by the Stokes number (Equation 1.59). This controls the degree to which they are advected with the gas or subject to radial drift of dust due to drag-induced torques (Whipple, 1973; Weidenschilling, 1977) (see Figure 1.5).

Birnstiel et al. (2012) showed that dust drift could be well-approximated by a simple model considering two populations: a small population of well-coupled monomer grains, that can grow into larger dust, and a large population of dynamically less well-coupled grains.

At each radius in the disc the maximum size a of the dust grain distribution (as represented by this large population) is allowed to grow as

$$\frac{a}{\dot{a}} = \frac{1}{\varepsilon\Omega}, \tag{5.5}$$

assuming that the fraction of dust grain collisions that lead to growth is not suppressed (see Ormel et al., 2017; Booth & Owen, 2020). Growth stops once the dust size reaches the lower of the fragmentation-limited or drift-limited regime (Birnstiel et al., 2012):

$$a_{\mathrm{frag}} = 0.37\frac{2}{3\pi}\frac{\Sigma_{\mathrm{gas}}}{\rho_{\mathrm{s}}\alpha}\frac{u_{\mathrm{f}}^2}{c_{\mathrm{S}}^2} \tag{5.6}$$

$$a_{\mathrm{drift}} = 0.55\frac{2}{\pi}\frac{\Sigma_{\mathrm{dust}}}{\rho_{\mathrm{s}}}\frac{v_{\mathrm{K}}^2}{c_{\mathrm{S}}^2}\left|\frac{\mathrm{d}\ln\mathrm{P}}{\mathrm{d}\ln\mathrm{R}}\right|^{-1} \tag{5.7}$$

Numerical values assumed for dust properties are listed in Table 5.1.

To implement the evolution, we use the model of Booth et al. (2017) which uses the relative dust-gas velocities to update the dust mass fractions based on Laibe & Price (2014). However, we updated their model to use the relative velocities given by the following formulae from Dipierro et al. (2018), which includes higher order terms than discussed in Section 1.3.2 which capture the effects of dust feedback (although the differences should only be significant when $St \gg 1$). The azimuthal and radial components of the gas velocity are

$$v_{r,\mathrm{gas}} = -\frac{\lambda_1}{(1+\lambda_0)^2+\lambda_1^2}v_P + \frac{1+\lambda_0}{(1+\lambda_0)^2+\lambda_1^2}v_{\mathrm{visc}} \tag{5.8}$$

$$v_{\phi,\mathrm{gas}} = \frac{1}{2}\frac{1+\lambda_0}{(1+\lambda_0)^2+\lambda_1^2}v_P + \frac{1}{2}\frac{\lambda_1}{(1+\lambda_0)^2+\lambda_1^2}v_{\mathrm{visc}}, \tag{5.9}$$

where $\lambda_k = \sum_i \frac{\varepsilon_i}{1-\varepsilon}\frac{St_i^k}{1+St_i^2}$. ε_i is the fraction of mass in dust species i (such that the total dust mass fraction is $\varepsilon = \sum_i \varepsilon_i$) - with two species in the two population model. $v_{\mathrm{visc}} = \frac{3}{\Sigma_G}\frac{\partial}{\partial R}\left(\nu R^{1/2}\Sigma_G\right)$ is the velocity induced by viscous torques and $v_P = \frac{c_{\mathrm{S}}^2}{v_{\mathrm{K}}}\frac{\mathrm{d}\ln\mathrm{P}}{\mathrm{d}\ln\mathrm{R}}$. From these, the radial velocity of dust species i relative to the gas may be calculated as

$$\Delta v_{r,i} = \frac{2v_{\phi,\mathrm{gas}}St_i - v_{r,\mathrm{gas}}St_i^2}{1+St_i^2}. \tag{5.10}$$

Table 5.1 Numerical Values of Gas, Dust and Photoevaporation Model Parameters in the Basic Model. Variations to these in Section 5.4 are included in round brackets.

Parameter	Value	Reference
Viscosity (α)	10^{-3}	Rosotti et al. (2019a)
Aspect Ratio at 1 au (h_0)	0.033 (0.025)	Rosotti et al. (2019a)
Initial Mass ($M_{\mathrm{disc},0}$)	$\{1,3,10,30,100\}$ $\mathrm{M_J}$	-
Initial Scale Radius (R_C)	$\{10,30,100\}$ au	-
Stellar Mass (M_*)	1.0 $\mathrm{M_\odot}$ (0.1 $\mathrm{M_\odot}$)	-
Internal Dust Density (ρ_s)	1.0 g cm^{-3}	Tazzari et al. (2016), Pollack et al. (1994)
Fragmentation velocity (u_f)	10 m s^{-1}	Gundlach & Blum (2015)
Initial/Minimum size (a_0)	0.1 μm	-
Initial dust-to-gas ratio (ε)	0.01	Bohlin et al. (1978)
X-ray Luminosity (L_X)	0 erg s^{-1} (5×10^{28}, $10^{30}, 10^{31}$ erg s^{-1})	Preibisch et al. (2005), Güdel et al. (2007a)
EUV Photon Flux (Φ)	0 s^{-1} (10^{42} s^{-1})	Pascucci & Sterzik (2009)

5.2.3 Calculation of Observers' Equivalent Dust Mass

Although dust masses are easily retrieved directly from the model by integrating the dust surface density over the disc area, the observational data to which we wish to compare is based on masses inferred from the sub-mm flux densities (Ansdell et al., 2016). To ensure we compare like-for-like, we thus calculate an "observers' equivalent dust mass" in the following way (identical to the "synthetic dust mass" calculation of Pinilla et al., 2020).

We first use Equation 1.64 (which neglects scattering and assumes the disc is vertically isothermal and face-on), to calculate the sub-mm flux density from the disc (c.f. Tanaka et al., 2005; Tazzari et al., 2016; Pinilla et al., 2020). The temperature used for this calculation is the gas temperature described in 5.2.1, which works out to be:

$$T(R) \approx 290 \left(\frac{R}{1\ \mathrm{au}}\right)^{-0.5} \mathrm{K}. \tag{5.11}$$

The aspect ratio used to define this temperature follows (Rosotti et al., 2019b,a) and produces a temperature similar to that used since Hayashi (1981). Although such temperatures seem necessary in these smooth disc models to reproduce typical disc fluxes, it is worth noting that this is quite high and would, for example, predict snowlines to occur at much larger radii than is typically observed. Nevertheless, the effect on observed lifetime distribution is negligible as both the mm fluxes and the accretion rates during the early evolution are linear in the temperature (Sellek et al., 2020b).

For the opacities $\kappa(a_{\max})$, we use tabulations that assume compact grains with composition that approximates that of Pollack et al. (1994) and the optical constants used by Tazzari et al. (2016). The opacities are most sensitive to the choice of optical constants for the carbonaceous material, which here come from Zubko et al. (1996) who assume it is in an amorphous form. This produces a relatively high mm opacity compared with the Beckwith et al. (1990) value used by observers (which is an extrapolation from the infrared to the mm). While alternative forms of carbon, such as refractory organics (Stognienko et al., 1996) may result in lower mm opacities (Birnstiel et al., 2018), the opacities we use have had previous success in reproducing the flux-radius relationship (Rosotti et al., 2019a), whereas the DSHARP (Birnstiel et al., 2018) opacities cannot without highly effective dust trapping (Zormpas et al., 2022).

We then use Equation 1.65 (Hildebrand, 1983) to calculate the "observers' equivalent dust mass" from the calculated sub-mm flux densities as this is what is used in our comparison data sets. Although other studies have used more sophisticated prescriptions for $T_{\rm dust}$ that depend on the stellar luminosity and/or the disc's flux profile (e.g. Andrews et al., 2013; Barenfeld et al., 2016; Tripathi et al., 2017), for consistency with Ansdell et al. (2016), we use a single dust temperature $T_{\rm dust} = 20$ K and $\kappa_\nu = 10\ {\rm cm^2\ g^{-1}} \left(\frac{\nu}{1000\ {\rm GHz}}\right)$ (Beckwith et al., 1990). We rescale the masses quoted in Manara et al. (2020) to use the same dust temperature and opacity as Ansdell et al. (2016).

These calculations are performed at 890 μm when comparing to Lupus or 880 μm when comparing to Upper Sco, though this makes negligible difference.

5.2.4 Summary of Nomenclature

For what concerns the masses, the "true dust mass" is the actual mass in dust that our models predict a disc would contain. The "observers' equivalent dust mass" ($M_{\rm d,obs}$) is the mass in dust that an observer would infer from the same model, given the fluxes that we calculate. The details of this calculation are given in Section 5.2.3. The "observers' equivalent disc mass" is the total mass that an observer would infer given standard assumptions i.e. 100 times the "observers' equivalent dust mass".

Throughout this work we use "system age" t to refer to the true age of the star and disc. The "accretion timescale" $t_{\rm acc}$ is the ratio of the observer's equivalent disc mass to the accretion rate. For the $\gamma = 1$, constant α, viscous models we employ, $t_{\rm acc} = 2(t + t_\nu)$. Hence at late times, when $t \gg t_\nu$, $t_{\rm acc} \sim 2t$. Thus, we use the term "inferred viscous age" to refer to the age as estimated from the accretion timescale under this viscous model ($t_{\rm acc}/2$).

5.3 Basic Dust Evolution Model without Photoevaporation

As a baseline for comparison, I first present the evolution of 15 disc models spanning a grid of initial radii and masses that do not include any internal photoevaporation. These models are shown as the coloured tracks in each panel of Figure 5.1. Between 1 and 3 Myr the tracks are plotted with thick, solid, lines. Outside of these times, the tracks are plotted with fainter, dashed, lines of the same colour. The length of the solid section thus indicates how rapidly the disc evolves within this age window, to give an indication of the amount of time the disc spends at its location in the plane of the two quantities defining the panel. The same models are shown in Figure 5.2 with the solid sections corresponding to disc locations at ages between 5 and 10 Myr.

5.3.1 Without Accounting for Dust

The upper-left 'Theoretical' panel of Figure 5.1 shows the accretion rate against the disc's gas mass. Each model evolves from top-right towards bottom-left along a power-law track corresponding to $\dot{M}_{\rm acc} \propto M_{\rm disc}^3$. This is consistent with predictions from viscous theory; Lodato et al. (2017) showed that individual discs should evolve along trajectories given by

$$\dot{M}_{\rm acc} = \frac{1}{2(2-\gamma)} \frac{M_{\rm disc,0}}{t_\nu} \left(\frac{M_{\rm disc}}{M_{\rm disc,0}} \right)^{5-2\gamma}. \tag{5.12}$$

As detailed in Section 5.2.4, $t_{\rm acc} = 2(t+t_\nu)$; in the panel we thus indicate lines where $M_{\rm disc}/\dot{M}_{\rm acc} = 2t$, for several values of t. At a given time, a disc's inferred viscous age is older by a factor of $1+t_\nu/t$ than the true system age, due to the finite value of the initial viscous time t_ν. This means that, particularly at young ages, the models are located slightly below and to the right of the line where their inferred viscous ages are equal to the true system ages. Moreover, since $t_\nu \propto R_{\rm C}$ (Equation 1.45), a degree of scatter in $R_{\rm C}$ leads to a spread in $t_{\rm acc}$ at a given time, (i.e. perpendicular to the linear trend between $\dot{M}_{\rm acc}$ and $M_{\rm disc}$).

This behaviour is most clearly seen in the endpoints of the tracks' solid sections; at each end a displacement from the indicated contours of inferred viscous age is seen, which is greater for larger $R_{\rm C}$. As the cluster ages $1+t_\nu/t \to 1$ so the effect of the viscous timescale becomes relatively less important and the spread in $t_{\rm acc}$ at a given time reduces - this can be seen in the figure since the ends of the solid sections are closer together than their starts. Lodato et al. (2017) highlight another consequence: for a given initial disc mass at a given time, discs with a larger viscous timescale have retained larger masses. This leads to a slightly sub-linear relationship between accretion rate and disc mass across a population of discs.

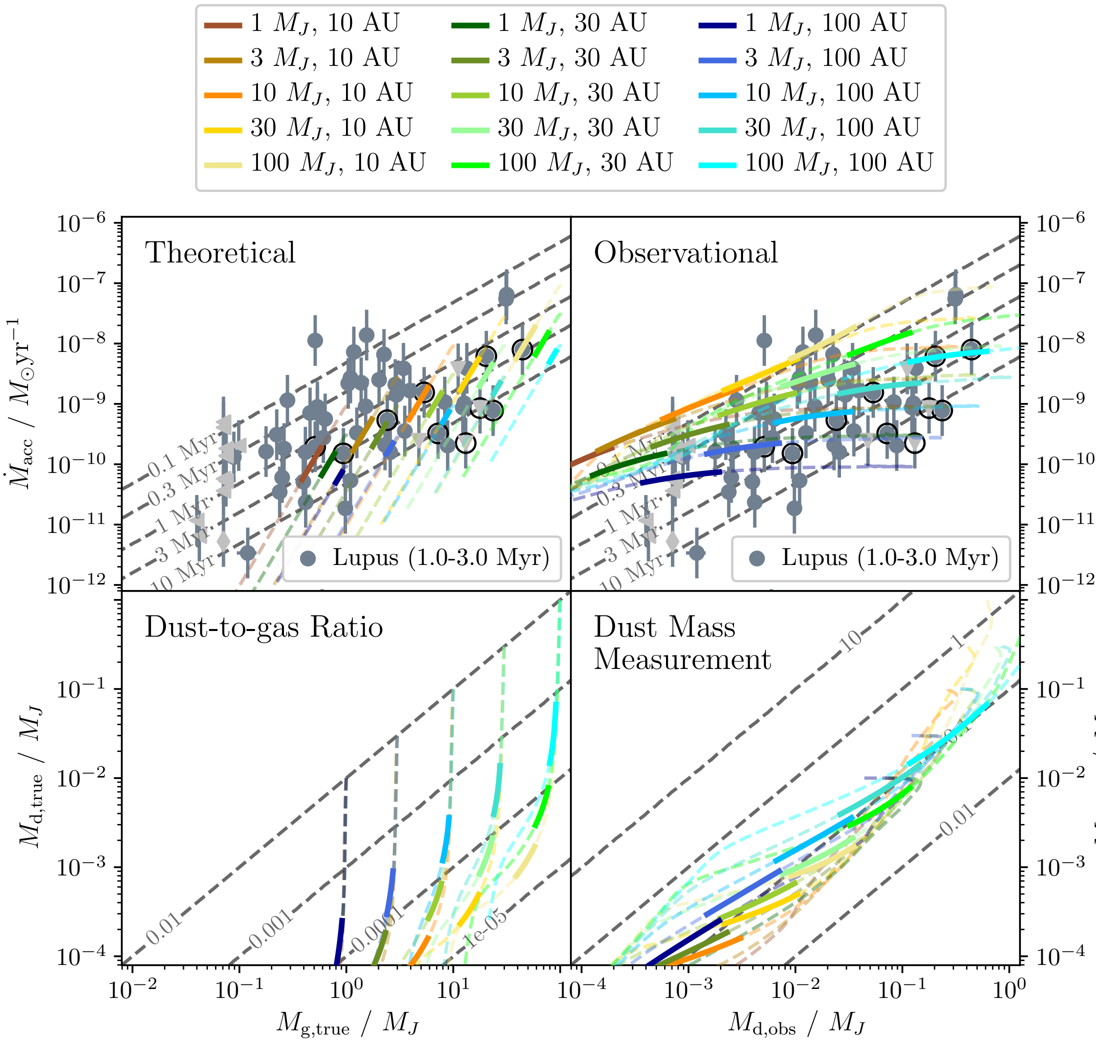

Fig. 5.1 Model tracks using a dust evolution model are indicated by coloured dashed/solid lines with the solid section corresponding to $1-3$ Myr. Upper left: the ‘theoretical’ plane shows the accretion rate against the gas mass; dashed grey lines show the expected location at the labelled time in the limit where $t \gg t_\nu$ (i.e. the labels represent the inferred viscous age). Lower left: the plane of true dust masses against gas masses; dashed grey lines show the dust-to-gas ratio. Lower right: the plane of true dust masses against observers’ equivalent dust mass; dashed grey lines show the ratio between the two. Upper right: the ‘observational’ plane of accretion rate against the observers’ equivalent dust mass; the dashed grey lines are labelled with the inferred viscous age assuming a gas-to-dust ratio of 100. The grey points in the upper panels show the accretion rate (Alcalá et al., 2014, 2017) and inferred gas mass (assuming a gas-to-dust ratio of 100) or dust mass (Ansdell et al., 2016) for the discs in Lupus, with the marker shape indicating whether the object has complete data (dark circle), is a non-accretor (light downward triangle), a non-detection (light leftward triangle) or neither an accretor nor a detection (light diamond). Discs which have been identified in the literature as transition discs are circled.

However, we see that for much of the data, which is taken from Lupus, the inferred viscous age (as indicated by the dashed lines) $\frac{M_{\rm disc}}{2\dot{M}_{\rm acc}} < 1$ Myr i.e. the discs appear too young. A reasonable range of accretion rates is produced, which implies this could be because the models are overmassive. The findings of Lodato et al. (2017) quantify this conclusion; they used the degree of scatter in $t_{\rm acc}$ as a proxy for the disc age relative to the initial viscous timescale and use the observed scatter of the data to constrain the distribution of ages and initial viscous timescales in their population synthesis models. Although their $\langle t_{\rm acc} \rangle \approx 2.5$ Myr was greater than estimated mean true age ($\langle t \rangle \approx 1.6$ Myr), it was still too young to agree with the predictions from viscous models if $\gamma < 1.2$. Equivalently, the evolutionary tracks would need a shallower slope < 2.6 - such that the accretion rate declines more slowly and the mass more rapidly - in order to go through more of the region occupied by the data.

5.3.2 The Effect of Including Dust

Rather than adjusting the viscous stresses to produce a faster dispersal of the disc mass, we instead consider that since the measurements are of dust mass, radial drift of large grains could be responsible. We therefore now consider in turn the reduction in the dust mass that drift can cause, how the resulting mm fluxes would be interpreted by observers in terms of a dust mass, and how these masses compare to the correlation.

The lower-left 'Dust-to-gas Ratio' panel of Figure 5.1 shows how the relative masses of dust and gas evolve in the model. If the discs evolved with a constant dust-to-gas ratio, then the tracks would be parallel to the dashed lines. However, it is apparent that although the disc models are started at the ISM ratio of 0.01, due to radial drift the dust masses drop much more rapidly than the gas masses. Between 1 and 3 Myr, the dust depletion can be anywhere between a factor of 10 and 1000 for little change in gas mass. This is broadly consistent with the factor ~ 50 decline in mass between the median Class 0 dust mass in Perseus and median Class II dust mass in Lupus (Tychoniec et al., 2020). From the start/end points of the solid tracks (most easily seen in the blue tracks for 100 au models), we see that at a given time, the dust depletion is more severe for lower disc masses. The dust dynamics are controlled by the Stokes number, which is inversely proportional to surface density (Equation 1.59), so in lower mass discs, the grains do not have to grow to so large a size before they have the same dynamics and drift sets in sooner. Moreover, at a given mass, the more compact a disc, the steeper the tracks and the more severe the dust depletion, as the dust is concentrated close to the star where radial drift timescales (which for fragmentation-limited dust scales $\propto R^{1/2}$) are low.

The lower-right ‘Dust Mass Measurement’ panel of Figure 5.1 shows the true dust mass in each model, plotted against the dust mass estimated from the sub-mm flux densities ($M_{\mathrm{d,obs}}$, henceforth “observers’ equivalent dust mass”) calculated as in Section 5.2.3. At 1 and 3 Myr, the solid tracks lie around the dashed line labelled 0.1, indicating that the true dust masses may be around a factor of 10 lower than estimated. That observed dust masses may be overestimates (except for the most massive or most highly inclined discs) was also the conclusion of more sophisticated Monte Carlo radiative transfer calculations conducted by Miotello et al. (2017). In our case, there are two factors contributing to this discrepancy. Firstly, we use an opacity that is also varying in space and time because it depends on the grain size, and which is a typically a factor of a few times higher than the single value assumed by the estimates (Equation 1.65). Moreover, the observers’ equivalent dust masses are all calculated for a single dust temperature of 20 K. For our temperature model (Equation 5.11), the disc would not reach this sort of temperature until outside 200 au, whereas the emission would mostly be from dust at smaller radii, and thus a range of higher temperatures. This means that less dust is needed to produce the same flux (cf Figure 9 of Pascucci et al., 2016, where assuming emission at the gas temperature, rather than 20 K produced higher mm fluxes).

This result was already shown for these dust evolution, temperature and opacity models by Rosotti et al. (2019a) who concluded that in practice, when using an opacity appropriate to compact grains, the flux was dominated by material with an opacity that was higher than the value used by observers: the effect of using a larger opacity was more important than any ‘invisible’ mass (either at low opacities or in optically thick regions). Recall however that the opacity is highly dependent on poorly-constrained properties such as the composition (particularly the nature of the carbonaceous component) and grain porosity, and this may affect the exact factor to which the observers’ equivalent and true masses differ. Similarly the disc temperatures are not well-known, and colder disc models would show less discrepancy between these values. However as we shall see, for the observed dust masses to be reconciled with these particular models, the disagreement must be, realistically, at least this large. Similarly, Rosotti et al. (2019a); Zormpas et al. (2022) found that a large opacity is necessary to produce fluxes that agree with the observed flux-radius relationship.

Between the accuracy of the observers’ equivalent dust masses, which appear to be overestimates by a factor ~ 10, and the declining dust-to-gas ratio, which leads to underestimates by a factor of 10-1000 when converting from the dust mass to gas mass, we conclude that the observers’ equivalent disc masses may be underestimated by a factor of anywhere between 1 and 100. This effect is largest for the most compact, and least massive, discs. This would mean that the inferred viscous ages are likewise systematically underestimates of the true system age.

In the upper-right 'Observational' panel of Figure 5.1, we see that therefore the tension is reduced when we compare, like-for-like, the data from Lupus and the models in terms of the observers' equivalent dust mass. The effect of radial drift is to deplete the dust mass more rapidly without affecting the accretion rate, so the model tracks become much flatter and can pass through more of the region occupied by the data. Moreover this happens on appropriate timescales: the tracks' solid sections (representing the regions of the $\dot{M}_{\rm acc} - M_{\rm dust}$ plane accessible to the models between 1 and 3 Myr) have moved to coincide much better with the data's main locus. The accessible region is bounded by the most massive discs at high accretion rates, and the least massive at low accretion rates. Moreover, it is bounded at high $t_{\rm acc}$ by the largest discs for two reasons: firstly, the large viscous timescale in these discs, and secondly the relatively inefficient radial drift, which has prevented such a strong depletion in mass. Since drift is responsible for reducing the measured $t_{\rm acc}$, and there is a dependence of drift efficiency on the initial disc radius, the spread perpendicular to the lines of constant age is much increased compared to the predictions of viscous theory alone. This is consistent with the finding of Mulders et al. (2017) that a scatter in the dust-to-gas ratio could help explain the scatter in the data, but in this case it occurs in a systematic sense.

Moreover, in the upper-right corner, we see that the location in this plane of large massive discs at 1 Myr is little changed from the predictions of viscous theory. However, as we go to increasingly low-mass discs we see more of a shift in the location of the solid track sections, consistent with the more efficient drift. An important consequence of this is that at a given initial disc radius (viscous timescale), the trend of accretion rates with dust masses is flattened slightly below linear, consistent with measurements of the slope in Lupus/Chamaeleon in the range $0.7 - 0.8$ (Manara et al., 2016; Mulders et al., 2017) - this is reflected in the slope of the upper/lower limits of the accessible regions.

5.3.3 Impact of Dust at Different Ages

Between 1 and 3 Myr, the larger discs in the sample continue to lose dust rapidly, whereas in smaller discs the loss of dust has decelerated since the low dust surface densities lengthen the dust's collisional growth timescale, thus limiting the resupply of drifting dust grains. Thus, the larger discs begin to catch up (as indicated by the blue tracks in the upper-right "Observational" panel of Figure 5.1 being more horizontal than the yellow/orange) - for a coeval population of discs, the spread in $t_{\rm acc}$ decreases as it would for a purely viscous model.

Notably though, the low $t_{\rm acc}$ limit of the region accessible to the models doesn't evolve significantly because the initially compact discs, which define that limit, also evolve along it.

This leads to a constant upper locus at an inferred viscous age of ~ 0.1 Myr. This key result does not simply arise from the evolution of the true dust masses, for which the limit moves to higher $t_{\rm acc}$ as accretion rates decline, but results from an interplay between this and the relationship between the true and observers' equivalent dust masses, which changes as the dust size and location evolve.

Therefore the accessible region's size on these timescales is largely set by the evolution of the largest discs. The length of the solid section of their tracks implies that they spend several Myr in the vicinity of the observed systems. Conversely, the more extended dashed tracks to the right of the solid section indicate that the position in this plane evolves more rapidly during the first Myr; thus systems are less likely to be observed in this part of the diagram.

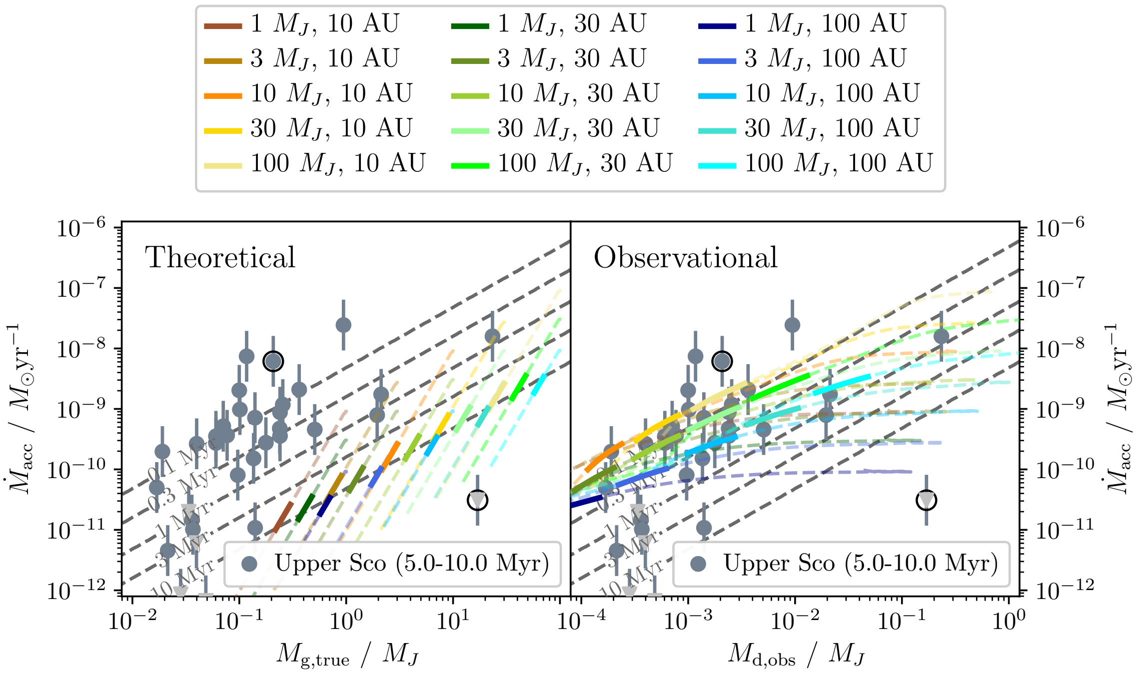

Fig. 5.2 As the upper panels of Figure 5.1 compared to data for Upper Sco from Manara et al. (2020), with the dust masses rescaled to use a consistent temperature and opacity across regions. In each panel, the solid section of the tracks indicates the area covered by the models at ages between 5 and 10 Myr.

We now focus on even older ages, as appropriate to Upper Sco. Figure 5.2 compares the same models as discussed so far to the data from Manara et al. (2020) (rescaled such that the temperature and opacity used to infer the masses are consistent with those used for Lupus and hence with the method we use to estimate masses from our models), with model locations 5 and 10 Myr highlighted. It is clear from the left panel that, as discussed by Manara et al.

(2020), a purely viscous model would be in stark contrast to the location and spread of the data in the $\dot{M}_{\rm acc} - M_{\rm disc}$ plane if the inferred disc masses were accurate. Indeed the region occupied by the models on these timescales lies totally separate to the data.

However, when dust evolution is included in the models and the models are plotted in terms of the observers' equivalent dust masses, as in the right panel, we again see the strong effects of drift which allow several intermediate accretion rate sources to be explained. In accordance with what was described between 1 and 3 Myr, the upper locus to the region accessible to the drift models at $t_{\rm acc} \sim 0.1$ Myr still hasn't evolved. Thus, the interplay between the effects of radial drift and the changing spatial distribution of the dust provides a good explanation for why in any mass bin, the upper limit to the accretion rates doesn't seem to change between regions (Manara et al., 2020). Moreover, the larger disc model tracks have turned parallel to this upper locus; the tracks' solid portions are similarly short to those in Figure 5.1, indicating that the models spend a large amount of time in the vicinity of the bulk of data so we are not overly sensitive to the region's exact age.

The range of modelled observers' equivalent dust masses also mostly encompasses the observed masses. In this context, the larger-mass discs seen in Lupus could be understood as the progenitors of the lower-mass discs in Upper Sco, with a corresponding decline in the accretion rate of a given source with age.

Conversely, five sources which lie within the mass range covered by the models, but at too high accretion rates, could be accounted for by external photoevaporation. This process potentially plays a role in disc evolution in Upper Sco (Rosotti et al., 2017; Manara et al., 2020) as there is a considerably higher stellar density than in Lupus (Damiani et al., 2019), which should result in more discs exposed to large FUV fluxes (Trapman et al., 2020). Alternatively, Zagaria et al. (2021) found that in binaries, not only does tidal truncation of the disc cause it to maintain a constant accretion timescale (Rosotti & Clarke, 2018), but it can also accelerate the dust depletion by radial drift. Consequently Zagaria et al. (2022) showed that the observed distribution of $t_{\rm acc}$ is significantly skewed towards lower values ~ 0.1 yr for binaries, and that radial drift evolution models with $20 \lesssim R_t/\mathrm{au} \lesssim 50$ can pass through the right part of parameter space to explain these otherwise high accretors.

The models also produce some very low-mass discs at $\sim 10^{-4}$ $\mathrm{M_J}$ with accretion rates just below 10^{-10} $\mathrm{M_\odot}$ yr^{-1}. Since the sample of Manara et al. (2020) pre-selected only those sources with statistically significant sub-mm detections (Barenfeld et al., 2016), it is not clear whether these "transparent accretors" are present amongst the sub-mm non-detections in Upper Sco.

5.3.4 Basic Model: Summary

Comparing the upper-left and upper-right panels of Figure 5.1 or the two panels of Figure 5.2, we see that by reducing the dust mass through radial drift, the dust evolution model represents a great improvement in reconciling theory with observations in both younger regions like Lupus and older regions like Upper Sco. Specifically, it can explain discs that would otherwise appear too young, i.e. have too low a mass given their accretion rate at their likely ages. It also increases the range of possible accretion rates at any one mass to be more consonant with the scatter in $t_{\rm acc}$ seen in the data, and predicts an upper locus at an inferred viscous age of ~ 0.1 Myr that does not evolve with time.

However there remain several data points, particularly those at high inferred viscous ages ~ 10 Myr in Lupus (i.e. at large masses for their accretion rates), which are not explained by the radial drift models. Moreover, no model with a dust mass high enough to have been detected in ALMA surveys (i.e. with $M_{\rm dobs} \gtrsim 10^{-3}\ M_{\rm J}$) is seen to have accretion rates much below $\sim 10^{-10}\ {\rm M}_{\odot}\ {\rm yr}^{-1}$, while several observed systems in both Lupus and Upper Sco do.

The discs with the highest $M_{\rm d,obs}$ could be explained by the basic model if they are younger than 1 Myr as radial drift would have had less time to deplete the dust. However, as we have argued, the evolution through this region is very rapid, so we would not expect many sources to be observed in this region. A more reasonable explanation would be that these discs were initially large, with $R_{\rm C}$ greater than the 100 au maximum used so far, such that radial drift becomes even less efficient.

Since once dust is included, the observations which are not reproduced by the model are now at high $t_{\rm acc}$, a more intriguing remedy to these conflicts would be to consider internal photoevaporation, which we argue could be appropriate for two reasons. Firstly, once the accretion rate falls low enough this may quench accretion rapidly through the opening of a gap and isolation of the inner disc, while trapping the remaining dust in the outer disc. This could help explain low accretion rates at moderate dust masses and should certainly avoid a large number of discs with modest accretion rates and low masses. Secondly, it has, at least historically, been connected to transition discs since both involve an inside-out mode of clearing and several discs at large $t_{\rm acc}$ are identified as such. In the next section I therefore present models that include internal photoevaporation.

5.4 Impact of Internal Photoevaporation

As discussed throughout this thesis, the mass-loss rates due to internal photoevaporation are still quite uncertain. Thus I explore the effects of two photoevaporation models, an EUV model (Alexander & Armitage, 2007) and an X-ray model (Picogna et al., 2019), starting with the former as its smaller mass-loss rates will help establish a lower limit on the effect of photoevaporation (while the higher mass-loss rate X-ray models will provide an upper limit).

5.4.1 EUV Photoevaporation

The EUV photoevaporation prescription given in Alexander & Armitage (2007) requires an ionising flux Φ. As discussed in the introduction (Section 1.2.4), the value of Φ is hard to determine directly, so we choose a rough upper limit of 10^{42} photons s^{-1}. For a solar-mass star, this corresponds to a total mass-loss rate of 4.05×10^{-10} $\mathrm{M}_{\odot}$ yr^{-1}. We ran models for the same parameters as before, and present our results in Figure 5.3.

In the upper-left panel showing the accretion rate and gas mass, the evolutionary tracks are no longer straight lines, but curve downwards. This signifies the accretion rate being starved, then switched off, by the photoevaporative wind. In the lower-left panel, we see that the dust mass eventually levels off - this is due to remnant dust being trapped outside the gap that is opened at small radii.

In the upper-right panel, we see that the photoevaporating models do represent a further improvement in terms of which observed discs could be explained. A small number of discs on the right of the plot, with masses previously too large for their accretion rate, are now accessible to the models between 1 and 3 Myr since the accretion rates are reduced, though many remain unexplained - this is not a large surprise as the accretion rates are here much larger than the photoevaporation rate. In particular, our models are not really effective at explaining the transition discs in this region - which are large, bright and have high accretion rates - as has commonly been found in the literature (e.g. Owen et al., 2012).

More importantly, the evolution is no longer towards very low masses and moderate accretion rates at late times. Instead, at dust masses $M_{\mathrm{dust}} < 10^{-2}$ $\mathrm{M_J}$, the accretion rates now extend to previously inaccessible values (lower than $\sim 10^{-10}$ $\mathrm{M}_{\odot}$ yr^{-1}). As such the models evolve through the region occupied by the data points at low accretion rates: at first glance the best agreement with the indicated masses would generally seem to be for the 30 au discs or the more massive 100 au discs. Although the tracks for the 10 au discs extend into regions that have lower masses than the datapoints shown, it is worth noting that many discs only have upper limits on their dust mass (with the markers placed at this limit) and these could turn out to be compatible with such evolutionary tracks. Thus, the data do not currently

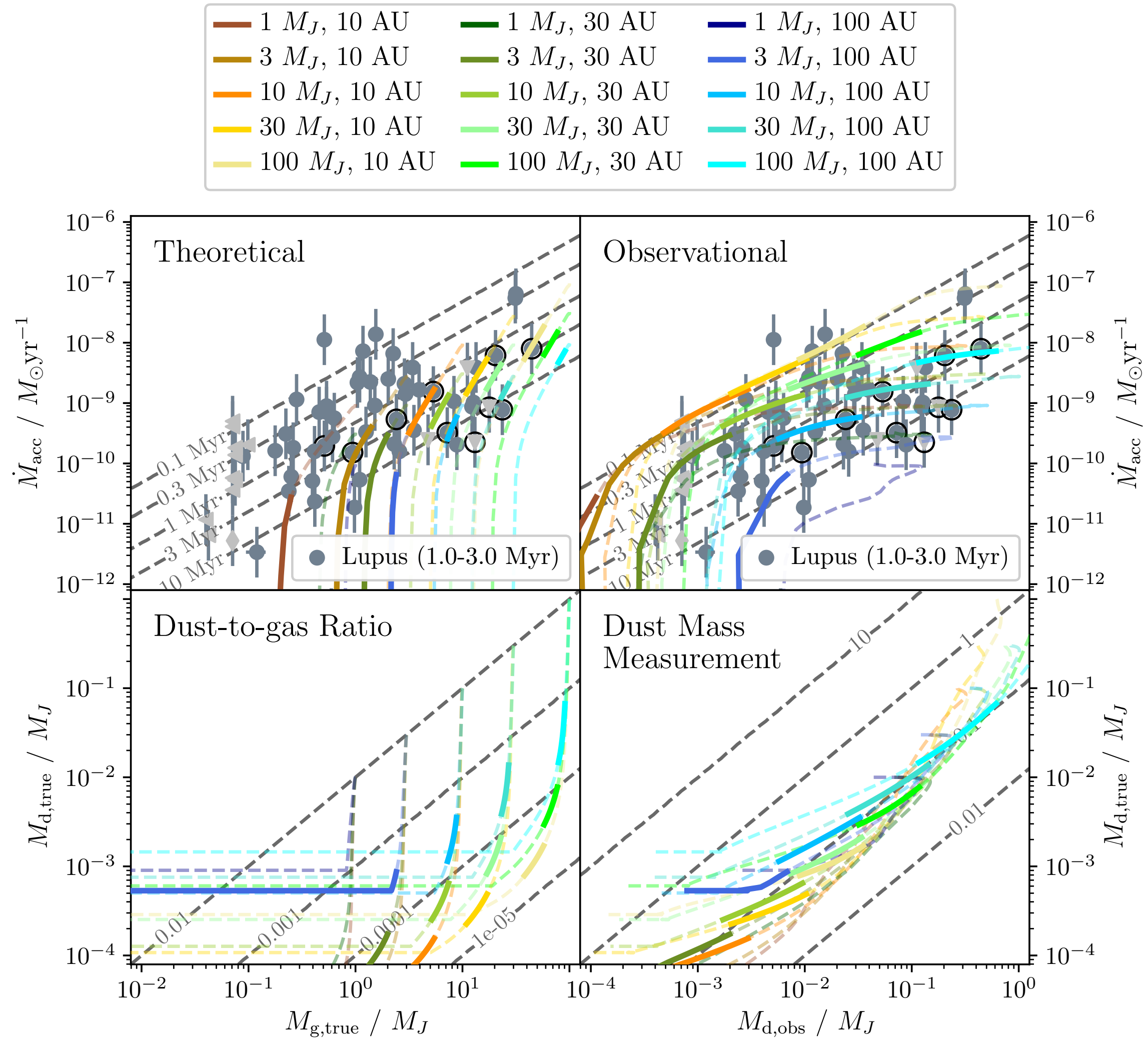

Fig. 5.3 As with Figure 5.1, but with EUV photoevaporation produced by an ionising photon flux $\Phi = 10^{42}$ s^{-1}. The solid sections indicate system ages of $1-3$ Myr and the data are from Lupus.

rule out these sources being in agreement with the most compact disc models, although high sensitivity dust measurements would be required to confirm this.

However, the question of timing is important. $\sim 18\%$ of the Lupus data lie below the track for the non-photoevaporating model with 1 M_J and 100 au and so need photoevaporation to explain. By comparison, four models (the lowest mass discs, which are preferentially removed by photoevaporation, Somigliana et al., 2020) pass through appropriately low accretion rates $< 10^{-10}$ $M_\odot$ yr^{-1} on the $1-3$ Myr timescale; this is $\sim 29\%$ of the discs which survive to at least 1 Myr. However, how likely we are to observe discs at low accretion rates depends on how rapidly the discs evolve through the region relative to their age. The solid tracks here are much longer than in the non-photoevaporating models, implying a more rapid evolution: it typically takes a few tenths of a Myr for the accretion rates to decline from 10^{-10} to $< 10^{-12}$ $M_\odot$ yr^{-1}. Overall, it is not inconceivable that $10-20\%$ of the discs should lie at such low accretion rates: the true proportion of discs that would be found here somewhere between 1 and 3 Myr will depend on how the initial parameters are distributed, but the similarity of these proportions to within a factor 2 implies that this should not be hard to achieve. A full population synthesis, with a realistic, continuous, distribution of masses, radii and observation times - rather than a parameter space investigation - would be necessary to more precisely quantify how well observations of the lowest accretion rates are reproduced by these models.

Finally, although the lowest mass large disc seems to cross a region at relatively high mass for low accretion rates, where no discs are observed, it does so on timescales shorter than 1 Myr. Thus, such discs cannot be conclusively ruled out as existing in the initial population and we may conclude that EUV photoevaporation can do a good job of producing the low-accretion-rate discs in the right mass range and avoiding arbitrarily low-mass discs that are still accreting.

5.4.2 X-ray Photoevaporation

The prescription for the X-ray photoevaporation rates given in Picogna et al. (2019) has a mass-loss rate determined by the stellar X-ray luminosity (Equation 5.2). Observationally, X-ray luminosities lie roughly in the range $5 \times 10^{28} < L_X/\mathrm{erg\ s^{-1}} < 10^{31}$, with a median value of $1-2 \times 10^{30}$ erg s^{-1}, and are correlated with stellar mass (Preibisch et al., 2005; Güdel et al., 2007a). To span this range, we test luminosities of 5×10^{28} erg s^{-1}, 10^{30} erg s^{-1}, and 10^{31} erg s^{-1}; the low and high values are close to the mean values for stars of 0.1 $M_\odot$ and 3 $M_\odot$ respectively (Güdel et al., 2007a), roughly the stellar mass range spanned by the Lupus sample. The evolutionary tracks under each X-ray luminosity are compared in Figure 5.4.

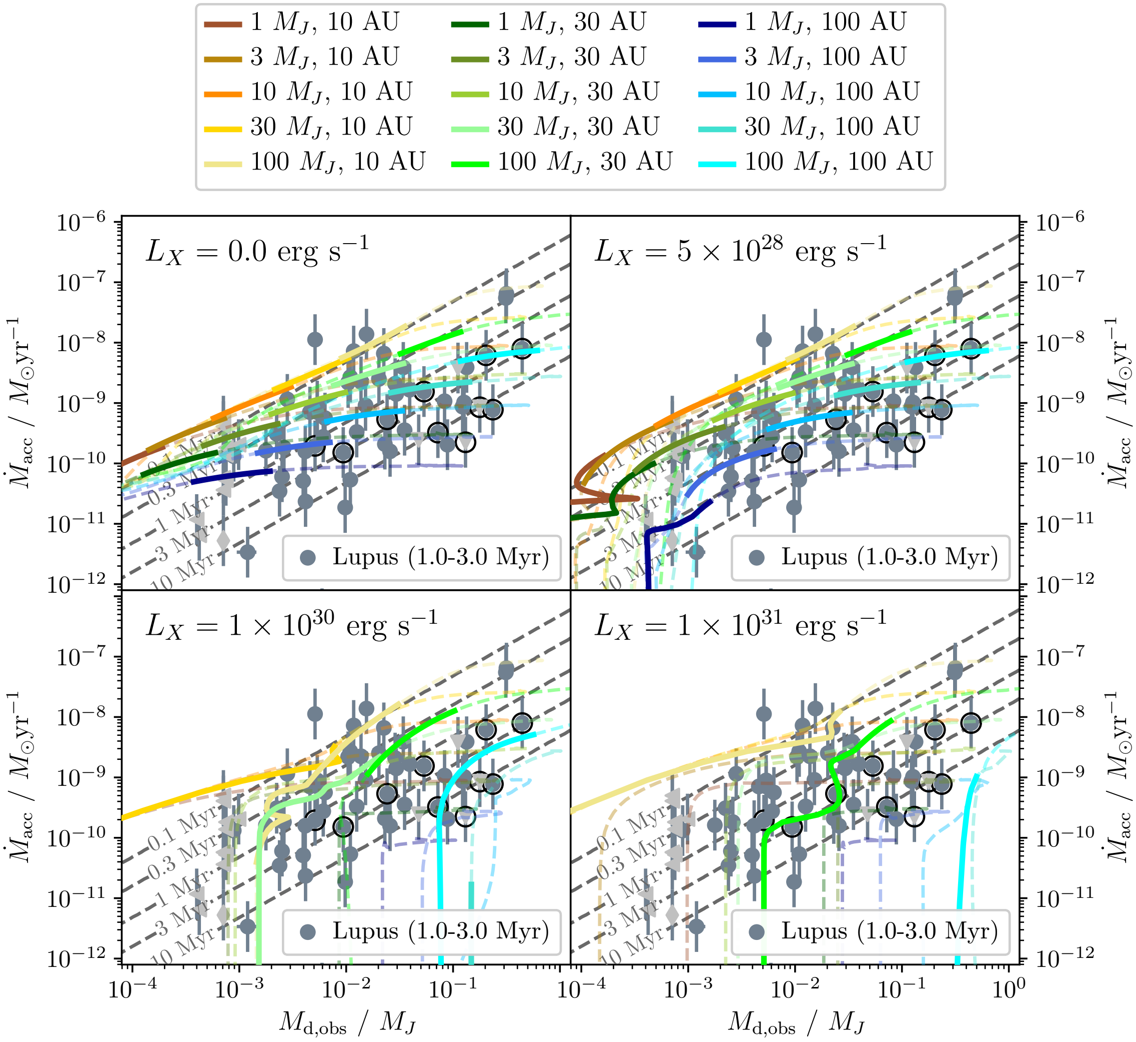

Fig. 5.4 As with the upper-right panel of Figure 5.1, but with X-ray photoevaporation produced by different X-ray luminosities.

The models subjected to $L_X = 5 \times 10^{28}$ erg s^{-1} are presented in the upper-right panel of Figure 5.4; this luminosity produces a mass-loss rate of 3.71×10^{-10} M$_\odot$ yr^{-1}, similar to that in the EUV model presented above. The evolution is qualitatively very similar to the EUV case. The mass-loss due to EUV photoevaporation is concentrated into a narrower range of radii than in the X-ray case. Consequently X-rays are slightly slower at opening a gap in the disc. This means that more dust can deplete before accretion is switched off, which is most obvious in that the initially large discs are dispersed at slightly lower masses, perhaps moderately more consistent with the data. Nevertheless, there is little difference between these models and those using an EUV prescription.

For $L_X = 10^{30}$ erg s^{-1} (lower-left panel of Figure 5.4), the area spanned by the evolutionary tracks largely fails to reproduce the data. Very few discs have sufficiently efficient radial drift for the dust depletion to be consistent with the sources which only have upper limits on the mass. Those that do are a very limited range of low-mass, compact, discs, which have low enough densities but large enough mass-loss rates in the outer disc that the extended X-ray–driven photoevaporation clears them from the outside in, rather than by opening a gap. Consequently, rather than trapping dust, the lowering of gas surface densities raises the Stokes number and accelerates the loss of dust to drift; the discs disperse at much lower masses ($M_{\rm d,obs} \sim 10^{-6} - 10^{-5}$ M$_{\rm J}$) than the upper limits.

Another potential issue is that the initially large discs are dispersed at relatively high dust masses and all pass through a region not occupied by the data. As with the EUV models that did similarly, this is not problematic if they do so on timescales shorter than 1 Myr; however the more massive of these discs do survive more than 1 Myr. It is not, however, impossible that some discs do reside in this area. Some sources (plotted as downward pointing triangles) in the right mass range are classed as potentially non-accreting - as they have accretion luminosity consistent with chromospheric noise (Alcalá et al., 2017; Manara et al., 2020) - and hence their measurements could be considered upper limits. It is likewise possible that some discs that we consider too massive to agree with the basic dust evolution models could also be explained as initially large discs shortly before their dispersal by photoevaporation.

Finally, we consider $L_X = 10^{31}$ erg s^{-1} (lower-right panel of Figure 5.4), which is really most appropriate for a relatively massive $\sim 3\ M_\odot$ star - a rare occurrence at the upper end of the observed range. In this case, only the most massive discs survive to 1 Myr. Considering a hypothetical scenario in which these high mass-loss rates are appropriate for all stellar masses, then to resolve this timescale issue, we might invoke the cluster being younger than measured. Then, however, as with $L_X = 10^{30}$ erg s^{-1}, it would once again be very hard to explain the lowest mass discs: with this mass-loss rate, the gap usually opens before radial drift has long enough to deplete the observers' equivalent dust mass to $\lesssim 10^{-2}$ M$_{\rm J}$. Such a high mass-loss rate across the cluster is thus incompatible with both the timescales and disc masses in the region, which given the uncertainties in the photoevaporation models, puts a useful constraint on the acceptable mass-loss rates. Conversely, if these mass-loss prescriptions are right, then the massive stars to which they mostly likely apply should start with very massive discs.

5.4.3 Stellar Mass Dependence

The paucity of models with high L_X that reproduce lower mass discs and sources without sub-mm detections may not be a large issue once one accounts for the dimension of stellar mass. As discussed, $L_X = 10^{30}$ erg s^{-1} and $L_X = 10^{31}$ erg s^{-1} are only appropriate for $\sim 1\ M_\odot$ and $\sim 3\ M_\odot$ stars respectively, whereas the IMF results in the least massive stars being the most common (Chabrier, 2003). For low-mass stars, the lower luminosities should be more typical.

To explore this, we run additional sets of models both without photoevaporation and with $L_X = 5 \times 10^{28}$ erg s^{-1} for discs around stars of mass $0.1\ M_\odot$ and compare our results to the Lupus sample split on a mass of $0.3\ M_\odot$. The initial dependence of initial disc mass and radius on stellar mass is unknown, though Somigliana et al. (2022) recently inferred possible power law scalings from the evolution of the dependence of mass and accretion rate (Testi et al., 2022). Since we run a grid of models this is not of great importance, though we limit the initial disc masses $\leq 10\ \mathrm{M_J}$ since a disc-star mass ratio ~ 0.1 is typically taken as the limit of gravitational stability. The variation of disc temperature with stellar mass is also poorly understood - observationally there appears to be little correlation (Tazzari et al., 2017), but theoretical radiative transfer models find steeper relationships depending on the assumptions about opacities and stellar evolutionary models (Sinclair et al., 2020). Here, we choose to assume a fairly maximal temperature dependence $T \propto M_*^{1/3}$.

The right-hand panels of Figure 5.5 show the results of these additional models. The panels from Figure 5.4 showing the evolution for a solar-mass star are replicated on the left for ease of comparison.

In the non-photoevaporating case, we see very little effect of stellar mass, with only a small preference towards lower masses at a given accretion rate. This is because the effect of less efficient radial drift for drift-limited dust around lower mass stars (Pascucci et al., 2016), leading to more dust retention, is largely balanced by the cooler temperatures at which we assume the dust emits. Because these models do not extend to such high initial masses, they also cannot explain the highest mass or accretion rate discs, but this is not a problem as these are typically found around higher mass stars (Andrews et al., 2013; Ansdell et al., 2016; Pascucci et al., 2016).

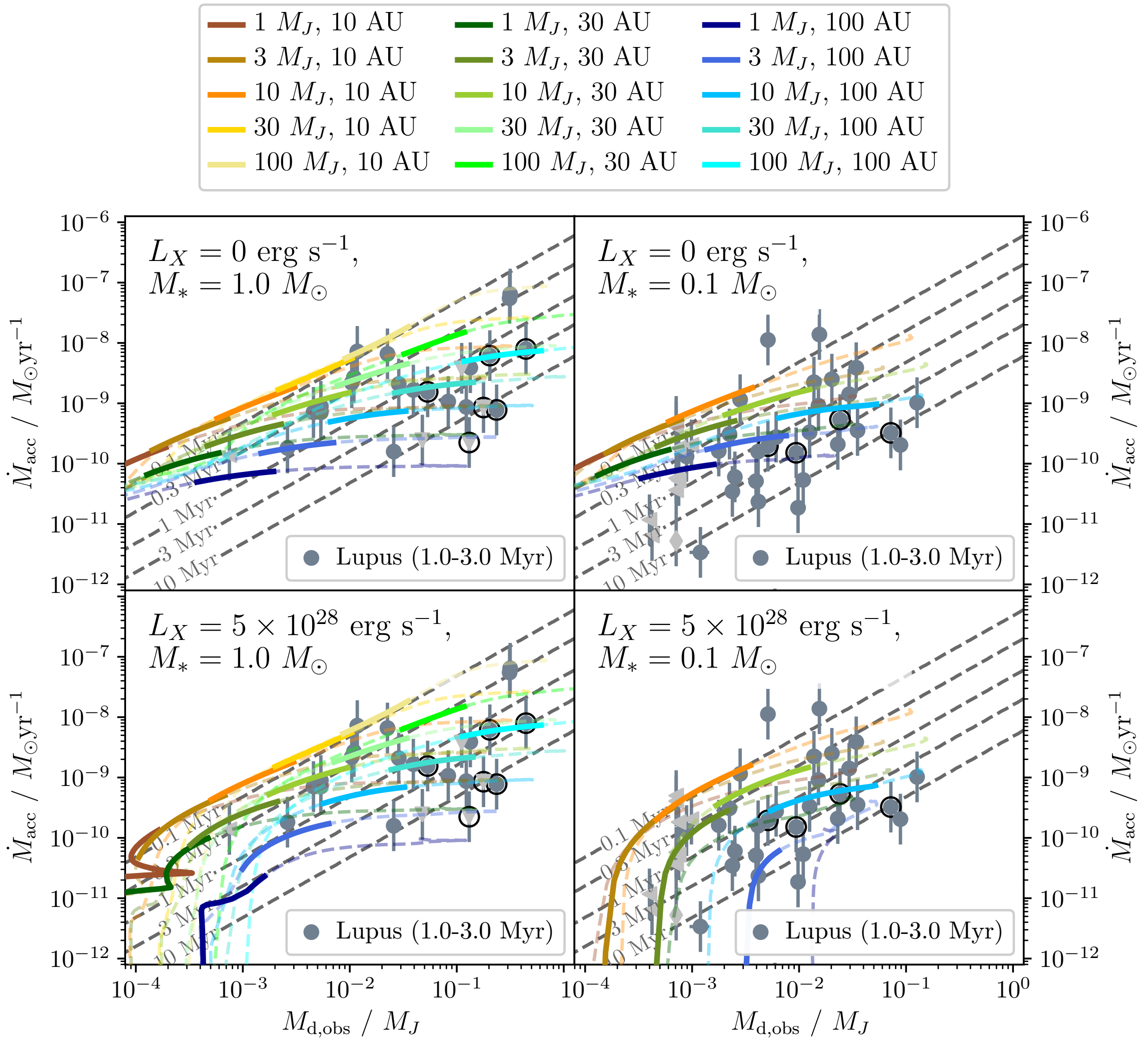

Fig. 5.5 Effect of changing the stellar mass on both a non-photoevaporating model (top) and an X-ray photoevaporation model (bottom). Each panel contains data from the Lupus; the 1.0 models show discs around stars $> 0.3\ M_\odot$ while the 0.1 models show discs around stars $< 0.3\ M_\odot$.

At low accretion rates, a slightly bigger difference emerges once photoevaporation is considered. Because of the slower radial drift around low-mass stars in the drift-limited phase, more dust is retained once the gap opens and the accretion rates decline. This is reflected in the observers' equivalent dust masses at dispersal. Consequently, only the most compact disc models can now reproduce the sources with disc non-detections. This will only present a challenge if the upper limits on mm flux found by Ansdell et al. (2016) turn out to correspond to flux measurements significantly lower than these upper limits, in which case they could potentially be explained as having a below-average L_X.

Moreover, we have now divided the data in Figure 5.5 such that stars $< 0.3\ M_\odot$ are compared to the 0.1 models and stars $> 0.3\ M_\odot$ are compared to the 1.0 models. Here we see that except for one upper limit, all the higher M_* sample are found at $M_{\rm d,obs} \gtrsim 3 \times 10^{-3} M_{\rm J}$ whereas the sample with lower disc masses and low accretion rates that were a challenge to reproduce with the higher L_X prescriptions are indeed all around low-mass stars for which lower L_X is typical. As all the higher mass sample have, where detected, accretion rates above $10^{-10}\ M_\odot\ {\rm yr}^{-1}$, it is not clear which part of the plot they pass through as they disperse but they are not inconsistent with the high L_X prescriptions, so long as they have sufficiently high initial disc masses $\gtrsim 10\ M_{\rm J}$ so that they survive to at least 1 Myr.

5.4.4 The Role of Internal Photoevaporation in Upper Sco

Figure 5.6 shows the EUV photoevaporation models from Figure 5.3 at 5 to 10 Myr, compared to the discs in Upper Sco (Manara et al., 2020). As was the case at earlier times, photoevaporation extends the area accessible to the models down to lower accretion rates, and prevents discs reaching very low masses, which are not present in the current sample. We reiterate that since Manara et al. (2020) only surveyed cluster members with sub-mm disc detections, at the lowest masses we lack information about how the plane is populated, specifically whether the accretion rates are high ("transparent accretors"), or whether they are more consistent with being starved by photoevaporation.

As aforementioned, at low dust-disc masses, the accretion rates extend down to very similar values. Since photoevaporation becomes effective once the accretion rate becomes of order the mass-loss rate, a given photoevaporation rate sets a floor scale to the accretion rates, beyond which the decline in the accretion rate and subsequent gas disc dispersal happens rapidly. Thus, if we assume that at any time at least some discs should have accretion rates approaching the photoevaporation rate and should thus be approaching dispersal, we would expect not to see an evolution in the lower limit of the observed accretion rates. A similar suggestion was made by Ercolano et al. (2014): that the trend between accretion rates and stellar mass could simply reflect the dependence of X-ray photoevaporation rates on stellar

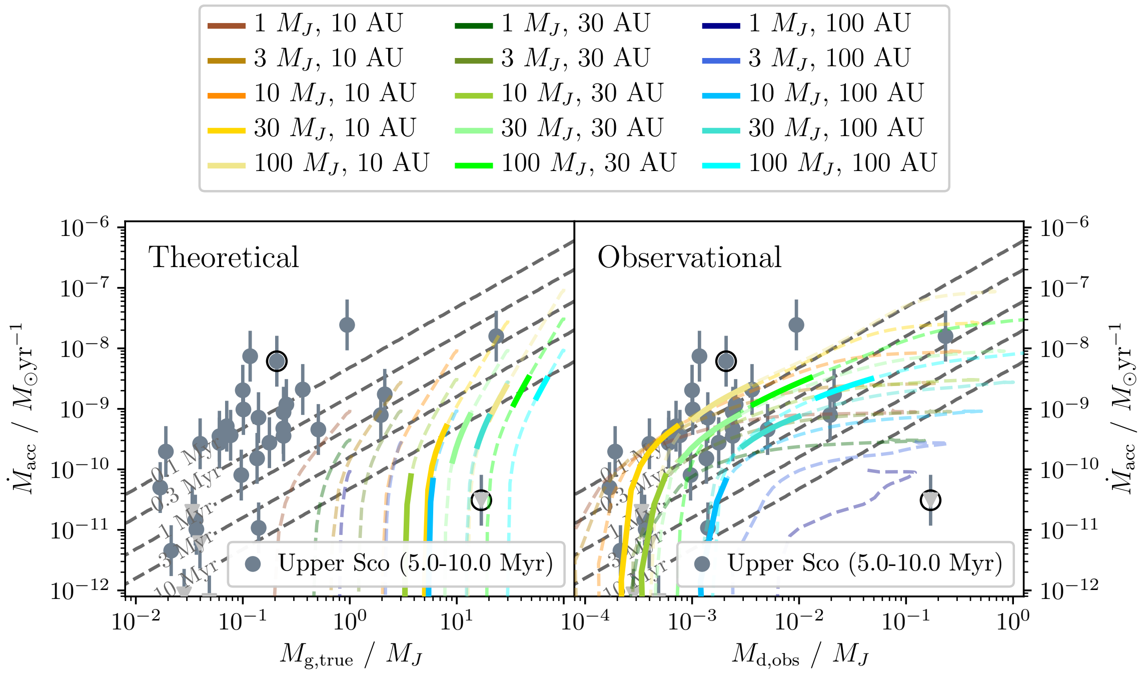

Fig. 5.6 Models with EUV photoevaporation produced by an ionising photon flux $\Phi = 10^{42}$ s^{-1}. As the upper panels of Figure 5.3 but with data from Manara et al. (2020). The solid sections indicate system ages of $5-10$ Myr.

mass (principally via the X-ray luminosity) if one assumes that we are most likely to see the discs just before the photoevaporative wind opens a gap and hence disc accretion rates are most likely to be recorded at their lowest value before dispersal.

This gives a very satisfying explanation for the similar distributions of accretion rate in any one mass bin between Upper Sco and younger regions. The upper limit is set by the non-evolving upper locus at ~ 0.1 Myr produced by the radial drift dust model as discussed in Section 5.3.3, while the lower limit is set by the onset of rapid dispersal by photoevaporation.

However, Figure 5.7 shows one potential drawback for our 0.1 $M_\odot$ models with X-ray photoevaporation. By the age of Upper Sco, none of these discs would have ongoing accretion above 10^{-10} $M_\odot$ yr^{-1}, in contrast to observed accretion above this level onto stars as low as 0.12 M$_\odot$ (Manara et al., 2020). Therefore, the observations for low-mass stars would be better fit by a lower photoevaporation rate, i.e. by a model with $L_{\rm X} < 5 \times 10^{28}$ erg s^{-1}. This is not impossible since there can be ~ 0.6 dex scatter about the mean luminosity at a given mass (Preibisch et al., 2005). However, as I discuss more in 5.5.1, more recent photoevaporation prescriptions by Picogna et al. (2021) predict photoevaporation rates $\sim 4 \times 10^{-9}$ $M_\odot$ yr^{-1} for 0.1 $M_\odot$ stars (compared to 4×10^{-10} $M_\odot$ yr^{-1} in our lowest $L_{\rm X}$ models) which would worsen the problem considerably.

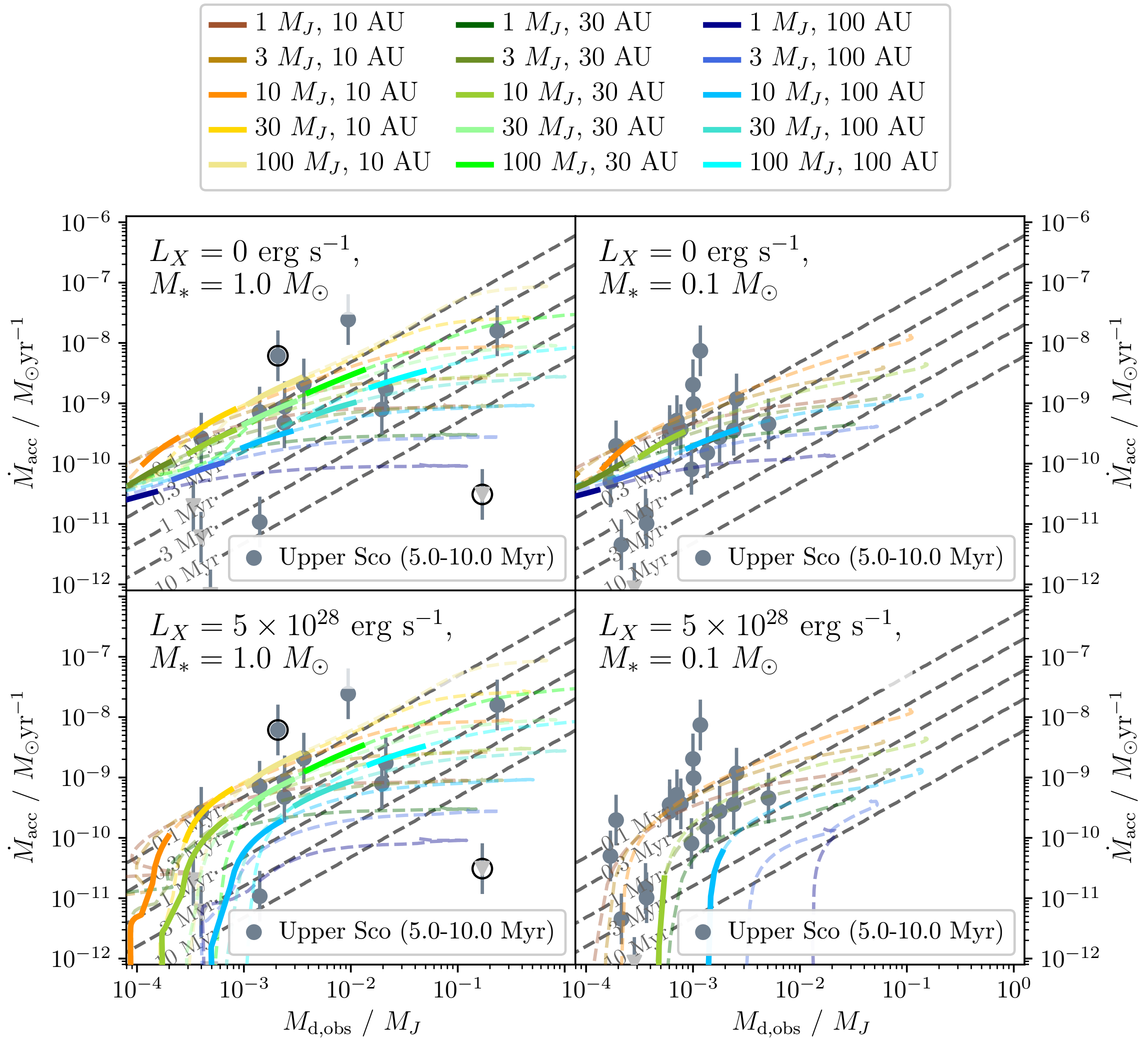

Fig. 5.7 Effect of changing the stellar mass on both a non-photoevaporating model (top) and an X-ray photoevaporation model (bottom) at late times ($5 - 10$ Myr). Each panel contains data from Upper Scorpius; the 1.0 models show discs around stars $> 0.3\ M_\odot$ while the 0.1 models show discs around stars $< 0.3\ M_\odot$.

Overall, this therefore largely seems to preclude X-ray photoevaporation from explaining the surviving accreting discs in Upper Sco unless the mass-loss rates are highly overestimated.

5.5 Discussion

5.5.1 Choice of Photoevaporation Prescription

Recently, Appelgren et al. (2023) conducted a population synthesis study of disc models which, similarly to ours, include viscous evolution, grain growth and drift, and photoevaporation. They use more recent Picogna et al. (2021) and Komaki et al. (2021) prescriptions for X-ray and FUV photoevaporation respectively. They also plot the evolution of their population in the $\dot{M} - M_{\rm dust}$ plane but do not calculate an observers' equivalent dust mass. Consequently, while drift allows them to reach much smaller $t_{\rm acc}$ than viscous accretion alone, they more or less skirt the low-mass edge of the observational data.

They also find distinct fates for the two photoevaporation prescriptions. In all discs, the Picogna et al. (2021) rates halted accretion in ≤ 3 Myr. Similarly, Emsenhuber et al. (2023), found that the for median $L_{\rm X}$, the disc lifetime is never more than about 4 Myr using the same rates. This is in stark contrast to the existence of accreting discs beyond this time and results from high mass-loss rates in those models even for low-mass stars.

In contrast, Appelgren et al. (2023)'s models using Komaki et al. (2021) rates - which have a lower $\dot{M}$ - all lasted for at least 6 Myr; while this helps the existence of accreting discs in older regions like Upper Sco, not one model passes through the region of low accretion rates seen in all regions as they have lost all but a tiny fraction of their dust by the time of dispersal.

Overall, it seems the results are therefore most sensitive to the overall mass-loss rate as this sets the time of gas opening, which in turn sets the retained dust mass at dispersal. While it currently seems difficult to reproduce both these masses and the accreting lifetimes of disc, using alternative photoevaporation prescriptions wouldn't qualitatively change the outcomes of this work so long as our models reasonably bracket the space of possible $\dot{M}$.

One possibility advanced by Emsenhuber et al. (2023) is that the presence of material close to the star - for example in a magnetic wind from the inner disc - could screen the outer disc from some of the X-ray and lead to lower photoevaporation rates. Alternatively infall could replenish disc masses against photoevaporation, extending their lifetimes. Though Appelgren et al. (2023) include disc infall in their model, this doesn't significantly extend the lifetime of their discs because it only occurs for $O(0.1\ \text{Myr})$. However, based on large-scale nebulosity discovered near several Class II protoplanetary discs (Gupta et al., 2023) - some of which have interferometric detections of large-scale gas structures with morphologies and kinematics consistent with infall (Tang et al., 2012; Ginski et al., 2021; Huang et al., 2020, 2021, 2022, 2023) - infall could be happening much later in a significant way; Dullemond et al. (2019) advance a model where this could result when discs encounter low-mass remnants of the natal molecular cloud.

5.5.2 Dust Trapping in Substructures

Several observed discs have dust masses much higher than our models at equivalent ages. This suggests that radial drift may need to be slowed to explain them. In models of smooth discs, a higher level of turbulence, or a smaller velocity at which collisions between grains result in fragmentation (as has been suggested by Gundlach et al., 2018; Musiolik & Wurm, 2019), would result in smaller, better-coupled, grains. In this case, drift would only become significant once the gas surface densities became low enough, which would result in a rapid decrease in disc mass only once $\dot{M}_{\rm acc} \sim 10^{-10}\ M_{\odot}\ {\rm yr}^{-1}$ (Appelgren et al., 2020). If fewer grain collisions lead to coagulation, the dust grows more slowly and the supply of drifting dust is reduced; once the dust reaches the regime predicted by Equation 1.63, this will mean that the dust mass is proportionally higher. The impact of these parameters is explored more thoroughly in Sellek et al. (2020b), however it is unlikely that any of these quantities should vary between discs in a way that can allow us to continue to explain both the low $t_{\rm acc}$ and high $t_{\rm acc}$ cases.

A more interesting possibility would be some discs including pressure bumps that trap the grains. Indeed, several discs in both Lupus and Upper Sco where we need extra dust retention in our models are known to host annular substructures (in particular, GW Lup (Sz 71) and HD 143006 (in Upper Sco) have very high contrast rings that could certainly trap dust Dullemond et al., 2018) and substructures appeared ubiquitous in the DSHARP sample (Andrews et al., 2018; Huang et al., 2018), though this was biased towards bright - and therefore massive - discs.

Nevertheless radial drift must be efficient in at least some discs for us to explain the low $t_{\rm acc}$ and multiple lines of evidence support a dichotomy between faint discs with efficient drift and bright discs with dust traps. While the average disc mass declines with cluster age, the most massive discs in each cluster see to have a roughly constant mass (Ansdell et al., 2020), suggesting a minority of discs hold onto their dust mass for several Myr (Michel et al., 2021). Pinilla et al. (2018) show that the slope of the relation between $M_{\rm dust}$ and M_* is much shallower for transition discs than full discs and modelling by Pinilla et al. (2020) confirmed that the shallow relationship for discs with substructures could be explained by pressure bumps trapping dust (so long as boulder formation within the traps is inhibited). There are also proposed chemical dichotomies between compact and extended discs suggesting that volatiles may be trapped outside snowlines in structured discs while they are deposited in the inner disc by unimpeded pebble drift in compact discs (Banzatti et al., 2020; van der Marel et al., 2021).

The most tantalising explanation for the annular features is that they result from the presence of planets (e.g. Papaloizou & Lin, 1984; Paardekooper & Mellema, 2004; Zhang et al., 2018). Sinclair et al. (2020) suggest that it becomes harder for planets to open gaps around lower mass hosts, so we may also expect fewer traps at lower disc masses. By categorising discs as either structured, extended or compact, van der Marel & Mulders (2021) showed that the statistics of these discs as a function of stellar mass were similar to those of different planetary system architectures: namely giant planets, which would be required to open substructures, occur with similar patterns to structured or extended discs, while compact discs have more similar statistics to systems of super-Earths.

In the older sample from Upper Scorpius, there are only two discs at too high mass to be explained by the photoevaporating models, relatively few compared to Lupus. Rosotti et al. (2013) found that a giant planet would reduce the accretion flow in the inner disc allowing photoevaporation to clear the disc sooner than otherwise. Thus if giant planets are more common in high-mass discs, they could have shorter lifetimes (despite initially holding onto their dust) than lower-mass structureless counterparts, with mostly only the latter surviving to the age of Upper Sco.

5.5.3 Magnetically-driven Winds

Finally, I comment on the relative behaviour of magnetically driven winds compared to photoevaporation. When accretion is driven purely by MHD winds, models evolve at a constant $t_{\rm acc}$ due to the lack of viscous spreading, rather than evolving towards $t_{\rm acc} \sim t$ (Tabone et al., 2022b). In the absence of dust evolution, the distribution of $t_{\rm acc}$ that we observe would therefore be largely independent of a region's age (as indeed observed Manara et al., 2020) and simply reflect the initial distribution. However, only if the torque depends on the surface density, the discs disperse in a finite time (Equation 1.52) and do so in the fashion $t_{\rm acc} \rightarrow 0$. Although not accounting for dust effects, Tabone et al. (2022a) showed that in such a model, the same distribution of $t_{\rm acc}$ that would explain the decay of disc fractions with time can also successfully fit the $\dot{M} - M_{\rm dust}$ relationship in Lupus.

Therefore, determining whether individual discs evolve towards small or large $t_{\rm acc}$ at the end of their lifetimes would be a good way to distinguish observationally whether magnetically-driven winds or photoevaporation are ultimately responsible for protoplanetary disc dispersal (Manara et al., 2022).

5.6 Conclusions

In this chapter, I investigated the impact that photoevaporation has on protoplanetary disc evolution - and how this allows us to constrain its strength and role in disc dispersal - by coupling different mass-loss prescriptions to a model of gas and dust evolution in discs and following the evolution for a range of initial parameters. By modelling the sub-mm fluxes produced by the models - and the corresponding values of dust mass that an observer would deduce from them - I compared these models to observational estimates of disc mass (from sub-mm fluxes) and stellar accretion rates (from the UV continuum excess) from two star-forming regions of different ages: Lupus (1-3 Myr) and Upper Sco (5-10 Myr).

Due to the growth and radial drift of dust (which can lower the dust-to-gas ratio by over an order of magnitude, Figure 5.1), models accounting for dust evolution better reproduce the distribution of observed sources in the plane of accretion rate versus (observers' equivalent) dust mass than purely viscous models of gas evolution. Previously it had been puzzling that many sources have $t_{\rm acc} = M_{\rm disc}/\dot{M}_{\rm acc}$ values much less than the star-forming regions' ages, while viscous models predict that $t_{\rm acc} > 2t$. Dust drift accounts for these sources, while increasing the distribution's scatter in a way that depends mostly on the initial disc radius, since this determines the timescale on which the bulk of the dust grains start to undergo drift.

However as a consequence of its success, this model leaves discs at high $t_{\rm acc}$ which can no longer be explained without strongly impeding the radial drift of dust (as might be the case if these discs contain pressure bumps that trap grains; Section 5.5.2). A subset of these - though not including many bright, highly accreting transition discs (which in general have historically been linked to photoevaporation) - can be explained as sources where the accretion rate has fallen below typical photoevaporation rates: these are discs with dust masses of $\sim 10^{-3}$ $\rm M_J$ but very low accretion rates $< 10^{-10}$ $\rm M_\odot\ yr^{-1}$.

In these discs, internal photoevaporation acts to starve accretion onto the star: a cavity has opened and the accretion rate is rapidly declining at approximately constant dust mass (since the dust becomes trapped outside the cavity). Relatively low photoevaporation rates $\lesssim 10^{-9}$ $\rm M_\odot\ yr^{-1}$ - as appropriate to an EUV-driven model with $\Phi = 10^{42}$ $\rm s^{-1}$ or an X-ray model with $L_{\rm X} = 5 \times 10^{28} \rm erg\ s^{-1}$ - are required to reproduce the observed dust masses as discs pass through these low accretion rates (Figure 5.4), else the discs instead trap too much dust outside their cavity. Most discs - including these - are found around low-mass stars, which should generally have low photoevaporation rates, so for the prescriptions we use, the data do not discriminate between models where photoevaporation is EUV or X-ray–driven. However, X-ray photoevaporation prescriptions by Picogna et al. (2021) raised the photoevaporation rate for low-mass stars considerably. Our models would suggest that the rates predicted by these most recent X-ray photoevaporation models are too high to allow sufficient radial drift to take place before dispersal. Moreover, even low photoevaporation rate models struggle to leave many accreting systems by the age of Upper Sco.

Therefore, I conclude that photoevaporation, through the UV switch mechanism, seems important for counteracting the tendency of radial drift to disperse discs at low t_{acc}, thus populating the low-accretion-rate part of the accretion rate - dust mass plane. This includes setting a natural lower scale to the accretion rates that doesn't evolve in time. However, there are significant challenges regarding the timescale upon which it does so unless the rates are relatively low, which seems to preclude the most recent X-ray photoevaporation models.

Chapter 6

Conclusions and Outlook

At the start of this thesis I posed three key questions regarding the importance of photoevaporation of protoplanetary discs:

1. What sort of high-energy radiation is most important for wind driving?
2. How important are photoevaporative winds for protoplanetary disc evolution and dispersal?
3. Can observations of winds be understood using photoevaporation, or must magnetic fields be invoked?

Subsequently I have approached constraining the role of photoevaporation in disc evolution from two distinct directions.

Firstly, I have sought to advance our understanding of the hydrodynamics and thermodynamics of photoevaporation in an effort to build more accurate models that resolve existing theoretical uncertainties about the nature of the winds. To this end, in Chapter 2, I demonstrated how self-similar solutions for thermal winds generalise to non-isothermal winds launched from an elevated base, verified that they still agreed with hydrodynamic simulations, and developed an explanation for their launch velocities. In Chapter 3, I compared temperatures calculated by different codes for an EUV-driven wind, revealing the importance of comprehensively treating the coolants to correctly obtaining these and quantifying the role played by X-ray frequency in determining how effectively material is heated sufficiently to launch a wind (finding that energies ~ 500 eV are most effective).

Secondly, I have attempted to place observational constraints on winds using forward modelling. In Chapter 4, I applied the models of Chapter 2 along with the MOCASSIN code explored in 3 to interpret the luminosities and shapes of blueshifted emission lines from the wind - with a particular focus on [Ne II] emission from T Cha - finding that a high mass-loss rate wind, a high-luminosity spectrum, and a smaller inner wind radius are the best fit to the data. Finally, in the most direct link to the title, in Chapter 5, I studied demographics in the plane of accretion rates and dust masses using disc evolution models and explored the tracks that photoevaporating discs follow in this plane.

However, even now, certain challenges remain. As discussed in Chapter 5, while some photoevaporation seems necessary to induce inside-out clearing in a way that causes the accretion rate to drop below $10^{-10}\ M_\odot\ \mathrm{yr}^{-1}$, the presence of discs undergoing accretion above this rate for ~ 10 Myr around low-mass stars is hard to explain if they have significant mass-loss rates. This sets a tight limit on how strong photoevaporation can be for these systems. Moreover, despite radial drift being efficient, strong photoevaporation rates much above $10^{-9}\ M_\odot\ \mathrm{yr}^{-1}$ would not allow disc dust masses to decline to frequently observed levels. Thus disc demographics seem to argue in favour of low (but non-zero) photoevaporation rates, perhaps most consistent with EUV-driven models.

However, Chapter 4 revealed that such weak mass-loss rates seem to be incompatible with the ratios of lines from different ions: the relative brightness of observed [Ne II] and [Ar II] emission relative to [Ne III] and [Ar III] requires the winds to be dense enough that they are largely optically thick to the EUV and only weakly ionised. Moreover mass-loss rates $\gtrsim 10^{-8}\ M_\odot\ \mathrm{yr}^{-1}$ are required for the winds to have enough emitting material to reproduce the observed luminosities.

These two scenarios may possibly be reconciled by considering that demographics are most sensitive to the most common systems - which are low-mass stars - while the focus of Chapter 4 was on more massive systems (with all Ne II LVCs being measured for stars earlier then M1 spectral type, Pascucci et al., 2020). Indeed various works do find increasing photoevaporation rates with stellar mass (Owen et al., 2012; Picogna et al., 2021; Komaki et al., 2021). Thus a focus for future theoretical work should be to further explore this dimension, taking full account that the dominant heating and cooling channels may change (for example the relative strength of X-ray and FUV varies with mass, and in Chapter 3 I suggested that adiabatic cooling may be relatively more important for lower density winds). These must be more rigorously tested against trends such as the longer lifetime of inner discs around less-massive stars (Bayo et al., 2012). From an observational perspective, future surveys could valuably constrain multiple Ne emission lines for discs around lower-mass stars (as Fang et al., 2023a, did for O I) which are also typically longer lived and more slowly accreting, and thus build a larger sample from which we can understand the generality of the interpretations I made in Chapter 4. For example, do there exist discs where Ne III is brighter than Ne II implying a highly ionised, low $\dot{M}$ wind?

Furthermore, the forward models for T Cha and V4046 Sgr best match the relatively broad emission lines if the emission mostly comes from radii inside the gravitational radius, contrary to photoevaporation where most mass-loss is expected outside. JWST observations of Ne II emission from these discs should be able to at least place an upper limit on its radial extension and confirm whether the wind is indeed launched at close-in radii, which are potentially more in line with magnetically-driven models. However such conclusions about the viability of photoevaporation as I draw here have been made without any direct line profile modelling for magnetically-driven winds; a valuable exercise would therefore be to produce such models that can be compared directly to photoevaporation.

A requirement for a magnetically-driven wind would align with a recent trend in the protoplanetary disc community, where magnetic winds as the source of accretion stresses have been receiving more attention due to the weak turbulence and viscosity estimated for discs, as well as recent advances in global magnetohydrodynamic simulations. However, magnetically-driven winds are also subject to radiative heating and cooling of the sort found in photoevaporative winds, and hence are currently subject to similar thermochemical modelling uncertainties depending on the focus made by each work on different parts of the spectrum or different cooling channels. Therefore, regardless of whether the predominant channel of wind mass-loss in protoplanetary discs turns out to be magnetic or purely photoevaporative, the efforts made here towards understanding the roles that FUV, EUV, and X-ray play in the heating of winds - and atoms and molecules to the cooling - and hence advance the thermochemical models towards a correct solution should be invaluable to the field as a whole. Building on the underlying insights established throughout this thesis, the prospect is bright for an ongoing project using PLUTO and PRIZMO to produce the most accurate radiation hydrodynamic simulations of photoevaporation to date, and systemically study the effects of different spectra and cooling networks, hopefully laying the current discrepancies to rest.

Finally I note that to date models have almost exclusively - with the exception of Wölfer et al. (2019) - assumed homogeneous abundances that follow a certain ISM pattern. However the winds take their material from discs which evolve chemically, showing evidence for processes including sequestration of elements into refractory compounds (e.g. Kama et al., 2019) and radial transport (Sturm et al., 2022). In Chapter 4, I speculated that V4046 Sgr and TW Hya may show depletion of O relative to Ne in their winds given similarities to the host stars' anomalous chromospheric abundances. Since many of these trace species affected by chemical evolution play important roles in the heating and/or cooling of winds, coupling simulations to chemically-evolving disc models will be crucial for understanding wind behaviour throughout the disc's lifetime.

References

Abrahamsson E., Krems R. V., Dalgarno A., 2007, ApJ, 654, 1171

Adams F. C., Lada C. J., Shu F. H., 1987, ApJ, 312, 788

Adams F. C., Hollenbach D., Laughlin G., Gorti U., 2004, ApJ, 611, 360

Agra-Amboage V., Cabrit S., Dougados C., Kristensen L. E., Ibgui L., Reunanen J., 2014, A&A, 564, A11

Alcalá J. M., et al., 2014, A&A, 561, A2

Alcalá J. M., et al., 2017, A&A, 600, A20

Alcalá J. M., Manara C. F., France K., Schneider C. P., Arulanantham N., Miotello A., Günther H. M., Brown A., 2019, A&A, 629, A108

Alexander R. D., 2008, MNRAS, 391, L64

Alexander R. D., Armitage P. J., 2007, MNRAS, 375, 500

Alexander R. D., Clarke C. J., Pringle J. E., 2004a, MNRAS, 348, 879

Alexander R. D., Clarke C. J., Pringle J. E., 2004b, MNRAS, 354, 71

Alexander R. D., Clarke C. J., Pringle J. E., 2005, MNRAS, 358, 283

Alexander R. D., Clarke C. J., Pringle J. E., 2006a, MNRAS, 369, 216

Alexander R. D., Clarke C. J., Pringle J. E., 2006b, MNRAS, 369, 229

Alexander R., Pascucci I., Andrews S., Armitage P., Cieza L., 2014, in Beuther H., Klessen R. S., Dullemond C. P., Henning T., eds, Protostars and Planets VI. p. 475 (arXiv:1311.1819), doi:10.2458/azu_uapress_9780816531240-ch021

Anders E., Grevesse N., 1989, Geochim. Cosmochim. Acta, 53, 197

Andre P., Montmerle T., 1994, ApJ, 420, 837

Andre P., Ward-Thompson D., Barsony M., 1993, ApJ, 406, 122

Andrews S. M., Williams J. P., 2005, ApJ, 631, 1134

Andrews S. M., Rosenfeld K. A., Kraus A. L., Wilner D. J., 2013, ApJ, 771, 129

Andrews S. M., et al., 2018, ApJ, 869, L41

Ansdell M., et al., 2016, ApJ, 828, 46

Ansdell M., Williams J. P., Manara C. F., Miotello A., Facchini S., van der Marel N., Testi L., van Dishoeck E. F., 2017, AJ, 153, 240

Ansdell M., et al., 2018, ApJ, 859, 21

Ansdell M., et al., 2020, AJ, 160, 248

Appelgren J., Lambrechts M., Johansen A., 2020, A&A, 638, A156

Appelgren J., Lambrechts M., van der Marel N., 2023, arXiv e-prints, p. arXiv:2303.07297

Ardila D. R., Basri G., Walter F. M., Valenti J. A., Johns-Krull C. M., 2002, ApJ, 566, 1100

Ardila D. R., et al., 2013, ApJS, 207, 1

Argiroffi C., Maggio A., Peres G., 2007, A&A, 465, L5

Argiroffi C., Maggio A., Peres G., Drake J. J., López-Santiago J., Sciortino S., Stelzer B., 2009, A&A, 507, 939

Armitage P. J., Simon J. B., Martin R. G., 2013, ApJ, 778, L14

Arulanantham N., France K., Hoadley K., Schneider P. C., Espaillat C. C., Günther H. M., Herczeg G. J., Brown A., 2021, AJ, 162, 185

Arulanantham N., et al., 2023, arXiv e-prints, p. arXiv:2301.01761

Asplund M., Grevesse N., Sauval A. J., 2005, in Barnes Thomas G. I., Bash F. N., eds, Astronomical Society of the Pacific Conference Series Vol. 336, Cosmic Abundances as Records of Stellar Evolution and Nucleosynthesis. p. 25

Audard M., Güdel M., Sres A., Raassen A. J. J., Mewe R., 2003, A&A, 398, 1137

Auddy S., Basu S., Valluri S. R., 2016, Advances in Astronomy, 2016, 574327

Avenhaus H., et al., 2018, ApJ, 863, 44

Avery L. W., House L. L., 1968, ApJ, 152, 493

Bae J., Isella A., Zhu Z., Martin R., Okuzumi S., Suriano S., 2022a, arXiv e-prints, p. arXiv:2210.13314

Bae J., et al., 2022b, ApJ, 934, L20

Bai X.-N., 2017, ApJ, 845, 75

Bailey J., 1998, MNRAS, 301, 161

Bajaj N., in prep.

Balbus S. A., Hawley J. F., 1992, ApJ, 400, 610

Balbus S. A., Gammie C. F., Hawley J. F., 1994, MNRAS, 271, 197

Ballabio G., Alexander R. D., Clarke C. J., 2020, MNRAS, 496, 2932

Banzatti A., Pontoppidan K. M., 2015, ApJ, 809, 167

Banzatti A., Pascucci I., Edwards S., Fang M., Gorti U., Flock M., 2019, ApJ, 870, 76

Banzatti A., et al., 2020, ApJ, 903, 124

Banzatti A., et al., 2022, AJ, 163, 174

Bar-Nun A., Herman G., Laufer D., Rappaport M. L., 1985, Icarus, 63, 317

Barenfeld S. A., Carpenter J. M., Ricci L., Isella A., 2016, ApJ, 827, 142

Barrier E. F. L., Clarke C. J., Sellek A. D., in prep.

Bast J. E., Brown J. M., Herczeg G. J., van Dishoeck E. F., Pontoppidan K. M., 2011, A&A, 527, A119

Bayo A., Barrado D., Huélamo N., Morales-Calderón M., Melo C., Stauffer J., Stelzer B., 2012, A&A, 547, A80

Beckwith S. V. W., Sargent A. I., Chini R. S., Guesten R., 1990, AJ, 99, 924

Bell K. L., Berrington K. A., Thomas M. R. J., 1998, MNRAS, 293, L83

Benisty M., et al., 2021, ApJ, 916, L2

Benítez-Llambay P., Masset F. S., 2016, ApJS, 223, 11

Bertout C., Basri G., Bouvier J., 1988, ApJ, 330, 350

Béthune W., Lesur G., Ferreira J., 2017, A&A, 600, A75

Birnstiel T., Klahr H., Ercolano B., 2012, A&A, 539, A148

Birnstiel T., et al., 2018, ApJ, 869, L45

Blandford R. D., Payne D. G., 1982, MNRAS, 199, 883

Blum J., Wurm G., 2008, ARA&A, 46, 21

Bohlin R. C., Savage B. D., Drake J. F., 1978, ApJ, 224, 132

Booth R. A., Clarke C. J., 2021, MNRAS, 502, 1569

Booth R. A., Owen J. E., 2020, MNRAS, 493, 5079

Booth R. A., Clarke C. J., Madhusudhan N., Ilee J. D., 2017, MNRAS, 469, 3994

Booth A. S., et al., 2021, ApJS, 257, 16

Briceño C., et al., 2019, AJ, 157, 85

Brickhouse N. S., Cranmer S. R., Dupree A. K., Luna G. J. M., Wolk S., 2010, ApJ, 710, 1835

Brinkman A. C., et al., 2001, A&A, 365, L324

Brown J. M., et al., 2007, ApJ, 664, L107

Bushouse H., et al., 2022, JWST Calibration Pipeline, doi:10.5281/zenodo.7714020, https://doi.org/10.5281/zenodo.7714020

Cahill E., Whelan E. T., Huélamo N., Alcalá J., 2019, MNRAS, 484, 4315

Calvet N., Muzerolle J., Briceño C., Hernández J., Hartmann L., Saucedo J. L., Gordon K. D., 2004, AJ, 128, 1294

Carrera D., Simon J. B., Li R., Kretke K. A., Klahr H., 2021, AJ, 161, 96

Chabrier G., 2003, PASP, 115, 763

Chadney J. M., Galand M., Unruh Y. C., Koskinen T. T., Sanz-Forcada J., 2015, Icarus, 250, 357

Chambers J., 2019, ApJ, 879, 98

Chatterjee S., Tan J. C., 2014, ApJ, 780, 53

Chiang E. I., Goldreich P., 1997, ApJ, 490, 368

Clarke C. J., 2007, MNRAS, 376, 1350

Clarke C. J., Alexander R. D., 2016, MNRAS, 460, 3044

Clarke C. J., Pringle J. E., 2006, MNRAS, 370, L10

Clarke C. J., Gendrin A., Sotomayor M., 2001, MNRAS, 328, 485

Cleeves L. I., Öberg K. I., Wilner D. J., Huang J., Loomis R. A., Andrews S. M., Czekala I., 2016, ApJ, 832, 110

Cohen M., Harrington J. P., Hess R., 1984, ApJ, 283, 687

Coleman G. A. L., Haworth T. J., 2022, MNRAS, 514, 2315

Curran R. L., Argiroffi C., Sacco G. G., Orlando S., Peres G., Reale F., Maggio A., 2011, A&A, 526, A104

Currie T., et al., 2022, Nature Astronomy, 6, 751

D'Alessio P., Calvet N., Hartmann L., 2001, ApJ, 553, 321

Damiani F., Prisinzano L., Pillitteri I., Micela G., Sciortino S., 2019, A&A, 623, A112

David T. J., Hillenbrand L. A., Gillen E., Cody A. M., Howell S. B., Isaacson H. T., Livingston J. H., 2019, ApJ, 872, 161

Dennison B., Turner B. E., Minter A. H., 2005, ApJ, 633, 309

Dere K. P., Landi E., Mason H. E., Monsignori Fossi B. C., Young P. R., 1997, A&AS, 125, 149

Dere K. P., Del Zanna G., Young P. R., Landi E., Sutherland R. S., 2019, ApJS, 241, 22

Dijkstra M., 2017, arXiv e-prints, p. arXiv:1704.03416

Dipierro G., Laibe G., Alexander R., Hutchison M., 2018, MNRAS, 479, 4187

Draine B. T., 2003a, ApJ, 598, 1017

Draine B. T., 2003b, ApJ, 598, 1026

Draine B. T., 2011, Physics of the Interstellar and Intergalactic Medium

Draine B. T., Bertoldi F., 1996, ApJ, 468, 269

Drake J. J., Testa P., Hartmann L., 2005, ApJ, 627, L149

Drążkowska J., Alibert Y., 2017, A&A, 608, A92

Du F., et al., 2017, ApJ, 842, 98

Dullemond C. P., Juhasz A., Pohl A., Sereshti F., Shetty R., Peters T., Commercon B., Flock M., 2012, RADMC-3D: A multi-purpose radiative transfer tool, Astrophysics Source Code Library, record ascl:1202.015 (ascl:1202.015)

Dullemond C. P., et al., 2018, ApJ, 869, L46

Dullemond C. P., Küffmeier M., Goicovic F., Fukagawa M., Oehl V., Kramer M., 2019, A&A, 628, A20

Edwards S., Fischer W., Hillenbrand L., Kwan J., 2006, ApJ, 646, 319

Eisner J. A., et al., 2018, ApJ, 860, 77

Emsenhuber A., Burn R., Weder J., Monsch K., Picogna G., Ercolano B., Preibisch T., 2023, arXiv e-prints, p. arXiv:2301.04656

Epstein P. S., 1924, Physical Review, 23, 710

Ercolano B., Clarke C. J., 2010, MNRAS, 402, 2735

Ercolano B., Owen J. E., 2010, MNRAS, 406, 1553

Ercolano B., Owen J. E., 2016, MNRAS, 460, 3472

Ercolano B., Barlow M. J., Storey P. J., Liu X. W., 2003, MNRAS, 340, 1136

Ercolano B., Barlow M. J., Storey P. J., 2005, MNRAS, 362, 1038

Ercolano B., Young P. R., Drake J. J., Raymond J. C., 2008a, ApJS, 175, 534

Ercolano B., Drake J. J., Raymond J. C., Clarke C. C., 2008b, ApJ, 688, 398

Ercolano B., Clarke C. J., Drake J. J., 2009, ApJ, 699, 1639

Ercolano B., Mayr D., Owen J. E., Rosotti G., Manara C. F., 2014, MNRAS, 439, 256

Ercolano B., Jennings J., Rosotti G., Birnstiel T., 2017, MNRAS, 472, 4117

Ercolano B., Picogna G., Monsch K., Drake J. J., Preibisch T., 2021, MNRAS, 508, 1675

Erkal J., et al., 2022, A&A, 666, A188

Espaillat C., et al., 2007, ApJ, 664, L111

Espaillat C., et al., 2013, ApJ, 762, 62

Facchini S., Clarke C. J., Bisbas T. G., 2016, MNRAS, 457, 3593

Fang M., et al., 2018, ApJ, 868, 28

Fang M., Pascucci I., Edwards S., Gorti U., Hillenbrand L. A., Carpenter J. M., 2023a, arXiv e-prints, p. arXiv:2301.09240

Fang M., et al., 2023b, arXiv e-prints, p. arXiv:2305.07929

Fatuzzo M., Adams F. C., 2008, ApJ, 675, 1361

Fedele D., van den Ancker M. E., Henning T., Jayawardhana R., Oliveira J. M., 2010, A&A, 510, A72

Fedele D., et al., 2018, A&A, 610, A24

Ferland G. J., 1979, MNRAS, 188, 669

Ferreira J., 1997, A&A, 319, 340

Field G. B., Somerville W. B., Dressler K., 1966, ARA&A, 4, 207

Flaccomio E., Damiani F., Micela G., Sciortino S., Harnden F. R. J., Murray S. S., Wolk S. J., 2003, ApJ, 582, 398

Flaherty K. M., et al., 2017, ApJ, 843, 150

Flaherty K., et al., 2020, ApJ, 895, 109

Font A. S., McCarthy I. G., Johnstone D., Ballantyne D. R., 2004, ApJ, 607, 890

Francis L., van der Marel N., 2020, ApJ, 892, 111

Franz R., Picogna G., Ercolano B., Birnstiel T., 2020, A&A, 635, A53

Franz R., Ercolano B., Casassus S., Picogna G., Birnstiel T., Pérez S., Rab C., Sharma A., 2022a, A&A, 657, A69

Franz R., Picogna G., Ercolano B., Casassus S., Birnstiel T., Rab C., Pérez S., 2022b, A&A, 659, A90

Gahm G. F., Fredga K., Liseau R., Dravins D., 1979, A&A, 73, L4

Gaia Collaboration et al., 2022, arXiv e-prints, p. arXiv:2208.00211

Galli D., Palla F., 1998, A&A, 335, 403

Galván-Madrid R., Liu H. B., Izquierdo A. F., Miotello A., Zhao B., Carrasco-González C., Lizano S., Rodríguez L. F., 2018, ApJ, 868, 39

Gammie C. F., 1996, ApJ, 457, 355

Gangi M., et al., 2020, A&A, 643, A32

Gárate M., et al., 2021, A&A, 655, A18

Gautier D., Hersant F., Mousis O., Lunine J. I., 2001, ApJ, 550, L227

Getman K. V., et al., 2005, ApJS, 160, 319

Getman K. V., Feigelson E. D., Garmire G. P., Broos P. S., Kuhn M. A., Preibisch T., Airapetian V. S., 2022, ApJ, 935, 43

Ginski C., et al., 2021, ApJ, 908, L25

Glassgold A. E., Najita J., Igea J., 1997, ApJ, 480, 344

Glassgold A. E., Najita J. R., Igea J., 2007, ApJ, 656, 515

Glover S. C. O., 2015, MNRAS, 451, 2082

Glover S. C. O., Abel T., 2008, MNRAS, 388, 1627

Glover S. C. O., Jappsen A. K., 2007, ApJ, 666, 1

Gorti U., Hollenbach D., 2004, ApJ, 613, 424

Gorti U., Hollenbach D., 2009, ApJ, 690, 1539

Gorti U., Hollenbach D., Dullemond C. P., 2015, ApJ, 804, 29

Grant S. L., et al., 2021, ApJ, 913, 123

Grassi T., Ercolano B., Szűcs L., Jennings J., Picogna G., 2020, MNRAS, 494, 4471

Greaves J. S., Rice W. K. M., 2010, MNRAS, 407, 1981

Gressel O., Ramsey J. P., Brinch C., Nelson R. P., Turner N. J., Bruderer S., 2020, ApJ, 896, 126

Grevesse N., Noels A., 1993, in Prantzos N., Vangioni-Flam E., Casse M., eds, Origin and Evolution of the Elements. pp 15–25

Güdel M., Telleschi A., 2007, A&A, 474, L25

Güdel M., et al., 2007a, A&A, 468, 353

Güdel M., Skinner S. L., Mel'Nikov S. Y., Audard M., Telleschi A., Briggs K. R., 2007b, A&A, 468, 529

Güdel M., et al., 2010, A&A, 519, A113

Güdel M., et al., 2018, A&A, 620, L1

Guenther E. W., Esposito M., Mundt R., Covino E., Alcalá J. M., Cusano F., Stecklum B., 2007, A&A, 467, 1147

Guillot T., Ida S., Ormel C. W., 2014, A&A, 572, A72

Gullbring E., Hartmann L., Briceño C., Calvet N., 1998, ApJ, 492, 323

Gundlach B., Blum J., 2015, ApJ, 798, 34

Gundlach B., et al., 2018, MNRAS, 479, 1273

Günther H. M., Liefke C., Schmitt J. H. M. M., Robrade J., Ness J. U., 2006, A&A, 459, L29

Gupta A., et al., 2023, A&A, 670, L8

Habing H. J., 1968, Bulletin of the Astronomical Institutes of the Netherlands, 19, 421

Haffert S. Y., Bohn A. J., de Boer J., Snellen I. A. G., Brinchmann J., Girard J. H., Keller C. U., Bacon R., 2019, Nature Astronomy, 3, 749

Haisch Karl E. J., Lada E. A., Lada C. J., 2001, ApJ, 553, L153

Hartigan P., Edwards S., Ghandour L., 1995, ApJ, 452, 736

Hartmann L., Calvet N., Gullbring E., D'Alessio P., 1998, ApJ, 495, 385

Hawley J. F., Gammie C. F., Balbus S. A., 1995, ApJ, 440, 742

Haworth T. J., Clarke C. J., 2019, MNRAS, 485, 3895

Haworth T. J., Clarke C. J., Owen J. E., 2016, MNRAS, 457, 1905

Haworth T. J., Facchini S., Clarke C. J., Cleeves L. I., 2017, MNRAS, 468, L108

Haworth T. J., Clarke C. J., Rahman W., Winter A. J., Facchini S., 2018, MNRAS, 481, 452

Hayashi C., 1981, Progress of Theoretical Physics Supplement, 70, 35

Hendler N. P., et al., 2018, MNRAS, 475, L62

Herbig G. H., 1960, ApJS, 4, 337

Herczeg G. J., Hillenbrand L. A., 2008, ApJ, 681, 594

Herczeg G. J., Wood B. E., Linsky J. L., Valenti J. A., Johns-Krull C. M., 2004, ApJ, 607, 369

Herczeg G. J., Najita J. R., Hillenbrand L. A., Pascucci I., 2007, ApJ, 670, 509

Hildebrand R. H., 1983, QJRAS, 24, 267

Hollenbach D., McKee C. F., 1979, ApJS, 41, 555

Hollenbach D., Johnstone D., Lizano S., Shu F., 1994, ApJ, 428, 654

Hu X., Tan J. C., Zhu Z., Chatterjee S., Birnstiel T., Youdin A. N., Mohanty S., 2018, ApJ, 857, 20

Huang J., et al., 2018, ApJ, 869, L42

Huang J., et al., 2020, ApJ, 898, 140

Huang J., et al., 2021, ApJS, 257, 19

Huang J., et al., 2022, ApJ, 930, 171

Huang J., Bergin E. A., Bae J., Benisty M., Andrews S. M., 2023, ApJ, 943, 107

Huélamo N., de Gregorio-Monsalvo I., Macias E., Pinte C., Ireland M., Tuthill P., Lacour S., 2015, A&A, 575, L5

Hutchison M. A., Clarke C. J., 2021, MNRAS, 501, 1127

Hutchison M. A., Price D. J., Laibe G., Maddison S. T., 2016, MNRAS, 461, 742

Igea J., Glassgold A. E., 1999, ApJ, 518, 848

Jaquet R., Staemmler V., Smith M. D., Flower D. R., 1992, Journal of Physics B Atomic Molecular Physics, 25, 285

Jensen E. L. N., Mathieu R. D., 1997, AJ, 114, 301

Johansen A., Oishi J. S., Mac Low M.-M., Klahr H., Henning T., Youdin A., 2007, Nature, 448, 1022

Johansen A., Blum J., Tanaka H., Ormel C., Bizzarro M., Rickman H., 2014, in Beuther H., Klessen R. S., Dullemond C. P., Henning T., eds, Protostars and Planets VI. pp 547–570 (arXiv:1402.1344), doi:10.2458/azu_uapress_9780816531240-ch024

Johnstone D., Hollenbach D., Bally J., 1998, ApJ, 499, 758

Jones M. G., Pringle J. E., Alexander R. D., 2012, MNRAS, 419, 925

Joy A. H., 1945, ApJ, 102, 168

Kama M., Shorttle O., Jermyn A. S., Folsom C. P., Furuya K., Bergin E. A., Walsh C., Keller L., 2019, ApJ, 885, 114

Kama M., et al., 2020, A&A, 634, A88

Kant I., 1755, Allgemeine Naturgeschichte und Theorie des Himmels

Kashyap V., Drake J. J., 2000, Bulletin of the Astronomical Society of India, 28, 475

Kastner J. H., Huenemoerder D. P., Schulz N. S., Canizares C. R., Weintraub D. A., 2002, ApJ, 567, 434

Kastner J. H., et al., 2018, ApJ, 863, 106

Kenyon S. J., Hartmann L., 1987, ApJ, 323, 714

Keppler M., et al., 2018, A&A, 617, A44

Khajenabi F., Shadmehri M., Pessah M. E., Martin R. G., 2018, MNRAS, 475, 5059

King G. W., et al., 2018, MNRAS, 478, 1193

Klaassen P. D., Mottram J. C., Maud L. T., Juhasz A., 2016, MNRAS, 460, 627

Klaassen P. D., et al., 2021, MNRAS, 500, 2813

Koepferl C. M., Ercolano B., Dale J., Teixeira P. S., Ratzka T., Spezzi L., 2013, MNRAS, 428, 3327

Komaki A., Nakatani R., Yoshida N., 2021, ApJ, 910, 51

Kramida A., Ralchenko Y., Reader J., NIST ASD Team 2022, NIST Atomic Spectra Database, doi:10.18434/T4W30F, https://physics.nist.gov/asd

Krems R. V., Jamieson M. J., Dalgarno A., 2006, ApJ, 647, 1531

Krolik J. H., Kallman T. R., 1983, ApJ, 267, 610

Kuiper R., Klahr H., Dullemond C., Kley W., Henning T., 2010, A&A, 511, A81

Kwan J., Krolik J. H., 1981, ApJ, 250, 478

Lada C. J., 1987, in Peimbert M., Jugaku J., eds, IAU Symposia Vol. 115, Star Forming Regions. p. 1

Lada C. J., Wilking B. A., 1984, ApJ, 287, 610

Lahuis F., van Dishoeck E. F., Blake G. A., Evans Neal J. I., Kessler-Silacci J. E., Pontoppidan K. M., 2007, ApJ, 665, 492

Laibe G., Price D. J., 2014, MNRAS, 444, 1940

Landi E., Del Zanna G., Young P. R., Dere K. P., Mason H. E., Landini M., 2006, ApJS, 162, 261

Laplace P.-S., 1796, Exposition du systeme du monde

Law C. J., et al., 2022, ApJ, 932, 114

Lebouteiller V., Barry D. J., Spoon H. W. W., Bernard-Salas J., Sloan G. C., Houck J. R., Weedman D. W., 2011, ApJS, 196, 8

Levermore C. D., Pomraning G. C., 1981, ApJ, 248, 321

Liffman K., 2003, PASA, 20, 337

Lin D. N. C., Pringle J. E., 1987, MNRAS, 225, 607

Liu B., Ji J., 2020, Research in Astronomy and Astrophysics, 20, 164

Lodato G., Scardoni C. E., Manara C. F., Testi L., 2017, MNRAS, 472, 4700

Lodato G., et al., 2023, MNRAS, 518, 4481

London R., 1978, ApJ, 225, 405

López-Martínez F., Gómez de Castro A. I., 2015, MNRAS, 448, 484

Louvet F., Dougados C., Cabrit S., Mardones D., Ménard F., Tabone B., Pinte C., Dent W. R. F., 2018, A&A, 618, A120

Lucy L. B., 1999, A&A, 344, 282

Lynden-Bell D., Pringle J. E., 1974, MNRAS, 168, 603

Maloney P. R., Hollenbach D. J., Tielens A. G. G. M., 1996, ApJ, 466, 561

Manara C. F., et al., 2013, A&A, 551, A107

Manara C. F., et al., 2016, A&A, 591, L3

Manara C. F., et al., 2017, A&A, 604, A127

Manara C. F., Morbidelli A., Guillot T., 2018, A&A, 618, L3

Manara C. F., et al., 2020, A&A, 639, A58

Manara C. F., Ansdell M., Rosotti G. P., Hughes A. M., Armitage P. J., Lodato G., Williams J. P., 2022, arXiv e-prints, p. arXiv:2203.09930

Martinez-Brunner R., et al., 2022, MNRAS, 510, 1248

Matsuyama I., Johnstone D., Murray N., 2003, ApJ, 585, L143

McGinnis P., Dougados C., Alencar S. H. P., Bouvier J., Cabrit S., 2018, A&A, 620, A87

Mesa D., et al., 2019, A&A, 632, A25

Mewe R., 1991, A&A Rev., 3, 127

Michel A., van der Marel N., Matthews B. C., 2021, ApJ, 921, 72

Mignone A., Bodo G., Massaglia S., Matsakos T., Tesileanu O., Zanni C., Ferrari A., 2007, ApJS, 170, 228

Miotello A., Bruderer S., van Dishoeck E. F., 2014, A&A, 572, A96

Miotello A., et al., 2017, A&A, 599, A113

Miotello A., Kamp I., Birnstiel T., Cleeves L. I., Kataoka A., 2022, arXiv e-prints, p. arXiv:2203.09818

Miret-Roig N., et al., 2020, A&A, 642, A179

Mulders G. D., Pascucci I., Manara C. F., Testi L., Herczeg G. J., Henning T., Mohanty S., Lodato G., 2017, ApJ, 847, 31

Mulders G. D., Pascucci I., Ciesla F. J., Fernandes R. B., 2021, ApJ, 920, 66

Müller A., et al., 2018, A&A, 617, L2

Musiolik G., Wurm G., 2019, ApJ, 873, 58

Najita J. R., Kenyon S. J., 2014, MNRAS, 445, 3315

Najita J. R., Carr J. S., Strom S. E., Watson D. M., Pascucci I., Hollenbach D., Gorti U., Keller L., 2010, ApJ, 712, 274

Nakatani R., Hosokawa T., Yoshida N., Nomura H., Kuiper R., 2018a, ApJ, 857, 57

Nakatani R., Hosokawa T., Yoshida N., Nomura H., Kuiper R., 2018b, ApJ, 865, 75

Natta A., Testi L., Muzerolle J., Randich S., Comerón F., Persi P., 2004, A&A, 424, 603

Natta A., Testi L., Alcalá J. M., Rigliaco E., Covino E., Stelzer B., D'Elia V., 2014, A&A, 569, A5

Nelson R. P., Gressel O., Umurhan O. M., 2013, MNRAS, 435, 2610

Neufeld D. A., Kaufman M. J., 1993, ApJ, 418, 263

Nisini B., Antoniucci S., Alcalá J. M., Giannini T., Manara C. F., Natta A., Fedele D., Biazzo K., 2018, A&A, 609, A87

Nomura H., Millar T. J., 2005, A&A, 438, 923

Nomura H., Aikawa Y., Tsujimoto M., Nakagawa Y., Millar T. J., 2007, ApJ, 661, 334

Olofsson J., et al., 2011, A&A, 528, L6

Olofsson J., et al., 2013, A&A, 552, A4

Omukai K., Hosokawa T., Yoshida N., 2010, ApJ, 722, 1793

Ormel C. W., Cuzzi J. N., 2007, A&A, 466, 413

Ormel C. W., Liu B., Schoonenberg D., 2017, A&A, 604, A1

Osterbrock D. E., 1962, ApJ, 135, 195

Osterbrock D. E., Ferland G. J., 2006, Astrophysics of gaseous nebulae and active galactic nuclei. University Science Books

Owen J. E., Clarke C. J., 2012, MNRAS, 426, L96

Owen T., Mahaffy P., Niemann H. B., Atreya S., Donahue T., Bar-Nun A., de Pater I., 1999, Nature, 402, 269

Owen J. E., Ercolano B., Clarke C. J., Alexander R. D., 2010, MNRAS, 401, 1415

Owen J. E., Ercolano B., Clarke C. J., 2011a, MNRAS, 411, 1104

Owen J. E., Ercolano B., Clarke C. J., 2011b, MNRAS, 412, 13

Owen J. E., Clarke C. J., Ercolano B., 2012, MNRAS, 422, 1880

Owen J. E., Hudoba de Badyn M., Clarke C. J., Robins L., 2013, MNRAS, 436, 1430

Paardekooper S. J., Mellema G., 2004, A&A, 425, L9

Papaloizou J., Lin D. N. C., 1984, ApJ, 285, 818

Parker E. N., 1958, ApJ, 128, 664

Pascucci I., Sterzik M., 2009, ApJ, 702, 724

Pascucci I., et al., 2007, ApJ, 663, 383

Pascucci I., et al., 2011, ApJ, 736, 13

Pascucci I., Ricci L., Gorti U., Hollenbach D., Hendler N. P., Brooks K. J., Contreras Y., 2014, ApJ, 795, 1

Pascucci I., Edwards S., Heyer M., Rigliaco E., Hillenbrand L., Gorti U., Hollenbach D., Simon M. N., 2015, ApJ, 814, 14

Pascucci I., et al., 2016, ApJ, 831, 125

Pascucci I., et al., 2020, ApJ, 903, 78

Pascucci I., Alexander R., Ballabio G., Clarke C., Gaspar A., Gorti U., 2021, Caught in the act of dispersing their disks? MIRI MRS can tell, JWST Proposal. Cycle 1, ID. #2260

Pascucci I., Cabrit S., Edwards S., Gorti U., Gressel O., Suzuki T., 2022, arXiv e-prints, p. arXiv:2203.10068

Pecaut M. J., Mamajek E. E., 2016, MNRAS, 461, 794

Pequignot D., 1990, A&A, 231, 499

Pfalzner S., Steinhausen M., Menten K., 2014, ApJ, 793, L34

Pfalzner S., Dehghani S., Michel A., 2022, ApJ, 939, L10

Pfeil T., Klahr H., 2019, ApJ, 871, 150

Picogna G., Ercolano B., Owen J. E., Weber M. L., 2019, MNRAS, 487, 691

Picogna G., Ercolano B., Espaillat C. C., 2021, MNRAS, 508, 3611

Pinilla P., Birnstiel T., Ricci L., Dullemond C. P., Uribe A. L., Testi L., Natta A., 2012, A&A, 538, A114

Pinilla P., et al., 2018, ApJ, 859, 32

Pinilla P., Pascucci I., Marino S., 2020, A&A, 635, A105

Pinte C., Ménard F., Duchêne G., Bastien P., 2006, A&A, 459, 797

Pinte C., Teague R., Flaherty K., Hall C., Facchini S., Casassus S., 2022, arXiv e-prints, p. arXiv:2203.09528

Pohl A., et al., 2017, A&A, 605, A34

Pollack J. B., Hollenbach D., Beckwith S., Simonelli D. P., Roush T., Fong W., 1994, ApJ, 421, 615

Pontoppidan K. M., Blake G. A., Smette A., 2011, ApJ, 733, 84

Powell D., Murray-Clay R., Schlichting H. E., 2017, ApJ, 840, 93

Powell D., Murray-Clay R., Pérez L. M., Schlichting H. E., Rosenthal M., 2019, ApJ, 878, 116

Preibisch T., et al., 2005, ApJS, 160, 401

Qiao L., Haworth T. J., Sellek A. D., Ali A. A., 2022, MNRAS, 512, 3788

Rab C., et al., 2022, A&A, 668, A154

Rafikov R. R., 2017, ApJ, 837, 163

Rapson V. A., Kastner J. H., Andrews S. M., Hines D. C., Macintosh B., Millar-Blanchaer M., Tamura M., 2015a, ApJ, 803, L10

Rapson V. A., et al., 2015b, ApJ, 810, 62

Ribas Á., Merín B., Bouy H., Maud L. T., 2014, A&A, 561, A54

Ribas Á., Bouy H., Merín B., 2015, A&A, 576, A52

Richert A. J. W., Getman K. V., Feigelson E. D., Kuhn M. A., Broos P. S., Povich M. S., Bate M. R., Garmire G. P., 2018, MNRAS, 477, 5191

Richling S., Yorke H. W., 1997, A&A, 327, 317

Rigliaco E., Natta A., Randich S., Testi L., Biazzo K., 2011, A&A, 525, A47

Rigliaco E., Pascucci I., Gorti U., Edwards S., Hollenbach D., 2013, ApJ, 772, 60

Robrade J., Schmitt J. H. M. M., Favata F., 2008, A&A, 486, 995

Rodenkirch P. J., Klahr H., Fendt C., Dullemond C. P., 2020, A&A, 633, A21

Rosotti G. P., Clarke C. J., 2018, MNRAS, 473, 5630

Rosotti G. P., Ercolano B., Owen J. E., Armitage P. J., 2013, MNRAS, 430, 1392

Rosotti G. P., Clarke C. J., Manara C. F., Facchini S., 2017, MNRAS, 468, 1631

Rosotti G. P., Booth R. A., Tazzari M., Clarke C., Lodato G., Testi L., 2019a, MNRAS, 486, L63

Rosotti G. P., Tazzari M., Booth R. A., Testi L., Lodato G., Clarke C., 2019b, MNRAS, 486, 4829

Sacco G. G., et al., 2012, ApJ, 747, 142

Sacco G. G., Kastner J. H., Forveille T., Principe D., Montez R., Zuckerman B., Hily-Blant P., 2014, A&A, 561, A42

Salz M., Banerjee R., Mignone A., Schneider P. C., Czesla S., Schmitt J. H. M. M., 2015, A&A, 576, A21

Savage B. D., Sembach K. R., 1996, ARA&A, 34, 279

Schmitt J. H. M. M., Robrade J., 2007, A&A, 462, L41

Schoonenberg D., Ormel C. W., 2017, A&A, 602, A21

Sellek A. D., Booth R. A., Clarke C. J., 2020a, MNRAS, 492, 1279

Sellek A. D., Booth R. A., Clarke C. J., 2020b, MNRAS, 498, 2845

Sellek A. D., Clarke C. J., Booth R. A., 2021, MNRAS, 506, 1

Shakura N. I., Sunyaev R. A., 1973, A&A, 500, 33

Shu F. H., Johnstone D., Hollenbach D., 1993, Icarus, 106, 92

Shull J. M., van Steenberg M. E., 1985, ApJ, 298, 268

Sicilia-Aguilar A., Hartmann L. W., Fürész G., Henning T., Dullemond C., Brandner W., 2006, AJ, 132, 2135

Simon M., Prato L., 1995, ApJ, 450, 824

Simon M. N., Pascucci I., Edwards S., Feng W., Gorti U., Hollenbach D., Rigliaco E., Keane J. T., 2016, ApJ, 831, 169

Sinclair C. A., Rosotti G. P., Juhasz A., Clarke C. J., 2020, MNRAS, 493, 3535

Skrutskie M. F., Dutkevitch D., Strom S. E., Edwards S., Strom K. M., Shure M. A., 1990, AJ, 99, 1187

Somigliana A., Toci C., Lodato G., Rosotti G., Manara C. F., 2020, MNRAS, 492, 1120

Somigliana A., Toci C., Rosotti G., Lodato G., Tazzari M., Manara C. F., Testi L., Lepri F., 2022, MNRAS, 514, 5927

Spitzer L., 1978, Physical processes in the interstellar medium, doi:10.1002/9783527617722.

Stecher T. P., Williams D. A., 1967, ApJ, 149, L29

Stelzer B., Neuhäuser R., 2001, A&A, 377, 538

Stelzer B., Schmitt J. H. M. M., 2004, A&A, 418, 687

Stempels H. C., Gahm G. F., 2004, A&A, 421, 1159

Stephens T. L., Dalgarno A., 1973, ApJ, 186, 165

Stognienko R., Henning T., Ossenkopf V., 1996, in Gustafson B. A. S., Hanner M. S., eds, Astronomical Society of the Pacific Conference Series Vol. 104, IAU Colloq. 150: Physics, Chemistry, and Dynamics of Interplanetary Dust. p. 427

Strömgren B., 1939, ApJ, 89, 526

Sturm J. A., McClure M. K., Harsono D., Facchini S., Long F., Kama M., Bergin E. A., van Dishoeck E. F., 2022, A&A, 660, A126

Suzuki T. K., Muto T., Inutsuka S.-i., 2010, ApJ, 718, 1289

Suzuki T. K., Ogihara M., Morbidelli A., Crida A., Guillot T., 2016, A&A, 596, A74

Swedenborg E., 1734, Opera Philosophica et Mineralia

Szulágyi J., Pascucci I., Ábrahám P., Apai D., Bouwman J., Moór A., 2012, ApJ, 759, 47

Tabone B., Rosotti G. P., Lodato G., Armitage P. J., Cridland A. J., van Dishoeck E. F., 2022a, MNRAS, 512, L74

Tabone B., Rosotti G. P., Cridland A. J., Armitage P. J., Lodato G., 2022b, MNRAS, 512, 2290

Takeuchi T., Lin D. N. C., 2005, ApJ, 623, 482

Takeuchi T., Clarke C. J., Lin D. N. C., 2005, ApJ, 627, 286

Tanaka H., Himeno Y., Ida S., 2005, ApJ, 625, 414

Tanaka K. E. I., Nakamoto T., Omukai K., 2013, ApJ, 773, 155

Tang Y. W., Guilloteau S., Piétu V., Dutrey A., Ohashi N., Ho P. T. P., 2012, A&A, 547, A84

Tarter C. B., Tucker W. H., Salpeter E. E., 1969, ApJ, 156, 943

Tayal S. S., 2007, ApJS, 171, 331

Tazzari M., et al., 2016, A&A, 588, A53

Tazzari M., et al., 2017, A&A, 606, A88

Teague R., et al., 2016, A&A, 592, A49

Telleschi A., Güdel M., Briggs K. R., Audard M., Palla F., 2007a, A&A, 468, 425

Telleschi A., Güdel M., Briggs K. R., Audard M., Scelsi L., 2007b, A&A, 468, 443

Testi L., et al., 2022, A&A, 663, A98

Tielens A. G. G. M., Hollenbach D., 1985, ApJ, 291, 722

Trapman L., Rosotti G., Bosman A. D., Hogerheijde M. R., van Dishoeck E. F., 2020, A&A, 640, A5

Tripathi A., Andrews S. M., Birnstiel T., Wilner D. J., 2017, ApJ, 845, 44

Tychoniec Ł., et al., 2020, arXiv e-prints, p. arXiv:2006.02812

Valenti J. A., Basri G., Johns C. M., 1993, AJ, 106, 2024

Verner D. A., Yakovlev D. G., 1995, A&AS, 109, 125

Verner D. A., Ferland G. J., Korista K. T., Yakovlev D. G., 1996, ApJ, 465, 487

Veronesi B., Paneque-Carreño T., Lodato G., Testi L., Pérez L. M., Bertin G., Hall C., 2021, ApJ, 914, L27

Walter F. M., 1986, ApJ, 306, 573

Walter F. M., Brown A., Mathieu R. D., Myers P. C., Vrba F. J., 1988, AJ, 96, 297

Wang L., Goodman J., 2017, ApJ, 847, 11

Wang L., Bai X.-N., Goodman J., 2019, ApJ, 874, 90

Weber M. L., Ercolano B., Picogna G., Hartmann L., Rodenkirch P. J., 2020, MNRAS, 496, 223

Weidenschilling S. J., 1977, MNRAS, 180, 57

Whelan E., Garcia P., 2008, in Bacciotti F., Testi L., Whelan E., eds, , Vol. 742, Jets from Young Stars II. p. 123

Whelan E. T., Pascucci I., Gorti U., Edwards S., Alexander R. D., Sterzik M. F., Melo C., 2021, ApJ, 913, 43

Whipple F. L., 1973, Radial Pressure in the Solar Nebula as Affecting the Motions of Planetesimals. p. 355

Wichittanakom C., Oudmaijer R. D., Fairlamb J. R., Mendigutía I., Vioque M., Ababakr K. M., 2020, MNRAS, 493, 234

Wilhelm M. J. C., Zwart S. P., Cournoyer-Cloutier C., Lewis S. C., Polak B., Tran A., Low M.-M. M., 2023, MNRAS,

Winter A. J., Clarke C. J., Rosotti G., Ih J., Facchini S., Haworth T. J., 2018, MNRAS, 478, 2700

Winter A. J., Ansdell M., Haworth T. J., Kruijssen J. M. D., 2020, MNRAS, 497, L40

Wölfer L., Picogna G., Ercolano B., van Dishoeck E. F., 2019, MNRAS, 490, 5596

Wölfer L., et al., 2023, A&A, 670, A154

Wolk S. J., Walter F. M., 1996, AJ, 111, 2066

Xie C. Y., in prep.

Xu Z., Herczeg G. J., Johns-Krull C. M., France K., 2021, ApJ, 921, 181

Yorke H. W., Kaisig M., 1995, Computer Physics Communications, 89, 29

Youdin A. N., Goodman J., 2005, ApJ, 620, 459

Zagaria F., Rosotti G. P., Lodato G., 2021, MNRAS, 504, 2235

Zagaria F., Clarke C. J., Rosotti G. P., Manara C. F., 2022, MNRAS, 512, 3538

Zahnle K. J., Kasting J. F., 1986, Icarus, 68, 462

Zhang S., et al., 2018, ApJ, 869, L47

Zormpas A., Birnstiel T., Rosotti G. P., Andrews S. M., 2022, A&A, 661, A66

Zubko V. G., Mennella V., Colangeli L., Bussoletti E., 1996, MNRAS, 282, 1321

van Boekel R., Güdel M., Henning T., Lahuis F., Pantin E., 2009, A&A, 497, 137

van Terwisga S. E., et al., 2020, A&A, 640, A27

van Terwisga S. E., Hacar A., van Dishoeck E. F., Oonk R., Portegies Zwart S., 2022, A&A, 661, A53

van der Marel N., Mulders G. D., 2021, AJ, 162, 28

van der Marel N., Bosman A. D., Krijt S., Mulders G. D., Bergner J. B., 2021, A&A, 653, L9

van der Marel N., et al., 2022, arXiv e-prints, p. arXiv:2204.08225